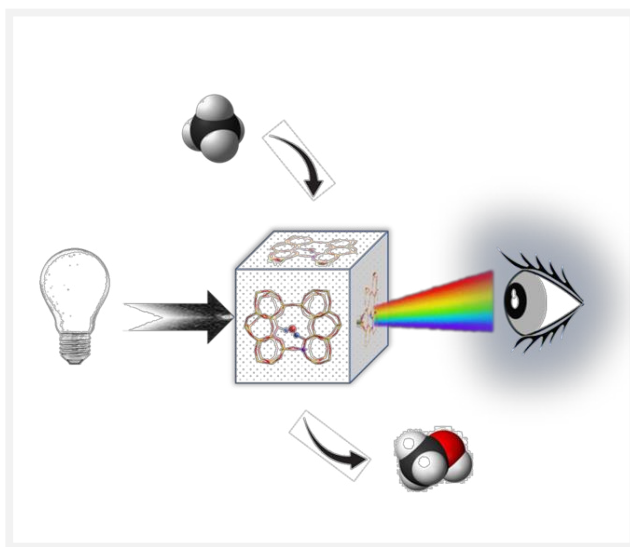




**Università degli Studi di Torino**  
Doctoral School of the University of Torino  
PhD Programme in Chemical and Materials Sciences XXXVI Cycle

## **Cu-based catalysts for C-H bond activation**



**Gabriele Deplano**

Supervisor:  
Prof. Silvia Bordiga

Co-supervisor:  
Dr. Matteo Signorile



## **Università degli Studi di Torino**

Doctoral School of the University of Torino

PhD Programme in Chemical and Materials Sciences XXXVI cycle

### **Cu-based catalysts for C-H bond activation**

Candidate: **Gabriele Deplano**

Supervisor: Prof. **Silvia Bordiga**

Co-supervisor: Dr. **Matteo Signorile**

Jury Members: Prof. **Lorenzo Mino**

University of Torino

Department of Chemistry

Prof. **Jeroen A. Van Bokhoven**

ETH Zürich

Department of Chemistry and Applied Biosciences

Prof. **Paola D'Angelo**

University of Roma La Sapienza

Department of Chemistry

Head of the Doctoral School: Prof. Alberto Rizzuti

PhD Programme Coordinator: Prof. Bartolomeo Civalleri

Torino, 2024

# Table of Contents

<b>Preface</b> .....	<b>1</b>
<b>1 Introduction</b> .....	<b>2</b>
1.1 C-H bond selective activation and the role of Cu .....	2
1.2 Characterization of Cu catalysts .....	4
<i>References</i> .....	6
<b>2 Cu-exchanged zeolites</b> .....	<b>21</b>
2.1 Materials & methods .....	21
2.1.1 <i>Cu zeolites</i> .....	21
2.1.2 <i>Experimental characterization of solid materials</i> .....	25
2.1.3 <i>Computational methods</i> .....	31
2.2 Reducibility of Cu in zeolites .....	33
2.3 Cu(II) and multinuclear species .....	49
2.4 Al distribution .....	57
<i>References</i> .....	66
<b>3 Cu-based organometallic complexes</b> .....	<b>78</b>
3.1 Materials & methods .....	78
3.1.1 <i>Cu complexes</i> .....	78
3.1.2 <i>Experimental characterization of complexes in solution</i> .....	81
3.1.3 <i>Computational methods</i> .....	86
3.2 Cu-bipyridyl complexes: multitechnique characterization and redox reversibility .....	88
3.3 Study on the oxidation of [Cu(6,6'-dimethyl-2,2'-bipyridyl) <sub>2</sub> ](PF <sub>6</sub> ) <sub>2</sub> with <i>t</i> BuOOH .....	96
3.4 Tetradentate Cu complexes .....	119
<i>References</i> .....	131
<b>Conclusions</b> .....	<b>137</b>
<b>Acknowledgments</b> .....	<b>138</b>



# Preface

The structure of this thesis work may appear somewhat confusing at first; this was, to a certain measure, both an inevitable and a wanted result. The PhD project from which it stems started along with (and was completely funded by) the ERC project titled “Unravelling the secrets of Cu-based catalyst for C-H activation (CuBE)”, which focused on the synthesis, characterization and eventual application of the titular materials. The project encompassed several types of Cu-based catalysts, both in the homogeneous (metallorganic complexes, enzymes) and the heterogeneous (zeolites, metal-organic frameworks) phase. My work in this context has primarily been in the investigation of two of these classes of materials through experimental and theoretical techniques; characterization (and the development of characterization tools) is meant to be the primary, cross-material focus of this thesis irrespective of the specific system under study.

The first class of materials investigated in this work is that of Cu-exchanged zeolites. The literature on these materials and their application is so vast that an equally lengthy document could be written as a systematic review on the topic, so three specific aspects were inquired in this instance: the characterization and quantification of Cu(I) species, the relationship between the Cu(I)/Cu(II) redox cycle and the formation of multimeric species, and the problem of the Al distribution in these materials.

Focus is then shifted towards Cu-based organometallic complexes, showcasing modified bipyridine and tetradentate imine-imidazole ligands. The former were subject to an extensive multitechnique characterization, which identified one of the complexes as candidate for catalytic activity; more sophisticated approaches to characterization were employed to investigate its oxidation by *tert*-butyl hydroperoxide and the resulting species. The latter was instead studied in its interaction with oxidizing/reducing agents, with the aim of characterizing the Cu(I)/Cu(II) cycle with a combined XAS/DFT approach.

# Chapter 1

## *Introduction*

### **1.1 C-H bond selective activation and the role of Cu**

The activation of the C-H bond of hydrocarbons is today a century-old problem, with first reports dating as far back as 1902 when Otto Dimroth reacted benzene with Hg(II) acetate, although the mechanistic aspects of the procedure used by Dimroth are not very close to modern approaches to this reaction.<sup>1-5</sup> The consequences that less impactful procedures to carry out this reaction(s) would have on the chemical industry in terms of energy consumption, resource management and environmental issues are hard to overstate, and it has been accordingly named a “Holy Grail” or “dream” reaction. A relevant example of this importance is the wide interest in the direct oxidation of CH<sub>4</sub> to CH<sub>3</sub>OH, as the alcohol analogue poses significantly reduced issues in transport and stocking of this resource. Anthropogenic sources account for almost two thirds of CH<sub>4</sub> worldwide emissions,<sup>6</sup> contributing to global warming due to its properties as greenhouse gas and wasting significant amounts of this energy-rich resource.<sup>7</sup> One of the reasons for the release of this gas in the atmosphere is the inefficiency in the application of the current technology for CH<sub>4</sub> valorisation in remote zones or small plants, with consequent flaring or plain air release in the worst case; even when proper treatment can be carried out, the syngas-based technologies currently used for this purpose are energy-intensive and often only viable for large-scale applications.<sup>8</sup> For these reasons, much scientific effort has been devoted to the development of catalytic procedures that could directly convert CH<sub>4</sub> to CH<sub>3</sub>OH, bypassing the syngas formation step of the reaction.<sup>9</sup> Ironically, the C-H bond in CH<sub>4</sub> is the most difficult to activate among simple alkanes, due to its high dissociation energy (440 kJ/mol) and its highly symmetrical structure. Even when activation of this bond is performed with acceptable yields, overoxidation to CO<sub>2</sub> is usually an issue due to the higher reactivity of partial oxidation products (*e.g.*, CH<sub>3</sub>OH). This *selectivity vs conversion* issue has plagued all the chemical systems proposed to carry out this reaction, as can be seen in Figure 1.1.

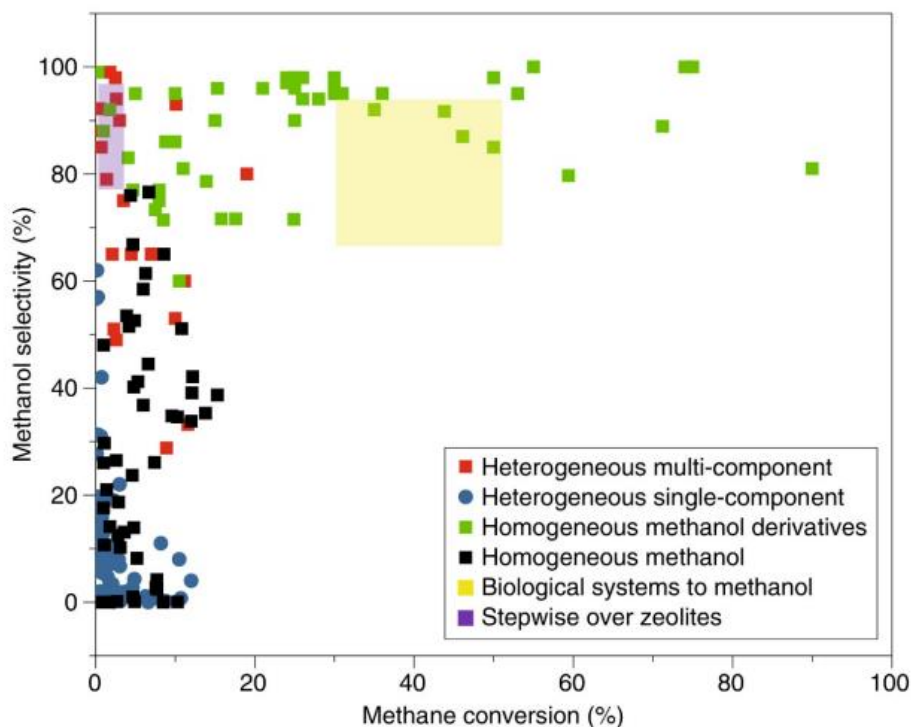


**Figure 1.1** Selectivity vs conversion for different systems for the direct conversion of  $\text{CH}_4$  to  $\text{CH}_3\text{OH}$ ; scatter points and graph from Ref<sup>10-12</sup>.

The highest conversions have historically been achieved by catalysts in the homogeneous phase, especially when converting  $\text{CH}_4$  to other derivatives (*e.g.*, methyl trifluoroacetate);<sup>13</sup> the drawback of these approaches, apart from the need for an additional step to obtain  $\text{CH}_3\text{OH}$ , has been the need for precious metal-based complexes and/or harsh reaction conditions (in terms of pressure and acidity of the medium). Materials that were able to retain high selectivity (*e.g.*, Cu-exchanged zeolites) have been instead characterized by very poor yields, also due to the chemical looping processes that need to be employed in most cases to perform the reaction using them. The interest soon shifted from trying to optimize conditions to make these materials perform better (since reaching economically viable industrial processes using them may not be even possible)<sup>14</sup> to understanding what makes them so selective and translate these conditions into different classes of catalysts. Another driving force for the quest of developing new catalysts with patterns that are known to enhance the reaction can be inferred by the yellow box in Figure 1.1: as is often the case for

catalytically demanding reactions, enzymatic systems like particulate methane monooxygenases (pMMOs) have been found to perform direct conversion of  $\text{CH}_4$  to  $\text{CH}_3\text{OH}$  in mild conditions (ambient temperature and pressure in aqueous solution) and using Cu as active metal.<sup>15–17</sup> Similarly, proteins from the lytic polysaccharide monooxygenase (LPMO) family have been discovered to selectively oxidize the C-H bond in long chain polysaccharides and could possibly be employed for similar reactions.<sup>18–30</sup> Synthetic “biomimetic” (or more accurately, biologically inspired)<sup>12</sup> catalysts trying to replicate these metal-organic patterns have been developed,<sup>31</sup> though no material that can satisfy requirements for industrial application has been found yet. Some authors have tried to exploit this enormous number of attempts as a starting point for top-down approaches, using the available data to develop kinetic models of the reaction to predict the characteristics needed to build a working catalyst<sup>32</sup> or even training machine learning algorithms with this data to directly predict chemical structures that would work.<sup>33</sup>

## 1.2 Characterization of Cu catalysts

The most common redox chemistry of Cu is centred around the 1-electron Cu(I)/Cu(II) couple, although Cu(III) has also been observed and studied.<sup>34</sup> Common inorganic salts of Cu(I) are generally unstable in aqueous solution, as disproportionation to metallic Cu and Cu(II) readily happens upon dissolution in  $\text{H}_2\text{O}$ . Stabilization of this oxidation state can be achieved by both inorganic and organic ligands generating species with differing redox potential. Cu(I) complexes are often characterized by low coordination numbers (2-4), both because of the low formal charge of the metal and the filled d-orbital set; when it is coordinated by four ligands, the metal site usually prefers tetrahedral configuration with respect with square planar. In contrast, Cu(II) is most often found in octahedral coordination with strong Jahn-Teller distortions. These general trends can be subject to great variability depending on the ligands, the solvent or host material and the reaction conditions. As an example, widely accepted notions in inorganic chemistry, like the aforementioned octahedral coordination of Cu(II), were revealed to only hold true in the solid state, while a wider variety of structurally plastic lower-coordinated geometries were found to exist in solution even for apparently simple ligands like  $\text{H}_2\text{O}$ ,<sup>35–42</sup>  $\text{CH}_3\text{CN}$ <sup>43</sup>



and NH<sub>3</sub>.<sup>44</sup> Because of this variability, a plethora of experimental and theoretical tools have been developed in the years to study the geometrical and electronic structure of these species in an attempt to find structure-property relationships. While X-ray diffraction is surely the most direct way to obtain structural parameters in a decisive manner,<sup>45–50</sup> many systems cannot be characterized using this technique: apart from the often challenging task of obtaining high-quality crystals for diffraction in single-crystal studies, samples that are not characterized by long-range order (like diluted Cu sites in zeolites and Cu complexes in solution) require different approaches. An increasing popularity of total scattering-based techniques (like pair distribution function analysis) in the recent years has allowed to retrieve this structural sensitivity even in disordered cases, with the caveats of intensive data analysis procedures and the requirement of synchrotron light.<sup>51–57</sup> A major role in structural determination has also been played by Cu K-edge EXAFS spectroscopy,<sup>58–75</sup> allowing for extremely accurate determination of bond distances in the vicinity of the metal atom regardless of long- or short-range order; the use of EXAFS (and X-ray spectroscopy in general) has been a staple of the materials science community for years, but use of this technique for studies in solution is also becoming frequent.<sup>34,37,40,41,43,76–80</sup> Although lab-scale instruments are becoming more common,<sup>81</sup> X-ray spectroscopy today remains a large-scale facility-dependent technique. Vibrational spectroscopies (mainly infrared and Raman) are often employed in lab-scale characterization to provide structural evidence for the formation of particular groups in the sample, via direct identification of functional groups or indirect observations (*e.g.*, perturbation of other vibrational modes or interaction of the sites with probe molecules).<sup>82–86,49,87–90,60,91,92</sup> Electronic spectroscopies involving transitions in the HOMO-LUMO (UV-Vis) or core-valence (XAS/XES) regions are routinely used as a probe for oxidation state and coordination geometry around Cu,<sup>60,67,93–97,34,71,98–102,43,82,83,85,98,103–109</sup> while EPR spectroscopy can retrieve similar and complementary information to electronic spectroscopy in this context<sup>42,110–117</sup> (and especially fine details can be investigated using pulsed techniques),<sup>118–123</sup> NMR spectroscopy is usually discarded as an option in the presence of paramagnetic Cu(II) species (with some notable exceptions).<sup>120,124–127</sup> Isothermal gas adsorption/desorption can be used to perform quantitative speciation studies on solid materials (see Appendix A3), and temperature-

programmed adsorption/desorption experiments have been used to both study thermal stability of adducts and identify species based on their evolution as a function of temperature.<sup>113,114,128–132</sup> Cutting-edge electron microscopy techniques can provide information on solid catalysts from the reactor to the atomistic scale with remarkable Z-contrast.<sup>133–135</sup> Virtually all techniques listed above can be and have been supported by quantum chemistry calculations in the frame of density functional of wavefunction theories, since reliable ways of calculating not only geometries and energies, but practically any kind of spectroscopy with unprecedented accuracy is available today for both periodic and molecular systems. Sophisticated molecular dynamic and metadynamic simulation schemes are also available for cases in which time evolution of the system is important and/or several minima in the potential energy surface require investigation of simulation of averaged properties. The need to extract, treat, interpret and predict an ever-increasing amount of data is reflected by the rise in popularity of multivariate statistical methods and machine learning-assisted approaches to characterization; one very powerful and practically cost-free example of these methods (*i.e.*, multivariate curve resolution)<sup>136–139</sup> is extensively applied to spectroscopic characterization in this document. As a final remark, the experimental techniques described above are rarely used in isolation in model conditions: the spread of multitechnique studies exploiting *in situ* (*i.e.*, in the temperature/pressure/chemical conditions of the reaction under investigation) and *operando* (*i.e.*, with simultaneous quantitative assessment of reaction products) conditions<sup>49,50,143–152,82,83,109,110,126,140–142</sup> can be taken as a testament of both the challenge of identifying active species and mechanisms in catalytic systems and the tremendous insight that can be gained by interfacing different techniques and analytical tools.

## References

1. Goldman, A. S. & Goldberg, K. I. Organometallic C—H Bond Activation: An Introduction. 10, 1–43 (2004).
2. Dimroth, O. Ueber die Mercurirung aromatischer Verbindungen. Berichte der Dtsch. Chem. Gesellschaft 35, 2032–2045 (1902).
3. Dimroth, O. Directe Einführung von Quecksilber in aromatische Verbindungen. Berichte der Dtsch. Chem. Gesellschaft 31, 2154–2156 (1898).

4. Dimroth, O. Ueber die Einwirkung von Quecksilberoxydsalzen auf aromatische Verbindungen. *Berichte der Dtsch. Chem. Gesellschaft* 32, 758–765 (1899).
5. Schramm, R. M., Klapproth, W. & Westheimer, F. H. THE MECHANISM OF AROMATIC MERCURATION. II Reaction Kinetics. (1950).
6. Bousquet, P. et al. Contribution of anthropogenic and natural sources to atmospheric methane variability. *Nature* 443, 439–443 (2006).
7. Solomon, D. Q., Qin, M., Manning, Z., Chen, M., Marquis, K.B., Averyt, M. T. and H. L. M. IPCC (2007). *Climate Change 2007: The Physical Science Basis*. (2007).
8. Taifan, W. & Baltrusaitis, J. CH<sub>4</sub> conversion to value added products: Potential, limitations and extensions of a single step heterogeneous catalysis. *Appl. Catal. B Environ.* 198, 525–547 (2016).
9. Sushkevich, V. L., Palagin, D., Ranocchiari, M. & Van Bokhoven, J. A. Selective anaerobic oxidation of methane enables direct synthesis of methanol. *Science* (80- ). 356, 523–527 (2017).
10. Ravi, M., Ranocchiari, M. & van Bokhoven, J. A. The Direct Catalytic Oxidation of Methane to Methanol—A Critical Assessment. *Angew. Chemie Int. Ed.* 56, 16464–16483 (2017).
11. Ravi, M., van Bokhoven, J. A., Ravi, M., van Bokhoven, J. A. & van Bokhoven Paul Scherrer, J. A. Homogeneous Copper-Catalyzed Conversion of Methane to Methyl Trifluoroacetate in High Yield at Low Pressure. *ChemCatChem* 10, 2383–2386 (2018).
12. Ravi, M. et al. Misconceptions and challenges in methane-to-methanol over transition-metal-exchanged zeolites. *Nat. Catal.* 2019 26 2, 485–494 (2019).
13. Kao, L. C., Hutson, A. C. & Sen, A. Low-Temperature, Palladium(II)-Catalyzed, Solution-Phase Oxidation of Methane to a Methanol Derivative. *J. Am. Chem. Soc.* 113, 700–701 (1991).
14. Lange, J. P., Sushkevich, V. L., Knorpp, A. J. & Van Bokhoven, J. A. Methane-to-Methanol via Chemical Looping: Economic Potential and Guidance for Future Research. *Ind. Eng. Chem. Res.* 58, 8674–8680 (2019).
15. Lieberman, R. L. & Rosenzweig, A. C. Crystal structure of a membrane-bound metalloenzyme that catalyses the biological oxidation of methane. *Nat.* 2005 4347030 434, 177–182 (2005).

16. Hanson, R. S. & Hanson, T. E. Methanotrophic bacteria. *Microbiol. Rev.* 60, 439–471 (1996).
17. Zhu, Y. et al. Structure and activity of particulate methane monooxygenase arrays in methanotrophs. *Nat. Commun.* 2022 131 13, 1–10 (2022).
18. Vaaje-Kolstad, G. et al. An oxidative enzyme boosting the enzymatic conversion of recalcitrant polysaccharides. *Science* (80-. ). 330, 219–222 (2010).
19. Quinlan, R. J. et al. Insights into the oxidative degradation of cellulose by a copper metalloenzyme that exploits biomass components. *Proc. Natl. Acad. Sci. U. S. A.* 108, 15079–15084 (2011).
20. Courtade, G. et al. Mechanistic basis of substrate-O<sub>2</sub> coupling within a chitin-active lytic polysaccharide monooxygenase: An integrated NMR/EPR study. *Proc. Natl. Acad. Sci. U. S. A.* 117, 19178–19189 (2020).
21. Bissaro, B., Kommedal, E., Røhr, Å. K. & Eijsink, V. G. H. Controlled depolymerization of cellulose by light-driven lytic polysaccharide oxygenases. *Nat. Commun.* 2020 111 11, 1–12 (2020).
22. Stepnov, A. A. et al. Unraveling the roles of the reductant and free copper ions in LPMO kinetics. *Biotechnol. Biofuels* 14, 1–14 (2021).
23. Kjaergaard, C. H. et al. Spectroscopic and computational insight into the activation of O<sub>2</sub> by the mononuclear Cu center in polysaccharide monooxygenases. *Proc. Natl. Acad. Sci. U. S. A.* 111, 8797–8802 (2014).
24. Kracher, D. et al. Extracellular electron transfer systems fuel cellulose oxidative degradation. *Science* (80-. ). 352, 1098–1101 (2016).
25. Frandsen, K. E. H. et al. The molecular basis of polysaccharide cleavage by lytic polysaccharide monooxygenases. *Nat. Chem. Biol.* 2016 124 12, 298–303 (2016).
26. Bissaro, B. et al. Oxidative cleavage of polysaccharides by monocopper enzymes depends on H<sub>2</sub>O<sub>2</sub>. *Nat. Chem. Biol.* 2017 1310 13, 1123–1128 (2017).
27. Kuusk, S. et al. Kinetics of H<sub>2</sub>O<sub>2</sub>-driven degradation of chitin by a bacterial lytic polysaccharide monooxygenase. *J. Biol. Chem.* 293, 523–531 (2018).
28. Chylenski, P. et al. Lytic Polysaccharide Monooxygenases in Enzymatic Processing of Lignocellulosic Biomass. *ACS Catal.* 9, 4970–4991 (2019).

29. Bissaro, B. et al. Molecular mechanism of the chitinolytic peroxygenase reaction. *Proc. Natl. Acad. Sci. U. S. A.* 117, 1504–1513 (2020).
30. Jones, S. M., Transue, W. J., Meier, K. K., Kelemen, B. & Solomon, E. I. Kinetic analysis of amino acid radicals formed in H<sub>2</sub>O<sub>2</sub>-driven CuI LPMO reoxidation implicates dominant homolytic reactivity. *Proc. Natl. Acad. Sci. U. S. A.* 117, (2020).
31. Baek, J. et al. Bioinspired Metal-Organic Framework Catalysts for Selective Methane Oxidation to Methanol. *J. Am. Chem. Soc.* 140, 18208–18216 (2018).
32. Latimer, A. A., Kakekhani, A., Kulkarni, A. R. & Nørskov, J. K. Direct Methane to Methanol: The Selectivity-Conversion Limit and Design Strategies. *ACS Catal.* 8, 6894–6907 (2018).
33. Nandy, A., Duan, C., Goffinet, C. & Kulik, H. J. New Strategies for Direct Methane-to-Methanol Conversion from Active Learning Exploration of 16 Million Catalysts. *JACS Au* 2, 1200–1213 (2022).
34. Geoghegan, B. L. et al. Combining Valence-to-Core X-ray Emission and Cu K-edge X-ray Absorption Spectroscopies to Experimentally Assess Oxidation State in Organometallic Cu(I)/(II)/(III) Complexes. *J. Am. Chem. Soc.* 144, 2520–2534 (2022).
35. Bowron, D. T. et al. The hydration structure of Cu<sup>2+</sup>: more tetrahedral than octahedral? *RSC Adv.* 3, 17803–17812 (2013).
36. Gómez-Salces, S., Aguado, F., Valiente, R. & Rodríguez, F. Unraveling the Coordination Geometry of Copper(II) Ions in Aqueous Solution through Absorption Intensity. *Angew. Chemie Int. Ed.* 51, 9335–9338 (2012).
37. Frank, P., Benfatto, M., Qayyam, M., Hedman, B. & Hodgson, K. O. A high-resolution XAS study of aqueous Cu(II) in liquid and frozen solutions: Pyramidal, polymorphic, and non-centrosymmetric. *J. Chem. Phys.* 142, (2015).
38. Pasquarello, A. et al. First Solvation Shell of the Cu(II) Aqua Ion: Evidence for Fivefold Coordination. *Science* (80-. ). 291, 856–859 (2001).
39. Benfatto, M., D’Angelo, P., Della Longa, S. & Pavel, N. V. Evidence of distorted fivefold coordination of the Cu<sup>2+</sup> aqua ion from an x-ray-absorption spectroscopy quantitative analysis. *Phys. Rev. B* 65, 174205 (2002).

40. Frank, P. et al. The solution structure of  $[\text{Cu}(\text{aq})]^{2+}$  and its implications for rack-induced bonding in blue copper protein active sites. *Inorg. Chem.* 44, 1922–1933 (2005).
41. Frank, P., Benfatto, M. & Qayyum, M.  $2+$  is structurally plastic and the axially elongated octahedron goes missing. *J. Chem. Phys.* 148, (2018).
42. de Almeida, K. J., Rinkevicius, Z., Hugosson, H. W., Ferreira, A. C. & Ågren, H. Modeling of EPR parameters of copper(II) aqua complexes. *Chem. Phys.* 332, 176–187 (2007).
43. D'Angelo, P. & Migliorati, V. Solvation structure of  $\text{Zn}^{2+}$  and  $\text{Cu}^{2+}$  ions in acetonitrile: A combined EXAFS and XANES study. *J. Phys. Chem. B* 119, 4061–4067 (2015).
44. Frank, P., Benfatto, M., Hedman, B. & Hodgson, K. O. Solution  $[\text{Cu}(\text{amm})]^{2+}$  is a strongly solvated square pyramid: A full account of the copper K-edge XAS spectrum within single-electron theory. *Inorg. Chem.* 47, 4126–4139 (2008).
45. Fickel, D. W. & Lobo, R. F. Copper coordination in Cu-SSZ-13 and Cu-SSZ-16 investigated by variable-temperature XRD. *J. Phys. Chem. C* 114, 1633–1640 (2010).
46. Beale, A. M., Lezcano-Gonzalez, I., Slawinski, W. A. & Wragg, D. S. Correlation between Cu ion migration behaviour and deNO<sub>x</sub> activity in Cu-SSZ-13 for the standard NH<sub>3</sub>-SCR reaction. *Chem. Commun.* 52, 6170–6173 (2016).
47. Deka, U. et al. Confirmation of isolated  $\text{Cu}^{2+}$  ions in SSZ-13 zeolite as active sites in NH<sub>3</sub>-selective catalytic reduction. *J. Phys. Chem. C* 116, 4809–4818 (2012).
48. Andersen, C. W. et al. Location of  $\text{Cu}^{2+}$  in CHA zeolite investigated by X-ray diffraction using the Rietveld/maximum entropy method. *IUCr* 1, 382–386 (2014).
49. Ipek, B. et al. Formation of  $[\text{Cu}_2\text{O}_2]^{2+}$  and  $[\text{Cu}_2\text{O}]^{2+}$  toward C-H Bond Activation in Cu-SSZ-13 and Cu-SSZ-39. *ACS Catal.* 7, 4291–4303 (2017).
50. Mentzen, B. F. & Bergeret, G. Crystallographic determination of the positions of the copper cations in zeolite MFI. *J. Phys. Chem. C* 111, 12512–12516 (2007).
51. Petkov, V. Nanostructure by high-energy X-ray diffraction. *Mater. Today* 11, 28–38 (2008).

52. Allan, P. K. et al. Pair distribution function-derived mechanism of a single-crystal to disordered to single-crystal transformation in a hemilabile metal–organic framework. *Chem. Sci.* 3, 2559–2564 (2012).
53. Rodriguez, J. A., Hanson, J. C. & Chupas, P. J. In-situ Characterization of Heterogeneous Catalysts.
54. Platero-Prats, A. E. et al. Addressing the characterisation challenge to understand catalysis in MOFs: the case of nanoscale Cu supported in NU-1000. *Faraday Discuss.* 201, 337–350 (2017).
55. Terban, M. W. & Billinge, S. J. L. Structural Analysis of Molecular Materials Using the Pair Distribution Function. *Chem. Rev.* 122, 1208–1272 (2022).
56. Mathiesen, J. K. et al. Exploring the mobility of Cu in bimetallic nanocrystals to promote atomic-scale transformations under a reactive gas environment. *J. Mater. Chem. A* 11, 9654–9667 (2023).
57. Xie, Z. L. et al. Bimetallic Copper/Ruthenium/Osmium Complexes: Observation of Conformational Differences Between the Solution Phase and Solid State by Atomic Pair Distribution Function Analysis. *Angew. Chemie Int. Ed.* 61, e202111764 (2022).
58. Grundner, S. et al. Single-site trinuclear copper oxygen clusters in mordenite for selective conversion of methane to methanol. *Nat. Commun.* 6, (2015).
59. Brezicki, G., Kammert, J. D., Gunnoe, T. B., Paolucci, C. & Davis, R. J. Insights into the Speciation of Cu in the Cu-H-Mordenite Catalyst for the Oxidation of Methane to Methanol. *ACS Catal.* 9, 5308–5319 (2019).
60. Lamberti, C. et al. XAFS, IR, and UV–Vis Study of the CuI Environment in CuI-ZSM-5. *J. Phys. Chem. B* 101, 344–360 (1997).
61. Zecchina, A. et al. Mono-, di-, and tricarbonylic species in copper(I)-exchanged zeolite ZSM-5: Comparison with homogeneous copper(I) carbonylic structures. *J. Phys. Chem. B* 103, 3833–3844 (1999).
62. Kuroda, Y., Itadani, A., Kumashiro, R., Fujimoto, T. & Nagao, M. Anomalous valence changes and specific dinitrogen adsorption features of copper ion exchanged in ZSM-5 zeolite prepared from an aqueous solution of  $[\text{Cu}(\text{NH}_3)_2]^+$ . *Phys. Chem. Chem. Phys.* 6, 2534–2541 (2004).

63. Lamberti, C. et al. CuI-Y and CuII-Y zeolites: a XANES, EXAFS and visible-NIR study. *Chem. Phys. Lett.* 269, 500–508 (1997).
64. Lamberti, C. et al. XANES, EXAFS and FTIR characterization of copper-exchanged mordenite. *J. Chem. Soc. Faraday Trans.* 94, 1519–1525 (1998).
65. Prestipino, C., Capello, L., D’Acapito, F. & Lamberti, C. Local structure of [CuI(CO)2]<sup>+</sup> adducts hosted inside ZSM-5 zeolite probed by EXAFS, XANES and IR spectroscopies. *Phys. Chem. Chem. Phys.* 7, 1743–1746 (2005).
66. Korhonen, S. T., Fickel, D. W., Lobo, R. F., Weckhuysen, B. M. & Beale, A. M. Isolated Cu<sup>2+</sup> ions: active sites for selective catalytic reduction of NO. *Chem. Commun.* 47, 800–802 (2010).
67. Borfecchia, E. et al. Revisiting the nature of Cu sites in the activated Cu-SSZ-13 catalyst for SCR reaction. *Chem. Sci.* 6, 548–563 (2014).
68. Alayon, E. M. C., Nachtegaal, M., Bodi, A., Ranocchiari, M. & Van Bokhoven, J. A. Bis(μ-oxo) versus mono(μ-oxo)dicopper cores in a zeolite for converting methane to methanol: an in situ XAS and DFT investigation. *Phys. Chem. Chem. Phys.* 17, 7681–7693 (2015).
69. Ikuno, T. et al. Formation of Active Cu-oxo Clusters for Methane Oxidation in Cu-Exchanged Mordenite. *J. Phys. Chem. C* 123, 8759–8769 (2019).
70. Alayon, E. M. C., Nachtegaal, M., Bodi, A. & Van Bokhoven, J. A. Reaction conditions of methane-to-methanol conversion affect the structure of active copper sites. *ACS Catal.* 4, 16–22 (2014).
71. J. A. Van Bokhoven, C. L. XAFS Techniques for Catalysts, Nanomaterials, and Surfaces. *XAFS Techniques for Catalysts, Nanomaterials, and Surfaces* (Springer International Publishing, 2017). doi:10.1007/978-3-319-43866-5.
72. Alayon, E. M. C., Nachtegaal, M., Kleymentov, E. & Van Bokhoven, J. A. Determination of the electronic and geometric structure of Cu sites during methane conversion over Cu-MOR with X-ray absorption spectroscopy. *Microporous Mesoporous Mater.* 166, 131–136 (2013).
73. Molokova, A. Y. et al. Elucidating the reaction mechanism of SO<sub>2</sub> with Cu-CHA catalysts for NH<sub>3</sub>-SCR by X-ray absorption spectroscopy. *Chem. Sci.* 14, 11521–11531 (2023).



74. Bordiga, S., Groppo, E., Agostini, G., Van Bokhoven, J. A. & Lamberti, C. Reactivity of surface species in heterogeneous catalysts probed by in situ x-ray absorption techniques. *Chem. Rev.* 113, 1736–1850 (2013).
75. van Bokhoven, J. A. & Lamberti, C. X-Ray Absorption and X-Ray Emission Spectroscopy: Theory and Applications. *X-Ray Absorpt. X-Ray Emiss. Spectrosc. Theory Appl.* 1–2, 1–845 (2015).
76. Persson, I. et al. EXAFS Study on the Coordination Chemistry of the Solvated Copper(II) Ion in a Series of Oxygen Donor Solvents. *Inorg. Chem.* 59, 9538–9550 (2020).
77. Zitolo, A., Chillemi, G. & D'Angelo, P. X-ray absorption study of the solvation structure of Cu<sup>2+</sup> in methanol and dimethyl sulfoxide. *Inorg. Chem.* 51, 8827–8833 (2012).
78. Carrera, F., Sánchez Marcos, E., Merklings, P. J., Chaboy, J. & Muñoz-Páez, A. Nature of metal binding sites in Cu(II) complexes with histidine and related N-coordinating ligands, as studied by EXAFS. *Inorg. Chem.* 43, 6674–6683 (2004).
79. Tromp, M. et al. Cu K-Edge EXAFS Characterisation of Copper(i) Arenethiolate Complexes in both the Solid and Liquid State: Detection of Cu–Cu Coordination. doi:10.1002/1521-3765(20021216)8:24.
80. Hall, K. R. et al. A Conserved Second Sphere Residue Tunes Copper Site Reactivity in Lytic Polysaccharide Monooxygenases. *J. Am. Chem. Soc.* 145, 18888–18903 (2023).
81. Zimmermann, P. et al. Modern X-ray spectroscopy: XAS and XES in the laboratory. *Coord. Chem. Rev.* 423, 213466 (2020).
82. Woertink, J. S. et al. A [Cu<sub>2</sub>O]<sup>2+</sup> core in Cu-ZSM-5, the active site in the oxidation of methane to methanol. *Proc. Natl. Acad. Sci. U. S. A.* 106, 18908–18913 (2009).
83. Vanelderen, P. et al. Spectroscopic definition of the copper active sites in mordenite: Selective methane oxidation. *J. Am. Chem. Soc.* 137, 6383–6392 (2015).
84. Snyder, B. E. R., Vanelderen, P., Schoonheydt, R. A., Sels, B. F. & Solomon, E. I. Second-Sphere Effects on Methane Hydroxylation in Cu-Zeolites. *J. Am. Chem. Soc.* 140, 9236–9243 (2018).

85. Smeets, P. J. et al. Oxygen precursor to the reactive intermediate in methanol synthesis by Cu-ZSM-5. *J. Am. Chem. Soc.* 132, 14736–14738 (2010).
86. Baldwin, M. J. et al. Spectroscopic Studies of Side-On Peroxide-Bridged Binuclear Copper(II) Model Complexes of Relevance to Oxyhemocyanin and Oxytyrosinase. *J. Am. Chem. Soc.* 114, 10421–10431 (1992).
87. Pappas, D. K. et al. Methane to Methanol: Structure-Activity Relationships for Cu-CHA. *J. Am. Chem. Soc.* 139, 14961–14975 (2017).
88. Giordanino, F. et al. Characterization of Cu-exchanged SSZ-13: a comparative FTIR, UV-Vis, and EPR study with Cu-ZSM-5 and Cu- $\beta$  with similar Si/Al and Cu/Al ratios. *Dalt. Trans.* 42, 12741–12761 (2013).
89. Concepción, P., Boronat, M., Millán, R., Moliner, M. & Corma, A. Identification of Distinct Copper Species in Cu-CHA Samples Using NO as Probe Molecule. A Combined IR Spectroscopic and DFT Study. *Top. Catal.* 60, 1653–1663 (2017).
90. Szanyi, J., Kwak, J. H., Zhu, H. & Peden, C. H. F. Characterization of Cu-SSZ-13 NH<sub>3</sub> SCR catalysts : an in situ FTIR study. *Phys. Chem. Chem. Phys.* 15, 2368–2380 (2013).
91. Turnes Palomino, G., Bordiga, S., Lamberti, C., Zecchina, A. & Otero Areán, C. Vibrational and optical spectroscopic studies on copper-exchanged ferrierite. *Stud. Surf. Sci. Catal.* 142, 199–206 (2002).
92. Dědeček, J., Sobalík, Z., Tvarůžková, Z., Kaucký, D. & Wichterlová, B. Coordination of Cu ions in high-silica zeolite matrices. Cu<sup>+</sup> photoluminescence, IR of NO adsorbed on Cu<sup>2+</sup>, and Cu<sup>2+</sup> ESR study. *J. Phys. Chem.* 99, 16327–16337 (1995).
93. Marberger, A. et al. Time-resolved copper speciation during selective catalytic reduction of NO on Cu-SSZ-13. *Nat. Catal.* 2018 13 1, 221–227 (2018).
94. Oord, R., Schmidt, J. E. & Weckhuysen, B. M. Methane-to-methanol conversion over zeolite Cu-SSZ-13, and its comparison with the selective catalytic reduction of NO<sub>x</sub> with NH<sub>3</sub>. *Catal. Sci. Technol.* 8, 1028–1038 (2018).
95. Anpo, M. et al. The relationship between the local structure of copper(I) ions on Cu<sup>+</sup>/zeolite catalysts and their photocatalytic reactivities for the decomposition of NO<sub>x</sub> into N<sub>2</sub> and O<sub>2</sub> at 275 K. *Coord. Chem. Rev.* 171, 175–184 (1998).

96. Garino, C., Borfecchia, E., Gobetto, R., van Bokhoven, J. A. & Lamberti, C. Determination of the electronic and structural configuration of coordination compounds by synchrotron-radiation techniques. *Coord. Chem. Rev.* 277–278, 130–186 (2014).
97. Singh, J., Lamberti, C. & Bokhoven, J. A. V. Advanced X-ray absorption and emission spectroscopy: in situ catalytic studies. *Chem. Soc. Rev.* 39, 4754–4766 (2010).
98. Solomon, E. I. et al. Copper active sites in biology. *Chem. Rev.* 114, 3659–3853 (2014).
99. Giordanino, F. et al. Interaction of NH<sub>3</sub> with Cu-SSZ-13 catalyst: A complementary FTIR, XANES, and XES study. *J. Phys. Chem. Lett.* 5, 1552–1559 (2014).
100. Martini, A. et al. Composition-driven Cu-speciation and reducibility in Cu-CHA zeolite catalysts: a multivariate XAS/FTIR approach to complexity. *Chem. Sci.* 8, 6836–6851 (2017).
101. Groothaert, M. H., Smeets, P. J., Sels, B. F., Jacobs, P. A. & Schoonheydt, R. A. Selective oxidation of methane by the bis ( $\mu$ -oxo) dicopper core stabilized on ZSM-5 and mordenite zeolites. *ACS Publ.* 127, 18 (2005).
102. Smeets, P., Groothaert, M., today, R. S.-C. & 2005, undefined. Cu based zeolites: A UV-vis study of the active site in the selective methane oxidation at low temperatures. Elsevier.
103. Jose, A. et al. The three-spin intermediate at the O–O cleavage and proton-pumping junction in heme–Cu oxidases. *Science* (80-. ). 373, 1225–1229 (2021).
104. Salzano, G. et al. Deciphering Copper Coordination in the Mammalian Prion Protein Amyloidogenic Domain. *Biophys. J.* 118, 676–687 (2020).
105. Vanelderen, P. et al. Cu-ZSM-5: A biomimetic inorganic model for methane oxidation. *J. Catal.* 284, 157–164 (2011).
106. Mae Alayon, E., Nachtegaal, M., Ranocchiari, M. & Van Bokhoven, J. A. Catalytic conversion of methane to methanol over Cu–mordenite. *Chem. Commun.* 48, 404–406 (2011).
107. Beznis, N. V., Weckhuysen, B. M. & Bitter, J. H. Cu-ZSM-5 zeolites for the formation of methanol from methane and oxygen: Probing the active sites and spectator species. *Catal. Letters* 138, 14–22 (2010).

108. Lim, H. et al. K $\beta$  X-ray Emission Spectroscopy of Cu(I)-Lytic Polysaccharide Monooxygenase: Direct Observation of the Frontier Molecular Orbital for H<sub>2</sub>O<sub>2</sub> Activation. *J. Am. Chem. Soc.* 145, 16015–16025 (2023).
109. Singha, A. et al. Tuning the Type 1 Reduction Potential of Multicopper Oxidases: Uncoupling the Effects of Electrostatics and H-Bonding to Histidine Ligands. *J. Am. Chem. Soc.* 145, 13284–13301 (2023).
110. Fischer, J. W. A. et al. Methane Oxidation over Cu<sup>2+</sup>/[CuOH]<sup>+</sup> Pairs and Site-Specific Kinetics in Copper Mordenite Revealed by Operando Electron Paramagnetic Resonance and UV/Visible Spectroscopy. *Angew. Chemie Int. Ed.* 62, e202303574 (2023).
111. Nielsen, D., Gao, Q., Janssens, T. V. W., Vennestrøm, P. N. R. & Mossin, S. Cu-Speciation in Dehydrated CHA Zeolites Studied by H<sub>2</sub>-TPR and In Situ EPR. *J. Phys. Chem. C* 127, 12995–13004 (2023).
112. Zhang, Y. et al. Probing Active-Site Relocation in Cu/SSZ-13 SCR Catalysts during Hydrothermal Aging by in Situ EPR Spectroscopy, Kinetics Studies, and DFT Calculations. *ACS Catal.* 10, 9410–9419 (2020).
113. Song, J. et al. Toward rational design of Cu/SSZ-13 selective catalytic reduction catalysts: implications from atomic-level understanding of hydrothermal stability. *ACS Publ.* 7, 8214–8227 (2017).
114. Gao, F. et al. Effects of Si/Al ratio on Cu/SSZ-13 NH<sub>3</sub>-SCR catalysts: Implications for the active Cu species and the roles of Brønsted acidity. *J. Catal.* 331, 25–38 (2015).
115. Gao, F. et al. Structure–activity relationships in NH<sub>3</sub>-SCR over Cu-SSZ-13 as probed by reaction kinetics and EPR studies. *J. Catal.* 300, 20–29 (2013).
116. Drosou, M., Mitsopoulou, C. A., Orio, M. & Pantazis, D. A. EPR Spectroscopy of Cu(II) Complexes: Prediction of g-Tensors Using Double-Hybrid Density Functional Theory. *Magnetochemistry* 8, 36 (2022).
117. Gómez-Piñeiro, R. J. et al. Decoding the Ambiguous Electron Paramagnetic Resonance Signals in the Lytic Polysaccharide Monooxygenase from *Photobacterium luminescens*. *Inorg. Chem.* 2022, 8035 (2022).
118. Bruzzese, P. C. et al. The Structure of Monomeric Hydroxo-Cu(I) Species in Cu-CHA. A Quantitative Assessment. *J. Am. Chem. Soc.* 144, 13079–13083 (2022).

119. Bruzzese, P. C. et al. 17O-EPR determination of the structure and dynamics of copper single-metal sites in zeolites. *Nat. Commun.* 2021 121 12, 1–13 (2021).
120. Wickramasinghe, N. P. & Ishii, Y. Sensitivity enhancement, assignment, and distance measurement in <sup>13</sup>C solid-state NMR spectroscopy for paramagnetic systems under fast magic angle spinning. *J. Magn. Reson.* 181, 233–243 (2006).
121. Moreno-González, M. et al. Evidence of a Cu<sup>2+</sup>-Alkane Interaction in Cu-Zeolite Catalysts Crucial for the Selective Catalytic Reduction of NO<sub>x</sub> with Hydrocarbons. *ACS Catal.* 7, 3501–3509 (2017).
122. Stamos, N. A. et al. Unusual <sup>31</sup>P Hyperfine Strain Effects in a Conformationally Flexible Cu(II) Complex Revealed by Two-Dimensional Pulse EPR Spectroscopy. *Inorg. Chem.* 59, 3666–3676 (2020).
123. Shanmugam, M. et al. <sup>13</sup>C and <sup>63,65</sup>Cu ENDOR studies of CO dehydrogenase from oligotropha carboxidovorans. Experimental evidence in support of a copper-carbonyl intermediate. *J. Am. Chem. Soc.* 135, 17775–17782 (2013).
124. Bühl, M. et al. Paramagnetic NMR of Phenolic Oxime Copper Complexes: A Joint Experimental and Density Functional Study. *Chem. – A Eur. J.* 22, 15328–15339 (2016).
125. Dawson, D. M. et al. High-resolution solid-state <sup>13</sup>C NMR spectroscopy of the paramagnetic metal–organic frameworks, STAM-1 and HKUST-1. *Phys. Chem. Chem. Phys.* 15, 919–929 (2012).
126. Del Giudice, D. et al. Two Faces of the Same Coin: Coupling X-Ray Absorption and NMR Spectroscopies to Investigate the Exchange Reaction Between Prototypical Cu Coordination Complexes. *Chem. – A Eur. J.* 28, e202103825 (2022).
127. Fusco, E., Ashbrook, S. E. & Bühl, M. <sup>13</sup>C pNMR shifts of MOFs based on Cu(II)-paddlewheel dimers – DFT predictions for spin–1/2 defects. *Phys. Chem. Chem. Phys.* 25, 31898–31906 (2023).
128. Chen, L., Janssens, T. V. W., Skoglundh, M. & Grönbeck, H. Interpretation of NH<sub>3</sub>-TPD Profiles from Cu-CHA Using First-Principles Calculations. *Top. Catal.* 62, 93–99 (2019).
129. Leistner, K., Xie, K., Kumar, A., Kamasamudram, K. & Olsson, L. Ammonia Desorption Peaks Can Be Assigned to Different Copper Sites in Cu/SSZ-13. *Catal. Letters* 147, 1882–1890 (2017).

130. Fan, C. et al. The influence of Si/Al ratio on the catalytic property and hydrothermal stability of Cu-SSZ-13 catalysts for NH<sub>3</sub>-SCR. *Appl. Catal. A Gen.* 550, 256–265 (2018).
131. Datka, J. & Kozyra, P. TPD–IR studies of CO desorption from zeolites CuY and CuX. *J. Mol. Struct.* 744–747, 991–996 (2005).
132. Wang, X., Arvidsson, A. A., Skoglundh, M., Hellman, A. & Carlsson, P. A. Desorption products during linear heating of copper zeolites with pre-adsorbed methanol. *Phys. Chem. Chem. Phys.* 22, 6809–6817 (2020).
133. Tang, X. et al. Atomic Insights into the Cu Species Supported on Zeolite for Direct Oxidation of Methane to Methanol via Low-Damage HAADF-STEM. *Adv. Mater.* 35, 2208504 (2023).
134. Sheppard, T. L. et al. In Situ Multimodal 3D Chemical Imaging of a Hierarchically Structured Core@Shell Catalyst. *J. Am. Chem. Soc.* 139, 7855–7863 (2017).
135. Schmidt, J. E., Oord, R., Guo, W., Poplawsky, J. D. & Weckhuysen, B. M. Nanoscale tomography reveals the deactivation of automotive copper-exchanged zeolite catalysts. *Nat. Commun.* 2017 81 8, 1–8 (2017).
136. Voronov, A. et al. Multivariate curve resolution applied to in situ X-ray absorption spectroscopy data: An efficient tool for data processing and analysis. *Anal. Chim. Acta* 840, 20–27 (2014).
137. Rochet, A., Ribeiro Passos, A., Legens, C. & Briois, V. Sulphidation study of a dried Ni/Al<sub>2</sub>O<sub>3</sub> catalyst by time-resolved XAS-MS combined with in situ Raman spectroscopy and multivariate Quick-XAS data analysis. *Catal. Struct. React.* 3, 33–42 (2017).
138. Pappas, D. K. et al. The Nuclearity of the Active Site for Methane to Methanol Conversion in Cu-Mordenite: A Quantitative Assessment. *J. Am. Chem. Soc.* 140, 15270–15278 (2018).
139. Guda, A. A. et al. Understanding X-ray absorption spectra by means of descriptors and machine learning algorithms. *npj Comput. Mater.* 2021 71 7, 1–13 (2021).

140. Pappas, D. K. et al. Influence of Cu-speciation in mordenite on direct methane to methanol conversion: Multi-Technique characterization and comparison with NH<sub>3</sub> selective catalytic reduction of NO<sub>x</sub>. *Catal. Today* 369, 105–111 (2021).
141. Negri, C. et al. Structure and Reactivity of Oxygen-Bridged Diamino Dicopper(II) Complexes in Cu-Ion-Exchanged Chabazite Catalyst for NH<sub>3</sub>-Mediated Selective Catalytic Reduction. *J. Am. Chem. Soc.* 142, 15884–15896 (2020).
142. Kvande, K. et al. Comparing the Nature of Active Sites in Cu-loaded SAPO-34 and SSZ-13 for the Direct Conversion of Methane to Methanol. *Catal.* 2020, Vol. 10, Page 191 10, 191 (2020).
143. Doronkin, D. E. et al. Operando spatially- and time-resolved XAS study on zeolite catalysts for selective catalytic reduction of NO<sub>x</sub> by NH<sub>3</sub>. *J. Phys. Chem. C* 118, 10204–10212 (2014).
144. Paolucci, C. et al. Isolation of the Copper Redox Steps in the Standard Selective Catalytic Reduction on Cu-SSZ-13. *Angew. Chemie Int. Ed.* 53, 11828–11833 (2014).
145. Tyrsted, C. et al. Nitrate–nitrite equilibrium in the reaction of NO with a Cu-CHA catalyst for NH<sub>3</sub>-SCR. *Catal. Sci. Technol.* 6, 8314–8324 (2016).
146. Kwak, J. H. et al. Following the movement of Cu ions in a SSZ-13 zeolite during dehydration, reduction and adsorption: A combined in situ TP-XRD, XANES/DRIFTS study. *J. Catal.* 314, 83–93 (2014).
147. Lomachenko, K. A. et al. The Cu-CHA deNO<sub>x</sub> Catalyst in Action: Temperature-Dependent NH<sub>3</sub>-Assisted Selective Catalytic Reduction Monitored by Operando XAS and XES. *J. Am. Chem. Soc.* 138, 12025–12028 (2016).
148. Yang, Y. et al. Active sites in Cu-SSZ-13 deNO<sub>x</sub> catalyst under reaction conditions: a XAS/XES perspective. *J. Phys. Conf. Ser.* 712, 012041 (2016).
149. Ivanin, I. A., Kruchinin, T. V., Udalova, O. V., Tedeeva, M. A. & Shilina, M. I. Synergistic Effect of the Catalytic Action of Copper and Cerium in the Oxidation of Carbon Monoxide on Modified Cu/Ce/ZSM-5 Zeolites. *Kinet. Catal.* 64, 655–670 (2023).
150. Fedyna, M. et al. Mechanistic stages of the SCR reaction – Insights into the trade-off between NO reduction and NH<sub>3</sub> oxidation over CuSSZ-13 catalysts via isotopic <sup>15</sup>NH<sub>3</sub> and <sup>18</sup>O<sub>2</sub> TPSR and steady state studies supported by IR 2D COS and DFT modeling. *Appl. Catal. B Environ.* 325, 122309 (2023).

151. Perdew, J. P. & Wang, Y. Accurate and simple analytic representation of the electron-gas correlation energy. *Phys. Rev. B* 45, 13244 (1992).
152. Diaz, D. E. et al. Impact of Intramolecular Hydrogen Bonding on the Reactivity of Cupric Superoxide Complexes with O–H and C–H Substrates. *Angew. Chemie Int. Ed.* 58, 17572–17576 (2019).



# Chapter 2

## *Cu-exchanged zeolites*

### 2.1 Materials & methods

#### 2.1.1 Cu-zeolites

The Cu-exchanged zeolites studied in this work belong to three classes of materials: Cu-ZSM-5 (MFI topology),<sup>1</sup> Cu-SSZ-13 (CHA topology),<sup>2</sup> Cu-MOR (MOR topology).<sup>3</sup> These materials show relatively narrow pore structures, ranging between 3.8 and 7.0 Å widths with 2- (MOR) and 3-dimensional channels (ZSM-5 and SSZ-13). A visualization of the three frameworks is depicted in Figure 2.1.

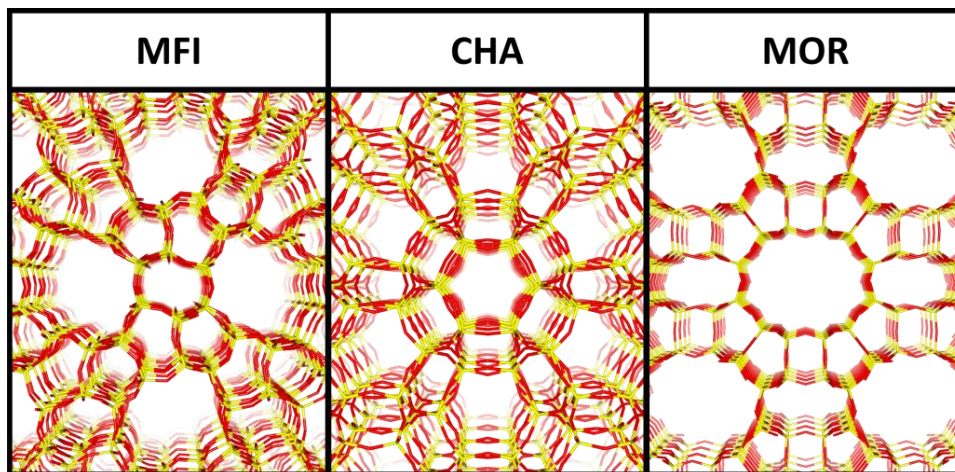


**Figure 2.1** Visualization of the three framework topologies of MFI, CHA and MOR. Colour code: O in red, Si in yellow. MFI is visualized along the crystallographic b axis, while CHA and MOR are visualized along the crystallographic c axis (based on the reference IZA structures).<sup>4</sup>

Preparation of these materials may be achieved through classical hydrothermal synthesis with the possible inclusion of seeds to direct the reaction product towards one specific framework topology; templating agents are sometimes used, especially when low Al concentrations are desired, or mesoporosity wants to be introduced.<sup>5</sup> Solution ion exchange protocols are usually employed to introduce Cu in the material as extraframework cation to substitute the ones

that resulted from the synthesis (most often  $\text{H}^+$ ,  $\text{NH}_4^+$  or alkali).<sup>6,7</sup> With respect to other possible methods (like sublimation of  $\text{CuCl}$ ), exchange in solution provides an easy way to introduce Cu using a water-soluble salt bearing a counteranion that can then be easily removed via calcination (e.g.,  $\text{Cu(II)}$  acetate). High temperature treatment of the material is often necessary regardless of the source of Cu before characterization, as water and other adsorbates can be present in the material and may need to be removed prior to characterization. A critical aspect of solution ion exchange is the control of pH of the resulting suspension: the speciation of Cu ions in the liquid phase is affected by the acidity of the solution, as is shown in Figure 2.2.

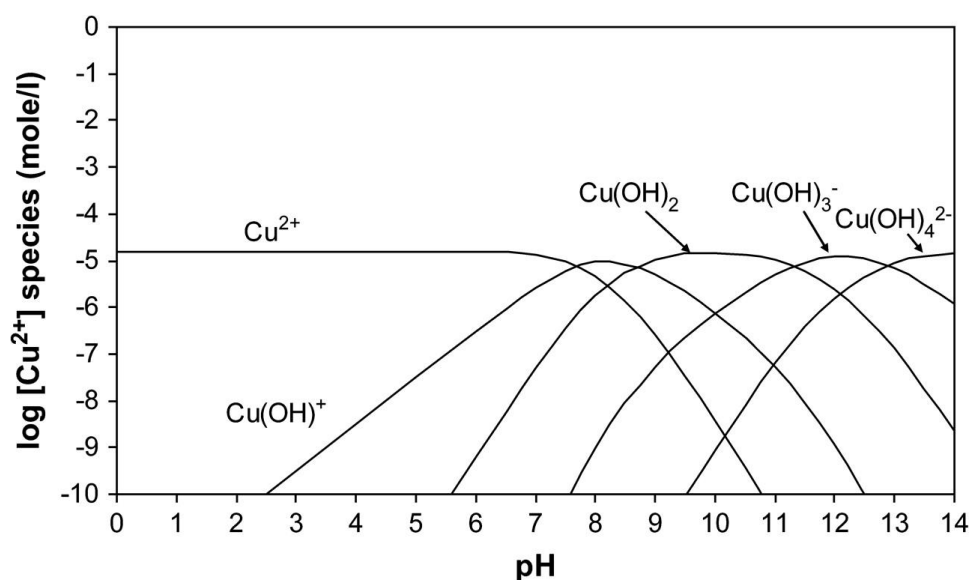


**Figure 2.2** Theoretical copper speciation for hydroxyl Cu complexes in pure water for a total copper concentration of 1 mg/l. Adapted from Ref<sup>8</sup>.

Depending on the pH, the formation of Cu hydroxide can be favoured, which is associated with the successive unwanted formation of Cu oxide aggregates in the solution or in the material after calcination;<sup>9</sup> in contrast, too low pH values result in an excess of  $\text{H}^+$  ions that compete with the Cu for ion substitution in the material, potentially slowing down the exchange and preventing high Cu loadings. The use of  $\text{Cu(II)}$  acetate as the source of the metal ion is then convenient, since it offers the possibility to prepare acetic acid/acetate buffers to accurately control the pH during exchange at the desired value (usually around 4-5 when high concentrations in the final material are the target). Cu

exchange is usually performed on  $\text{NH}_4^+$ -exchanged materials, independent of the cations already present in the as-synthesized material: the reason for this two-step exchange procedure is that it has been shown that exchanging Cu from  $\text{NH}_4^+$  instead of  $\text{H}^+$  or alkali usually leads to high Cu loadings more easily.<sup>10</sup> Since the metal is usually introduced as a  $\text{Cu}^{2+}$  cation, Cu/Al ratios are in the range 0-0.5; in cases where the Cu site is reduced, the additional positive charge needed to balance the negative one from the framework is usually attributed to acidic protons resulting in some way from the reaction. Cu/Al ratios >0.5 are usually ascribed to the formation of isolated clusters in the pores as the only way to accumulate non-framework-bound Cu. The list of the materials discussed throughout this work is reported in Table 2.1.

**Table 2.1** List of Cu-zeolites used in this work. All Si/Al and Cu/Al are reported as molar ratios. Unless specified otherwise, materials have been synthesized in the context of the iCSI (industrial Catalysis Science and Innovation) project. a) Commercial parent material from Zeolyst International (CBV 21A). b) Commercial parent material from Zeolyst International (CBV 5524G). c) Commercial parent material from Zeolyst International (CBV 2314). d) Cu exchange procedure performed by the author.

Name	Si/Al	Cu/Al	Reference
(0.48)Cu-CHA(15)	15	0.48	11
(0.35)Cu-CHA(5)	5	0.35	12
(0.32)Cu-MOR(11) <sup>a</sup>	11	0.36	13
(0.21)Cu-MOR(6.5)	6.5	0.21	14
(0.48)Cu-MFI(25) <sup>b,d</sup>	25	0.48	15
(0.35)Cu-MFI(11.5) <sup>c,d</sup>	11.5	0.35	15
Na-MOR	7.3	0	16
$\text{NH}_4$ -MOR	7.3	0	16

As a final note, care should be taken in determining the composition of the prepared materials. The final concentration of Cu in the material is not known *a priori*, and the Al content can be different compared to the stoichiometry used for the reactants during synthesis and/or can be modified during ion

exchange. If quantitative relationships want to be established between a reaction promoted by the catalyst and its composition (usually in terms of Si/Al and Cu/Al molar ratios, or of Al and Cu weight percentage), accurate measurements of such composition must be performed. A technique that is often used to retrieve these concentrations is energy-dispersive X-ray spectroscopy (EDS) from scanning electron microscopy (SEM); although this is surely useful to have an estimate of Cu incorporation in the material, SEM-EDS is not a quantitative technique for determination of Cu and especially Si and Al amounts in a porous, solid material for at least two reasons:

- 1) Less than roughly 10% of emission of core-excited atoms with  $Z < 15$  (such as Si and Al) consists of X-ray emission, while most of the relaxation occurs via (often undetected) Auger decay. This inherently limits the sensitivity of standard SEM-EDS measurements on light atoms.<sup>17</sup>
- 2) Accurate analytical methods for elemental analysis require the use of standard materials to build a calibration curve from which the unknown sample concentration is then interpolated, so that at least systematic errors can be compensated (or at least minimized). Such reference materials are difficult to produce for solid samples and specifically for complex matrices, so that in practice calibration-less measurements are often performed. This procedure can give sufficient semi-quantitative results but is, generally speaking, incorrect for absolute quantitative determination of elemental composition.<sup>18</sup>

Accurate quantitative information on the composition of these materials is achieved via elemental analysis techniques, such as inductively coupled plasma optical emission spectroscopy (ICP-OES) or microwave plasma atomic emission spectroscopy (MP-AES). Both of these techniques can be impractical, due to the need to dissolve the samples in solution for analysis; this is usually performed for silicates via digestion in HF, with some additional complications in case Si needs to be measured because of the volatility of Si fluorides.<sup>19</sup> The overall inconvenience of this sample pretreatment procedure, along with the possible lack of the necessary instrumentation, is probably the cause of the spread of SEM-EDS as a technique for elemental analysis in solids, which can contribute to inconsistency and possibly lack of reproducibility in the literature.

## 2.1.2 Experimental characterization of solid materials

Characterization of solid materials (in a broad sense) is an important but often challenging task that has sparked the interest of scientists interested in heterogeneous catalysis for many years. Compared to the homogeneous phase (*i.e.*, systems in solution) several complications arise, such as i) the more complicated procedure needed to obtain different concentrations of species that are homogeneously distributed in the material, ii) the harder and sometimes ill-defined task of obtaining standard reference materials, iii) the possible (and frequent) heterogeneity of active species, iv) the presence of an interface between the material and the reactants (solid-solid, solid-liquid, solid-gas), v) the role of an often complex and non-innocent matrix, vi) the different interaction of light with a solid compared to a liquid solution, the latter of which is usually characterized by transmission and absorption as the major components of interaction. Points v) and vi) have been of particular relevance in this work, as most of the characterization techniques that have been employed are spectroscopies. Additional challenges emerge when such techniques have to be adopted in *in situ/operando* mode, as the additional requirements of homogeneously subjecting a solid material to thermochemical treatment in a controlled environment while possibly testing its performance through online analytical techniques is not an easy task and strongly technique-dependent.

Transmission IR spectroscopy has been widely used to characterize the surface properties of porous materials and specifically Cu-zeolites. The data presented in this work were acquired on an Invenio R spectrophotometer from Bruker, equipped with a mercury cadmium telluride (MCT) cryodetector, a resolution of  $2\text{ cm}^{-1}$  and averaging 32 scans (64 for background spectrum, collected with an empty measurement chamber). Samples were prepared as self-supporting pellets of pressed powder; hydraulic press loads in the range 2-3 tons usually result in pellets without cracks, although some less sturdy materials (*e.g.*, MOFs)<sup>20</sup> could experience structure collapse or loss of crystallinity at these pressures. The resulting pellet was weighed on a precision scale and its area was measured by digitally evaluating its picture on graph paper via the ImageJ

software.<sup>21</sup> The pellet was then placed in a gold envelope as an inert structural support and inserted in a glass cell equipped with IR-transparent windows (usually KBr), which can then be connected to a vacuum line for thermochemical treatment. Gas probe molecules (*i.e.*, CO) were introduced through a vacuum line connected to the cell during measurement from a CO-filled glass balloon; pressure of the gas in the  $10^{-4}$ -100 mbar range was measured through a multiscale Pirani gauge. The spectrum of the material was acquired in transmission mode and plotted in absorbance scale; this is not formally correct, as absorbance as a quantity presupposes that all non-transmitted light is absorbed, while scattering effects on these materials are often present. For this reason, it is always important not to use the raw reading of absorbance in the spectrum as proportional to concentration, but to consider scattering effects in the considered spectral region and, when possible, subtract a background spectrum of the sample prior to the reaction of interest. Another important variable to consider for signal intensity is the thickness of the pellet, which is usually unknown and very difficult to measure. If comparisons between different samples want to be drawn, care should be taken to at least normalize the spectra to the thickness of the pellet: this is usually achieved by normalization to overtone peaks of bulk vibration modes, the fundamentals of which are too intense to be measured in transmission mode. Specific cells that allow to heat the sample and flow gas reactants in the sample environment while spectra are being measured are available commercially for transmission, diffuse reflectance or attenuated total reflectance IR spectroscopy; these systems allow to get closer to *operando* conditions, but need to be thoroughly tested for air-tightness to be reliable, as even trace amounts of water leaking in the cell from the atmosphere can have a dramatic effect on these materials.

Raman spectroscopy is a vibrational technique that can be used in a complementary manner to IR for the study of these materials. It presents several advantages, such as i) selectivity towards symmetrical vibrational modes (in contrast to IR), ii) possibility to extend the energy range to lower wavenumbers (down to  $300\text{ cm}^{-1}$  in the case of this work, compared to  $500\text{ cm}^{-1}$  for IR), iii) possibility to work in resonant conditions, selectively enhancing the intensity of specific vibrations. The main drawbacks associated with the use of

this technique in this context are the inherent low cross-section of the Raman scattering, reflecting in low S/N ratios and thus long acquisition times, and the possible interference of fluorescence from species in the sample (*e.g.*, Cu(I), carbonaceous residues). In favourable cases, however, Raman spectroscopy can provide otherwise unattainable information, as will be shown in Section 2.3. The sample was inserted in a capillary in powder form; reactive gases were flown through the ends of the capillary, and heating was achieved through a coil connected to an electrical power supply. All spectra were collected with a Renishaw inVia Raman microscope spectrometer, equipped with a He-Cd laser (Kimmon Koha IK series) emitting at 442 nm as excitation source. The excitation light was focused on samples through a 20x objective, analyzed by a 2400 lines/mm grating and detected by a CCD detector. The laser power was set to ca. 0.1 mW at the sample, in order to avoid sample degradation induced by the radiation.

UV-Vis-NIR diffuse reflectance (DR) spectroscopy has been widely used to study Cu-zeolites, as it is able to probe the states around the Fermi energy of solid materials that contain transition metals and obtain specific information about the metal centre. In the case of Cu-zeolites, the negligible absorption of the matrix in almost the entirety of the explored range of wavenumbers allows to probe d-d and charge transfer (CT) transitions due to Cu, which are highly affected by the speciation of the metal centre. The reactivity involved in the reactions studied in this work mainly involves the Cu(I)/Cu(II) redox couple; since Cu(I) has a  $d^{10}$  electronic configuration, in which d-d transitions are not observed, the technique also offers the possibility to check the evolution of the oxidation state of the metal during reaction. Powdered samples are usually the preferred form for DR spectroscopy, as diffuse reflectance is maximized in these conditions; coincidentally, this also makes the system closer to reactor conditions in which catalytic tests are performed and is thus particularly fit for *in situ/operando* setups. Developing such a setup was one of the main objectives of this work: a scheme of the result is shown in Figure 2.3.

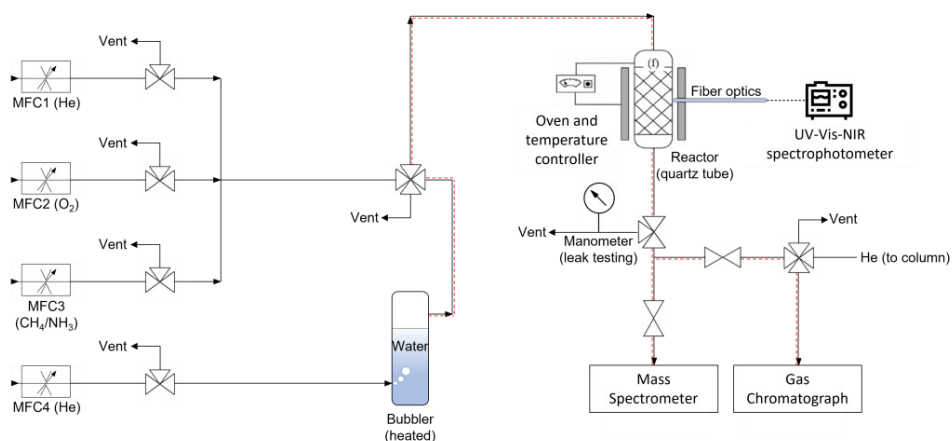


**Figure 2.3** Scheme of the experimental setup developed to perform operando UV-Vis-NIR DR spectroscopy on solid samples.

The setup is comprised of 4 mass flow controllers (MFC) that allow accurate gas flows to reach the sample through stainless steel and/or inert plastic tubes. One of the MFC lines is connected to a temperature-controlled bubbler for wet gas experiments, and all lines after the bubbler are heated to prevent condensation within the tubes. A straight quartz tube (9 mm internal diameter) contains the sample powder (ca. 100 mg) positioned on a quartz wool plug, and a thermocouple is inserted in the tube approximately at the same height as the sample, which is then inserted in an oven; the temperature is read through the thermocouple and controlled in a very accurate and responsive manner through a PID. A custom made, temperature resistant (up to 600°C) fibre optic is inserted in the oven and probes the sample through the reactor wall perpendicular to it. Light in the UV-Vis-NIR range is produced by an Avantes AvaLight-DH-S light source (including both a deuterium and a halogen lamp), which is then shone on the sample through the fibre; reflected light is then recollected by the outer channels of the fibre and analyzed via an Avantes AvaSpec-ULS2048XL-EVO detector. Since absorption bands in solids are usually very broad compared to species in solution, 100  $\mu\text{m}$  slits were used to enhance light collection and improve time resolution (<5 s/spectrum in most cases). The effluents can then be directed towards a mass spectrometer and/or a gas chromatograph for product quantification. Since absorption bands (especially CT transitions) can be very intense depending on the sample, use of the Kubelka-Munk function is not proper and can lead to heavily distorted



spectra;<sup>22-24</sup> for this reason, all spectra are collected and reported as reflectance (%) using tetrafluoroethylene powder as blank for 100% reflectance. Since the data obtained using this setup did not fit with discussion topics reported throughout this chapter, some examples of data acquisition and setup development are reported in Appendix A1.

X-ray absorption spectroscopy (XAS) is one of the most used techniques in the materials science community to study solid samples, especially metal sites dispersed in light matrices, involving electronic transitions from core states to unoccupied states or the continuum via photoelectric effect. XAS in transmission mode is a bulk-sensitive technique with exceptional element-selectivity; it can have time resolution of minutes or even seconds per spectrum depending on the energy range (for Cu), can be coupled with other spectroscopies (*e.g.*, DRIFTS) and XRD and can be used in *in situ* and *operando* configuration. It is still mostly a large-scale facility dependent technique, although recent progress has been made for laboratory sources. Although not discussed in this work, surface specific information can be obtained using electron yield detection, and particularly dilute samples can be measured in strongly absorbing matrices using fluorescence detection (see Sections 2.4 and 3.3). The XAS spectrum is usually divided in two zones depending on the incident energy of the X-ray beam, namely the X-ray absorption near edge structure (XANES) region below and just above the edge energy and the extended x-ray absorption fine structure (EXAFS) region some tens of eV above the edge energy. The XANES region gives information about the oxidation state and the coordination geometry of the probed element, while the EXAFS region is used to get accurate information on the coordination number and the distance of atoms in the close proximity (up to ca. 6 Å, depending on data quality) of the element after a fitting procedure. EXAFS spectra can also provide information on the identity of the neighbouring atoms if their atomic number is sufficiently different; this ability, and specifically the possibility to distinguish contributions from heavy atoms has been greatly enhanced by recent developments such as wavelet transform analysis (see Section 2.3 and Appendix A2). XAS experiments performed through this work were performed at different light sources and in different configurations. The experiments described in Section 2.2 were performed at the BM23 beamline of the

European Synchrotron Radiation Facility (ESRF, Grenoble, France)<sup>25</sup> using the Microtomo cell,<sup>26</sup> allowing for thermochemical treatment of the sample in pellet form during spectral acquisition. More detailed information on the cell and beamline characteristics can be found in Appendix A5. The experiments described in Section 2.3 were performed at the XAFS beamline of Elettra Sincrotrone Trieste (Basovizza, Italy) on pre-activated sample pellets that had been stored in a glovebox, vacuum-sealed in plastic bags and stored in an N<sub>2</sub>-filled canister for transportation. More detailed information on the beamline characteristics can be found in Appendix A2. The experiments described in Section 2.4 were performed at the Phoenix II beamline of the Swiss Light Source (SLS, Villigen, Switzerland), equipped with an Apple-II undulator. Each material was pressed into 9 mm diameter self-supporting pellet and placed in the 6-slot Cu holder (also used to heat the pellets to the required temperature) inside the vacuum sample chamber (10<sup>-5</sup>-10<sup>-6</sup> mbar). When necessary, the sample was exposed to diluted O<sub>2</sub> directly in the sample chamber and re-evacuated prior to measurement. The Al K-edge spectra were acquired in fluorescence mode employing a planar grating monochromator to scan the incident energy. The incoming beam intensity (I<sub>0</sub>) was monitored by measuring the drain current from a Ni covered thin polyethylene foil placed in the beam path, while the X-ray fluorescence signal was detected by a single-element Si drift diode. Al K-edge spectra were recorded in the 1420-1836 eV range with a 0.2 eV resolution in the XANES region and a 2.5 eV resolution in the EXAFS region. Spectra were aligned in edge energy according to spectra of an Al foil acquired in the same conditions. The Athena software from the Demeter package<sup>27</sup> was used for spectra normalization and visualization.

Isothermal volumetric adsorption measurements allow to indirectly probe and quantify the Cu(I) content in Cu-zeolites, exploiting the selective adsorption of CO on such sites. Experiments were performed on a commercial volumetric apparatus (Micromeritics ASAP 2020, Norcross GA) at 50°C. The sample was inserted as pellet fragments in a custom quartz volumetric cell with connections that allow thermochemical treatment of the sample prior to measurement. The burette was placed in a thermal jacket filled with thermostatic fluid, allowing for precise temperature control. All activation procedures for the samples have been performed on vacuum lines replicating

the ones employed for IR spectroscopy applied to the same study. Details on the gases and the treatment can be found in Appendix A3 and in Section 2.2.

### 2.1.3 Computational methods

Structure optimization on the materials presented in the next sections have been performed in the frame of density functional theory (DFT) using the CRYSTAL17 software,<sup>28</sup> which is specifically designed to exploit symmetry in solid systems. All periodic structures and adducts were optimized at the B3LYP level<sup>29,30</sup> with D3 correction for dispersive forces;<sup>31</sup> triple-zeta basis sets of the Ahlrichs family<sup>32</sup> were chosen for Cu and atoms of the adsorbed species (NH<sub>3</sub>, CO), while framework atoms were described by double-zeta basis sets specifically built for similar cases.<sup>33,34</sup> All energetics were calculated on the obtained models by calculating harmonic frequencies on a subset of atoms consisting of the Cu cation, the sorbed molecule(s) when present, the framework Al and its surrounding atoms up to the second coordination sphere (4 O and 4 Si). Variations in electronic energy ( $\Delta E$ ), enthalpy ( $\Delta H$ ) and Gibbs free energy ( $\Delta G$ ) at the relevant temperatures and pressures were calculated according to Equation 2.1:

$$\Delta X = \sum X_{products} - \sum X_{reactants} \quad \text{with } X = E, H \text{ or } G \quad \text{Eq. 2.1}$$

All additional parameters and settings are specified in Appendices A3 and A5.

Calculation of pre-edge and rising-edge XANES spectra was performed in the frame of time-dependent density functional theory (TD-DFT) using the ORCA software (version 5.0.3).<sup>35–37</sup> Cluster models of the involved species were cut from the optimized periodic structures described previously using the Moldraw software,<sup>38</sup> including the absorber element and its nearest neighbouring atoms, saturating any dangling bond on the Si with H atoms. Systematically more complex clusters were cut to include only Cu and the first, second, or third O-Si units shells around Al, respectively; in cases in which small rings would be cut off too crudely with this approach, the whole ring structure was kept instead. Spectra were calculated on these cluster models and showed converged spectral features already at the mid-complexity level (*i.e.*, Cu,

adsorbed molecules, two Si-O shells around Al plus saturating H atoms) and were thus used for all TD-DFT calculations. An example of such structures is portrayed in Figure 2.4 for clarity.

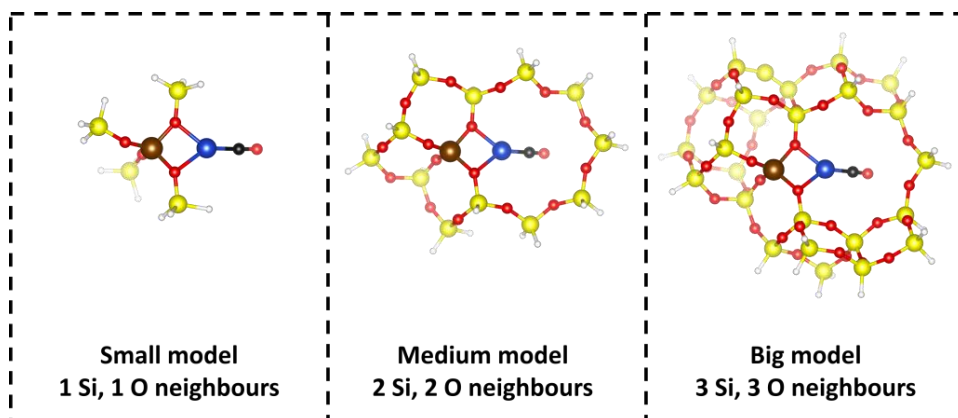


**Figure 2.4** Examples of cluster models cut from the optimized periodic structure for Cu in the 8-member ring of Cu-MOR. Colour code: H in white, C in black, O in red, Al in brown, Si in yellow, Cu in blue.

The TD-DFT calculations were performed within the Tamm-Dancoff approximation using the range-separated hybrid GGA CAM-B3LYP functional.<sup>39</sup> The ZORA approximation<sup>40</sup> was employed to account for relativistic effects, in conjunction with the ZORA-def2-TZVP(-f) basis set recontracted for the purpose by Pantazis and coworkers.<sup>41</sup> The auxiliary SARC/J basis set<sup>41–43</sup> was used in conjunction with the resolution of identity (RI) approximation for Coulomb integrals (as is default in ORCA 5.0). Spin-orbit coupling was considered using the spin-orbit mean field approximation (SOMF(1X)), and TightSCF settings (2.5E-7 tolerance in energy) were used for wavefunction convergence. The excitation space was mapped from the 1s core orbital of Cu to any unoccupied state up to 300 roots, with a maximum value of the Davidson expansion space of 900 (MaxDim 900). Contributions from the electric quadrupole were considered (DoQuad True) and natural transition orbitals (NTO) were calculated to aid in the interpretation of the spectra (DoNTO true); NTOs were rendered using the `orca_plot` utility and visualized using the VESTA software.<sup>44</sup> All spectra were obtained by applying Gaussian broadening of 2.3 width to the calculated electronic transitions via the `orca_mapspc` utility and shifted by -5 eV (Cu) or +34 eV (Al) to match experimental spectra.

Multivariate curve regression (MCR) using the alternating least squares (ALS) algorithm was performed on XAS spectra using the graphical user interface developed by Jaumot *et al.* in the MATLAB environment;<sup>45</sup> the specific settings that were used in the data decomposition procedure can be found in Appendices A3 and A5.

## 2.2 Reducibility of Cu in zeolites

Compared to the plethora of  $\text{Cu}_x\text{O}_y$  species that have been characterized for Cu(II), Cu(I) is usually described as a bare cation electrostatically bound to the framework negative charge in the proximity of an Al site (in the conditions that characterize these reactions). This is to be expected to some level from basic inorganic chemistry arguments stemming from ligand field theory, as well as from examples of systems in the homogeneous phase.<sup>46,47</sup> The single positive charge of this relatively soft cation is balanced by the framework without the need for additional anions, and Cu(I) is usually characterized by lower coordination numbers compared to Cu(II). The species that have been addressed as responsible for the activation of the C-H bond by Cu-zeolites almost exclusively consist of Cu(II) species, possibly forming adducts or multinuclear Cu that include O atoms.<sup>48,49</sup> Cu(I) is usually invoked as the redox partner of Cu(II) in a one-electron mechanism that is somehow coupled with the oxidation reaction occurring on the C atom of the alkane; as such, spectroscopic, reactivity and mechanistic studies have mainly focused on the Cu(II) state and investigated the Cu(I) counterpart as a necessary but ultimately secondary focus in the catalytic or stepwise reaction profile. Some reports in the literature, however, suggest that the maximum concentration of Cu(I) that is attainable in the material correlates with productivity,<sup>12</sup> suggesting that either the possibility to form Cu(I) is necessary to form the actual active species, or that a fraction of “redox inert” sites are present in the materials, leading to an overall lower concentration of active Cu sites. Moreover, Artsiusheuski *et al.* very recently explored the key role of Cu(I) sites in the conversion of  $\text{CH}_3\text{OH}$  to gaseous alkanes and olefins over Cu-exchanged mordenite.<sup>50</sup> It is thus apparent that ways to characterize and quantify the amount of Cu(I) present in the zeolite at a given time during reaction can

provide useful information on the performance of the catalyst. Unfortunately, not many techniques are available for this task, as the  $d^{10}$  configuration (and thus singlet spin state) of these species precludes the use of EPR spectroscopy, as well as the information usually attainable by d-d transitions in electronic spectra. In the past decades, XAS has been frequently used as a reliable selective tool to detect and characterize Cu(I) species in Cu-zeolites; the use of linear combination fitting (LCF) or multivariate algorithms has further allowed to quantify in a reliable way the amount of Cu(I) in these materials, and is often the technique of choice to study variations in the oxidation state of Cu.<sup>12,14,51-53</sup> Unfortunately, XAS is still mainly a synchrotron-based technique, especially if good time resolution is needed, leading to cost and time issues even in cases when the proposal for an experiment is accepted. For this reason, developing cheap, easy, and lab-scale techniques to measure and quantify Cu(I) in these materials is an interesting although challenging feat. Decades of studies on adsorption of probe molecules on metal centres in Cu-zeolites led to the description of stable, structurally well-defined adducts of Cu with carbon monoxide; depending on temperature and CO partial pressure, several  $\text{Cu}^0$ ,  $\text{Cu}^+$  and  $\text{Cu}^{2+}$  adducts with multiple coordinating CO molecules are possible, but around room temperature only  $[\text{Cu}(\text{CO})]^+$  is able to form and be stable upon evacuation in Cu-ZSM-5.<sup>54-57</sup> Cu(I) monocarbonyls could then be used as selective, quantifiable markers provided that a reliable experimental technique is able to retrieve the concentration of these adducts in the material. IR spectroscopy has been used as a convenient way to characterize these species, since the characteristic vibrational frequency of the  $[\text{Cu}(\text{CO})]^+$  adduct is shifted with respect to the stretching frequency of gaseous CO and falls in a range of the IR spectrum where basically no spectral interference occurs. IR spectra showing the process of CO adsorption and subsequent evacuation of CO on a pre-reduced sample of Cu-ZSM-5 (Si/Al = 11.5, Cu/Al = 0.35) are shown in Figure 2.5.

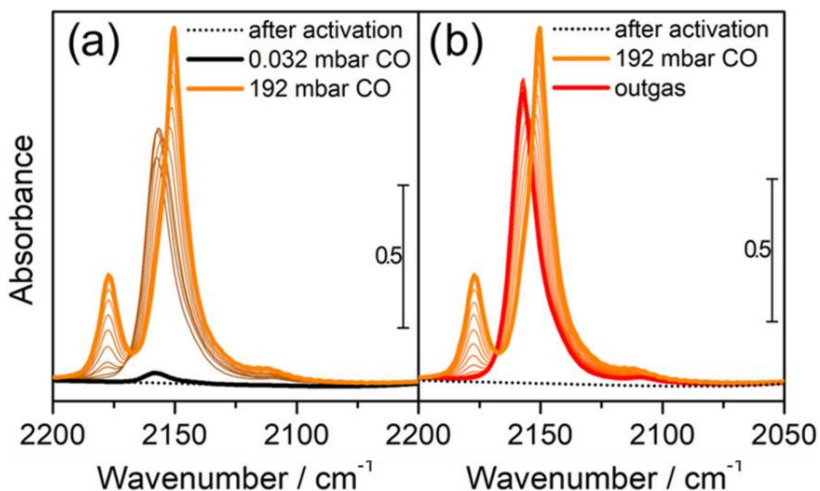


**Figure 2.5** Interaction of CO over the pre-reduced (0.35)Cu-MFI(11.5) sample. (a) Effect of increasing pressure of CO (from black to orange). (b) Effect of outgassing on the sample exposed to 192 mbar of CO (from orange to red). Adapted from Appendix A3.

As can be seen from Figure 2.5a, and in agreement with the literature on the topic, increasing pressure of CO on the sample leads to the formation of mono and dicarbonyl species on Cu(I), characterized by vibrations at 2157  $\text{cm}^{-1}$  (stretching of CO in  $[\text{Cu}(\text{CO})]^+$ ) and 2178, 2151  $\text{cm}^{-1}$  (symmetric and asymmetric stretching of CO in  $[\text{Cu}(\text{CO})_2]^+$ ), respectively. The shift in CO stretching frequencies of these adducts with respect to the one of non-interacting CO in the gas phase<sup>58</sup> (2143  $\text{cm}^{-1}$ , the rotovibrational profile of gaseous CO can be seen at high pressure in Figures 2.5a and 2.5b) has been justified in terms of strong  $\sigma$ -donation with partial  $\pi$ -back-donation contributions.<sup>59,60</sup> An additional band at 2108  $\text{cm}^{-1}$  grows in parallel to the one at 2157  $\text{cm}^{-1}$ , which is consistent with Cu(I)<sup>13</sup>CO adducts forming from the <sup>13</sup>CO isotopologue.<sup>61–63</sup> It is interesting to note that all the vibrations pertaining to these complexes present very defined and symmetric profiles with small bandwidth, testifying to the formation of very homogeneous and structurally well-defined species, resembling what has been found for similar Cu-carbonyls in the homogeneous phase.<sup>57</sup> Figure 2.5b shows that upon outgassing (residual pressure <  $5 \times 10^{-5}$  mbar) the Cu(I) dicarbonyl adducts revert to  $[\text{Cu}(\text{CO})]^+$ ; even after prolonged vacuum treatment the intensity of the monocarbonyl band does not undergo significant changes, confirming the irreversibility of this species at 50°C (the assumed sample temperature after long exposure to the IR beam).

Unfortunately, the molar attenuation coefficient for the vibration at  $2157\text{ cm}^{-1}$  is not known (and it is not guaranteed to be the same *a priori* for all similar species in different materials), making it impossible to retrieve the concentration of  $[\text{Cu}(\text{CO})]^+$  by use of IR spectroscopy alone. Since Cu(I) monocarbonyls are the only species that form irreversibly at  $50^\circ\text{C}$ , however, the formation of these species after a specific thermochemical treatment could be assessed by isothermal adsorption volumetry experiments by following this procedure:

- 1) The sample is exposed to the reaction conditions for which the amount of Cu(I) needs to be quantified. In validating this technique, reaction of Cu-ZSM-5 samples with  $\text{NH}_3$  at  $500^\circ\text{C}$  for 30 minutes followed by evacuation was employed as a reproducible way to quantitatively reduce the Cu in the material to Cu(I).
- 2) A (primary) CO adsorption isotherm is measured on the material at  $50^\circ\text{C}$ : at the pressures where a plateau is observed, all possible adducts are formed (mainly  $\text{Cu}^+$  mono- and multicarbonyls); after the sample is outgassed, only the Cu(I) monocarbonyls remain.
- 3) A (secondary) CO adsorption isotherm is measured on the same material at  $50^\circ\text{C}$ : since all Cu(I) is already present as  $[\text{Cu}(\text{CO})]^+$  adducts, only the reversible species (all possible adducts apart from  $[\text{Cu}(\text{CO})]^+$ ) would form, leading to a lower isotherm at plateau pressures.
- 4) Subtraction of the secondary isotherm from the primary isotherm provides the number of irreversible species at plateau pressures; if  $[\text{Cu}(\text{CO})]^+$  are the only irreversible species, the amount of adsorbed CO at plateau corresponds to the amount of Cu(I) in the sample.

An example of this procedure applied to the same sample shown in Figure 2.5 is reported in Figure 2.6.



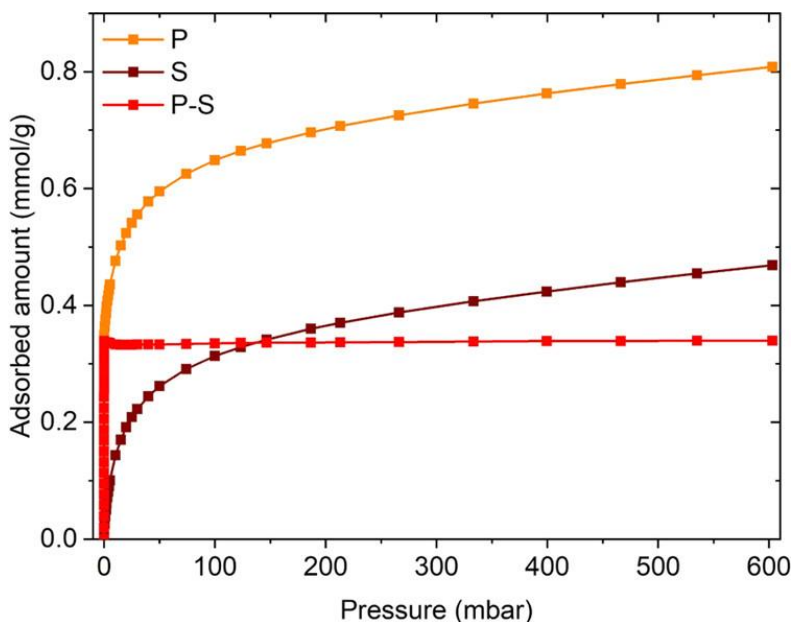


**Figure 2.6** CO adsorption isotherms performed at 50 °C on the pre-reduced (0.35)Cu-MFI(11.5) sample. Orange: primary isotherm (P); brown: secondary isotherm (S); red: difference between the primary and secondary isotherm (P-S), used to calculate the amount of irreversibly bound CO. Adapted from Appendix A3.

Once the amount of adsorbed CO is retrieved, the fraction of Cu(I) in the sample is easily calculated from the equation:

$$Cu(I)(\%) = (n_{ads} * FW_s) * 100$$

Where  $Cu(I)(\%)$  is the percentage of Cu(I) in the sample,  $n_{ads}$  is the amount of adsorbed CO (in units of  $mmol_{CO}/g_{sample}$ ) and  $FW_s$  is the formula weight of the sample (in units of  $g_{sample}/mmol_{Cu}$ ), easily calculated from the known concentration of the sample. Repeated measurements on the same sample retrieved a concentration of Cu(I) after pre-reduction in  $NH_3$  at 500°C of ~90%, in line with data from XAS; relative standard deviations in the measurements were found to be below 5%, attesting to the robustness of this method.

The reliability of this technique was further investigated by cross-checking it against IR data on a series of Cu-ZSM-5 samples presenting different Al and Cu concentrations. Figure 2.7 shows the IR spectra of four pre-reduced Cu-ZSM-5 materials after interaction with CO and the correspondence with volumetric data on the same set of samples.

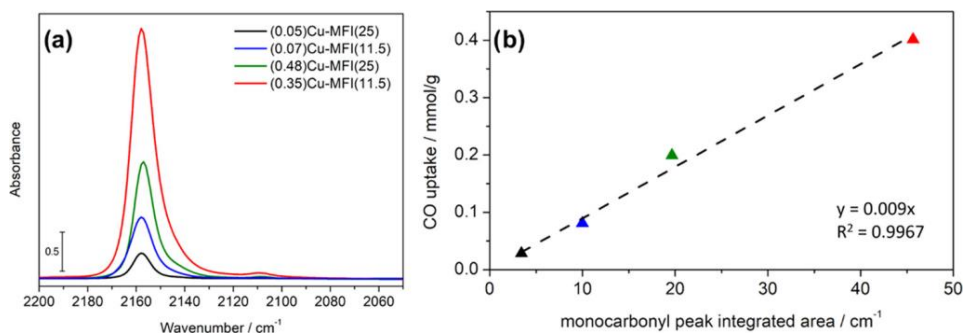


**Figure 2.7** CO adsorbed on the four reference Cu-ZSM-5 samples; number in parentheses reflect composition of the samples in molar ratios, according to (Cu/Al)Cu-MFI(Si/Al). (a) IR spectra of the samples after interaction with 200 mbar CO and outgassing. (b) Uptake of irreversibly bound CO on the samples versus integrated area of the Cu(I) monocarbonyl species. Adapted from Appendix A3.

The IR spectra portrayed in Figure 2.7a (normalized to framework modes as detailed in Appendix A3) follow the trend in total Cu content among the samples, with more intense  $[\text{Cu}(\text{CO})]^+$  fingerprint bands in samples with higher Cu loading. Moreover, the integrated area of the monocarbonyl band correlates well with the CO uptake measured by isothermal adsorption volumetry, as highlighted in Figure 2.7b. This finding confirms the fact that the two techniques, although relying on different principles and experimental apparatuses, can describe and measure the phenomenon in reliably comparable ways. The quantification obtained by the volumetry experiments was thus applied to retrieve the molar attenuation coefficient of the vibrational feature of  $[\text{Cu}(\text{CO})]^+$ . While the Beer-Lambert law is often a fair approximation for spectra collected in the homogeneous phase (although care needs to be taken whenever using this equation to avoid the many pitfalls that can characterize this limiting law),<sup>64</sup> applications to solid materials tend to be more complex and need to be carefully checked both *a priori* and *a posteriori*;<sup>65</sup> in this case, scattering contribution to absorbance were eliminated by subtracting the spectrum of the material prior to CO adsorption, and linearity was checked for a series of Cu concentrations in an appropriate absorbance range. In favourable cases, the relationship between integrated absorbance and concentration is linear, and the Beer-Lambert equation can be expressed in terms of spectroscopic and geometrical parameters of the sample as follows:

$$A = \varepsilon \frac{Cw}{S}$$

Where  $A$  is the integrated area (in absorbance) of a band referring to a specific vibration (in this case, the vibrational feature of  $[\text{Cu}(\text{CO})]^+$  at  $2157 \text{ cm}^{-1}$ , in units of  $\text{cm}^{-1}$ ),  $\varepsilon$  is the integrated molar attenuation coefficient of the same vibrational mode (in units of  $\text{cm}/\mu\text{mol}$ ),  $C$  is the concentration of the species associated with the vibrational mode (in units of  $\mu\text{mol/g}$ ),  $w$  is the mass of the sample (in units of  $\text{g}$ ) and  $S$  is the geometrical surface of the sample pellet (in units of  $\text{cm}^2$ ). From a series of IR experiments like the ones portrayed in Figure 2.7a (without normalizing for framework modes) and coupled volumetric measurements on the same materials, a least-squares linear regression of  $A$  vs  $Cw/S$  provides the molar attenuation coefficient as the slope of the line, as illustrated in Figure 2.8.

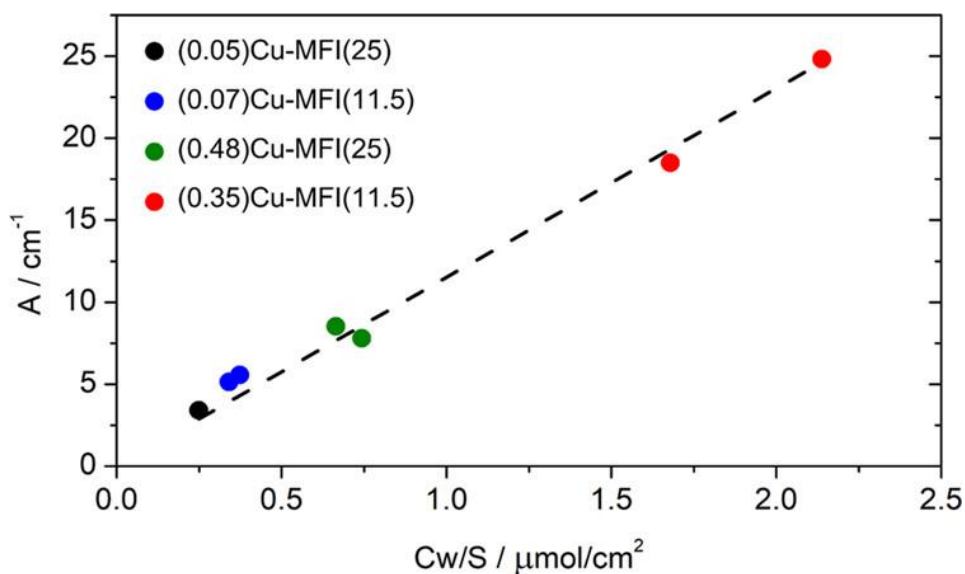


**Figure 2.8** Linear model for quantifying the molar attenuation coefficient relative to the Cu(I) monocarbonyl adducts. Points with the same colour indicate replicas measured on different pellets of the same material.  $R^2$  for the linear model is 0.992. Adapted from Appendix A3.

In this specific case,  $\varepsilon$  was measured to be  $11.5 \pm 0.3 \text{ cm}/\mu\text{mol}$ , a rather high number compared to signals involved in adducts with other absorbed molecules; as a comparison, the attenuation coefficient for a diagnostic band of pyridine adsorbed on Brønsted acid protons in zeolites is  $\varepsilon(\text{B})_{1545} = 1.09\text{-}1.54$

cm/ $\mu$ mol.<sup>66</sup> Such a high attenuation coefficient guarantees that even low amounts of Cu(I) can be detected and quantified via IR spectroscopy in a wide range of Cu-ZSM-5 materials (0.16-2.6 wt% in this case), although spectra of samples with high concentrations of Cu(I) and overall high Cu loadings could be problematic due to signal saturation problems with thick pellets.

The choice of Cu-ZSM-5 as a benchmark material for this study was made based on the simplicity and homogeneity of the possible sites for Cu in this topology (small, straight pores with no side pockets), as well as the abundance of literature studies on the material and its properties with respect to adsorption of probe molecules on the Cu sites. Although one might be tempted to extend the methodology to other materials, as interactions of CO with Cu in zeolites have been described for many topologies,<sup>54,67-69</sup> the stability of these adducts in different structural environments might present some differences if quantification is an aim. Moreover, the same reduction treatment applied to different materials could lead to different qualitative and quantitative results, so an independent technique to address this problem must be employed for the task. Coincidentally, not many cases of XAS applied to study and quantify the interaction of CO with Cu-zeolites other than Cu-ZSM-5 have been reported in the literature, making it an interesting topic on both the fundamental and applied sides. A set of 6 Cu-zeolite samples with different topology and composition were considered for this study; their characteristics are summarized in Table 2.1 (Section 2.1). This specific set of samples was chosen because of the ample characterization data collected on them in previous studies (see related publications) and because of the general abundance of literature studying these specific framework types for several reactions (*e.g.*, NH<sub>3</sub>-SCR, DMTM). *In situ* XAS measurements were collected on the materials replicating the reduction protocol used for the IR/volumetry experiments (using gas flows instead of static treatment for convenience), subsequently exposing the sample to CO and finally performing a temperature-programmed desorption (TPD) protocol; a schematic representation of the steps involved in the *in situ* experiments is reported in Figure 2.9.

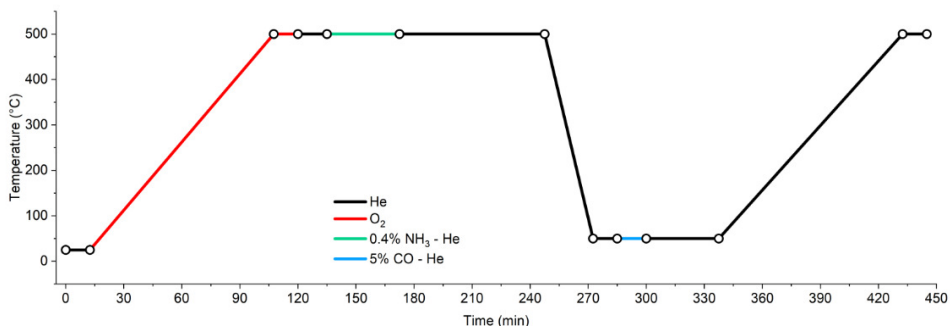


**Figure 2.9** Scheme of the thermochemical treatment employed in the *in situ* XAS experiments for all Cu-zeolite samples reported in Table 2.1. All heating ramps were set to 5°C/min, while cooling was performed without a constant ramp rate at the highest speed possible (ca. 30°C/min). Adapted from Appendix A5.

The complete dataset resulting from the experiment can be found in Appendix A5. The pure spectral and concentration profiles retrieved with MCR analysis on the reaction steps at 500°C are displayed in Figure 2.10 for the sample with higher Cu loading in each framework.

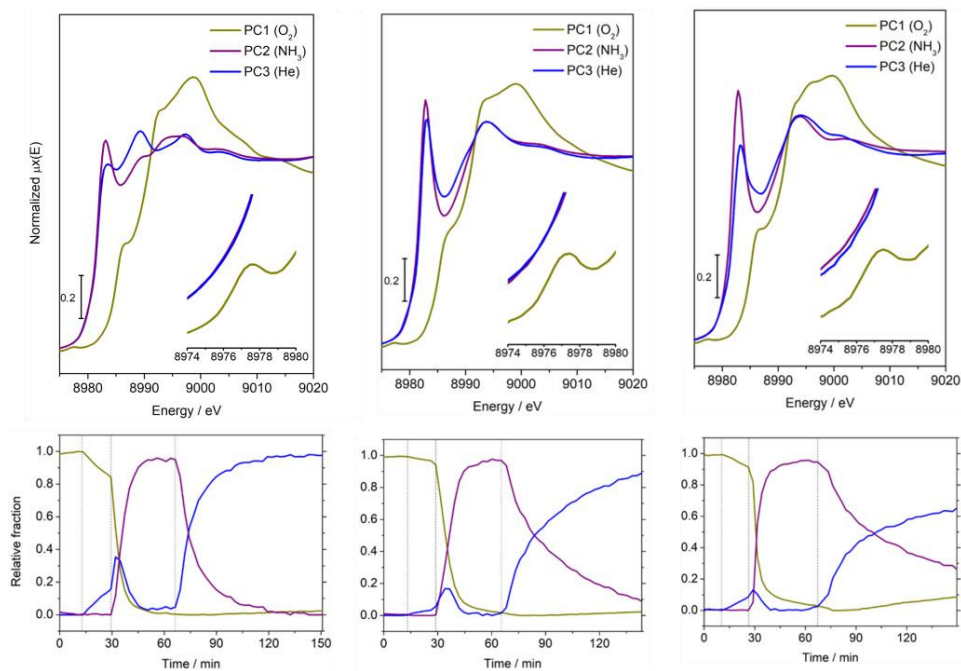


**Figure 2.10** Pure spectral (top) and concentration (bottom) profiles extracted by MCR-ALS on (0.35)Cu-CHA(5), (0.32)Cu-MOR(11) and (0.35)Cu-MFI(11.5) (from left to right) during the steps

at 500°C described in Figure 2.9. Insets: zoom on the 1s-3d transition zone of the edge. Adapted from Appendix A5.

The general spectral features of these samples (Figure 2.10, top panels) agree with the abundant literature on the topic. PC1 is easily associated to Cu(II) species (with some residual Cu(I) in the case of Cu-CHA, probably due to self-reduction phenomena),<sup>70,71</sup> as testified by the weak dipole-forbidden 1s→3d transition at 8978 eV and the shakedown transition at 8987 eV (both characteristic of Cu<sup>2+</sup>), as well as a shift in absorption edge at higher energies compared to the other spectra and a higher intensity of the white line, suggesting relatively high coordination numbers (4-6).<sup>72,73</sup> PC2 and PC3, in contrast, are consistent with low-coordinated (1-3) Cu(I) species from the very intense 1s→4p transition at 8983 eV characteristic of Cu<sup>+</sup> and a low white line intensity.<sup>72,73</sup> PC2 is likely attributable to linear diamino [Cu(NH<sub>3</sub>)<sub>2</sub>]<sup>+</sup> complexes that have been shown to form in the zeolite matrix in similar conditions,<sup>74,75</sup> while PC3 is probably representative of bare Cu<sup>+</sup> ions coordinated to the framework after removal of NH<sub>3</sub> due to the high-temperature treatment in inert atmosphere. Interestingly, PC2 and PC3 in the case of Cu-CHA materials are significantly different compared to the other frameworks, with a more structured rising edge/white line profile; this could be due to minute but significant structural differences in the vicinity of Cu induced by the CHA framework and the known mobility of [Cu(NH<sub>3</sub>)<sub>2</sub>]<sup>+</sup> adducts described in these materials.<sup>75</sup> The concentration profiles (Figure 2.10, bottom panels) hint at a quantitative formation of linear Cu(I) amino complexes for all materials, with NH<sub>3</sub> desorption rates that follow the order CHA>>MOR>MFI (from faster to slower); indeed, some residual NH<sub>3</sub> coordinated on Cu after evacuation at high temperature was observed in the case of the previously discussed Cu-ZSM-5 materials, further displaced from the metal sites after interaction with CO (see Appendix A3 for more details). Another interesting aspect is the transient formation of bare Cu(I) ions right after interaction of NH<sub>3</sub> with the samples (PC3 at ~ 30 min in Figure 2.10, lower panels): the first molecules of NH<sub>3</sub> diffusing in the oxidized sample react with Cu(II) to form bare Cu(I) sites, that then react with additional NH<sub>3</sub> molecules to form the linear adducts. After cooling down the samples, the sample was exposed to CO and subsequently flushed with He to desorb the reversible adducts; the results from MCR analysis of these reaction steps are reported in Figure 2.11.

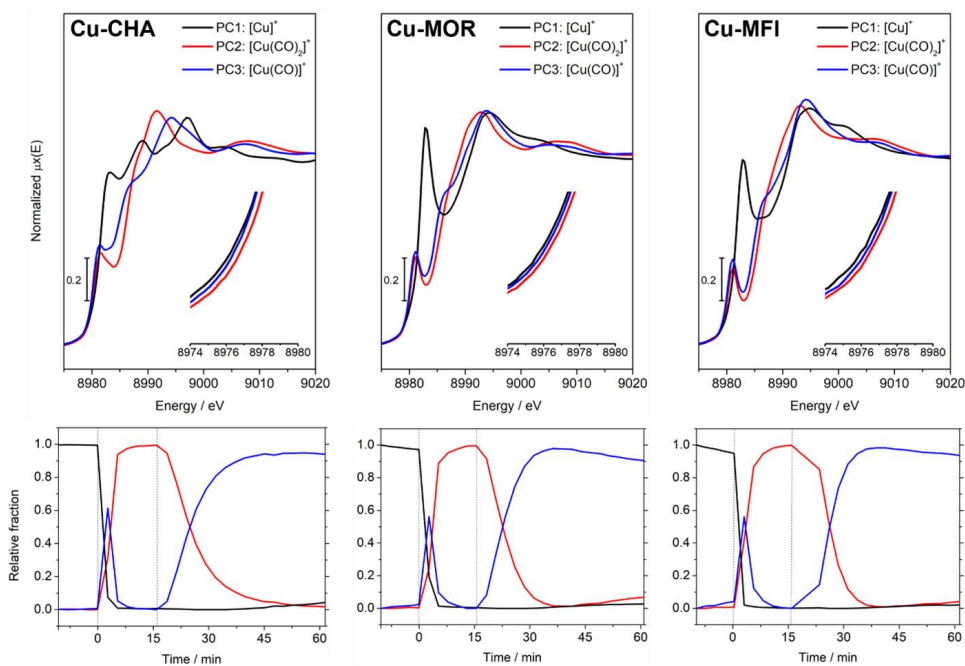


**Figure 2.11** Pure spectral (top) and concentration (bottom) profiles extracted by MCR-ALS on (0.35)Cu-CHA(5), (0.32)Cu-MOR(11) and (0.35)Cu-MFI(11.5) (from left to right) during the steps at 50°C described in Figure 2.9. Insets: zoom on the 1s→3d transition zone of the edge. Adapted from Appendix A5.

The initial states at 50°C (PC1) in this spectral series match well the final states described in Figure 2.10, confirming that the Cu sites do not significantly change upon temperature decrease. The literature is very scarce on XAS spectra of the interaction of CO with Cu-zeolites, but some species have been reported and assigned before<sup>76</sup> without assigning the origin of the different spectral features. Considering the concentration profiles shown in Figure 2.11 (bottom panels) and the general trend in carbonyl formation in these materials, it is safe to assume that PC2 and PC3 from Figure 2.11 (top panels) correspond to  $[\text{Cu}(\text{CO})_2]^+$  and  $[\text{Cu}(\text{CO})]^+$  species, respectively; this is further testified by the transient formation of PC3 as soon as CO is introduced in the cell, corresponding to a first fraction of monocarbonyls forming until the Cu(I) sites are saturated and the dicarbonyls start forming. Upon flushing with He, the  $[\text{Cu}(\text{CO})_2]^+$  species revert back to  $[\text{Cu}(\text{CO})]^+$ ; although these species appear to be stable in these conditions, some amount of desorption to form bare Cu(I) sites can be noticed from the recovery of a fraction of PC1 in the case of Cu-CHA and from an increase in the 1s→4p transition of bare Cu(I) in the original

spectra (see Appendix A5). To understand the origin of the peculiar rising edge profile of the spectra corresponding to  $[\text{Cu}(\text{CO})]^+$  and  $[\text{Cu}(\text{CO})_2]^+$ , simulation of XANES spectra for the species involved in this reaction are reported in Figure 2.12.

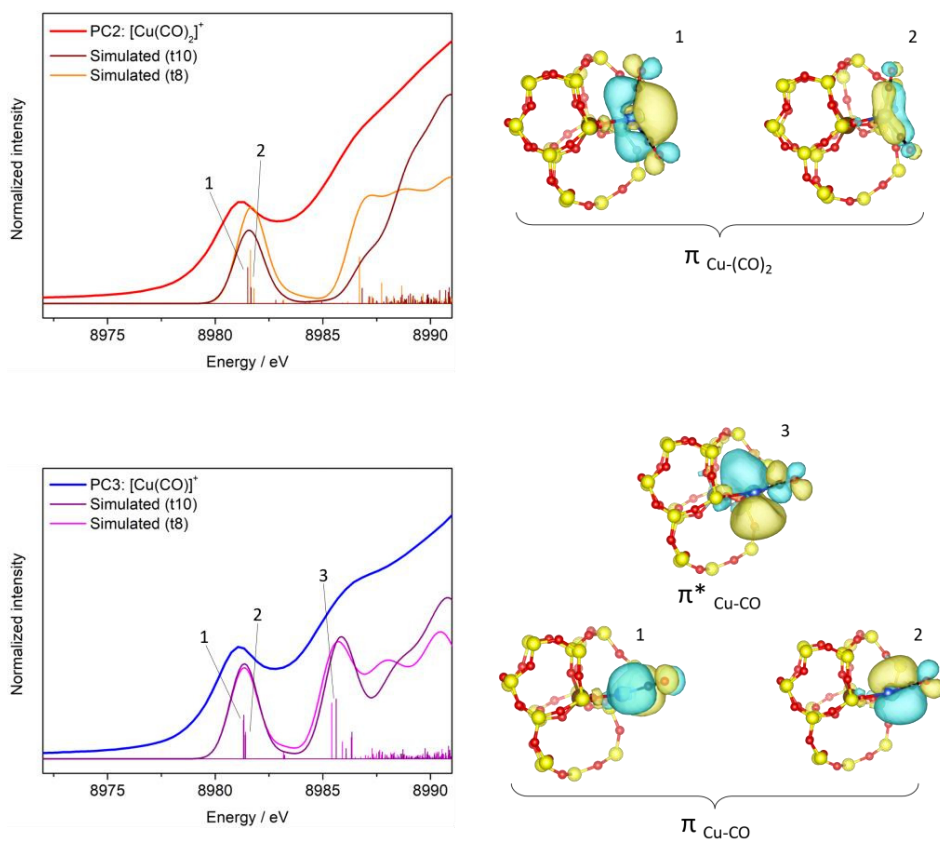


**Figure 2.12** Pure spectral profiles extracted by MCR-ALS on (0.35)Cu-MFI(11.5) corresponding to the  $[\text{Cu}(\text{CO})_x]^+$  adducts shown in Figure 2.11 (right panel) and comparison with calculated XANES spectra of the corresponding adducts for two crystallographic sites of Al (t8 and t10). The bar plots correspond to the position of each transition as described by TD-DFT. Structures on the right depict natural transition orbitals associated with the transitions marked in the spectra (isovalue = 0.02).

For both adducts the calculated spectra match quite well the experiment, with recognisable features that are well described by the NTO analysis. The feature at 8981 eV that is present without significant shift for both adducts is due to a doublet of almost degenerate  $1s \rightarrow \pi$  transition from the core electron orbital of



the metal to the set of bonding  $\pi$  orbitals between the Cu and the CO molecule(s) (transitions marked as 1 and 2 in Figure 2.12). The transition present at 8986.5 eV in the spectrum of  $[\text{Cu}(\text{CO})]^+$  is assigned to a  $1s \rightarrow \pi^*$  transition from the core electron orbital to an antibonding  $\pi^*$  orbital between Cu and CO; this transition also appears as a doublet, although the corresponding  $\pi^*$  orbital of the set is shifted at higher energies as it partially overlaps to more diffuse orbitals (not shown for brevity). In the case of  $[\text{Cu}(\text{CO})_2]^+$ , the mixing is so severe that the  $1s \rightarrow \pi^*$  transitions are not as well defined and lie at even higher energies (resulting in the weaker shoulder at ca. 8987 eV in the spectrum). The partial overlap of these orbitals with those of some atoms in the framework in the case of the more sterically hindered  $[\text{Cu}(\text{CO})_2]^+$  complexes is responsible for the more pronounced loss of degeneracy in the  $\pi$  set that act as acceptor for the transition at 8986.5 eV, as can be noticed by both the split in the calculated transitions (0.15 vs 0.06 eV for  $[\text{Cu}(\text{CO})_2]^+$  and  $[\text{Cu}(\text{CO})]^+$  respectively in both Al sites) and the slightly larger width of the band associated to this transition in  $[\text{Cu}(\text{CO})_2]^+$  compared to  $[\text{Cu}(\text{CO})]^+$ . This effect is likely responsible for the shift in the position of both  $1s \rightarrow \pi^*$  and  $1s \rightarrow \pi$  transitions depending on the Al site (negligible in the case of  $[\text{Cu}(\text{CO})]^+$ ). Given the differences in the calculated rising edge XANES for these species in all three frameworks (not shown for brevity), an argument could be made on the possible different population of Al sites in these materials; although this falls outside of the scope of this study, some additional considerations on this topic will be presented in Section 2.4.

To investigate the thermal stability of the remaining  $[\text{Cu}(\text{CO})]^+$  adducts, as well as the possible reactivity at higher temperatures, a TPD protocol was performed as last step of the treatment for all materials. The resulting spectral and concentration profiles from MCR are shown in Figure 2.13.

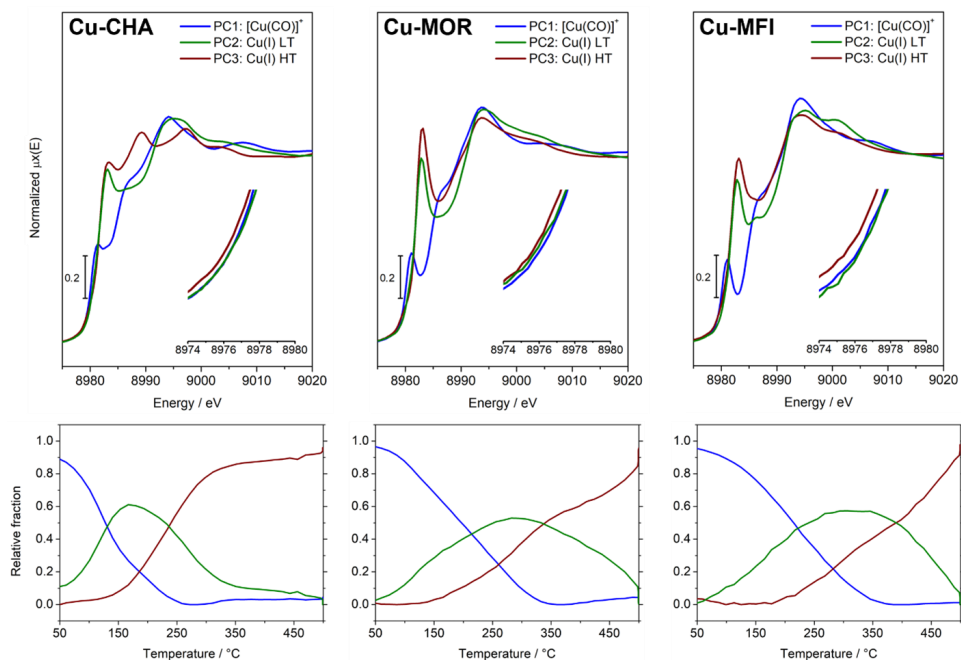


**Figure 2.13** Pure spectral (top) and concentration (bottom) profiles extracted by MCR-ALS on (0.35)Cu-CHA(5), (0.32)Cu-MOR(11) and (0.35)Cu-MFI(11.5) (from left to right) during the TPD protocol described in Figure 2.9. Insets: zoom on the 1s  $\rightarrow$  3d transition zone of the edge. Adapted from Appendix A5.

For all three materials, thermal treatment results in the subsequent appearance of two species ascribable to bare Cu(I) coordinated to the framework; while both of these species resemble the ones obtained after  $\text{NH}_3$  desorption (Figure 2.10, top panels), they appear to be predominant at different temperatures, possibly hinting at different equilibrium positions of Cu depending on the temperature. The exception to this trend is Cu-CHA, for which only the low-temperature Cu(I) species resembles the state after  $\text{NH}_3$  desorption, while the high-temperature one is more similar to the spectra of Cu(I) in the other materials. This peculiar behaviour could be due to the narrow pore structure of CHA, in which recent studies have proposed  $\text{NH}_3$ -mediated mobilization of Cu(I).<sup>75,77</sup> Furthermore, as can be noticed from the concentration profiles (Figure 2.13, bottom panels), the thermal stability of the monocarbonyl adducts in Cu-CHA is lower compared to the other materials, with the depletion of these species occurring at ca. 250°C for CHA compared with ca. 350°C for the other framework types. Energetics for two representative sites for each topology were calculated using DFT to further

inquire this difference in stability; the resulting temperature-pressure phase diagrams are reported in Figure 2.14.

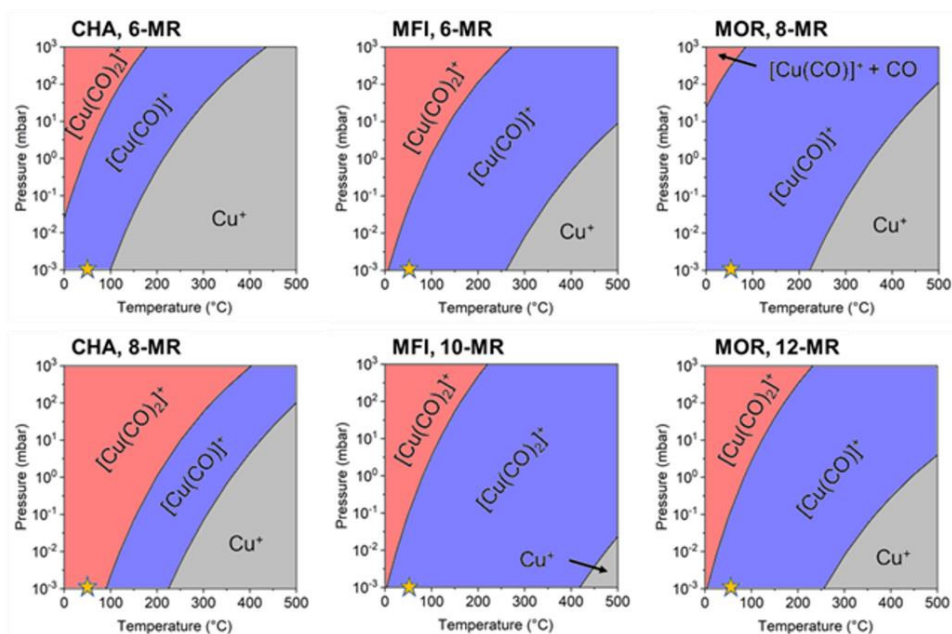


**Figure 2.14** Temperature-pressure phase diagrams calculated for the bare Cu(I) sites and  $[\text{Cu}(\text{CO})_x]^+$  adducts for the two representative sites chosen for each framework topology. Stars in the picture indicate the conditions at which volumetric measurements are performed to measure the amount of monocarbonyl complexes. As can be seen in the top-rightmost panel, the  $[\text{Cu}(\text{CO})_x]^+$  adduct is not stable in the 8-membered ring of MOR and is thus labelled as  $[\text{Cu}(\text{CO})]^+ + \text{CO}$ . Adapted from Appendix A5.

In agreement with experimental data, the calculated thermal stability at low CO partial pressures ( $10^{-3}$  mbar) of  $[\text{Cu}(\text{CO})]^+$  adducts for Cu-CHA is significantly lower than for the other frameworks in the calculated sites; in particular, supposing an equal population of the two sites in all cases, the average decomposition temperature for Cu-CHA is  $162^\circ\text{C}$  compared to  $275^\circ\text{C}$  and  $340^\circ\text{C}$  for MOR and MFI, respectively. From the calculated contributions to Gibbs free energy, this striking difference is mostly due to enthalpic rather than entropic factors (see Appendix A5 for details). This trend could also explain the different amounts of  $\text{Cu}^+$  measured for these materials using isothermal adsorption volumetry, the results of which are shown in Table 2.2.

**Table 2.2**  $\text{Cu}^+$  concentrations measured by isothermal volumetric adsorption of CO at 50 °C on the 3 Cu-zeolite samples discussed in this section.

Sample	CO uptake (mmol/g)	$\text{Cu}^+$ concentration (%)
(0.35)Cu-CHA(5)	0.480	60.6
(0.32)Cu-MOR(11)	0.322	74.6
(0.35)Cu-MFI(11.5)	0.401	89.1

From this set of measurements, it appears that a lower amount of Cu(I) is formed in Cu-MOR and especially in Cu-CHA, in clear contradiction with the XAS data. This discrepancy can be rationalized in terms of a different stability of the monocarbonyl Cu(I) adducts in the three frameworks, considering the different timescales to which the two measurements are subject (less than 1h of inert gas flow for XAS, up to several hours for volumetry); in this frame, kinetic factors of CO desorption from stable but long-term partially reversible  $[\text{Cu}(\text{CO})]^+$  adducts are consistent with the differences measured by the two techniques.

Overall, this set of experiments explored the often-neglected Cu(I) side of Cu-zeolite reactivity, with a particular attention at Cu reducibility as a function of sample composition and topology. All samples in the investigated subset showed similar response to the chosen reduction treatment, with quantitative formation of Cu(I) and no detectable sign of metallic Cu. Although with some kinetic effects to keep in mind depending on the sample, CO isothermal adsorption volumetry is a useful tool to consider when quantification of Cu(I) sites is needed but access to a large-scale facility is not available. In the case of Cu-ZSM-5, validation of this technique has been provided on a set of samples and has been applied to build a reliable model for quantification via IR spectroscopy, widening the toolbox of lab techniques that can be used for the task. Last but not least, a series of computational and statistical tools has been applied to a large (but not enormous) dataset allowing for in-depth knowledge about the thermodynamic, kinetic and spectroscopic features of Cu(I)-carbonyl adducts, with insights on the peculiar electronic structure of these species and its influence on spectroscopic properties.

## 2.3 Cu(II) and multinuclear species

Compared to Cu(I), Cu(II) species described in DMTM studies in zeolites present dramatic variability in their structure depending on the host material, the Cu concentration and the reaction conditions. This heterogeneity is not surprising, considering the different properties of this cation: the increase in charge requires an additional counterion to balance, which can originate from the framework or from extraframework species, and Cu(II) usually prefers higher coordination (octahedral, 6-coordinated) compared to Cu(I) (tetrahedral, 4-coordinated). Jahn-Teller distortions (that are unlikely for the  $d^{10}$  configuration of Cu(I)) further contribute in forming less symmetric structures in case of Cu(II). Some trends have been identified on the behaviour of Cu(II) relative to framework topology/composition, such as the preference to form  $\text{Cu}(Z)_2$  sites (where Z denotes ligation to a framework site contributing one negative charge equivalent) over  $\text{Cu}(Z)(\text{OH})$  in high-Al materials.<sup>51</sup> In recent years, more and more species have been identified as active sites for DMTM, typically presenting the form  $\text{Cu}_x\text{O}_y\text{H}_z$ . Monomeric Cu(II) species like  $[\text{CuOH}]^+$  pairs have been recently proposed to be active in some conditions as identified by EPR and resonance Raman spectroscopies,<sup>78</sup> but the majority of research has focused on studying multinuclear species of the type  $\text{Cu}_x\text{O}_y$ , where two or more Cu atoms are connected by one or two O atoms. Since the Cu(I)/Cu(II) redox cycle and the local environment of Cu both play an essential role in the reactivity of DMTM, their response to a series of gas-phase reactants was investigated in an attempt to correlate the extent of oxidation with the proximity of Cu atoms; XAS was the technique of choice due to its sensitivity to both of these properties even in disordered systems. The same Cu-MOR material described in the previous section ( $\text{Si}/\text{Al} = 6.5$ ,  $\text{Cu}/\text{Al} = 0.21$ ) was employed for this study, since previously characterized materials based on commercial precursors showed significant  $\text{TiO}_2$  pollution that could hinder the analysis, as identified by Raman spectroscopy shown in Figure 2.15.

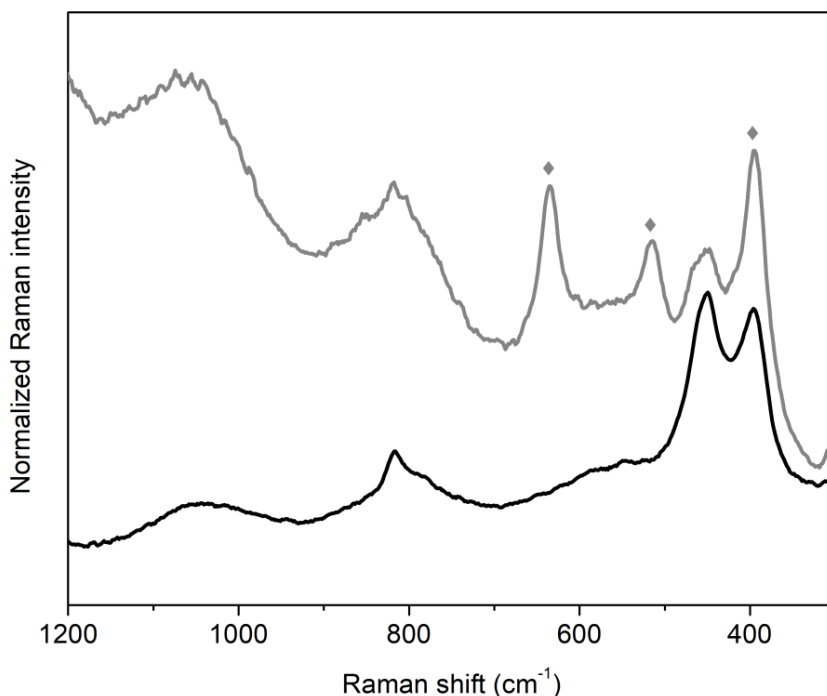


**Figure 2.15** Raman spectra ( $\lambda = 442 \text{ nm}$ ) of the (0.18)Cu-MOR(7) material described by Pappas et al.<sup>13</sup> (grey) and the (0.21)Cu-MOR(6.5) material discussed in Section 2.2 (black). Grey diamonds indicate vibrations due to amounts of  $\text{TiO}_2$  present in the material. Adapted from Appendix A2.

The material shown in grey in Figure 2.15 presents characteristic signals at 395, 515 and  $635 \text{ cm}^{-1}$  which have been assigned to the anatase phase in  $\text{TiO}_2$ , most likely originating from the commercial material that was ion-exchanged with Cu to obtain the final material.<sup>13</sup> Since the parent Na-MOR material (CBV10A, Zeolyst) is frequently employed as a starting material for the synthesis of Cu-MOR samples, the in-house-synthesized (0.21)Cu-MOR(6.5) material was preferred. A series of thermochemical treatments was applied to this material to study their effect on the redox speciation of Cu and the formation of Cu pairs. The explored conditions are illustrated in Table 2.3.

**Table 2.3** Thermochemical treatments explored to study the redox reactivity and its influence in Cu pair formation in (0.21)Cu-MOR(6.5). All samples have been outgassed in vacuum at 500°C before their respective treatment.

Sample n°	Treatment conditions	Treatment temperature
1	NH <sub>3</sub>	500°C
2	NH <sub>3</sub>	250°C
3	H <sub>2</sub>	250°C
4	CO	250°C
5	CH <sub>4</sub>	250°C
6	Vacuum (<10 <sup>-4</sup> mbar)	250°C
7	O <sub>2</sub>	500°C
8	NH <sub>3</sub> followed by O <sub>2</sub>	500°C

The XAS spectra collected for each thermochemical treatment are reported in Figure 2.16, comprising the XANES part of the spectra and the FT-EXAFS spectra as well as a linear combination fit (LCF) reconstruction of the dataset obtained by using samples 1 and 8 as references (details in Appendix A2).

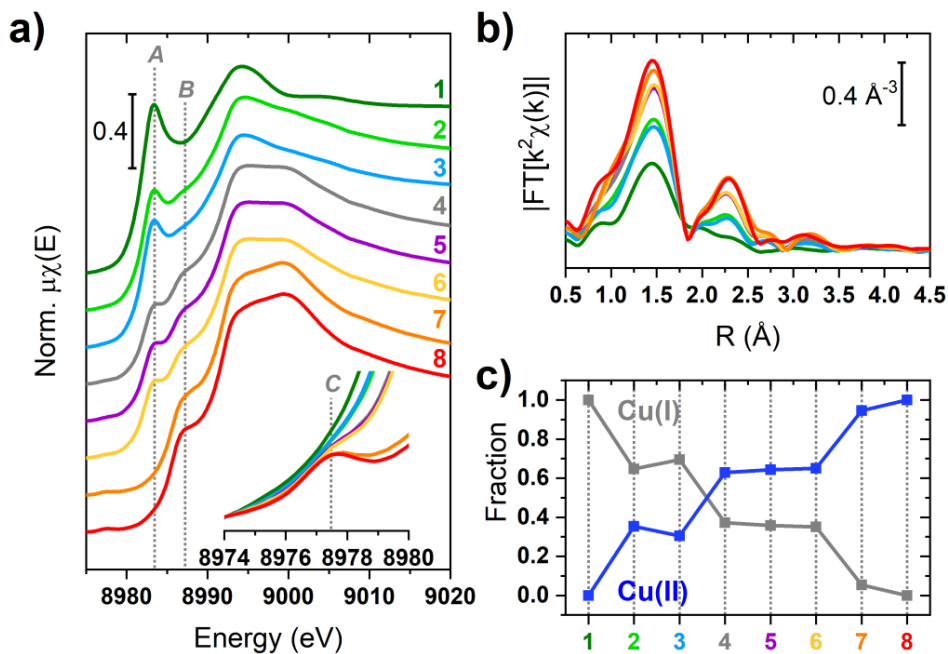


**Figure 2.16** XAS spectra collected on (0.21)Cu-MOR(6.5) after the thermochemical treatments listed in Table 2.3. a) Normalized XANES spectra; inset: zoom on the  $1s \rightarrow 3d$  transition zone of the edge. b) Phase-uncorrected,  $k^2$ -weighted FT-EXAFS spectra. c) LCF reconstruction of the XANES dataset shown in panel a, using as references spectra 1 and 8. Adapted from Appendix A2.

As can be noticed from Figure 2.16a, the extent of reduction achieved by treatment in  $\text{NH}_3$  is markedly temperature-dependent: when reduction was carried out at  $500^\circ\text{C}$  virtually all Cu was reduced, in agreement with the data shown in Section 2.3 (Figure 2.10), while the sample reduced at  $250^\circ\text{C}$  showed a residual amount of Cu(II). This difference in amount of Cu(I) is evident in the XANES spectra presenting a more intense  $\text{Cu}^+ 1s \rightarrow 3d$  transition at 8983 eV for sample 1, as well as a less intense white line and a weak first-shell peak in the FT-EXAFS spectrum due to neighbouring O atoms, consistent with a low-coordinated Cu(I) site attached to the framework. By comparison, sample 2 shows a weak but noticeable contribution from a  $\text{Cu}^{2+} 1s \rightarrow 3d$  transition at 8978 eV in the XANES spectrum, as well as a structured second-shell peak in the FT-EXAFS, consistent with higher coordination and stemming mainly from Cu-Al/Si and Cu-Cu single scattering contributions. The other samples are characterized by the same features with an increasing abundance of Cu(II) from 1 to 8: treatment in  $\text{H}_2$  at  $250^\circ\text{C}$  results in roughly the same amount of Cu(I) as



treatment with  $\text{NH}_3$  at the same temperature. Exposure to  $\text{CH}_4$  or  $\text{CO}$  leads to an even lower amount of  $\text{Cu(I)}$  (less than 50% according to LCF), and appear to be no more effective in reducing the sample than the self-reduction phenomena triggered by vacuum treatment at  $500^\circ\text{C}$ .<sup>70,71</sup> Lastly, exposure to  $\text{O}_2$  yields quantitatively oxidized samples with no detectable trace of  $\text{Cu(I)}$ , independent of the pre-reduction treatment (partial self-reduction in vacuum vs quantitative reduction in  $\text{NH}_3$ ). This clear but qualitative trend in oxidation state depending on the treatment is confirmed and quantified via LCF, and is correlated to structural features by the EXAFS spectra. Unfortunately, specific Cu-Cu contributions hinting at the formation of Cu pairs are not resolved in the FT-EXAFS spectra, as such contributions are expected to occur at distances of 2.8-3.4 Å based on DFT models and reports from the literature.<sup>79</sup> Strong contributions do not appear to be present in this zone of the EXAFS spectra of the pure  $\text{Cu(I)}$  state characteristic of sample 1, but they would nonetheless be indistinguishable from the signal due to framework atoms (taking phase correction into account) in case of  $\text{Cu(II)}$ . Contributions that overlap in R-space could, however, be resolved in k-space of the EXAFS spectrum for elements with sufficiently different atomic number, as the backscattering amplitude factor for heavier elements present additional maxima at higher wavenumbers; this is the case for Cu, that is characterized by a maximum in the backscattering amplitude factor at ca.  $7 \text{ \AA}^{-1}$  that is absent for framework atoms (considering Cu-X single scattering contributions, where X = Cu, Si, Al or O). The information concerning distance from the absorber and nature of the scatterer can then be simultaneously pictured in so called wavelet-transformed (WT) EXAFS spectra, effectively showing a 2D-map of the R- and k-space in which the scattering phenomenon is observed. Figure 2.17 portrays WT-EXAFS maps for the samples listed in Table 2.3 in the zone of interest for the supposed Cu-Cu contributions.

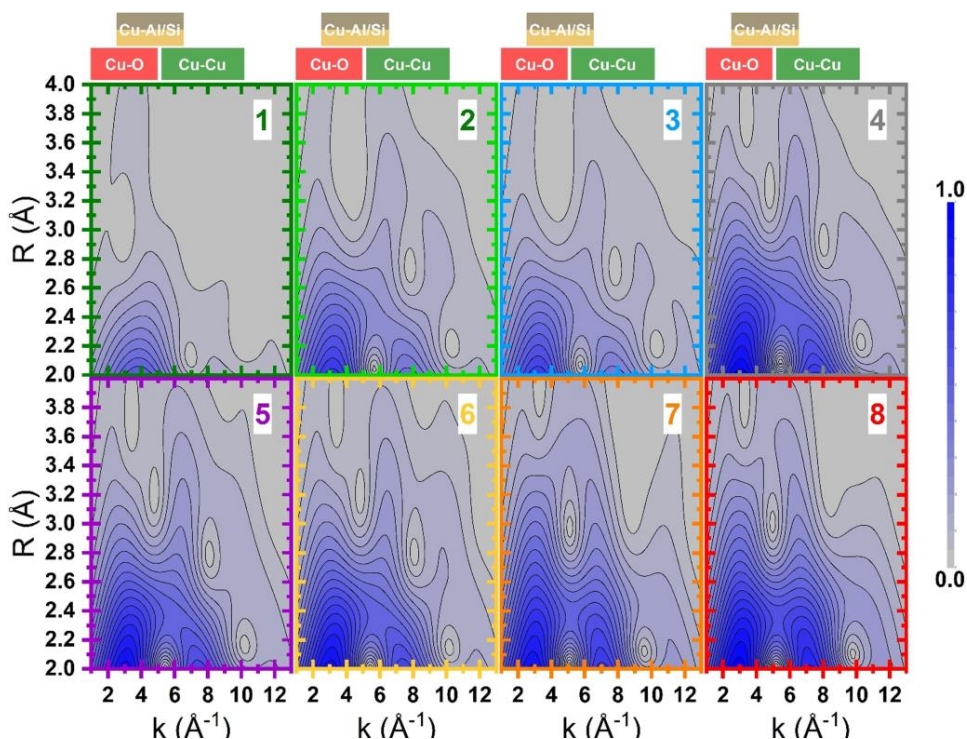


**Figure 2.17** WT-EXAFS spectra obtained on (0.21)Cu-MOR(6.5) after the thermochemical treatments listed in Table 2.3. Boxes on top of the figure represent the zones in  $k$ -space associated with principal contributions from the single scattering paths listed in the box. Adapted from Appendix A2.

As can be noticed from the figure, a first lobe is present for all samples at values of  $k = 2.0\text{-}4.0 \text{ \AA}^{-1}$  and  $R = 2.0\text{-}3.0 \text{ \AA}$ , corresponding to contributions from the framework atoms and following the trend qualitatively described for FT-EXAFS. Interestingly, a distinct contribution at similar  $R$ -values but at  $k$ -values of  $6.0\text{-}8.0 \text{ \AA}^{-1}$  appears as the amount of Cu(II) increases, related to specific contributions from Cu-Cu scattering paths. This finding directly correlates the oxidation of Cu to Cu(II) to the formation of Cu-pairs at a relatively short distance (thus probably bridged by a single O atom) that are not present when the majority of the metal is present as Cu(I) (at least within the ca.  $5 \text{ \AA}$  distance detectable by EXAFS). This qualitative observation was quantitatively assessed by integrating the WT-EXAFS maps in the  $2.0\text{-}4.0 \text{ \AA}$  range (where Cu-Cu contributions appear) to yield the corresponding power density functions  $\Phi^R(k)$ ; the result of this operation for all WT-EXAFS spectra is depicted in Figure 2.18.

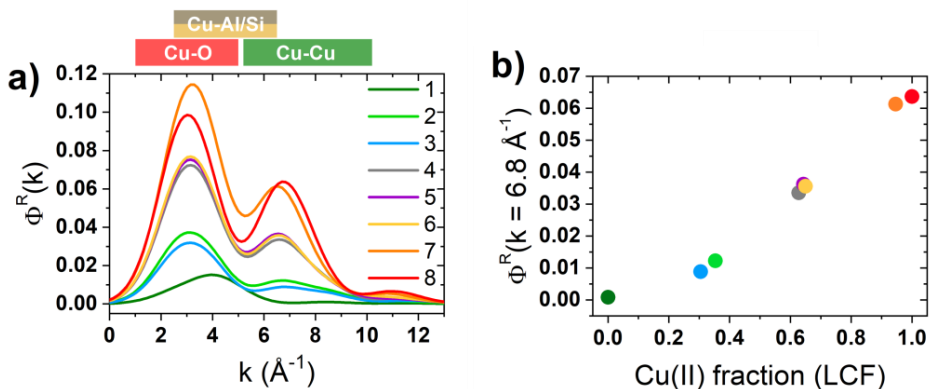


**Figure 2.18** a) Power density functions calculated for the WT-EXAFS spectra depicted in Figure 2.17. Boxes on top of the figure represent the zones in  $k$ -space associated with principal contributions from the single scattering paths listed in the box. b) Concentration of Cu(II) retrieved from LCF-XANES vs power density function evaluated at  $6.8 \text{ \AA}^{-1}$  for each spectrum, showing the correlation between the two quantities. Adapted from Appendix A2.

As can be noticed from the  $\Phi^R(k)$ , the contribution from Cu-Cu scattering paths to the WT-EXAFS spectra depicted in Figure 2.17 showed a clear quantitative relationship with the amount of Cu(II) present in the sample. Fits of the FT-EXAFS spectra based on different possible multinuclear Cu species are consistent with a mono- $\mu$ -oxo dicopper site ( $[\text{Cu}^{\text{II}}\text{-O-Cu}^{\text{II}}]^{2+}$ ), already described in the literature, and exclude the presence of side-on and end-on peroxo dicopper sites ( $[\text{Cu}^{\text{II}}\text{-OO-Cu}^{\text{II}}]^{2+}$ ) (see Appendix A2 for more details on the EXAFS fitting procedure and the models used for the study). As additional experimental evidence on the formation of these species, Figure 2.19 reports the resonance Raman spectra of (0.21)Cu-MOR(6.5) in its hydrated form and after oxidation in  $\text{O}_2$  at  $500^\circ\text{C}$ .

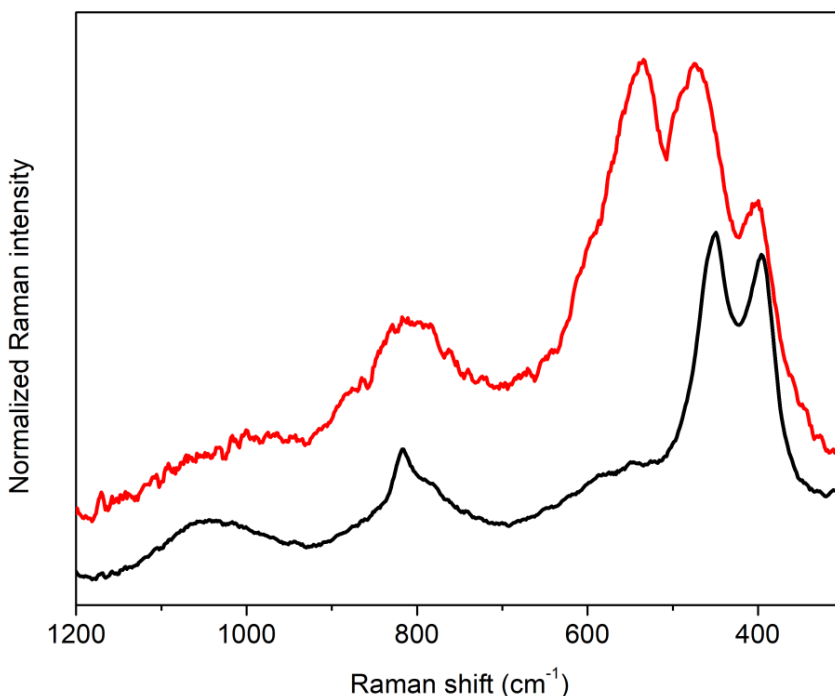


**Figure 2.19** Resonance Raman spectra ( $\lambda = 442 \text{ nm}$ ) of the (0.21)Cu-MOR(6.5) material discussed in Section 2.2 in its hydrated form (black) and after oxidation at  $500^\circ\text{C}$  in pure  $\text{O}_2$  (red). Grey diamonds indicate vibrations due to amounts of  $\text{TiO}_2$  present in the material. The spectra have been normalized to the vibrational mode of the MOR framework at  $400 \text{ cm}^{-1}$ . Adapted from Appendix A2.

In the hydrated sample, characteristic framework vibrations can be noticed at  $400$  and  $450 \text{ cm}^{-1}$  involving 5- and 4-membered rings, respectively, as well as broader contributions at ca.  $800$  and  $1100 \text{ cm}^{-1}$  corresponding to symmetric and antisymmetric T-O-T vibrations (where T = Si or Al) for both state of the sample, in agreement with literature on zeolites and other silicates.<sup>80–82</sup> The oxidized sample presents additional features at  $470$ ,  $535$ ,  $875$  and ca.  $1000 \text{ cm}^{-1}$ : these features are consistent with the formation of two families of  $[\text{Cu}^{\text{II}}\text{-O-Cu}^{\text{II}}]^{2+}$ , probably situated in the constrained side-pocket sites of the Cu-MOR, according to an in-depth study on a Cu-MOR sample treated in similar conditions.<sup>83</sup> In particular, the vibrations at  $470$  and  $875 \text{ cm}^{-1}$  have been assigned to the symmetric and antisymmetric stretch of the Cu-O-Cu core, while the vibrations at  $535$  and  $1000 \text{ cm}^{-1}$  are due to a perturbed T-site

vibration and its combination with the symmetric stretching of Cu-O-Cu, respectively.

Although the finding that Cu(II) forms multinuclear species more readily than Cu(I) may seem trivial, a direct and quantitative correlation between the oxidation state and Cu pairing was established for a series of samples by just using *ex situ* XAS data with the aid of advanced data treatment procedures. The amount of information extracted from a relatively small experimental set is considerable, and this methodology can be used to add species-selective features to the already element-selective nature of XAS by exploiting the bidimensional (R- and k-space) nature of WT-EXAFS.

## 2.4 Al distribution

The fact that different frameworks and compositions of Cu-zeolites can promote the formation of different Cu species, with subsequent impact on reactivity, is at least partially due to the different possible configuration of Al isomorphous substituents in the lattice. As an example of this impact, the distance and positions of the negative charges induced by Al sites in the pores affects the average Cu-Cu distance and the possibility to form bridged multinuclear species; the abundance and position of Al sites has been also correlated to the formation of Cu(Z)<sub>2</sub> redox-inert Cu sites,<sup>51</sup> contributing to the well-known non-monotonic relationship between Cu loading and catalyst performance.<sup>12</sup> It is not surprising then that several synthetic procedures have attempted to direct Al atoms in the framework towards specific patterns or completely random, well-dispersed distributions.<sup>84,85</sup> In parallel, many characterization techniques have been proposed to determine the siting of Al atoms due to a particular synthesis procedure; some of these methods are based on techniques that are intrinsically sensitive to properties of Al (like solid-state <sup>27</sup>Al MAS NMR,<sup>86–97</sup> anomalous scattering XRD<sup>98</sup> and atom probe tomography<sup>99–101</sup>), while other approaches exploit selective interaction (adsorption/desorption) of probe molecules with protons or other cations associated with Al atoms/pairs<sup>102–104</sup> or other cation-specific techniques<sup>95,105,106</sup>. In the context of this rich interest in solving the “Al

distribution problem”, some attempts were also made in directly probing the Al K-edge with XAS,<sup>56,107–113</sup> which should in principle be very sensitive to the local environment of Al atoms in the framework. One of the caveats of using this technique is that the registered spectra display an average of all probed sites, making it difficult to quantitatively assess the different siting; the amount of octahedral Al (deriving from steaming-induced dealumination) is easily determined from features of the XANES spectra, while creative approaches involving simulation of EXAFS using molecular dynamics and simulation of XANES features were used to explore the Al proximity and the effect of H<sub>2</sub>O in the pores. Since spectral features depending on Al siting have been both predicted and observed to be extremely similar to each other, an approach based on molecular dynamics-assisted machine learning to extract information on the two-body pair distribution function associated with the Al sites and on their specific amount in the investigated catalysts. The training set required to perform this study was generated considering all possible symmetry-restricted Al sites for a given sample composition, with the aim of calculating Al K-edge XANES and EXAFS spectra to correlate with experiments. The sample set this study consisted of a series of H-, Na-, K- and Cu-exchanged zeolites mainly of the MOR topology, that were measured in their hydrated form and after dehydration at 450°C; as specified in Table 2.1, these samples were prepared in the context of the iCSI project and have been thoroughly characterized in a previous publication.<sup>16</sup> Given the energy range required to measure Al K-edge spectra, Cu L<sub>3</sub>-edge spectra were also measured where relevant; as the latter are still under treatment, they will not be presented in this work. The choice of mordenite as the main framework under investigation was made based on the number of independent crystallographic sites in this topology: with only 4 non-equivalent T-sites available, MOR should display enough variability in Al coordination environment to detect changes in the spectra, but without making the number of possible combinations impractical for calculations. As a comparison, the CHA framework presents only 1 independent T-site (meaning all Al sites should be virtually identical) while the MFI framework presents 12 (leading to increased calculation cost and likely having different structures with indistinguishable properties). In a simplified one-particle electron-hole picture, K-edge transitions consist of core-to-valence transitions between orbitals (below the edge energy) and of core-to-continuum transitions with the ejected

electron interacting mainly with nearby scattering atoms (above the edge energy). This means that the XANES part of the spectrum can be considered as a fairly local property of the system, and the calculated spectra for a given Al site should be approximately independent on the vicinity of other Al atoms in the framework (especially considering the distance imposed by Löwenstein’s rule). XANES spectra for the 4 independent T-sites in the post-edge region of the spectrum, calculated with a multiple scattering approach, are shown in Figure 2.20.

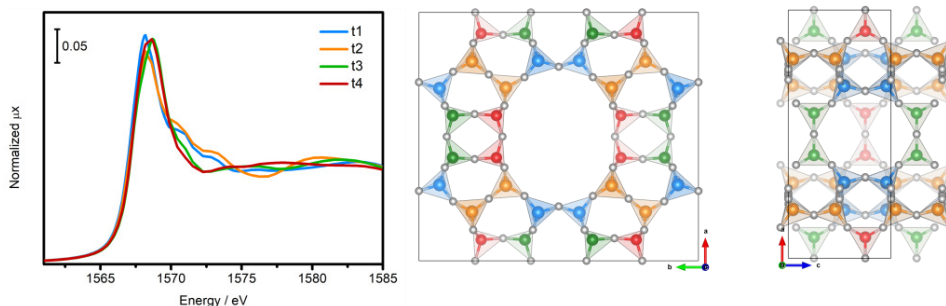


**Figure 2.20** Left: simulated Al K-edge XANES spectra for the four symmetry-independent tetrahedral sites in MOR. Right: position of the sites inside the MOR framework (view along the crystallographic c and b axes). Simulations were performed on optimized structures using the FDMNES code.

Although the simulated spectra look very similar, some significant differences are present, and machine learning-based approaches have proven to be able to extract significant information even from apparently indistinguishable XANES spectra.<sup>114–117</sup> Of course, the simple case of single substitution of a Si with an Al T-site is scarcely representative of a real system, which is most likely comprised of a non-uniform extended substitution of Al and a given composition of the material in terms of Al/Si ratio; at the same time, multiple substitutions turn the problem into a combinatorial study, with the number of possible structures increasing according to the binomial coefficient:

$$\binom{n}{k} = \frac{n!}{k!(n-k)!}$$

where n is the number T-sites and k is the occupancy by Al atoms. Some back-of-the-envelope calculations quickly lead to the conclusion that for the Al/Si of

11 (eventually expandable to 7) considered in this study, use of the MOR primitive cell as an extended system consists of a first practical solution, as summarized in Figure 2.21.

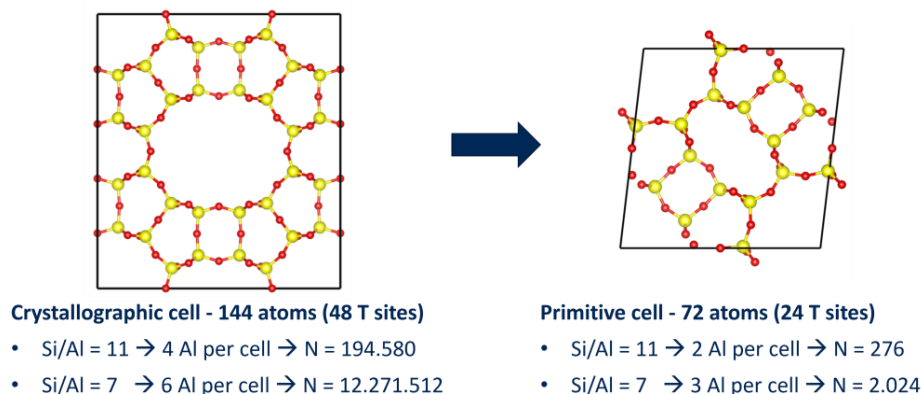


**Figure 2.21** Structure of the all-Si crystallographic (left) and primitive (right) cell of MOR, with the corresponding number of Al substitutions and possible structures calculated according to the binomial coefficient of sites and occupancy. Colour code: Si in yellow, O in red.

The 276 structures obtained via double substitution in the primitive cell do not take into account that some combinations are symmetry-equivalent, and removal of redundant Al couples using space group symmetry operators leads to 48 independent configurations; only 38 of these structures respect Löwenstein's rule (*i.e.*, Al sites are not allowed to share coordination by the same O) and are thus accepted in the set. Charge balance is obtained by inclusion of a light cation ( $\text{Na}^+$  as a first case), which can be located in the 8- or 12-membered ring for some Al positions (accommodation in side pockets was not considered at this stage): after these considerations, the final set of structures included 138 configurations. Of course, introducing a cation in a proportion different from 1:1 with Al would lead to an even higher number of possible sites, further increasing the complexity of the problem. Another challenge in dealing with these materials from a computational point of view is the exceptional flexibility of the Si-O-Si bond angles, which in silicates span between  $90^\circ$ - $180^\circ$ ; this flexibility gives rise to an extremely flat PES, which makes it difficult to find the global minimum from educated guesses only and can require post-HF treatment for very accurate results.<sup>34</sup> Since global minimum search strategies based on molecular dynamics like simulated



annealing were too expensive for this screening, we adopted a simplified scheme described in the literature that can lead to similar results at a fraction of the cost by optimization-quick heating-quick cooling cycles to obtain minimum structures and energies.<sup>118</sup> An initial ranking of structure stability could then be obtained by considering the Boltzmann population of configurations according to the relative energy. In order to account for hydration effects, since implicit solvation is not expected to simulate well the specific interactions of H<sub>2</sub>O molecules on hydrophilic sites; attempts on including such effects in the periodic models almost never converged and led to significant increase of the computational cost when they did, with a single solvation cycle costing up to 10 SCF cycles. Explicit solvation using 12 molecules of solvent per cell (as reported in the literature from experiments with similar materials)<sup>119</sup> was integrated in the model and treated with a reoptimization and molecular dynamics treatment (H<sub>2</sub>O molecules only, 10 ps, NVT ensemble, T = 127 °C) followed by simulated annealing. This methodology was applied to obtain models of dry/hydrated structures for Na-MOR and NH<sub>4</sub>-MOR (the dry form of which consists of H-MOR due to NH<sub>3</sub> desorption). According to this method, an average of 3 structures accounted for >80% of Boltzmann population of the configurations. It should be stressed again that the models used for calculations were characterized by a different Si/Al ratio compared to the actual materials (11 vs 7.3, respectively); a more consistent (though extremely more expensive, as noted in Figure 2.21) composition will be the topic of another work.

The most stable structure for each hydrated case and its corresponding dry configuration were used to calculate XANES spectra within the one-particle approximation using TD-DFT. Based on the supposed local nature of K-edge XANES orbital-based transitions, cluster models obtained by cutting the periodic structures were used as a basis for these calculations. Since each structure based on the primitive cell contained two distinct Al sites, a calculation on the cluster including both Al atoms was compared with calculations on smaller sub-clusters including one Al at a time; the results are shown in Figure 2.22.

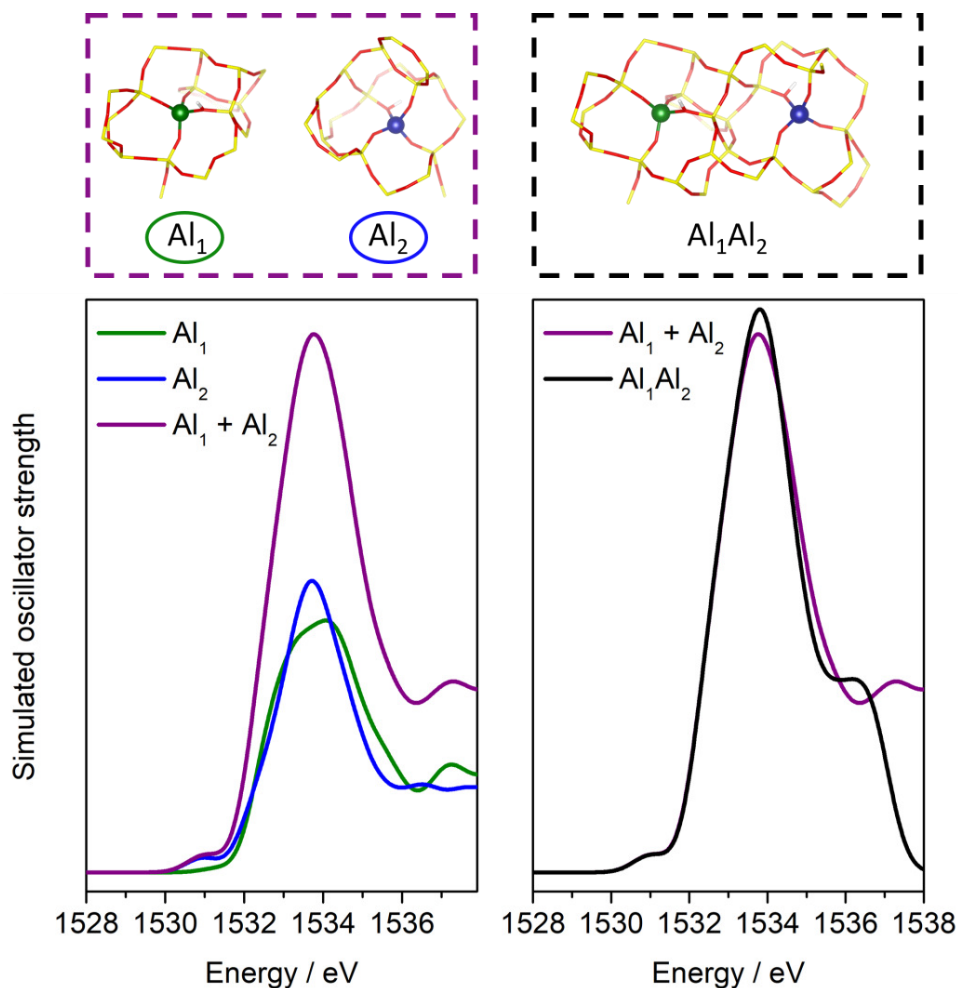


**Figure 2.22** Calculated Al K-edge XANES spectra of the H-MOR clusters obtained from the most stable hydrated  $\text{NH}_4$ -MOR periodic structures ( $\text{Si}/\text{Al} = 11$ , corresponding to 2 Al sites per primitive cell) shown on top. Left: comparison of simulated spectra for the two Al sites calculated on separate sub-clusters and their sum. Right: comparison of the spectra obtained as a sum of spectra for two different sites and the spectrum for a cluster comprising both Al atoms.

Encouragingly, the pre- and rising-edge profiles of the simulated spectra for the two different Al sites in the same configuration (labelled as Al<sub>1</sub> and Al<sub>2</sub> in Figure 2.22) display similar but distinct features. NTO analysis of the transitions involved in these calculated spectra is not trivial: compared with Cu K-edge, where core-to-valence transitions often involve well-separated and localized metal d orbitals in the pre-edge, Al orbitals are usually similar in energy and symmetry to ligand orbitals and give rise to diffuse, hard to interpret molecular

orbitals.<sup>120</sup> Some of these features will be discussed shortly in comparison with experimental data and with reports from the literature. Another important aspect is the striking similarity between the sum of the spectra due to individual Al sites ( $Al_1 + Al_2$ ) and the spectrum calculated on the full cluster model including both sites ( $Al_1Al_2$ ) portrayed in Figure 2.22 (right panel): apart from differences in the high energy region (which is not well-described by orbital-based approaches anyway), probably due to the difference in number of calculated states/number of atoms in the cluster, the pre- and rising-edge part of the spectra are identical, confirming that separating the contribution of the two Al sites gives consistent results with larger models.

Calculated XANES spectra within the TD-DFT frame almost always exhibit a systematic shift in energy compared to the experimental spectra due to shortcomings of DFT. Ideally, since this shift is often found to be consistent within K-edge calculations for the same element, one would calculate the spectrum on a reference sample for which features are reliably known to determine the shift, which would then be applied to other cases. In this case, the shift could not be determined a priori due to both the lack of evident pre-edge signals for the Al K-edge in standard samples and the overall scarcity of TD-DFT studies at this edge in the literature. The discussion of these spectra is thus based on similarity with previous findings and comparison with the general structure of the experimental data. For instance, Vjunov *et al.* calculated similar spectral profiles with a different computational setup, and assigned a shift of +15.6 eV to the computed spectra based on similarity with the experiment;<sup>113</sup> although care should be taken in assigning calculated features within an orbital-based approach at energies above the edge, the general shape of the edge is well-reproduced and comprises features in the pre-edge that match with the experiment (*vide infra*). Based on this reasoning, a shift of +34.0 eV is assigned to the Al K-edge spectra calculated in this work, which is the difference from the shift found by Vjunov *et al.* due to the difference in computational setup. Comparison of experimental and computed spectra for the hydrated ( $NH_4^-$ ) and dehydrated ( $H^-$ ) MOR samples are shown in Figure 2.23.

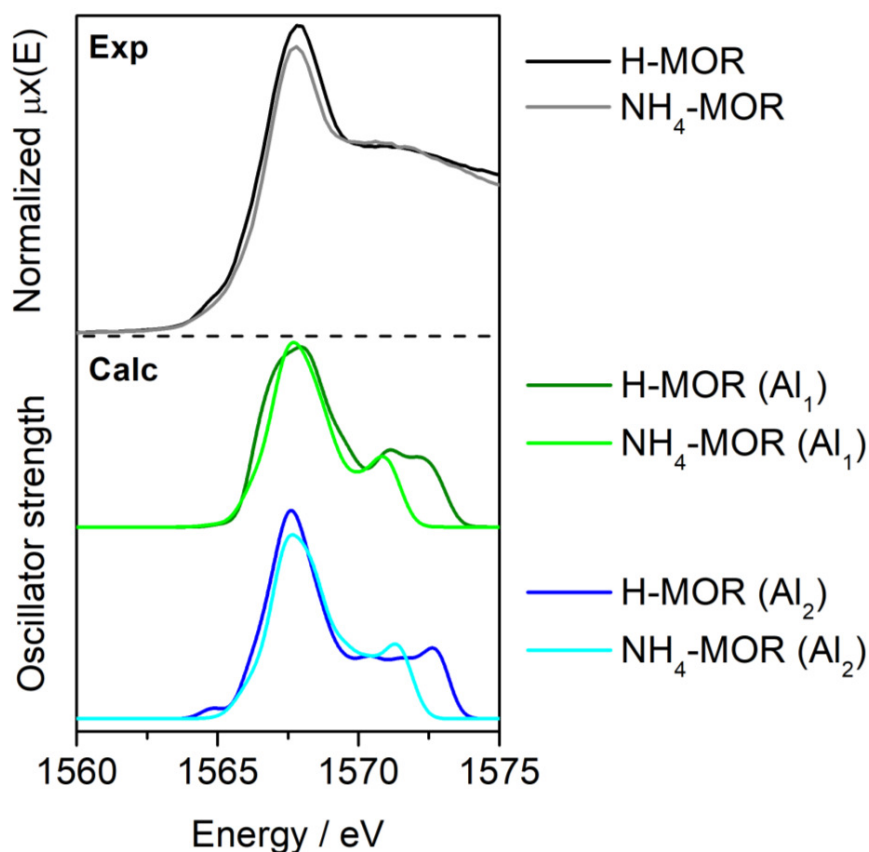


**Figure 2.23** Top: experimental Al K-edge XANES spectra of a NH<sub>4</sub>-MOR sample in its hydrated (NH<sub>4</sub><sup>+</sup> cation) and dehydrated (H<sup>+</sup> cation) forms. Bottom: calculated Al K-edge XANES spectra of the (hydrated) NH<sub>4</sub>-MOR and (dehydrated) H-MOR clusters described in Figure 2.22.

Interestingly, the spectra calculated for the Al<sub>2</sub> cluster bear a striking resemblance to the experimental set, hinting at a possible preferential siting in the material. In contrast, the calculated spectra for hydrated forms of Al<sub>1</sub> and Al<sub>2</sub> clusters are almost identical and very similar to the hydrated experimental spectrum (and hydrated forms of similar materials, not shown here for the sake of brevity). This suggests that hydration somehow masks the differences between different sites, as suggested by the models showing coordination of the cations by H<sub>2</sub>O molecules with subsequent weaker interaction with the framework in the proximity of Al. Indeed, the peculiar pre-edge feature that emerges at ca. 1565 in the experimental and calculated spectra for the dehydrated materials has been correlated by Vjunov *et al.* to the presence of

the non-solvated H<sup>+</sup> cation, inducing a distortion in the AlO<sub>4</sub><sup>-</sup> unit. Although the NTOs for this transition are very diffuse and difficult to interpret, previous studies<sup>121–123</sup> on the appearance of a similar pre-edge feature in several aluminosilicates have correlated it with the ability of the Al 3s orbital to hybridize with O 2s and 2p orbitals if symmetry of the AlO<sub>4</sub><sup>-</sup> unit is lowered due to vibrations (at high temperature) or if a cation is close enough to the structure to distort the tetrahedra. This is the case for these models, where the average Al-O distance in hydrated clusters is 1.75 Å, but one of the bonds is significantly lengthened when H<sub>2</sub>O is removed, as showed in Table 2.4.

**Table 2.4** Bond lengths associated to Al-O bonds in the hydrated and dehydrated models for Al<sub>1</sub> and Al<sub>2</sub> clusters.

Structure	Average Al-O distance	Al-O(-H) distance
NH <sub>4</sub> -MOR (Al <sub>1</sub> )	1.76 Å	/
NH <sub>4</sub> -MOR (Al <sub>2</sub> )	1.76 Å	/
H-MOR (Al <sub>1</sub> )	1.78 Å	1.94 Å
H-MOR (Al <sub>2</sub> )	1.78 Å	1.96 Å

The lengthened bond corresponds to the H-bound O atom in both cases. In the Al<sub>1</sub> cluster, the H<sup>+</sup> is in partial interaction with another O in the framework, possibly lowering the distortion effect on the AlO<sub>4</sub><sup>-</sup> unit; for comparison, the OH bond in the Al<sub>2</sub> cluster points towards the 12-membered ring without any further interactions of the H<sup>+</sup> with the framework.

Although the experimental data on the other samples needs to be treated and compared to the large computed dataset, these preliminary results are encouraging. Minute differences in the spectra can be interpreted in terms of orbital- or scattering-based approaches, subsequently tracing them back to structural differences induced by the Al sites and their interaction with the environment (framework, extra-framework cations, solvent). The ongoing work on these systems will focus on the analysis of the correlation between experimental/calculated spectral features and structural parameters, with the aim of training a machine-learning assisted model that could be able to

quantitatively determine key structural features in terms of Al siting depending on Al K-edge XAS spectra.

## References

1. <https://europe.iza-structure.org/IZA-SC/framework.php?STC=MFI>.
2. <https://europe.iza-structure.org/IZA-SC/framework.php?STC=CHA>.
3. <https://europe.iza-structure.org/IZA-SC/framework.php?STC=MOR>.
4. Baerlocher, C. & McCusker, L. B. <http://www.iza-structure.org/databases/>.
5. Wickleder, S., Housecroft, C., Pour, Z. A. & Sebakhy, K. O. A Review on the Effects of Organic Structure-Directing Agents on the Hydrothermal Synthesis and Physicochemical Properties of Zeolites. *Chem.* 2022, Vol. 4, Pages 431-446 4, 431–446 (2022).
6. Dyballa, M. et al. On How Copper Mordenite Properties Govern the Framework Stability and Activity in the Methane-to-Methanol Conversion. *ACS Catal.* 9, 365–375 (2019).
7. Dinh, K. T. et al. Continuous Partial Oxidation of Methane to Methanol Catalyzed by Diffusion-Paired Copper Dimers in Copper-Exchanged Zeolites. *J. Am. Chem. Soc.* 141, 11641–11650 (2019).
8. Cuppett, J. D., Duncan, S. E. & Dietrich, A. M. Evaluation of Copper Speciation and Water Quality Factors That Affect Aqueous Copper Tasting Response. *Chem. Senses* 31, 689–697 (2006).
9. Yashnik, S. & Ismagilov, Z. Cu-substituted ZSM-5 catalyst: Controlling of DeNO<sub>x</sub> reactivity via ion-exchange mode with copper–ammonia solution. *Appl. Catal. B Environ.* 170–171, 241–254 (2015).
10. Shelyapina, M. G. et al. Comprehensive Analysis of the Copper Exchange Implemented in Ammonia and Protonated Forms of Mordenite Using Microwave and Conventional Methods. *Mol.* 2019, Vol. 24, Page 4216 24, 4216 (2019).
11. Janssens, T. V. W. et al. A consistent reaction scheme for the selective catalytic reduction of nitrogen oxides with ammonia. *ACS Catal.* 5, 2832–2845 (2015).

12. Pappas, D. K. et al. Methane to Methanol: Structure-Activity Relationships for Cu-CHA. *J. Am. Chem. Soc.* 139, 14961–14975 (2017).
13. Pappas, D. K. et al. The Nuclearity of the Active Site for Methane to Methanol Conversion in Cu-Mordenite: A Quantitative Assessment. *J. Am. Chem. Soc.* 140, 15270–15278 (2018).
14. Deplano, G. et al. Copper Pairing in the Mordenite Framework as a Function of the CuI/CuII Speciation. *Angew. Chemie Int. Ed.* 60, 25891–25896 (2021).
15. Deplano, G. et al. Titration of Cu(I) Sites in Cu-ZSM-5 by Volumetric CO Adsorption. *ACS Appl. Mater. Interfaces* 14, 21059–21068 (2022).
16. Prodinge, S. et al. Cation-induced speciation of pore-size during mordenite zeolite synthesis. *J. Mater. Chem. A* 11, 21884–21894 (2023).
17. Müller, R. O. Photoelectrons, Fluorescent Yields, and Auger Electrons. in *Spectrochemical Analysis by X-Ray Fluorescence* 34–35 (Springer, Boston, MA, 1972). doi:10.1007/978-1-4684-1797-5\_4.
18. Newbury, D. E. & Ritchie, N. W. M. Is Scanning Electron Microscopy/Energy Dispersive X-ray Spectrometry (SEM/EDS) Quantitative? *Scanning* 35, 141–168 (2013).
19. Bossert, D. et al. A hydrofluoric acid-free method to dissolve and quantify silica nanoparticles in aqueous and solid matrices. *Sci. Reports* 2019 9, 1–12 (2019).
20. Collings, I. E. & Goodwin, A. L. Metal-organic frameworks under pressure. *J. Appl. Phys.* 126, 181101 (2019).
21. Schneider, C. A., Rasband, W. S. & Eliceiri, K. W. NIH Image to ImageJ: 25 years of image analysis. *Nat. Methods* 2012 9, 671–675 (2012).
22. Olinger, J. M. & Griffiths, P. R. Quantitative Effects of an Absorbing Matrix on Near-Infrared Diffuse Reflectance Spectra. *Anal. Chem.* 60, 2427–2435 (1988).
23. Sirita, J., Phanichphant, S. & Meunier, F. C. Quantitative analysis of adsorbate concentrations by diffuse reflectance FT-IR. *Anal. Chem.* 79, 3912–3918 (2007).

24. Meunier, F. C. Pitfalls and benefits of in situ and operando diffuse reflectance FT-IR spectroscopy (DRIFTS) applied to catalytic reactions. *React. Chem. Eng.* 1, 134–141 (2016).
25. Mathon, O. et al. The time-resolved and extreme conditions XAS (TEXAS) facility at the European Synchrotron Radiation Facility: the general-purpose EXAFS bending-magnet beamline BM23. *urn:issn:1600-5775* 22, 1548–1554 (2015).
26. Bellet, D. et al. A 1300 K furnace for in situ X-ray microtomography. *urn:issn:0021-8898* 36, 366–367 (2003).
27. Ravel, B. & Newville, M. ATHENA, ARTEMIS, HEPHAESTUS: data analysis for X-ray absorption spectroscopy using IFEFFIT. *urn:issn:0909-0495* 12, 537–541 (2005).
28. Erba, A., Baima, J., Bush, I., Orlando, R. & Dovesi, R. Large-Scale Condensed Matter DFT Simulations: Performance and Capabilities of the CRYSTAL Code. *J. Chem. Theory Comput.* 13, 5019–5027 (2017).
29. Becke, A. D. A new mixing of Hartree–Fock and local density-functional theories. *J. Chem. Phys.* 98, 1372–1377 (1993).
30. Lee, C., Yang, W. & Parr, R. G. Development of the Colle-Salvetti correlation-energy formula into a functional of the electron density. *Phys. Rev. B* 37, 785 (1988).
31. Grimme, S., Antony, J., Ehrlich, S. & Krieg, H. A consistent and accurate ab initio parametrization of density functional dispersion correction (DFT-D) for the 94 elements H–Pu. *J. Chem. Phys.* 132, (2010).
32. Schäfer, A., Huber, C. & Ahlrichs, R. Fully optimized contracted Gaussian basis sets of triple zeta valence quality for atoms Li to Kr. *J. Chem. Phys.* 100, 5829–5835 (1994).
33. Catti, M., Valerio, G., Dovesi, R. & Causà, M. Quantum-mechanical calculation of the solid-state equilibrium  $\text{MgO} + \alpha\text{-Al}_2\text{O}_3 - \text{MgAl}_2\text{O}_4$  (spinel) versus pressure. *Phys. Rev. B* 49, 14179 (1994).
34. Al Derzi, A. R., Gregušová, A., Runge, K. & Bartlett, R. J. Structure and properties of disiloxane: An ab initio and post-Hartree–Fock study. *Int. J. Quantum Chem.* 108, 2088–2096 (2008).



35. Neese, F. & Wiley, J. The ORCA program system. *Wiley Interdiscip. Rev. Comput. Mol. Sci.* 2, 73–78 (2012).
36. Neese, F. Software update: The ORCA program system—Version 5.0. *Wiley Interdiscip. Rev. Comput. Mol. Sci.* 12, e1606 (2022).
37. Neese, F., Wennmohs, F., Becker, U. & Riplinger, C. The ORCA quantum chemistry program package. *J. Chem. Phys.* 152, 224108 (2020).
38. Ugliengo, P., Viterbo, D. & Chiari, G. MOLDRAW: Molecular graphics on a personal computer. *Zeitschrift für Krist. - Cryst. Mater.* 207, 9–24 (1993).
39. Yanai, T., Tew, D. P. & Handy, N. C. A new hybrid exchange–correlation functional using the Coulomb-attenuating method (CAM-B3LYP). *Chem. Phys. Lett.* 393, 51–57 (2004).
40. Van Lenthe, E., Snijders, J. G. & Baerends, E. J. The zero-order regular approximation for relativistic effects: The effect of spin–orbit coupling in closed shell molecules. *J. Chem. Phys.* 105, 6505–6516 (1996).
41. Pantazis, D. A., Chen, X. Y., Landis, C. R. & Neese, F. All-electron scalar relativistic basis sets for third-row transition metal atoms. *J. Chem. Theory Comput.* 4, 908–919 (2008).
42. Pantazis, D. A. & Neese, F. All-electron scalar relativistic basis sets for the lanthanides. *J. Chem. Theory Comput.* 5, 2229–2238 (2009).
43. Pantazis, D. A. & Neese, F. All-electron scalar relativistic basis sets for the 6p elements. *Theor. Chem. Acc.* 131, 1–7 (2012).
44. Momma, K. & Izumi, F. VESTA: a three-dimensional visualization system for electronic and structural analysis. *urn:issn:0021-8898* 41, 653–658 (2008).
45. Jaumot, J., Gargallo, R., De Juan, A. & Tauler, R. A graphical user-friendly interface for MCR-ALS: a new tool for multivariate curve resolution in MATLAB. *Chemom. Intell. Lab. Syst.* 76, 101–110 (2005).
46. Conry, R. R. Copper: Inorganic & Coordination Chemistry. in *Encyclopedia of Inorganic Chemistry* (John Wiley & Sons, Ltd, 2005). doi:10.1002/0470862106.IA052.
47. Horváth, O. Photochemistry of copper(I) complexes. *Coord. Chem. Rev.* 135–136, 303–324 (1994).

48. Newton, M. A., Knorpp, A. J., Sushkevich, V. L., Palagin, D. & Van Bokhoven, J. A. Active sites and mechanisms in the direct conversion of methane to methanol using Cu in zeolitic hosts: a critical examination. *Chem. Soc. Rev.* 49, 1449–1486 (2020).
49. Park, M. B., Park, E. D. & Ahn, W. S. Recent progress in direct conversion of methane to methanol over copper-exchanged zeolites. *Front. Chem.* 7, 1–7 (2019).
50. Artsiusheuski, M. A., Verel, R., van Bokhoven, J. A. & Sushkevich, V. L. Mechanism of Hydrocarbon Formation in Methane and Methanol Conversion over Copper-Containing Mordenite. *ACS Catal.* 13, 5864–5875 (2023).
51. Martini, A. et al. Composition-driven Cu-speciation and reducibility in Cu-CHA zeolite catalysts: a multivariate XAS/FTIR approach to complexity. *Chem. Sci.* 8, 6836–6851 (2017).
52. Molokova, A. Y. et al. Elucidating the reaction mechanism of SO<sub>2</sub> with Cu-CHA catalysts for NH<sub>3</sub>-SCR by X-ray absorption spectroscopy. *Chem. Sci.* 14, 11521–11531 (2023).
53. Tyrsted, C. et al. Nitrate–nitrite equilibrium in the reaction of NO with a Cu-CHA catalyst for NH<sub>3</sub>-SCR. *Catal. Sci. Technol.* 6, 8314–8324 (2016).
54. Turnes Palomino, G., Bordiga, S., Lamberti, C., Zecchina, A. & Otero Areán, C. Vibrational and optical spectroscopic studies on copper-exchanged ferrierite. *Stud. Surf. Sci. Catal.* 142, 199–206 (2002).
55. Lamberti, C. et al. XANES, EXAFS and FTIR characterization of copper-exchanged mordenite. *J. Chem. Soc. Faraday Trans.* 94, 1519–1525 (1998).
56. Drake, I. J. et al. The local environment of Cu<sup>+</sup> in Cu-Y zeolite and its relationship to the synthesis of dimethyl carbonate. *J. Phys. Chem. B* 110, 11654–11664 (2006).
57. Zecchina, A. et al. Mono-, di-, and tricarbonylic species in copper(I)-exchanged zeolite ZSM-5: Comparison with homogeneous copper(I) carbonylic structures. *J. Phys. Chem. B* 103, 3833–3844 (1999).
58. Ewing, G. E. Infrared Spectra of Liquid and Solid Carbon Monoxide. *J. Chem. Phys.* 37, 2250–2256 (1962).

59. Lamberti, C., Zecchina, A., Groppo, E. & Bordiga, S. Probing the surfaces of heterogeneous catalysts by in situ IR spectroscopy. *Chem. Soc. Rev.* 39, 4951–5001 (2010).
60. Fernández-García, M., Conesa, J. C. & Illas, F. Effect of the Madelung potential value and symmetry on the adsorption properties of adsorbate/oxide systems. *Surf. Sci.* 349, 207–215 (1996).
61. Sárkány, J. Effects of water and ion-exchanged counterion on the FTIR spectra of ZSM-5. II. (Cu+CO)-ZSM-5: Coordination of Cu+CO complex by H<sub>2</sub>O and changes in skeletal T-O-T vibrations. *Top. Catal.* 18, 271–277 (2002).
62. Fan, C. et al. The influence of Si/Al ratio on the catalytic property and hydrothermal stability of Cu-SSZ-13 catalysts for NH<sub>3</sub>-SCR. *Appl. Catal. A Gen.* 550, 256–265 (2018).
63. Miessner, H., Landmesser, H., Jaeger, N. & Richter, K. Surface carbonyl species of copper supported on dealuminated Y zeolite. *J. Chem. Soc. Faraday Trans.* 93, 3417–3422 (1997).
64. Mayerhöfer, T. G., Pahlow, S. & Popp, J. The Bouguer-Beer-Lambert Law: Shining Light on the Obscure. *Chemphyschem* 21, 2029 (2020).
65. Morterra, C., Garrone, E., Bolis, V. & Fubini, B. An infrared spectroscopic characterization of the coordinative adsorption of carbon monoxide on TiO<sub>2</sub>. *Spectrochim. Acta Part A Mol. Spectrosc.* 43, 1577–1581 (1987).
66. Zholobenko, V. et al. Probing the acid sites of zeolites with pyridine: Quantitative AGIR measurements of the molar absorption coefficients. *J. Catal.* 385, 52–60 (2020).
67. Lamberti, C. et al. CuI-Y and CuII-Y zeolites: a XANES, EXAFS and visible-NIR study. *Chem. Phys. Lett.* 269, 500–508 (1997).
68. Datka, J. & Kozyra, P. TPD-IR studies of CO desorption from zeolites CuY and CuX. *J. Mol. Struct.* 744–747, 991–996 (2005).
69. Prestipino, C., Capello, L., D’Acapito, F. & Lamberti, C. Local structure of [CuI(CO)<sub>2</sub>]<sup>+</sup> adducts hosted inside ZSM-5 zeolite probed by EXAFS, XANES and IR spectroscopies. *Phys. Chem. Chem. Phys.* 7, 1743–1746 (2005).
70. Sushkevich, V. L. & Van Bokhoven, J. A. Revisiting copper reduction in zeolites: the impact of autoreduction and sample synthesis procedure. *Chem. Commun.* 54, 7447–7450 (2018).

71. Sushkevich, V. L., Smirnov, A. V. & Van Bokhoven, J. A. Autoreduction of Copper in Zeolites: Role of Topology, Si/Al Ratio, and Copper Loading. *J. Phys. Chem. C* 123, 9926–9934 (2019).
72. Kau, L.-S. et al. X-ray Absorption Edge Determination of the Oxidation State and Coordination Number of Copper: Application to the Type 3 Site in *Rhus vernicifera* Laccase and Its Reaction with Oxygen. *JACS* 109, 113–121 (1987).
73. DeBeer, S. et al. X-ray absorption edge and EXAFS studies of the blue copper site in stercyanin: Effects of axial amide coordination. *J. Phys. Chem. B* 104, 10814–10819 (2000).
74. Gomez-Lor, B., Iglesias, M., Cascales, C., Gutierrez-Puebla, E. & Monge, M. A. A diamine copper(I) complex stabilized in situ within the ferrierite framework. Catalytic properties. *Chem. Mater.* 13, 1364–1368 (2001).
75. Signorile, M., Borfecchia, E., Bordiga, S. & Berlier, G. Influence of ion mobility on the redox and catalytic properties of Cu ions in zeolites. *Chem. Sci.* 13, 10238–10250 (2022).
76. Lamberti, C. et al. XAFS, IR, and UV–Vis Study of the CuI Environment in CuI-ZSM-5. *J. Phys. Chem. B* 101, 344–360 (1997).
77. Paolucci, C. et al. Dynamic multinuclear sites formed by mobilized copper ions in NO<sub>x</sub> selective catalytic reduction. *Science* (80-. ). 357, 898–903 (2017).
78. Heyer, A. J. et al. Methane Activation by a Mononuclear Copper Active Site in the Zeolite Mordenite: Effect of Metal Nuclearity on Reactivity. *J. Am. Chem. Soc.* 144, 19305–19316 (2022).
79. Sushkevich, V. L., Safonova, O. V., Palagin, D., Newton, M. A. & van Bokhoven, J. A. Structure of copper sites in zeolites examined by Fourier and wavelet transform analysis of EXAFS. *Chem. Sci.* 11, 5299–5312 (2020).
80. Dutta, P. K., Rao, K. M. & Park, J. Y. Correlation of Raman spectra of zeolites with framework architecture. *J. Phys. Chem.* 95, 6654–6656 (1991).
81. Twu, J., Dutta, P. K. & Kresge, C. T. Vibrational spectroscopic examination of the formation of mordenite crystals. *J. Phys. Chem.* 95, 5267–5271 (1991).

82. Signorile, M., Bonino, F., Damin, A. & Bordiga, S. UV-Raman Fingerprint of Brønsted Sites in MFI Zeolites: A Useful Marker in Dealumination Detection. *J. Phys. Chem. C* 120, 18088–18092 (2016).
83. Vanelderen, P. et al. Spectroscopic definition of the copper active sites in mordenite: Selective methane oxidation. *J. Am. Chem. Soc.* 137, 6383–6392 (2015).
84. Bae, J. & Dusselier, M. Synthesis strategies to control the Al distribution in zeolites: thermodynamic and kinetic aspects. *Chem. Commun.* 59, 852–867 (2023).
85. Li, J., Gao, M., Yan, W. & Yu, J. Regulation of the Si/Al ratios and Al distributions of zeolites and their impact on properties. *Chem. Sci.* 14, 1935–1959 (2023).
86. Haouas, M., Taulelle, F. & Martineau, C. Recent advances in application of <sup>27</sup>Al NMR spectroscopy to materials science. *Prog. Nucl. Magn. Reson. Spectrosc.* 94–95, 11–36 (2016).
87. Gackowski, M., Podobiński, J., Broclawik, E. & Datka, J. IR and NMR Studies of the Status of Al and Acid Sites in Desilicated Zeolite Y. *Mol.* 2020, Vol. 25, Page 31 25, 31 (2019).
88. Wang, S. et al. Tuning the siting of aluminum in ZSM-11 zeolite and regulating its catalytic performance in the conversion of methanol to olefins. *J. Catal.* 377, 81–97 (2019).
89. Muraoka, K., Chaikittisilp, W., Yanaba, Y., Yoshikawa, T. & Okubo, T. Directing Aluminum Atoms into Energetically Favorable Tetrahedral Sites in a Zeolite Framework by Using Organic Structure-Directing Agents. *Angew. Chemie Int. Ed.* 57, 3742–3746 (2018).
90. Berkson, Z. J. et al. Preferential Siting of Aluminum Heteroatoms in the Zeolite Catalyst Al-SSZ-70. *Angew. Chemie* 131, 6321–6325 (2019).
91. Martineau-Corcus, C., Dědeček, J. & Taulelle, F. <sup>27</sup>Al-<sup>27</sup>Al double-quantum single-quantum MAS NMR: Applications to the structural characterization of microporous materials. *Solid State Nucl. Magn. Reson.* 84, 65–72 (2017).
92. Sklenak, S. et al. Aluminum Siting in Silicon-Rich Zeolite Frameworks: A Combined High-Resolution <sup>27</sup>Al NMR Spectroscopy and Quantum

Mechanics / Molecular Mechanics Study of ZSM-5. *Angew. Chemie Int. Ed.* 46, 7286–7289 (2007).

93. Dib, E. et al. ZSM-5 Zeolite: Complete Al bond connectivity and implications on structure formation from solid-state NMR and quantum chemistry calculations. *J. Phys. Chem. Lett.* 9, 19–24 (2018).

94. Holzinger, J., Beato, P., Lundegaard, L. F. & Skibsted, J. Distribution of Aluminum over the Tetrahedral Sites in ZSM-5 Zeolites and Their Evolution after Steam Treatment. *J. Phys. Chem. C* 122, 15595–15613 (2018).

95. Wang, S. et al. Relation of catalytic performance to the aluminum siting of acidic zeolites in the conversion of methanol to olefins, viewed via a comparison between ZSM-5 and ZSM-11. *ACS Catal.* 8, 5485–5505 (2018).

96. Liu, R. et al. Increasing the Number of Aluminum Atoms in T3 Sites of a Mordenite Zeolite by Low-Pressure SiCl<sub>4</sub> Treatment to Catalyze Dimethyl Ether Carbonylation. *Angew. Chemie Int. Ed.* 61, e202116990 (2022).

97. Wang, Z. et al. The Role of Organic and Inorganic Structure-Directing Agents in Selective Al Substitution of Zeolite. *J. Phys. Chem. Lett.* 12, 9398–9406 (2021).

98. Pinar, A. B. et al. Pinpointing and Quantifying the Aluminum Distribution in Zeolite Catalysts Using Anomalous Scattering at the Al Absorption Edge. *J. Am. Chem. Soc.* 143, 17926–17930 (2021).

99. Schmidt, J. E., Oord, R., Guo, W., Poplawsky, J. D. & Weckhuysen, B. M. Nanoscale tomography reveals the deactivation of automotive copper-exchanged zeolite catalysts. *Nat. Commun.* 2017 8, 1–8 (2017).

100. Schmidt, J. E. et al. Coke Formation in a Zeolite Crystal During the Methanol-to-Hydrocarbons Reaction as Studied with Atom Probe Tomography. *Angew. Chemie Int. Ed.* 55, 11173–11177 (2016).

101. Schmidt, J. E., Peng, L., Poplawsky, J. D. & Weckhuysen, B. M. Nanoscale Chemical Imaging of Zeolites Using Atom Probe Tomography. *Angew. Chemie Int. Ed.* 57, 10422–10435 (2018).

102. Prodingler, S. et al. Synthesis-Structure-Activity Relationship in Cu-MOR for Partial Methane Oxidation: Al Siting via Inorganic Structure-Directing Agents. *ACS Catal.* 12, 2166–2177 (2022).

103. Yakimov, A. V., Sushkevich, V. L., Van Bokhoven, J. A. & Copéret, C. Probing Acid Sites in MOR Zeolite Using Low-Temperature  $^{13}\text{C}$  Solid-State NMR Spectroscopy of Adsorbed Carbon Monoxide. *J. Phys. Chem. C* 126, 3681–3687 (2022).
104. Toyoda, H. et al. Clarification of acid site location in MSE-type zeolites by spectroscopic approaches combined with catalytic activity: comparison between UZM-35 and MCM-68. *Phys. Chem. Chem. Phys.* 24, 4358–4365 (2022).
105. Liu, L. et al. Direct Imaging of Atomically Dispersed Molybdenum that Enables Location of Aluminum in the Framework of Zeolite ZSM-5. *Angew. Chemie Int. Ed.* 59, 819–825 (2020).
106. Salvadori, E., Fusco, E. & Chiesa, M. Long-Range Spatial Distribution of Single Aluminum Sites in Zeolites. *J. Phys. Chem. Lett.* 13, 1283–1289 (2022).
107. Agostini, G. et al. In situ XAS and XRPD parametric rietveld refinement to understand dealumination of Y zeolite catalyst. *J. Am. Chem. Soc.* 132, 667–678 (2010).
108. Drake, I. J. et al. An in situ Al K-edge XAS investigation of the local environment of H<sup>+</sup>- and Cu<sup>+</sup>-exchanged USY and ZSM-5 zeolites. *J. Phys. Chem. B* 110, 11665–11676 (2006).
109. Hosseiniamoli, H. et al. Understanding Structure-Function Relationships in Zeolite-Supported Pd Catalysts for Oxidation of Ventilation Air Methane. *ACS Catal.* 8, 5852–5863 (2018).
110. Vjunov, A. et al. Quantitatively probing the Al distribution in zeolites. *J. Am. Chem. Soc.* 136, 8296–8306 (2014).
111. Van Bokhoven, J. A., Van der Eerden, A. M. J. & Koningsberger, D. C. Three-coordinate aluminum in zeolites observed with in situ x-ray absorption near-edge spectroscopy at the Al K-edge: Flexibility of aluminum coordinations in zeolites. *J. Am. Chem. Soc.* 125, 7435–7442 (2003).
112. Yamamoto, T., Kudo, T., Yamamoto, T. & Kawai, J. Analysis of coordination environment of aluminum species in zeolites and amorphous silica-alumina by X-ray absorption and emission spectroscopy. *Microporous Mesoporous Mater.* 182, 239–243 (2013).

113. Vjunov, A. et al. Tracking the Chemical Transformations at the Brønsted Acid Site upon Water-Induced Deprotonation in a Zeolite Pore. *Chem. Mater.* 29, 9030–9042 (2017).
114. Guda, A. A. et al. Understanding X-ray absorption spectra by means of descriptors and machine learning algorithms. *npj Comput. Mater.* 2021 71 7, 1–13 (2021).
115. Martini, A. et al. PyFitit: The software for quantitative analysis of XANES spectra using machine-learning algorithms. *Comput. Phys. Commun.* 250, 107064 (2020).
116. Martini, A. et al. Machine learning powered by principal component descriptors as the key for sorted structural fit of XANES. *Phys. Chem. Chem. Phys.* 23, 17873–17887 (2021).
117. Trummer, D. et al. Deciphering the Phillips Catalyst by Orbital Analysis and Supervised Machine Learning from Cr Pre-edge XANES of Molecular Libraries. *J. Am. Chem. Soc.* 143, 7326–7341 (2021).
118. Abatal, M., Ruiz-Salvador, A. R. & Hernández, N. C. A DFT-based simulated annealing method for the optimization of global energy in zeolite framework systems: Application to natrolite, chabazite and clinoptilolite. *Microporous Mesoporous Mater.* 294, 109885 (2020).
119. MEIER, W. M. The crystal structure of mordenite (ptilolite). *Zeitschrift für Krist. - Cryst. Mater.* 115, 439–450 (1961).
120. Altman, A. B. et al. Theory and X-ray absorption spectroscopy for aluminum coordination complexes - Al K-edge studies of charge and bonding in (BDI)Al, (BDI)AlR<sub>2</sub>, and (BDI)AlX<sub>2</sub> complexes. *J. Am. Chem. Soc.* 137, 10304–10316 (2015).
121. Manuel, D. et al. Experimental evidence of thermal fluctuations on the x-ray absorption near-edge structure at the aluminum K edge. *Phys. Rev. B - Condens. Matter Mater. Phys.* 85, 224108 (2012).
122. Brouder, C., Cabaret, D., Juhin, A. & Sainctavit, P. Effect of atomic vibrations on the x-ray absorption spectra at the K edge of Al in  $\alpha$ -Al<sub>2</sub>O<sub>3</sub> and of Ti in TiO<sub>2</sub> rutile. *Phys. Rev. B - Condens. Matter Mater. Phys.* 81, 115125 (2010).



123. Ducher, M., Blanchard, M., Vantelon, D., Nemausat, R. & Cabaret, D. Probing the local environment of substitutional Al<sup>3+</sup> in goethite using X-ray absorption spectroscopy and first-principles calculations. *Phys. Chem. Miner.* 43, 217–227 (2016).

# Chapter 3

## *Cu-based organometallic complexes*

### 3.1 Materials & methods

#### 3.1.1 Cu complexes

In their original, as-synthesized form the organometallic Cu complexes studied in Sections 3.2 and 3.3 are tetracoordinated Cu(I) complexes ligated by 2,2'-bipyridine-based ligands; these bidentate ligands chelate Cu via the two pyridine-like N atoms, and are characterized by reduced flexibility due to the extended aromatic system of which their backbone is composed. Although bipyridines usually exists in their *trans* form, which is the most stable conformer in crystalline form,<sup>1,2</sup> ligation to Cu in mononuclear complexes forces them to the *cis* conformation. Even though Cu(bipyridyl) and Cu(bipyridyl)<sub>3</sub> complexes have been observed and described in the literature, the present work focuses on Cu(bipyridyl)<sub>2</sub> complexes, in which the bipyridine ligands bind the Cu(I) site in tetrahedral geometry and differ due to small substituents in the 6,6' or 5,5' positions. The synthesis procedure (as detailed in Appendix A4) was performed by Barbara Centrella in the context of her currently ongoing PhD project; the process is rather simple, as it only requires the dissolution of the Cu(I) salt (in this case [Cu(CH<sub>3</sub>CN)<sub>4</sub>]PF<sub>6</sub>) and the ligand in ca. 1:2 proportion in CH<sub>2</sub>Cl<sub>2</sub>; stirring of the solution for 3h at room temperature in inert atmosphere lead to quantitative yields of the (possibly) substituted [Cu(2,2'-bipyridyl)<sub>2</sub>]PF<sub>6</sub> complex after filtration. A pictorial representation of the synthetic procedure is given in Figure 3.1.

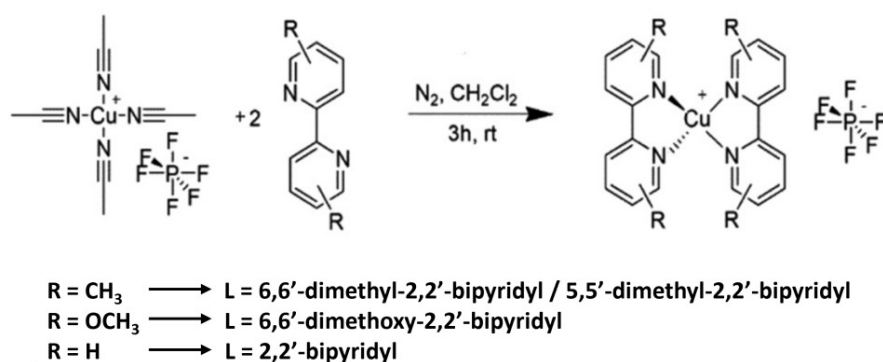


**Figure 3.1** Scheme of the synthetic procedure employed to obtain the substituted  $[\text{Cu}(\text{L})_2]\text{PF}_6$  complexes. Adapted from Appendix A4.

All samples are recovered as dark red-brown powders. Although they are air-stable and show no sign of long-term (in terms of months to years) decomposition, the original Cu(I) source needs to be stored in air-free, dry atmosphere to prevent oxidation of Cu(II). As traces of oxidized compounds were initially found in the first batches of samples, purification of the salt before use is desirable; this is easily achieved by dissolution in an apolar, non-coordinating solvent (like  $\text{CH}_2\text{Cl}_2$ ) and filtration to remove the insoluble oxidized fraction. For reasons discussed in the following sections, essentially due to the steric effects of the substituents, all complexes except  $[\text{Cu}(6,6'\text{-dimethyl-2,2'-bipyridyl})_2]\text{PF}_6$  are sensitive to even mildly coordinating solvents and were dissolved in  $\text{CH}_2\text{Cl}_2$  unless specified otherwise to avoid solvent-induced decomposition. Dissolution in  $\text{CH}_3\text{CN}$  for all complexes apart from  $[\text{Cu}(6,6'\text{-dimethyl-2,2'-bipyridyl})_2]\text{PF}_6$  was quickly followed by loss of colour and coordination of the Cu(I) by the solvent to revert to  $[\text{Cu}(\text{CH}_3\text{CN})_4]\text{PF}_6$ . Oxidation of the Cu(I) complexes was performed using  $\text{NOPF}_6$  (in powder form) or tert-butyl hydroperoxide (*t*BuOOH from now on, 5-6 M solution in decane). In all cases apart from reaction of  $[\text{Cu}(6,6'\text{-dimethyl-2,2'-bipyridyl})_2]\text{PF}_6$  with *t*BuOOH, the oxidized forms of the complexes exhibit a severely reduced solubility in  $\text{CH}_2\text{Cl}_2$  with manifest precipitation of coloured fine powders, effectively limiting the range of concentrations that can be employed to study them. To test the redox reversibility of the complexes, cyclohexene ( $\text{C}_6\text{H}_{10}$ ) was used as both a reducing agent and substrate for C-H bond oxidation.

Preparation of  $[\text{Cu}(6,6'\text{-dimethyl-2,2'\text{-bipyridyl)}_2(\text{H}_2\text{O})](\text{OTf})_2$  (OTf = triflate) and  $[\text{Cu}(6,6'\text{-dimethyl-2,2'\text{-bipyridyl)}_2](\text{ClO}_4)_2$ , employed as reference Cu(II) states and discussed in Section 3.3, has been performed according to literature procedure.<sup>3,4</sup> Briefly,  $[\text{Cu}(6,6'\text{-dimethyl-2,2'\text{-bipyridyl)}_2(\text{H}_2\text{O})](\text{OTf})_2$  was prepared by mixing 4 ml of a 0.25 M solution of  $\text{Cu}(\text{OTf})_2$  in  $\text{CH}_2\text{Cl}_2$  with 6 ml of a 0.38 M solution of 6,6'-dimethyl-2,2'-bipyridine in  $\text{CH}_2\text{Cl}_2$  (thus attaining a metal:ligand proportion of 1:2.2) in a reaction flask. The liquid immediately changed from a blue solution to a green suspension, and after 1h of stirring at room temperature in air the precipitate was filtrated, washed twice with diethyl ether and recovered as a light green powder in quantitative yield. The use of a chloride salt ( $\text{CuCl}_2$ ) as a metal source was avoided due to the possibility of the  $\text{Cl}^-$  anion to enter the first coordination sphere of the metal.  $[\text{Cu}(6,6'\text{-dimethyl-2,2'\text{-bipyridyl)}_2](\text{ClO}_4)_2$  was prepared by dissolving ca. 0.5 g of  $\text{Cu}(\text{ClO}_4)_2$  hexahydrate in 200 mL of  $\text{H}_2\text{O}$ , adding 0.5 g of 6,6'-dimethyl-2,2'-bipyridine and agitating vigorously for 1h. An excess of  $\text{KClO}_4$  was added as a solid and the resulting precipitate was filtered and washed with cold water. The resulting red/brown powder was vacuum-dried at 50 °C *in vacuo* for 1 h and stored in a Schlenk flask to avoid contact with air moisture. Due to the increased polarity of this compound compared to its Cu(I) analogue, its solubility in  $\text{CH}_2\text{Cl}_2$  is very poor;  $\text{CH}_3\text{NO}_2$  was thus employed as a polar, non-coordinating solvent to dissolve it.

The complexes presented in Section 3.4 are based on an N,N,N,N-tetradentate ligand that binds Cu in a structural motif based on imine and imidazole coordination, as portrayed in Figure 3.2.

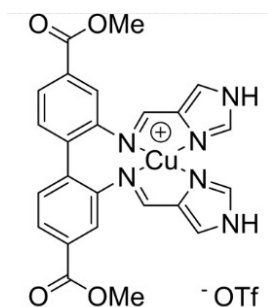


**Figure 3.2** Structure of the Cu(I) form of the tetradentate bis(imine-imidazole) complex described in Section 3.4. Adapted from Ref<sup>5</sup>.

Synthesis procedures for the Cu(I) and Cu(II) forms of the complex (referred to as IG01 and IG01b from now on) are reported elsewhere<sup>5</sup> and have been performed by Dr. Isabelle Gerz in the context of her PhD project,<sup>6</sup> together with basic characterization confirming their structure. Among a series of other similar complexes, this motif was chosen due to its structural similarity to the active site of pMMO and LPMO enzymes which are known to perform C-H bond cleavage.<sup>7-11</sup> Since redox activity of IG01 and IG01b were detected in interaction with *t*BuOOH and H<sub>2</sub>O<sub>2</sub>, catalytic tests for the oxidation of cyclohexane and cyclohexene using these complex/peroxide mixtures have been performed; the catalytic aspects of these systems are still under investigation and fall beyond the scope of this work, which will focus on the characterization of the oxidized/reduced forms using XAS and DFT.

### 3.1.2 Experimental characterization of complexes in solution

Vibrational spectroscopies can be very useful as a direct way to characterize the structure of metal complexes; compared to the solid materials reported in Chapter 2, however, some complications arise. Vibrational data on air-stable complexes can be easily acquired on the complexes in powder form, with the caveats that i) the structure of the complex can change upon dissolution due to crystal packing forces and/or specific solvation effects and ii) not all species that form in solution are necessarily possible to isolate in solid form. For this reason, acquisition of *in situ* vibrational data has been preferred when possible in this work. Collecting such data in solution is severely hindered by the presence of the solvent which is, by definition, present in dramatically larger amounts compared to the analyte. Furthermore, the concentration of the latter must often be kept low enough to be comparable to data acquired using other techniques (*e.g.*, UV-Vis spectroscopy) or to avoid aggregation phenomena; in the case of the complexes studied in this work, solubility issues also limit the use of higher concentrations. If electronic transitions are present in the UV-Vis range for the species under investigation, resonance conditions may be exploited in Raman spectroscopy to boost the selectivity on vibrations that involve the analyte, provided that the correct laser line is available and that the electronic transition(s) possesses favourable symmetry characteristics. Another possible advantage of Raman spectroscopy in the study of metal complexes is the possibility to extend the explored spectral region in the lower

wavenumbers region (down to  $10\text{ cm}^{-1}$  in extreme cases), adding the possibility to directly observe vibrations involving the metal centre; unfortunately, this was not the case for this study as the experimental setup only allowed to collection down to  $800\text{ cm}^{-1}$ . All spectra on powder or solution (nominal concentration  $1\text{ mM}$  in  $\text{CH}_2\text{Cl}_2$ ) were acquired using a  $244\text{ nm}$  ( $40984\text{ cm}^{-1}$ ) laser line. Measurements were performed on a Renishaw Raman microscope equipped respectively with an a Thorlabs UV-B  $15\times$  ( $\text{NA} = 0.31$ ) objective through which the laser light was focused on the sample. The resulting backscattered light (collected through the objective described above) was then analysed through a  $1\text{ mm}^{-1}$  grating. In order to prevent the possible thermal degradation of the investigated samples induced by the focused beam, a custom-made apparatus which allows holder movement (rotation) during measurements was adopted.<sup>12</sup> The presented spectra were obtained by averaging 3 consecutive measurements (from which the stability of the sample during the measurement was confirmed), each one resulting from the sum of 20 acquisitions of 20 s each.

Solvent effects can hardly be suppressed when performing IR spectroscopy on a sample in solution, and transmission spectroscopy is particularly problematic due to the absorption of the solvent completely blinding certain spectral windows. Multiple-reflection attenuated total reflectance (ATR) spectroscopy can be used to boost signals from the analyte, but has proven unsuccessful in this study. To minimize the effect of the solvent and collect IR spectra in transmission mode, an Omni-cell sandwich cell with adjustable optical path from Specac was used to minimize the thickness of the sample solution. A picture of the cell is portrayed in Figure 3.3.

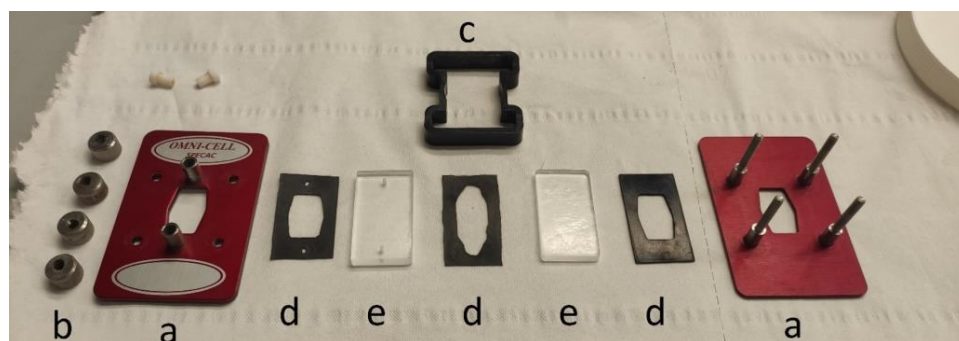


**Figure 3.3** Disassembled parts composing the Specac Omni-cell system: metal case (a), screw blocks (b) plastic support (c), inert rubber sheaths and spacer (d), KBr window (e).

The rubber spacer of the cell allows to select different thicknesses of the liquid introduced in the cell; 1 mm was chosen in this case to decrease blind regions in the spectrum due to intense absorption from the solvent. For the same reason,  $\text{CH}_2\text{Cl}_2$  was chosen as a solvent due to its symmetry and thus limited number of vibrational modes. Once assembled, the cell can be placed in vertical position to let the IR beam pass through the sample while guaranteeing liquid-tightness. The sample can be introduced in the cell cavity via the holes in the KBr windows; since the solution is very volatile and collection of spectra over a long time could not be guaranteed without evaporation, a new aliquot of sample was introduced in the cell for each measurement from a reaction reservoir. Spectra were collected on a 2 mM solution of complex in  $\text{CH}_2\text{Cl}_2$  using an Invenio R spectrophotometer from Bruker, equipped with a mercury cadmium telluride (MCT) cryodetector, a resolution of  $4\text{ cm}^{-1}$  and averaging 32 scans (64 for background spectrum, collected with a solvent-filled cell).

UV-Vis-NIR spectroscopy (Section 3.1) was performed on the samples with an Avantes AvaSpec-ULS2048XL-EVO fibre optics spectrometer (25  $\mu\text{m}$  slits), coupled to an Avantes AvaLight-DH-S light source (equipped with a deuterium and a halogen lamp). Fibre optics with a high-OH fused silica core of 100  $\mu\text{m}$  in diameter were used. Integration times and averaging were optimized for each sample to guarantee the best compromise between spectral and time resolution. The solutions were examined using Hellma flow-through high-performance quartz glass (QS grade) cuvettes with screw connections; depending on the concentration, a cuvette with an appropriate optical path length was selected between 0.1, 1 and 10 mm. The flow was regulated between the cuvette and the liquid reservoir by means of a peristaltic pump using FEP (fluorinated ethylene propylene), PTFE (polytetrafluoroethylene) and fluorinated rubber connections.

UV-Vis-NIR spectra coupled with EPR measurements (Section 3.2) were collected on a dispersive Agilent 8454 spectrophotometer on a 2 mm cuvette and on a 10 mm cuvette with a 40 ml reservoir and septum stopper. Sample aliquots (0.1 mL) were extracted with a micropipette after each UV-Vis spectrum and frozen for EPR analysis. Spectra for the kinetic analysis (reaction

order and rate constants) were collected on a Varian Cary5000 spectrophotometer (for the 10 mm optical path) and the fibre optics setup described for Section 3.1 (for the 1 mm optical path). The sample was reacted in a 25 ml flask with a stopper septum and measured via a Hellma quartz glass (QS grade) screw-cap cuvette filled with the solution (for the 10 mm optical path) or a flow-through high-performance quartz glass (QS grade) cuvette with screw connections (for the 1 mm optical path) to continuously flow solution from the reservoir. The flow was regulated between the cuvette and the liquid reservoir by means of a peristaltic pump using FEP (fluorinated ethylene propylene), PTFE (polytetrafluoroethylene) and fluorinated rubber connections.

EPR spectroscopy is one of the election techniques to study systems characterized by magnetic properties. The entity of the splitting between electron-spin levels induced by the magnetic field determines the exceptional sensitivity to compounds containing unpaired electrons, and thus to dilute solutions of paramagnetic metallorganic complexes. Due to its  $d^{10}$  electronic configuration, Cu(I) is EPR-silent, and any conversion to Cu(II) states is readily detected by the technique even in trace amounts (provided that the electronic ground state is in doublet spin configuration). The single unpaired electron of Cu(II) is not subject to zero-field splitting phenomena, yielding spectra that are often straightforward to interpret compared to other metals (*e.g.*, Cr or Fe).<sup>13,14</sup> Depending on the local coordination of the metal centre, continuous wave (CW) EPR spectra can change to reflect change in symmetry and nature of the ligands, providing information on speciation that is not retrievable by common NMR techniques for paramagnetic samples. CW X-band EPR spectra were collected on a Bruker E500 ELEXSYS spectrometer system equipped with an ER4116DM dual-mode cavity and an Oxford Instruments ESR 900 continuous-flow liquid helium cryostat interfaced with an ITC Mercury temperature controller (3.8-300 K range). The microwave unit was a high sensitivity ER049X Bruker superX bridge with integrated microwave frequency counter. A magnetic field controller ER083CS was calibrated externally using a ER035M Bruker NMR field probe. The spectra were analyzed, simulated and fitted using EasySpin.<sup>15</sup> All spin concentrations and relative ratios were calculated by the numerically-integrated area of the simulation corrected by the respective Aasa-



Vänngård factors.<sup>16</sup> Saturation effects were excluded by checking linearity between double integral of the spectrum and square root of power in a power series of a 1:1 CH<sub>3</sub>CN/CH<sub>2</sub>Cl<sub>2</sub> 1 mM solution of [Cu(6,6'-dimethyl-2,2'-bipyridyl)<sub>2</sub>(CH<sub>3</sub>CN)](ClO<sub>4</sub>)<sub>2</sub> in the range of 0.0079-5.02 mW; the power used in all experiments was set to 0.63 mW.

Cu K-edge XAS spectra on Cu(bipyridyl)<sub>2</sub> complexes (Section 3.3) were collected at the BM31 beamline at ESRF (Grenoble), in fluorescence mode using a Si-drift detector. The incident ( $I_0$ ) and was detected in the range within 8780 and 9800 eV (40 min/scan, 3 spectra collected per sample) using an ionization chamber filled with a mixture of He and Ar. The collected XAS spectra were then aligned in energy and normalized to unity edge jump using the Athena software from the Demeter package.<sup>17</sup> EXAFS fits on these systems have been performed by Daniele Bonavia in the context of his master's thesis project. The flow system for the solution (5 mM in CH<sub>2</sub>Cl<sub>2</sub>) was the same adopted for the fibre-optics UV-Vis analysis, while a Kapton capillary (internal diameter = 1.0 mm) connected to the hydraulic system was used as a flow-through cell.

Cu K-edge XAS spectra of tetradentate imine-imidazole complexes (Section 3.4) were collected at the BM31 beamline at ESRF (Grenoble). The experiments were conducted by introducing liquid samples (7.5 mM solutions in dimethylformamide) in a fixed-volume cell (Omni-cell, Specac) with optimized optical path length for transmission XAS measurements. Although close to the limits of the technique, transmission mode was still feasible in the case of these samples (maximum absorption <2.5 in all cases but one, edge jump in the range 0.1-1 in all cases). The volume of liquid was confined between two Kapton windows, and the specific optical path length was set via fluorinated rubber spacers of the required thickness, in order to guarantee both tightness and chemical inertness. Spectra were collected in transmission mode, using a water-cooled flat Si(111) double crystal monochromator. The incident ( $I_0$ ) and transmitted ( $I_1$ ) X-ray intensity was detected using 30 cm-length ionization chambers filled with a mixture of He and Ar. The XAS spectrum of a Cu metal foil was collected between measurements for energy calibration/alignment purposes. Continuous scans were performed in the 8860–10000 eV range, with a constant energy step of 0.5 eV; acquisition time was ca. 3.5 min/scan. The

collected XAS spectra were then aligned in energy and normalized to unity edge jump using the Athena software from the Demeter package.<sup>17</sup>

### 3.1.3 Computational methods

DFT simulations were performed with the ORCA 5.0.3 code.<sup>18–20</sup> All structures were optimized using the hybrid B3LYP functional<sup>21</sup> and the def2-TZVP basis set developed by Ahlrichs and coworkers.<sup>22</sup> The def2/J basis<sup>23</sup> sets along with chain of spheres approximation (RIJCOSX)<sup>24</sup> were used for the RI (resolution of identity) approximation to the Coulomb integrals. Dispersive forces were included in the calculation through the Grimme D3 empirical scheme with Becke–Johnson damping.<sup>25</sup> The effect of solvation was implicitly accounted for via the conductor-like polarizable continuum model (CPCM)<sup>26,27</sup> method; when solvent mixtures were employed, an average value of the dielectric constant and refraction index for the two solvents was used to approximate the properties of the mixture. Test calculations provided insignificant or inconsistent results when the counterion was added; this effect could be due to the non- or weak-coordinating nature of the counterions present in all complexes (OTf<sup>-</sup>, ClO<sub>4</sub><sup>-</sup>, PF<sub>6</sub><sup>-</sup>): their effect on the geometry due to purely electrostatic attraction to the complex cation could be overestimated in the absence of explicit solvent molecules, and they were thus not included in the final calculations. Initial models were geometrically optimized, and vibrational frequencies were computed; the absence of imaginary frequencies confirmed that minimum structures were obtained.

UV-Vis spectra in the full range and K-edge X-ray absorption spectra in the pre-edge region were calculated by time-dependent DFT within Tamm-Dancoff approximation with the CAM-B3LYP functional<sup>28</sup> on the optimized geometries. Relativistic effects were taken into account using the Douglas-Kroll-Hess (DKH)<sup>29</sup> approximation, with the recontracted DKH-def2-TZVP basis set.<sup>30</sup> The SARC/J basis sets<sup>30</sup> were used for the RI approximation to the Coulomb integrals. The oscillator strengths were computed based on the sum of the electric dipole, magnetic dipole and electric quadrupole contributions. The transitions were assigned based on the inspection of the natural transition orbitals. The XANES spectra along the relaxed PES scan presented in Figure 3.10 were calculated using the B3LYP functional to reduce computational cost; all

other settings were the same employed for the calculation of other XANES spectra. XANES spectral width was set to 2.3 eV for all spectra and a -6.0 eV shift was applied to match experimental spectra. UV-Vis spectral width was set to 2500 cm<sup>-1</sup> using the `orca_mapspc` utility; no shift was applied to the calculated spectra.

More accurate calculations involving the d-d transitions part of the UV-Vis spectra were performed within the CAS-SCF formalism using the def2-TZVP basis set.<sup>22</sup> The considered active space for Cu(II) species consisted of 9 electrons (according to the d<sup>9</sup> electron configuration) in 5 orbitals (the 3d set for Cu); attempts at including ligand orbitals or 4d metal shells in the active space due to partial overlap did not significantly change the calculated transitions and were thus excluded. Partial correction for the dynamic correlation was included via the NEVPT2 method.<sup>31–33</sup> Spectral width was set to 3000 cm<sup>-1</sup> using the `orca_mapspc` utility; no shift was applied to the calculated spectra.

Calculation of the g-tensor values for EPR were performed within the ZORA approximation<sup>34</sup> using the double-hybrid PBE0-DH functional,<sup>35</sup> ZORA-def2-TZVPP basis set for Cu and the ZORA-def2-TZVP basis set for all other atoms.<sup>30</sup> All other settings were chosen according to the detailed study by Drosou *et al.*<sup>36</sup>

Calculation of the g-tensor values for EPR were performed using hybrid B3PW91 functional,<sup>21,37</sup> aug-cc-pVTZ-J basis set<sup>38</sup> for Cu and the ZORA-def2-TZVP basis set for all other atoms.<sup>30</sup> All other settings were chosen according to the detailed study by Gómez-Piñeiro *et al.*<sup>39</sup>

Multivariate curve regression (MCR) using the alternating least squares (ALS) algorithm was performed on UV-Vis, EPR and IR spectra using the graphical user interface developed by Jaumot *et al.* in the MATLAB environment;<sup>40</sup> the specific settings that were used in the data decomposition procedure are specified in Table 3.1.

**Table 3.1** Constraints, convergence parameters and figures of merit upon convergence of the MCR procedures utilized on the listed techniques throughout Chapter 3. C = constraint applied to concentration profiles, S = constraint applied to spectral profiles.

<b>Constraint</b>	<b>UV-Vis</b>	<b>EPR</b>	<b>IR</b>
N° of pure species	3	2	3
Non-negativity	C, S	C	C, S
Unimodality	/	/	/
Closure	C	/	C
Max iterations	50	50	250
Convergence	0.1	0.1	0.1
<b>Figure of merit</b>	<b>UV-Vis</b>	<b>EPR</b>	<b>IR</b>
N° of iterations	2	14	198
$\sigma$ vs exp. Data	0.005	0.038	0.003
Lack of fit (PCA)	4.67%	0.039%	0.001%
Lack of fit (exp)	5.07%	4.73%	1.02%
R <sup>2</sup> at convergence	0.997	0.998	0.999

In the case of IR spectroscopy, zones of intense solvent absorption were removed from the input dataset in order to reduce random variability in the spectra and aid convergence.

### **3.2 Cu-bipyridyl complexes: multitechnique characterization and redox reversibility**

The use of bipyridine-based ligands to stabilize and exploit Cu(I)/Cu(II) metal centres is certainly not new, as 2,2'-bipyridine has been described as "the most widely used ligand".<sup>41</sup> The four-fold coordination easily accommodates typical coordination preferences of Cu(I) and Cu(II) metallic sites, while the bidentate

ligation of bipyridine guarantees reduced lability of the complexes. While tetrahedral coordination is perfectly compatible with Cu(I), once oxidation occurs the geometry tends toward a square-planar configuration; this can allow additional ligand molecules (*e.g.*, H<sub>2</sub>O) to enter the coordination sphere forming 5- and 6-coordinated species and possibly disrupting the simple bis bipyridine form and hindering back-reduction of the complex. This issue with redox reversibility of the Cu(I)/Cu(II) couple in bipyridine complexes has been addressed in research involving dye-sensitized solar cells, for which the redox cyclability is one of the key properties of the device. Even slight substitutions in the bipyridine ring can have an important impact on the redox potential of the couple, as has been studied by Giordano *et al.*,<sup>3</sup> due to both steric and electronic effects. It has been found that the simple inclusion of a methyl group in the 6,6' positions increases the half-wave redox potential (from cyclovoltammetry) of the couple by 428 mV compared to the unsubstituted system; as a comparison, substitution in the 5,5' position only has an impact of -79 mV on the potential. This increase of the redox potential, indicating a Cu(I) centre that is more difficult to oxidize, can be explained by the steric constraints imposed by the methyl moieties in the proximity of the metal atom in the case of [Cu(6,6'-dimethyl-2,2'-bipyridyl)<sub>2</sub>]PF<sub>6</sub>: for comparison, DFT-calculated PES scans around the angle formed between the two bipyridyl planes are reported in Figure 3.4 for [Cu(6,6'-dimethyl-2,2'-bipyridyl)<sub>2</sub>]<sup>+</sup> and [Cu(2,2'-bipyridyl)<sub>2</sub>]<sup>+</sup>.

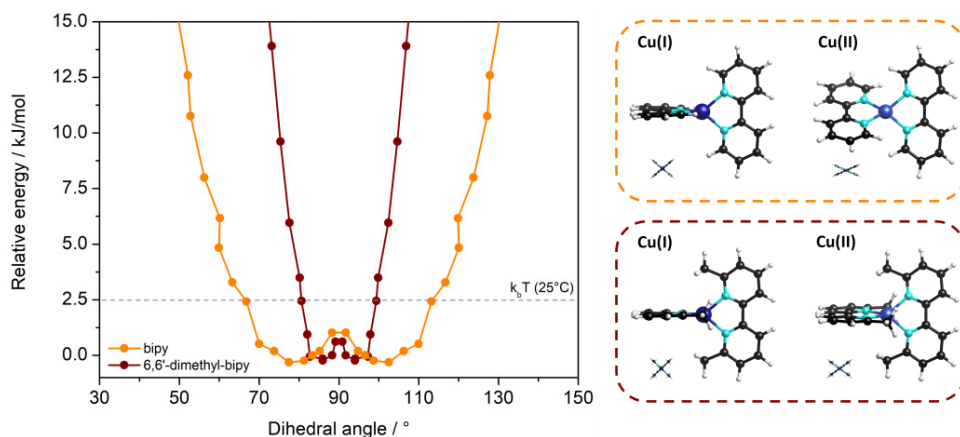


**Figure 3.4** Left: relaxed PES scans (electronic energies) of [Cu(2,2'-bipyridyl)<sub>2</sub>]<sup>+</sup> and [Cu(6,6'-dimethyl-2,2'-bipyridyl)<sub>2</sub>]<sup>+</sup> along the reaction coordinate consisting of the dihedral angle

between the two bipyridine planes. The dashed grey line indicates thermally accessible geometries at 25°C. Right: DFT minimum structures obtained for the Cu(I) and Cu(II) states of  $[\text{Cu}(2,2'\text{-bipyridyl})_2]^+$  and  $[\text{Cu}(6,6'\text{-dimethyl-2,2'\text{-bipyridyl})_2]^+$ . Colour code: H in white, N in cyan, C in black, Cu in blue. Relative energies are referred to the minimum point in each PES.

As can be noticed from the relaxed PES scans, the Cu(I) form of the unsubstituted bipyridyl complex is much more flexible around the angle determined by the bipyridine planes compared to the substituted one, essentially due to the steric constraints imposed by the methyl moieties close to the Cu centre. Consistently, the equilibrium geometry for the Cu(II) form of the unsubstituted complex is more twisted compared to the one of the complex bearing the methyl moieties, which appears substantially unchanged compared to its Cu(I) form. A summary of these geometric parameters is provided in Table 3.2.

**Table 3.2** Structural parameters calculated for the Cu(I) and Cu(II) forms of  $[\text{Cu}(6,6'\text{-dimethyl-2,2'\text{-bipyridyl})_2]^+$  and  $[\text{Cu}(2,2'\text{-bipyridyl})_2]^+$ . Numbers in parenthesis indicate parameters from experimental XRD data.<sup>42–44</sup>

Species	Angle in Cu(I) form	$\Delta$ angle Cu(I)/Cu(II)
$[\text{Cu}(2,2'\text{-bipyridyl})_2]^+$	83.4° (76.8°)	-44.3° (-38.6°)
$[\text{Cu}(6,6'\text{-dimethyl-2,2'\text{-bipyridyl})_2]^+$	88.3° (80.7°)	-22.6° (-19.3°)

The resistance of  $[\text{Cu}(6,6'\text{-dimethyl-2,2'\text{-bipyridine})_2]\text{PF}_6$  towards twisting of the bipyridine planes makes it unique among the set of complexes studied in this work. Upon oxidation using  $\text{NOPF}_6$  and  $t\text{BuOOH}$ , all complexes almost immediately reacted with a manifest change of colour from deep red to pale blue. The sole exception was  $[\text{Cu}(6,6'\text{-dimethyl-2,2'\text{-bipyridyl})_2]\text{PF}_6$ , which turned pale yellow upon oxidation with  $t\text{BuOOH}$  in the timescale of hours; resistance towards oxidation was connected to the more rigid structure of this complex compared to the others. The choice of the two different oxidizing agents (as discussed more in detail in Appendix A4) was made to distinguish the possible formation of oxygenated Cu(II) species after reaction with  $t\text{BuOOH}$  compared to a pure oxidation to Cu(II) without any additional species legating the metal. Examples in the literature reported the use of  $\text{NOPF}_6$  as a one-electron oxidizing agent that exploit the  $\text{NO}^+/\text{NO}$  redox couple with release of

NO in the gas phase after reaction.<sup>45,46</sup> No specific NO vibration features were detected by IR upon reaction, indicating that the nitrosyl radicals produced by the reaction effectively escape the solution phase and do not coordinate Cu as such, although EPR spectra on the oxidized phase of [Cu(6,6'-dimethyl-2,2'-bipyridyl)<sub>2</sub>]PF<sub>6</sub> after this reaction seem to indicate degradation of the complex. Nonetheless, since structural information on the oxidized forms of the complexes is not attainable with regular <sup>1</sup>H-NMR in solution due to the paramagnetic nature of the species, UV-Vis and Raman spectroscopies assisted by DFT calculations were exploited to study the behaviour of these systems. UV-Vis spectra of the four complexes listed in Figure 3.1 in their Cu(I) form and after oxidation are reported in Figure 3.5.

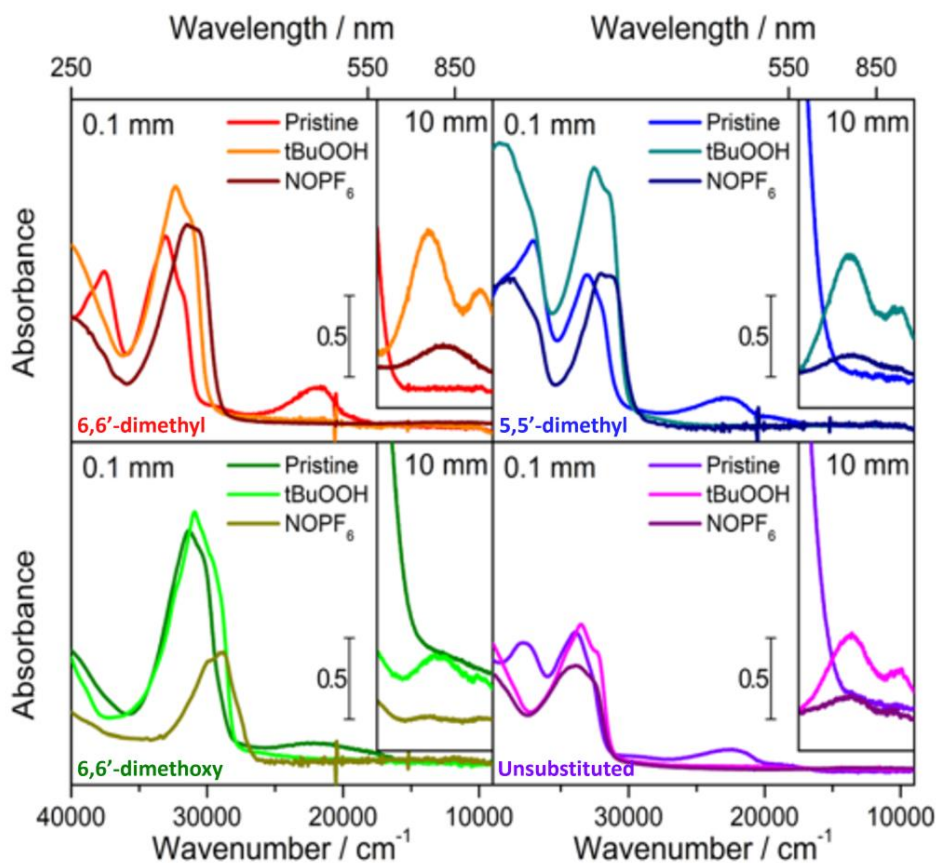


**Figure 3.5** UV-Vis spectra of the four complexes in their pristine form and after reaction with tBuOOH and NOPF<sub>6</sub>. Solutions were prepared with a concentration of 5 mM in CH<sub>2</sub>Cl<sub>2</sub>. Data in the inset show the spectra in the region 17500-9000 cm<sup>-1</sup>, in correspondence with the x-scale in

*the main panels. Main panel: 0.1 cm optical path. Inset: 1.0 cm optical path. The spectra for the two cuvette thicknesses were registered simultaneously on the same sample solution recirculating between the two and a reservoir. Spectra are reported in absorbance without any additional treatment. Adapted from Appendix A4.*

Spectra for all materials in their reduced form consist of two intense and structured transitions at ca. 38000 and 20000  $\text{cm}^{-1}$ ; similar transitions at slightly shifted wavenumbers are present also in the spectra of the ligands in solution and can be assigned (based on NTO analysis of simulated structures) to  $\pi \rightarrow \pi^*$  transitions between the conjugated aromatic systems; some of the structure in these bands in the spectra of the complexes appears to be due to metal to ligand charge transfer (MLCT) transitions from the Cu  $d_z$  orbitals to  $\pi^*$  orbitals of the ligands. The broad and asymmetric feature around 22500  $\text{cm}^{-1}$  only appears in the Cu(I) complexes with specific, ligand-dependent characteristics and was assigned to a MLCT from the Cu  $d_{xz}$  orbital to the  $\pi^*$  orbitals of the ligand system. This transition, which is the main reason for the deep red colour of the samples, is diagnostic of Cu(I) for the complexes; the corresponding Cu(II) also exhibited similar transitions but with much lower intensities, as will be shown in Section 3.3. Once oxidation occurs, many of the spectra appeared to lose intensity, in particular in the case of oxidation using  $\text{NOPF}_6$ : this is due to the sudden precipitation of part of the oxidized form, which formed a coloured powder at the bottom of the reaction flask (around the  $\text{NOPF}_6$  powder added in excess) after oxidation. Despite lowering of concentration in some cases, in the unsubstituted and in the 5,5'-dimethyl substituted samples the spectra of the oxidized species using  $\text{NOPF}_6$  and  $t\text{BuOOH}$  are very similar (right panels in Figure 3.5): the split between the two main bands above 30000  $\text{cm}^{-1}$  increases, and two weak bands appear at ca. 10000 and 14000  $\text{cm}^{-1}$  corresponding to d-d bands of Cu(II). In contrast, the two oxidizing agents appeared to have a different effect on the 6,6'-dimethyl and -dimethoxy substituted samples (left panels in Figure 3.5): a larger splitting in the bands in the UV region was also observed here, with specific differences in the band at ca. 30000  $\text{cm}^{-1}$  depending on the oxidizing agent; furthermore, in the case of the 6,6'-dimethyl substituted sample, oxidation with  $\text{NOPF}_6$  led to the formation of a single d-d band at ca. 12500  $\text{cm}^{-1}$ , while oxidation using  $t\text{BuOOH}$  yielded two d-d bands similar to the ones obtained for the other complexes. An additional band formed at 26500  $\text{cm}^{-1}$  upon oxidation of [Cu(6,6'-dimethyl-2,2'-



bipyridyl)<sub>2</sub>PF<sub>6</sub> with *t*BuOOH; this peculiar behaviour hinted at the formation of a different species depending on the oxidizing agent on the two 6,6' substituted complexes, most probably due to the proximity of the substituents to the Cu centre. The interaction of the complexes with *t*BuOOH was studied with Raman spectroscopy to characterize differences in their vibrational features upon oxidation: the resulting spectra are presented in Figure 3.6.

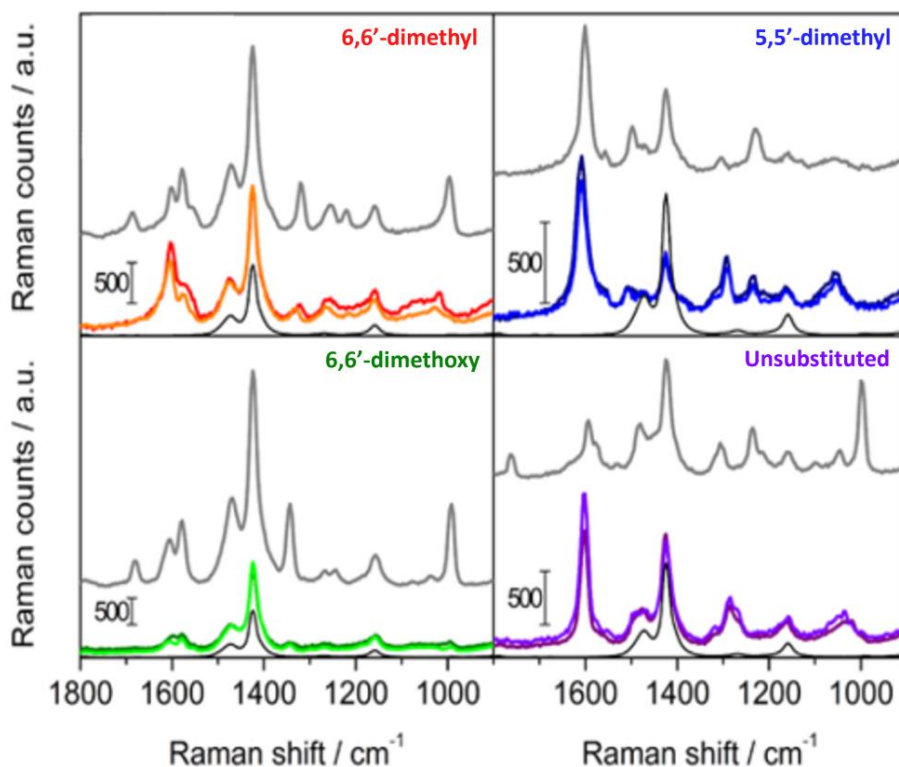


**Figure 3.6** Raman spectra ( $\lambda = 244$  nm) of the four complexes in their pristine form (darker colours) and after reaction with *t*BuOOH (lighter colours). Black and grey curves refer to spectra of the ligands and of pure  $\text{CH}_2\text{Cl}_2$ , respectively. Solutions were prepared with a concentration of 5 mM in  $\text{CH}_2\text{Cl}_2$ . Spectra were normalized to the  $\text{CH}_2\text{Cl}_2$  peak at  $1425$   $\text{cm}^{-1}$  for the sake of comparison. Adapted from Appendix A4.

For all complexes, oxidation using *t*BuOOH only resulted in minor changes in the vibrational features observed in Raman spectra; this fact, coupled with the absence of any characteristic band of the free ligands upon oxidation, suggests that the reaction with the peroxide does not substantially disrupt the backbone structure of the complex. Upon closer inspection, minor differences in the

spectra (especially for the unsubstituted and the 6,6'-dimethyl substituted complexes) arise upon oxidation: the peaks at 1028 and 1014  $\text{cm}^{-1}$ , respectively, displayed an shift to higher wavenumbers after oxidation of 10  $\text{cm}^{-1}$  (20  $\text{cm}^{-1}$  compared to the trans isomer of the bare ligands), while the corresponding bands for the other two complexes appear to only shift slightly. This vibrational mode was assigned via DFT to a breathing mode of the aromatic rings involving the N atoms, leading to its sensitivity to the presence and oxidation state of Cu. The combination of the information obtained from electronic and vibrational spectroscopies suggested that:

1. Both oxidizing agents are efficient in converting the complexes, probably in a quantitative way, from Cu(I) to Cu(II) states.
2. For two of the complexes,  $[\text{Cu}(6,6'\text{-dimethyl-2,2'\text{-bipyridyl)}_2]\text{PF}_6$  and  $[\text{Cu}(6,6'\text{-dimethoxy-2,2'\text{-bipyridyl)}_2]\text{PF}_6$ , the species obtained via the two oxidation pathways appear to be different.
3. The structural backbone of the complexes upon oxidation using *t*BuOOH is not disrupted nor is it severely modified.
4. The electronic structure involving the Cu centre and its surrounding is significantly different after oxidation.

To inquire the specific nature of the oxidized state of the complexes, cyclohexene was added to the oxidized samples as a reducing agent. UV-Vis spectra of all solutions remained unchanged after the addition, apart from the one containing  $[\text{Cu}(6,6'\text{-dimethyl-2,2'\text{-bipyridyl)}_2]\text{PF}_6$  oxidized using *t*BuOOH, as shown in Figure 3.7.

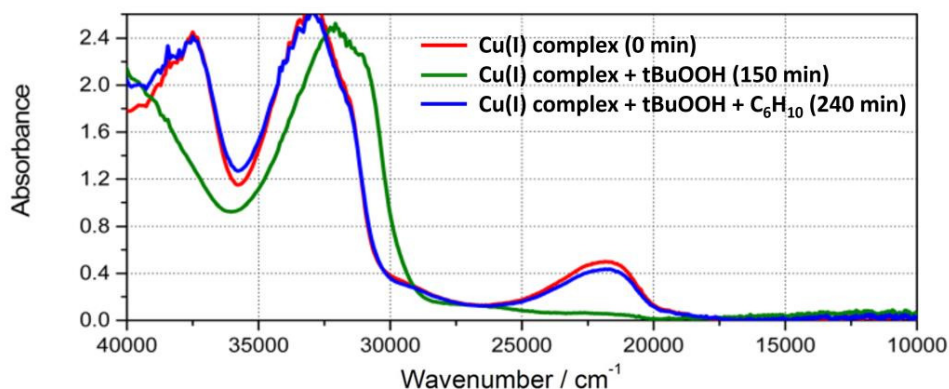


**Figure 3.7** UV-Vis spectra of  $[\text{Cu}(6,6'\text{-dimethyl-2,2'}\text{-bipyridyl})_2]\text{PF}_6$  in its Cu(I) form, after reaction with *t*BuOOH and after interaction with cyclohexene. Solutions were prepared with a concentration of 5 mM in  $\text{CH}_2\text{Cl}_2$ . Spectra are reported in absorbance without any additional treatment. Adapted from Appendix A4.

The spectrum of the complex after oxidation with *t*BuOOH and interaction with cyclohexene was found to be practically identical to the initial  $[\text{Cu}(6,6'\text{-dimethyl-2,2'}\text{-bipyridyl})_2]\text{PF}_6$ , with small intensity differences ascribable to dilution effects; quantitative reversal to the Cu(I) form after interaction with cyclohexene was also observed by XANES and EPR spectroscopies. The Cu(II) species obtained from the reaction of  $[\text{Cu}(6,6'\text{-dimethyl-2,2'}\text{-bipyridyl})_2]\text{PF}_6$  with *t*BuOOH appears to be the only reactive species towards cyclohexene, regenerating the original Cu(I) complex. This very interesting result highlights the possibility that this system can be exploited as i) a reversible Cu(I)/Cu(II) redox couple and ii) a catalyst for hydrocarbon oxidation reactions. Analysis of the solution after reaction with cyclohexene via GC-MS found amounts of cyclohexenone and cyclohexanone in the mixture, the latter of which is probably at least partly deriving from the tautomerization of cyclohexenol. The presence of oxygenated products of the starting alkene led to consider the possibility of a Cu(II) species containing at least one atom of O in its structure as a result of the oxidation of the original complex with *t*BuOOH: once cyclohexene is introduced in the mixture, this species would be able to both oxidize and oxygenate the alkene, reverting the complex back to its Cu(I) state. From the reaction products that were detected, the mechanism is unlikely to simply consist of an electrophilic addition on the alkene (due to at least partial retention of the unsaturated C=C bond), and seemed to involve in some way a saturated C-H bond; the electron-rich alkene moiety of the molecule likely has some aiding effect in the reaction, since addition of cyclohexane to the solution containing the oxidized complex did not yield any detectable oxidation product at room temperature in the timescale of several hours.

After a screening of the properties of the four complexes as a function of simple substitutions in the bipyridine backbone, the results seemed to indicate that substitution in the 6,6' position imparted peculiar properties at the electronic level on the complex. Of the two 6,6' substituted complexes,  $[\text{Cu}(6,6'\text{-dimethyl-2,2'}\text{-bipyridyl})_2]\text{PF}_6$  showed particularly slow oxidation kinetics when reacted with *t*BuOOH, and the resulting Cu(II) species was able to

both revert quantitatively to its Cu(I) form after reaction with cyclohexene and promote oxidation of the alkene with addition of an O to the structure to form oxygenated products with retention of the C=C double bond. The identity of this Cu(II) remained unknown at this point, as well as the actual role of such species in the oxygenation of the substrate; The study was further expanded to investigate the oxidation reaction of  $[\text{Cu}(6,6'\text{-dimethyl-2,2'}\text{-bipyridyl)}_2]\text{PF}_6$  with  $t\text{BuOOH}$ , possibly identifying the active species involved in the reaction with the alkene.

### **3.3 Study on the oxidation of $[\text{Cu}(6,6'\text{-dimethyl-2,2'}\text{-bipyridyl)}_2](\text{PF}_6)_2$ with $t\text{BuOOH}$**

The peculiar behaviour of  $[\text{Cu}(6,6'\text{-dimethyl-2,2'}\text{-bipyridyl)}_2]\text{PF}_6$  in its  $t\text{BuOOH}$ -assisted redox cycle presented in the previous section highlighted how the electronic structure of the complex significantly changes upon oxidation, while its overall structure remains virtually unchanged in its organic backbone. Although NMR characterization could not be straightforwardly performed on this oxidized species due to its paramagnetic nature, all experimental evidence pointed to an oxidation event exclusively centred on the metal with the possible formation of an adduct. In addition to UV-Vis spectroscopy, already presented in the previous section, Cu K-edge XAS spectroscopy was employed as a complementary electronic spectroscopy to explore the metal centre involved in this reaction. Due to its peculiar element selectivity, this technique has been applied to study fine details regarding Cu centres in heterogeneous, homogeneous and enzymatic systems over the years. The XANES part of the spectrum probes the core-to-valence electronic transitions of the material, accessing complementary information to the valence-centred states probed by UV-Vis and offering crucial information on the oxidation state and coordination environment of Cu; the EXAFS part can then be used to extract structural information on the neighbouring atoms surrounding the metal, with high accuracy in the determination of interatomic distances and coordination numbers. Unfortunately, the requirements to perform XAS in transmission mode could not be met for the solution of the complex, in which the dilution of the analyte and background absorption from the solvent (mainly due to the Cl

in  $\text{CH}_2\text{Cl}_2$ ) led to poor absorption due to the analyte and strong absorption from the matrix. Fluorescence detection had to be employed on the samples, leading to long acquisition times (in the order of hours per spectrum) and reduced signal/noise ratio. As an example of this effect, Figure 3.8 displays XAS spectra in the EXAFS regions for the  $[\text{Cu}(6,6'\text{-dimethyl-2,2'\text{-bipyridyl)}_2]\text{PF}_6$  complex in transmission mode (on the pelletized powder) and fluorescence mode (on a 5 mM solution of the sample in  $\text{CH}_2\text{Cl}_2$ ).

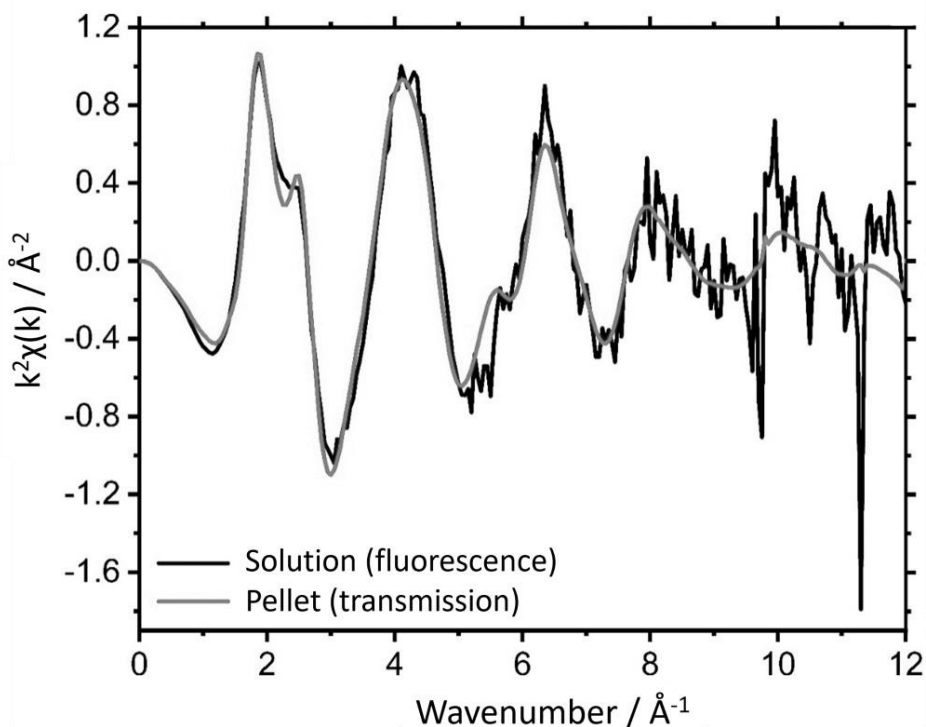


**Figure 3.8**  $k^2$ -weighted Cu K-edge EXAFS spectra of  $[\text{Cu}(6,6'\text{-dimethyl-2,2'\text{-bipyridyl)}_2]\text{PF}_6$  acquired in fluorescence mode (on a 5 mM solution of the complex in  $\text{CH}_2\text{Cl}_2$ ) and in transmission mode (on a sample pellet).

Although the EXAFS signal of the complex as a solid and in solution is extremely similar (hinting at a very similar structure in the vicinity of Cu in the two phases), a major loss in signal/noise ratio is evident in the case of fluorescence acquisition. The signal/noise ratio of the XANES part of the spectra was also affected by fluorescence acquisition, although to a lesser degree; the XANES spectra collected for  $[\text{Cu}(6,6'\text{-dimethyl-2,2'\text{-bipyridyl)}_2]\text{PF}_6$  before and after

reaction with *t*BuOOH, along with TD-DFT simulations for the Cu(I) and Cu(II) forms of the complex, are shown in Figure 3.9.

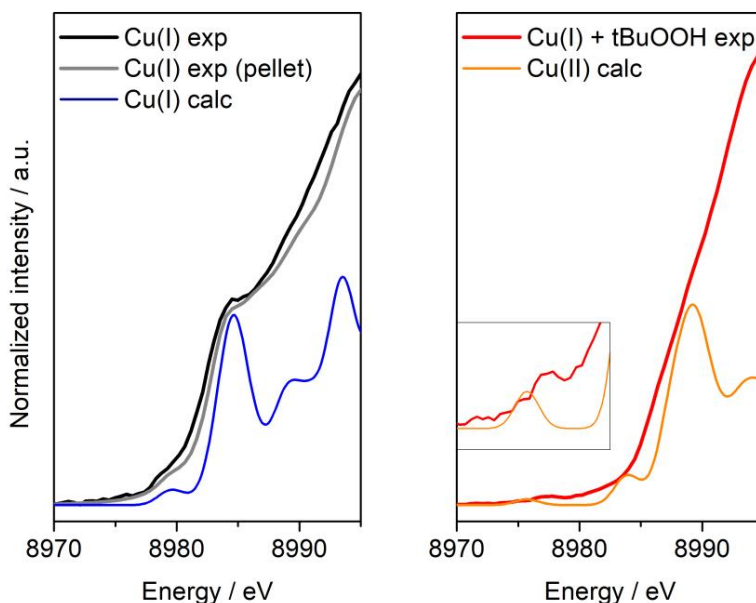


**Figure 3.9** Left panel: normalized pre-edge and rising edge XANES spectra of  $[\text{Cu}(6,6'\text{-dimethyl-}2,2'\text{-bipyridyl})_2]\text{PF}_6$  in solution (black) and pellet form (grey) along with TD-DFT simulated spectrum of  $[\text{Cu}(6,6'\text{-dimethyl-}2,2'\text{-bipyridyl})_2]^+$  (blue). Right panel: normalized pre-edge and rising edge XANES spectra of  $[\text{Cu}(6,6'\text{-dimethyl-}2,2'\text{-bipyridyl})_2]\text{PF}_6$  in solution after addition of *t*BuOOH (red) along with TD-DFT simulated spectrum of  $[\text{Cu}(6,6'\text{-dimethyl-}2,2'\text{-bipyridyl})_2]^{2+}$  (orange). Calculated spectra are displayed with an energy shift of  $-6$  eV and Gaussian lineshape width of  $2.3$  eV.

The initial state of  $[\text{Cu}(6,6'\text{-dimethyl-}2,2'\text{-bipyridyl})_2]\text{PF}_6$  (Figure 3.9, left panel) is consistent with a purely Cu(I) species, as confirmed by the absence of any  $\text{Cu}^{2+} 1s \rightarrow 3d$  transition at  $8978$  eV and the presence of the dipole-allowed  $\text{Cu}^+ 1s \rightarrow 4p$  transition at  $8983$  eV. NTO analysis on the calculated spectrum confirms the nature of this feature and allows to assign the feature at  $8979$  eV to a charge transfer transition of the  $1s$  core electron to a delocalized  $\pi$  system on the bipyridine rings. The spectrum collected on the pellet shows only minor differences compared to the one in solution, indicating a very similar coordinative environment around Cu and further testifying the rigidity of the structure for this complex; for comparison, the data for Cu(I) states in pellet

and solution are shown for the unsubstituted  $[\text{Cu}(2,2'\text{-bipyridyl})_2]\text{PF}_6$  in Figure 3.10, along with calculated XANES spectra for relaxed PES scan points along the angle between the bipyridine planes in both cases.

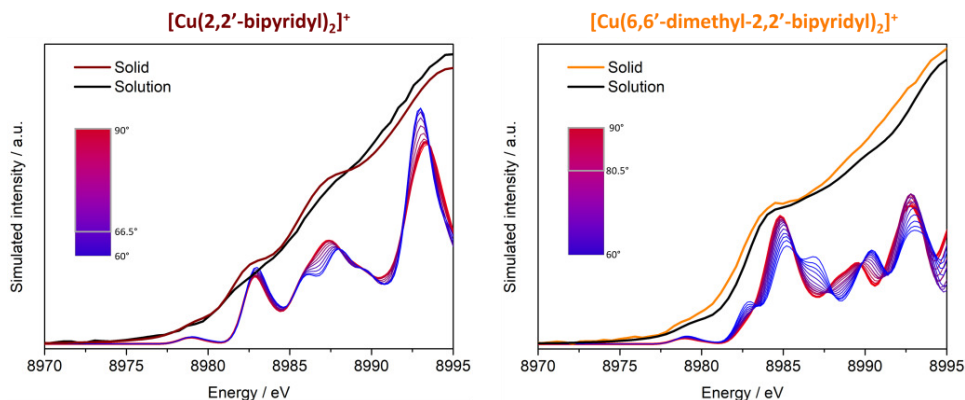


**Figure 3.10** Simulated (from blue to red) and experimental (thick lines) Cu K-edge XANES spectra (pre- and rising-edge features) for the two complexes. Minimum structure in thick red. Grey boxes in the legend indicate thermally accessible angles at 25°C. Left panel:  $[\text{Cu}(2,2'\text{-bipyridyl})_2]^+$ . Right panel:  $[\text{Cu}(6,6'\text{-dimethyl-2,2'-bipyridyl})_2]^+$ . The B3LYP functional was used to reduce computational cost.

As can be seen from the experimental spectra of  $[\text{Cu}(2,2'\text{-bipyridyl})_2]\text{PF}_6$ , dissolution in  $\text{CH}_2\text{Cl}_2$  has a significant effect on the spectral features, with the appearance of two prominent features at 8982.5 and 8987 eV. This behaviour can be explained at least partially by the wide range of accessible conformational angles along the bipyridine planes in this structure, as already portrayed in Figure 3.4; such a difference is reproduced by the change in calculated spectra on the different positions on the PES, that display minor but significant changes in features at energies compatibles with those observed in the experimental spectra (*i.e.*, those thermally accessible at 25 °C according to the PES reported in Figure 3.4). After reaction with *t*BuOOH (Figure 3.9, right panel), the experimental XANES spectrum is consistent with a Cu(II) species: the appearance of a weak dipole-forbidden  $\text{Cu}^{2+} 1s \rightarrow 3d$  transition at 8978 eV (see inset), the absence of any trace of the  $\text{Cu}^+ 1s \rightarrow 4p$  transition at 8983 eV and the slight but noticeable shift of the absorption edge to higher energy values are all in agreement with the oxidation of the metal centre. In this case, though, the simulated spectrum does not necessarily reproduce well the experiment: a small mismatch in the predicted position of the  $1s \rightarrow 3d$

transition and the intense predicted transition at 8989 eV suggest a simple oxidation of the metal centre with no further change in the structure is not likely. It has to be stated, though, that Cu(II) K-edge XANES rarely offers the possibility to discriminate between different coordination motifs: apart from some cases where high energy resolution fluorescence detected (HERFD) XANES is collected,<sup>47</sup> the Cu(II) K-edge does not usually show intense features and appears rather smooth (as is the case in Figure 3.9, right panel), making it difficult to reliably compare it with calculated spectra. To explore structural aspects of these species, EXAFS spectra for states corresponding to the ones shown in Figure 3.9 (left panel) were collected and are shown in Figure 3.11.

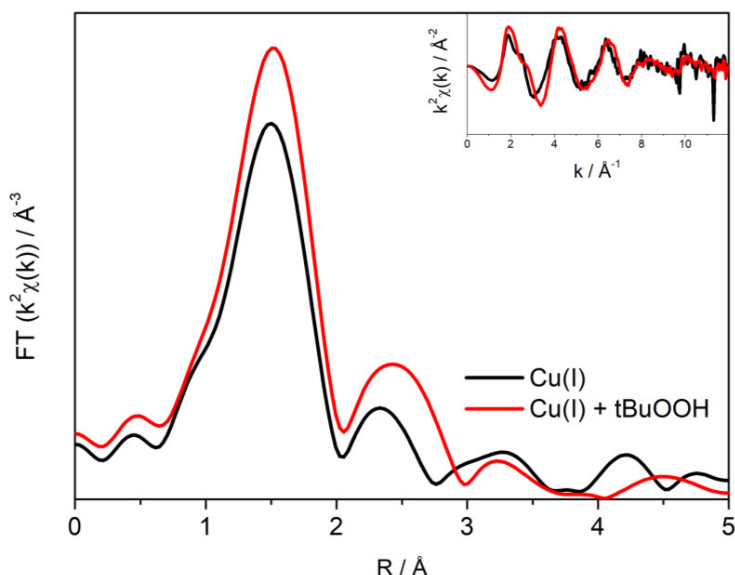


**Figure 3.11** Magnitude of FT-EXAFS spectra of  $[\text{Cu}(6,6'\text{-dimethyl-2,2'-bipyridyl})_2]\text{PF}_6$  before (black) and after (red) reaction with  $t\text{BuOOH}$ , obtained by Fourier transforming  $k^2\chi(k)$  spectra (inset) in the  $2.6\text{--}9.6 \text{ \AA}^{-1}$  range.

As can be seen from the FT-EXAFS spectra, oxidation using  $t\text{BuOOH}$  qualitatively results in an increase in the first- and second-shell contributions around Cu. First-shell fits of the spectra are consistent with a 4-fold coordination for the Cu(I) species, while a 5-fold coordination pattern around Cu is consistent with the oxidized species. A slight decrease in the Cu-N distance is predicted by the fits upon oxidation (from 2.01 to 1.99 Å), while the coordination number on Cu increases from 4 (4 N neighbours) to 5 (4 N neighbours + 1 light atom neighbour): in agreement with qualitative analysis of



the spectra, one additional atom appears to be present in the first coordination shell of Cu, with a fitted distance of 1.94 Å. Unfortunately, the identity of the 5<sup>th</sup> ligand could not be determined by this experiment due to the limited Z-contrast of EXAFS.

To further characterize the oxidized phase of the complex, EPR spectroscopy was performed on the sample along reaction with *t*BuOOH. Simultaneous UV-Vis characterization was performed on the same solution as a control technique; the resulting in situ UV-Vis/EPR spectrokinetic series is reported in Figure 3.12.

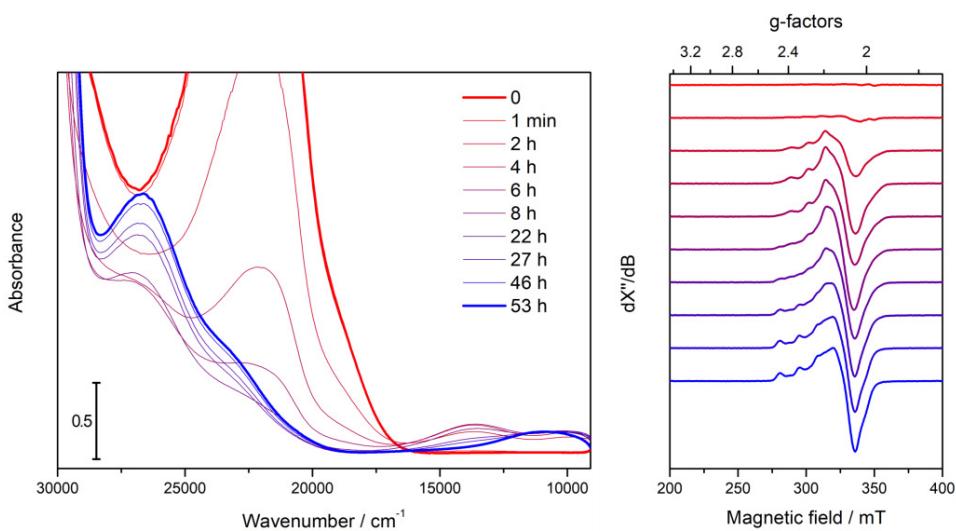


**Figure 3.12** Left panel: UV-Vis spectra of a 1 mM  $[\text{Cu}(6,6'\text{-dimethyl-2,2'\text{-bipyridyl)}_2]\text{PF}_6$  during reaction with *t*BuOOH (1:5 ratio) in a 1:1  $\text{CH}_3\text{CN}/\text{CH}_2\text{Cl}_2$  mixture. A 0.2 cm cuvette was used for the experiment. Right panel: X-band EPR spectra on the same solution.

The starting point of the reaction is consistent with a purely Cu(I) species, as the UV-Vis spectrum does not display any appreciable signal attributable to d-d transitions in the 17000-9000  $\text{cm}^{-1}$  zone and no signal is visible in the corresponding EPR spectrum (in agreement with the  $d^{10}$  EPR-silent configuration of Cu(I)). In the first 6 h of reaction, a significant loss of the Cu(I) species was observed (indicated by the drop in intensity of the 22700  $\text{cm}^{-1}$  MLCT transition in the UV-Vis), together with the appearance of a Cu(II) species characterized by two d-d transitions at ca. 13700 and 9700  $\text{cm}^{-1}$  (already observed in the previous section, Figure 3.5) and an intense EPR signal.

Interestingly, when the reaction was allowed to proceed for longer times, a new species appeared that indicated once again Cu(II) character, featuring a broad band at ca. 11000  $\text{cm}^{-1}$  in the UV-Vis spectrum and a remarkably different signal in the EPR spectrum. This evolution of the spectral profiles along reaction indicates that i) the initial Cu(I) species is converted (probably completely, according to UV-Vis) to a first Cu(II) species after reaction with *t*BuOOH, ii) this first Cu(II) species converts to a second Cu(II) species over time, with somewhat slower kinetics, that has remarkably different EPR features and slightly different UV-Vis features (especially in the d-d zone). To allow for a more specific identification of these species, MCR decomposition of the dataset shown in Figure 3.12 was performed; the resulting pure spectral and concentration profiles are reported in Figure 3.13.

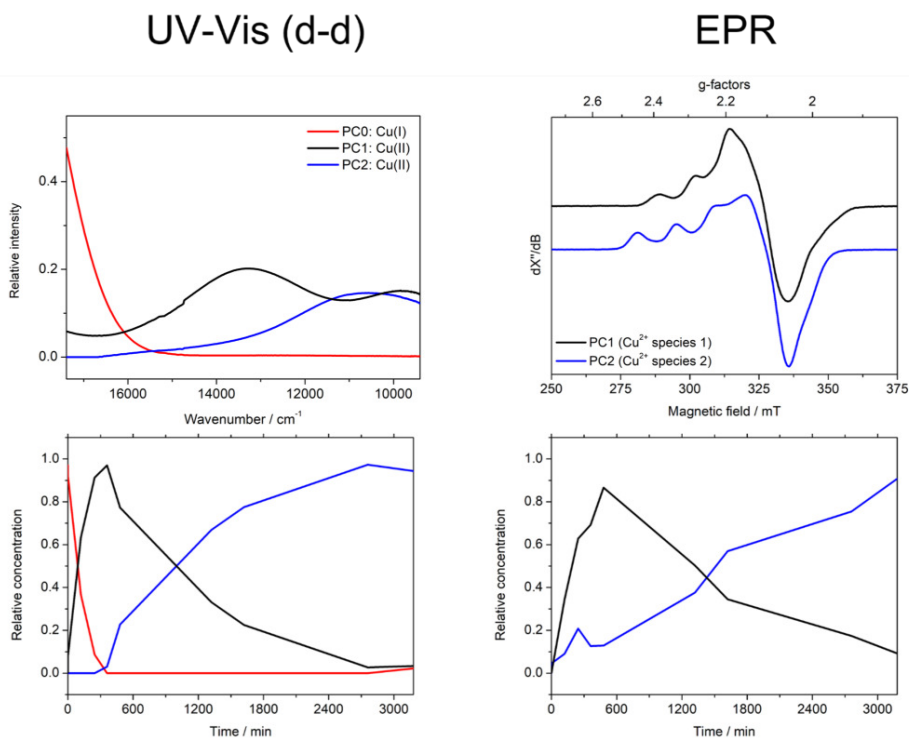


**Figure 3.13** Pure spectral and concentration profiles retrieved by the MCR-ALS algorithm applied to the reaction profiles of  $[\text{Cu}(6,6'\text{-dimethyl-2,2'\text{-bipyridyl)}_2]\text{PF}_6$  and *t*BuOOH. Top: pure spectral profiles obtained from MCR-ALS for UV-Vis (left) and EPR (right). Bottom: pure concentration profiles obtained from MCR-ALS for UV-Vis (left) and EPR (right).

The red species in Figure 3.13 (left panels) corresponds to the tail of the MLCT band associated to Cu(I), that was added to aid convergence in the algorithm but could not be completely inserted in the dataset in the d-d range due to differences in intensity. The black and blue spectra correspond to the first and second Cu(II) species that form upon oxidation of  $[\text{Cu}(6,6'\text{-dimethyl-2,2'\text{-bipyridyl)}_2]\text{PF}_6$  using  $t\text{BuOOH}$ , and will be referred to as PC1 and PC2 from this point for the sake of clarity; UV-Vis experiments confirm that both of these species revert to Cu(I) once exposed to an excess of cyclohexene, indicating that both are reactive towards the substrate or that equilibrium effects favour the formation of the more reactive species when the system is exposed to  $\text{C}_6\text{H}_{10}$ . Since the assignment of both species to a Cu(II) state is unambiguous at this point, the difference between PC1 and PC2 as registered by UV-Vis and EPR is consistent with a change in coordination environment around the metal site. In order to assess specific differences in the spectra, fits of the pure species in terms of spin-Hamiltonian EPR parameters were performed, as portrayed in Figure 3.14.

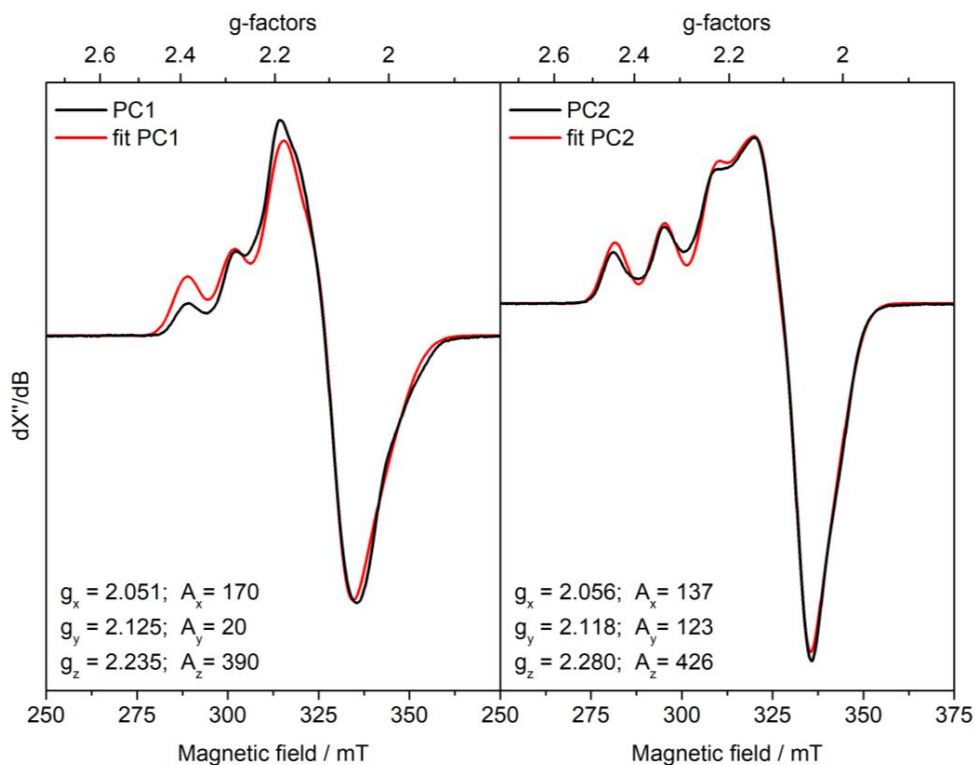


**Figure 3.14** Pure spectral profiles for the EPR dataset as retrieved from MCR (black curves) and best fits (red curves) with corresponding spin-Hamiltonian parameters.

The EPR spectra for the two species suggest that a change in the configuration of the ligands around the Cu(II) site occurs when PC1 is converted into PC2: both qualitative inspection of the spectrum of PC1 and fitted spin-Hamiltonian parameters indicate a more rhombic structure, similar to that found in  $[\text{Cu}(6,6'\text{-dimethyl-2,2'}\text{-bipyridyl})_2(\text{CH}_3\text{CN})](\text{ClO}_4)_2$ ,  $[\text{Cu}(6,6'\text{-dimethyl-2,2'}\text{-bipyridyl})_2(\text{H}_2\text{O})](\text{Otf})_2$  (shown in Figure 3.15) and  $[\text{Cu}(2,2'\text{-bipyridyl})_2(\text{CH}_3\text{OH})]\text{SO}_4$ ,<sup>48</sup> calculation of R-values as indicated in the literature<sup>49</sup> are consistent with a more rhombic, trigonal bipyramidal structure for PC1 and a more axial, square-based pyramidal structure for PC2.

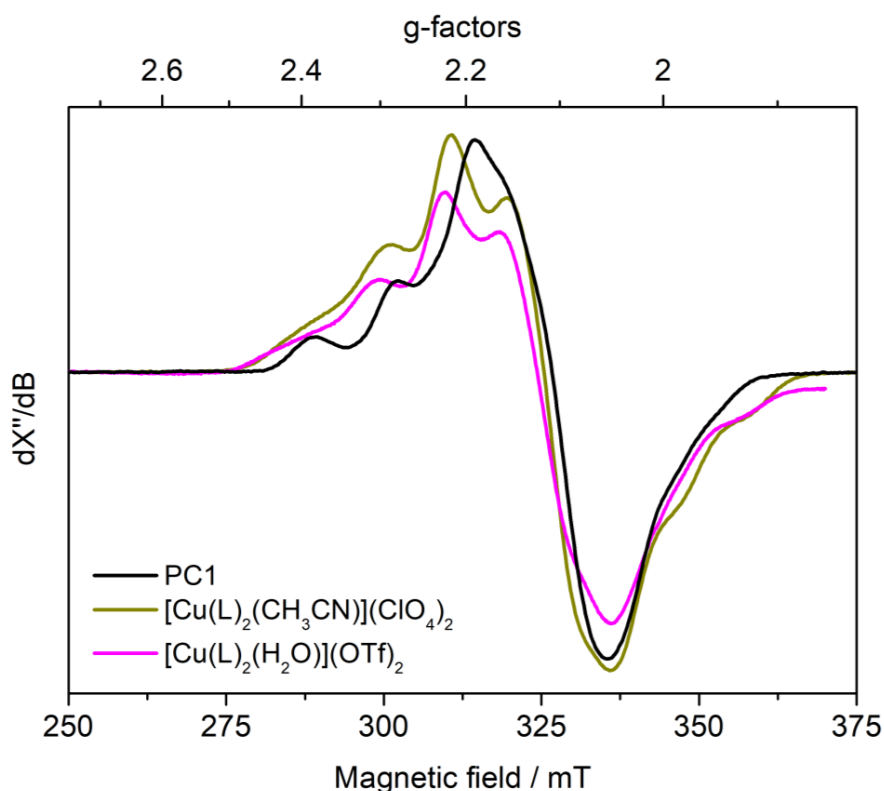


**Figure 3.15** X-band EPR spectra of a 1 mM solution of  $[\text{Cu}(6,6'\text{-dimethyl-2,2'}\text{-bipyridyl})_2(\text{CH}_3\text{CN})](\text{ClO}_4)_2$  (dark yellow) and  $[\text{Cu}(6,6'\text{-dimethyl-2,2'}\text{-bipyridyl})_2(\text{CH}_3\text{CN})](\text{ClO}_4)_2$  (magenta). The EPR spectrum of PC1 collected in the same experimental conditions as already portrayed in Figure 3.14 is reported in black for comparison.

In agreement with the values reported in Figure 3.14 and the similarity between the spectra portrayed in Figure 3.15, spin-Hamiltonian parameters for a series of adducts of the type  $[\text{Cu}(\text{6,6'}\text{-dimethyl-2,2'}\text{-bipyridyl})_2(\text{X})^{n-}]^{(2-n)+}$  calculated using DFT were found to be more similar to the ones fitted for PC1 when X was a small, neutral species or a Cl<sup>-</sup>; the results of these calculations are reported in Table 3.3.

**Table 3.3** Simulated spin-Hamiltonian parameters for adducts of the  $[\text{Cu}(\text{6,6'}\text{-dimethyl-2,2'}\text{-bipyridyl})_2(\text{X})^{n-}]^{(2-n)+}$  type. The row marked with "/" is relative to the simulated  $[\text{Cu}(\text{6,6'}\text{-dimethyl-2,2'}\text{-bipyridyl})_2]^+$  complex without additional ligands. The rows highlighted in green report the fitted parameters for PC1 and PC2. *g*-tensors were considered rhombic if calculated  $|g_x - g_y| > 0.07$ .

X =	<i>g<sub>z</sub></i>	<i>A<sub>z</sub></i> / MHz	<i>g</i> -tensor
PC1	2.235	390	rhombic
PC2	2.280	426	axial
/	2.296	-475	axial
OH <sup>-</sup>	2.260	-569	axial
OOH <sup>-</sup>	2.254	-546	axial
O <sup>2-</sup>	2.237	-330	axial
OO <sup>-</sup>	2.082	-58	axial
H <sub>2</sub> O	2.244	385	rhombic
tBuOH	2.246	368	rhombic
tBuO <sup>-</sup>	2.288	-524	axial
tBuOO <sup>-</sup>	2.258	-546	axial
H <sup>-</sup>	2.163	-491	axial
Cl <sup>-</sup>	2.250	-428	rhombic
CH <sub>2</sub> Cl <sup>-</sup>	2.186	426	axial
CHCl <sub>2</sub> <sup>-</sup>	2.207	-488	axial
CH <sub>3</sub> CN	2.246	-346	rhombic

In contrast, assignment of PC2 from calculated EPR values proved particularly difficult due to the variety of values obtained and the high number of possible consistent species. It is worth to mention that the simulated DFT structures that most resemble the structural insight given by EXAFS spectroscopy (in terms of Cu-X distance) appear to be oxygenated, monovalent anions, with Cu-O distances that approach the 1.94 Å fitted distance with deviations of 0.02 Å on average (compared to 0.1 Å differences in the case of other species and even larger deviations in average Cu-N<sub>bipy</sub> distances). Similarly, the characteristic features of the d-d bands retrieved from MCR for PC1 and PC2 (as reported in Figure 3.13, top-left panel) are summarized in Table 3.4.

**Table 3.4** Parameters relative to the d-d transitions retrieved by Gaussian curve fitting of spectra for the two species formed after reaction of [Cu(6,6'-dimethyl-2,2'-bipyridyl)<sub>2</sub>]PF<sub>6</sub> with tBuOOH.

Species	Band energy / cm <sup>-1</sup>	Band splitting / cm <sup>-1</sup>	FWHM / cm <sup>-1</sup>	ε / M <sup>-1</sup> cm <sup>-1</sup>
PC1	13701, 9671	4030	3684, 2935	144, 76
PC2	10914, 8189	2725	3775, 2903	103, 53

The molar absorption coefficient (ε) of the bands assigned to d-d transitions is relatively weak (the MLCT transition for Cu(I) is roughly one order of magnitude more intense) due to their low dipole transition moment and in line with values found in the literature for Cu(II) species.<sup>50,51</sup> As was already qualitatively observed, the broad band in the spectrum of PC2 is comprised of two partially overlapping absorptions; the possibility of additional components at lower wavenumbers was excluded by inspection of extended spectra encompassing the NIR region. Apart from a different position of the bands, the split between the two d-d bands is severely affected by the change in coordination environment. Calculation of UV-Vis spectra was performed on the same structures used for EPR simulations to check if the trends from the two spectroscopies were in line; the results for the possible [Cu(6,6'-dimethyl-2,2'-bipyridyl)<sub>2</sub>(X)<sup>n-</sup>]<sup>(2-n)+</sup> adducts listed in Table 3.4 in the MLCT and d-d zones are shown in Figure 3.16, together with their respective MCR profiles.

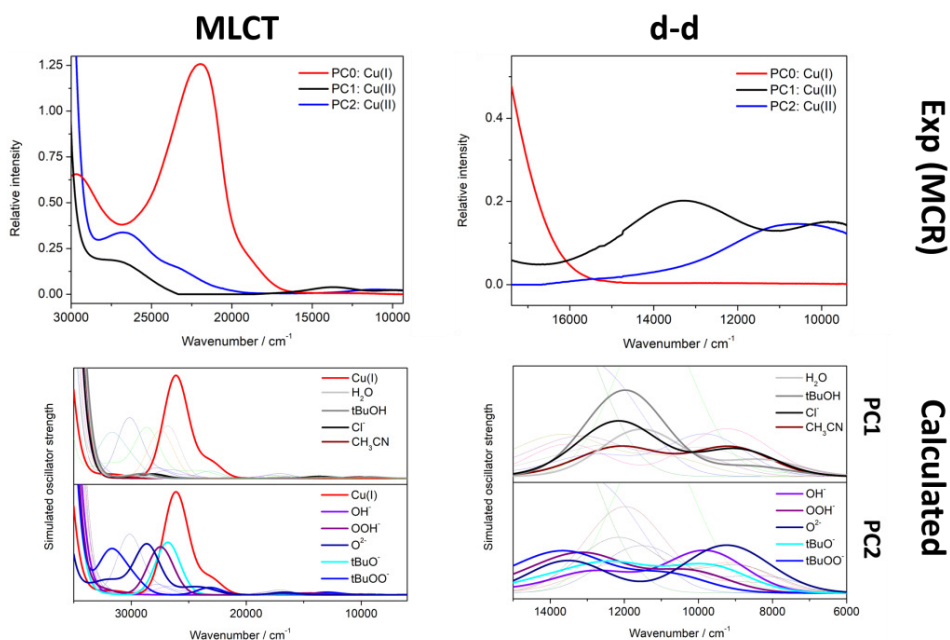


**Figure 3.16** Top: pure spectral profiles retrieved by the MCR-ALS algorithm corresponding to  $[\text{Cu}(6,6'\text{-dimethyl-2,2'\text{-bipyridyl)}_2]\text{PF}_6$ , PC1 and PC2 in the MLCT (left) and d-d (right) transitions zones. Bottom: simulated UV-Vis spectra for adducts of the  $[\text{Cu}(6,6'\text{-dimethyl-2,2'\text{-bipyridyl)}_2(\text{X})^n]^{(2-n)+}$  type in the MLCT (left) and d-d (right) transitions zone; the simulated spectrum for  $[\text{Cu}(6,6'\text{-dimethyl-2,2'\text{-bipyridyl)}_2]^+$  is reported in red in the MLCT zone for comparison's sake. The two sub-figures (labelled PC1 and PC2) refer to the species consistent with EPR and EXAFS analysis as reported above.

The calculated UV-Vis spectra were found to be consistent with what was previously deduced from EXAFS and EPR spectroscopy. In the MLCT region (Figure 3.16, left panel) small neutral ligands (together with  $\text{Cl}^-$  and  $\text{OH}^-$ ) result in very low CT transitions in the Cu(II) state, consistently with the MCR-retrieved spectrum for PC1; meanwhile, negatively charged ligands binding via an O atom result in more intense CT transition (although they are all weaker than the Cu(I) MLCT), in line with the spectrum retrieved for PC2. A similar situation was found for the calculated transitions in the d-d zone (Figure 3.16, right panel), although no significant bathochromic shift was found in the spectra listed as candidates for PC2 compared to PC1.

The concentration profiles presented in Figure 3.13 (bottom panels) suggested slower kinetics for the second reaction (*i.e.*, the conversion of PC1 to PC2): in 1:5 proportions between complex and peroxide, PC1 peaks in concentration at

ca. 6.7 h from the start of the reaction, while PC2 reaches a plateau after up to 50 h. A semi-quantitative fit of the concentration profiles (supposing first-order kinetics for all species involved) led to an estimate of  $k_1 \approx 10k_2$ , where  $k_1$  and  $k_2$  are the rate constant for the first and second reaction, respectively. Even though the agreement was not point-to-point, the concentration profiles retrieved using MCR on the two separate techniques were in very good agreement, especially considering the different conditions in which they were registered (continuous monitoring in the same cuvette in the case of UV-Vis vs aliquots measured in EPR tubes) and the different sources of error involved for them (mainly the uncertainty in weighing the powder for UV-Vis vs additional uncertainty in dispensing the liquid in each EPR tube with micropipettes). To further validate the reliability of this method, spin quantification on EPR spectra was performed by means of a standard solution of  $[\text{Cu}(6,6'\text{-dimethyl-}2,2'\text{-bipyridyl)}_2(\text{CH}_3\text{CN})](\text{ClO}_4)_2$  complex; the comparison between the MCR-extracted profiles and the one obtained from spin quantification is reported in Figure 3.17.

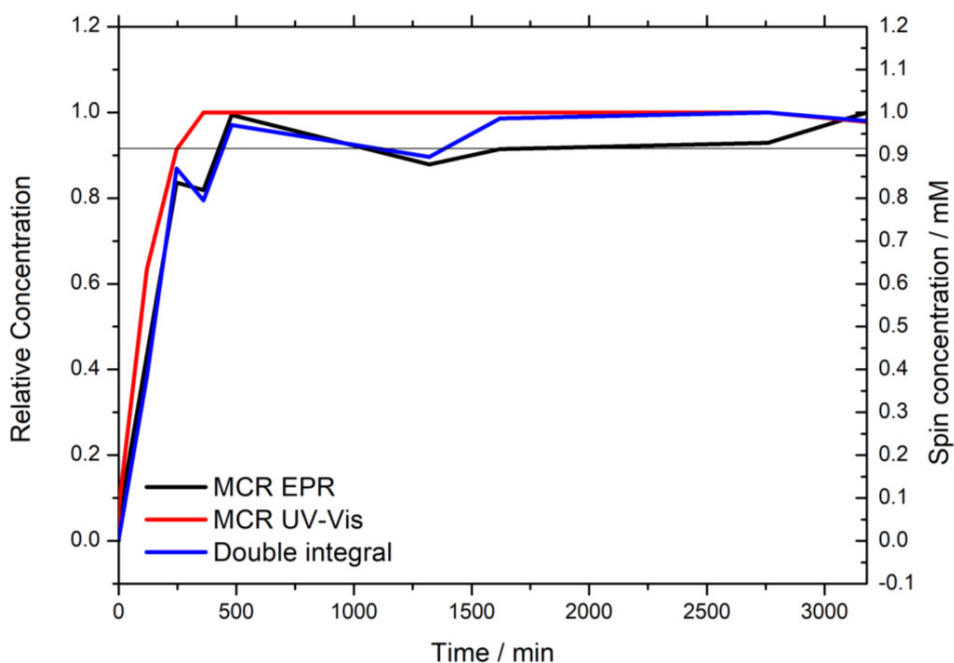


**Figure 3.17** Comparison of concentration profiles obtained from MCR on EPR data (black curve), MCR on UV-Vis data (red curve) and spin quantification (blue curve). The relative concentration of Cu(II) for the spin quantification procedure (left axis) was obtained by dividing the absolute



amount by the total Cu concentration, while the MCR curves were obtained by summing the relative amounts of PC1 and PC2 in each step. The horizontal line is placed in correspondence of the total Cu concentration (right axis).

The relative amounts obtained by MCR are in line with the spin quantification curve, which is in turn consistent with the total amount of Cu within the expected experimental error. Even the dip in the concentration registered for MCR-EPR at ca. 400 min is reproduced by the spin quantification, making it possible to ascribe this partially off-trend point to small systematic errors associated to the sample preparation for EPR measurements. By combining the spin quantification and the relative proportions of the species obtained through MCR, the Aasa-Vänngård factors<sup>16</sup> could be calculated for PC1 and PC2 and the total concentration of Cu(II) was calculated on the experimental points in which Cu(I) was not present in significant amounts (< 1%, 400 min from reaction start) according to the formula:

$$C_{sa} = C_{st} \frac{J_{sa} g_{st}^{(AV)} T_{sa} MA_{st}}{J_{st} g_{sa}^{(AV)} T_{st} MA_{st}} \sqrt{\frac{P_{st} f_{st} G_{st} SC_{st}}{P_{sa} f_{sa} G_{sa} SC_{sa}}}$$

Where  $C$  is the molar concentration,  $J$  is the double integral of the EPR signal,  $g^{(VA)}$  is the Aasa-Vänngård factor for a species (a weighted average was used according to MCR concentrations),  $T$  is the temperature,  $MA$  is the modulation amplitude,  $P$  is the microwave power,  $f$  is the diameter of the EPR tube,  $G$  is the detector gain,  $SC$  is the number of scans per spectrum and the subscripts “ $sa$ ” and “ $st$ ” indicate sample and standard, respectively. An average deviation of 1.5% was obtained compared to the known total Cu concentration of the solution, testifying to the accuracy of this methodology to quantify Cu(II) species in a mixture and assigning the relative concentrations.

To retrieve more accurate information about the kinetics of these two reactions (involving conversion of  $[\text{Cu}(6,6'\text{-dimethyl-2,2'\text{-bipyridyl)}_2]\text{PF}_6$  to PC1 and PC1 to PC2, respectively; *reaction 1* and *reaction 2* henceforth), a spectrokinetic study was conducted exploiting the Ostwald method of flooding. Briefly, if the two known reactants have unknown reaction order, and

supposing that the kinetic process is represented by a single reaction rate constant, the reaction rate can be written as:

$$v(t) = k[A](t)^x[B](t)^y$$

Where  $v(t)$  is the reaction rate for the process,  $k$  is the rate constant,  $[A](t)$  and  $[B](t)$  are the concentrations of the two reagents as a function of time, and  $x$  and  $y$  are the reaction orders for A and B, respectively. If B is present in excess in the mixture,  $[B](t) \approx [B]_0$  at any given point of the reaction, and the reaction rate becomes:

$$v(t) = k'[A](t)^x$$

With  $k' = k[B]_0^y$ . By monitoring the time dependence of  $[A]$ , and if the reaction is first-order in A, the equation:

$$\ln[A] = -k't + \ln[A]_0$$

Is found to be linear and the conditional  $k'$  rate constant specific for a given  $[B]_0$  can be retrieved. By varying the excess of B (*i.e.*,  $[B]_0$ ) the reaction order  $y$  for B and the general reaction rate constant  $k$  can be calculated with a  $\ln[B]_0$  vs  $\ln(k')$  linear plot according to:

$$\ln(k') = \ln(k) + y\ln[B]_0$$

With the slope and the exponentiation of the intercept yielding the reaction order for B and the general reaction rate constant, respectively. The two reactions were run with a *t*BuOOH:Cu ratio of 1, 10, 20, 60, 100 and 200 and monitored spectroscopically with UV-Vis: the intensity of the MLCT band at  $21626 \text{ cm}^{-1}$  was used to quantify the decay over time of  $[\text{Cu}(6,6'\text{-dimethyl-2,2'\text{-bipyridyl)}_2]\text{PF}_6$  (thus characterizing reaction 1), while a two-components fit of the d-d zone of the spectrum was used to quantify the conversion of PC1 to PC2 over time (thus characterizing reaction 2). An example of the spectral series obtained through this method is shown in Figure 3.18.

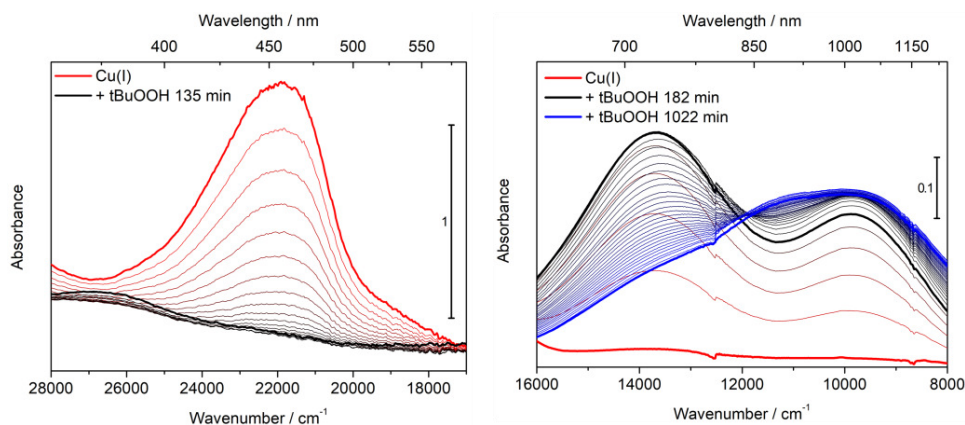


**Figure 3.18** Spectrokinetic series of reactions 1 and 2 as monitored by *in situ* UV-Vis spectroscopy. The starting solution of  $[\text{Cu}(6,6'\text{-dimethyl-2,2'\text{-bipyridyl)}_2]\text{PF}_6$  was 2 mM in a 1:1  $\text{CH}_3\text{CN}/\text{CH}_2\text{Cl}_2$  mixture in all cases. Left panel: UV-Vis spectra in the MLCT region of  $[\text{Cu}(6,6'\text{-dimethyl-2,2'\text{-bipyridyl)}_2]\text{PF}_6$  during reaction with  $t\text{BuOOH}$  (1:20 ratio). Right panel: UV-Vis spectra in the d-d region of  $[\text{Cu}(6,6'\text{-dimethyl-2,2'\text{-bipyridyl)}_2]\text{PF}_6$  during reaction with  $t\text{BuOOH}$  (1:10 ratio).

All plots of  $\ln[A]$  vs  $t$  (where  $A = [\text{Cu}(6,6'\text{-dimethyl-2,2'\text{-bipyridyl)}_2]\text{PF}_6$  and PC1 for reactions 1 and 2, respectively) and  $\ln[t\text{BuOOH}]_0$  vs  $\ln(k')$  displayed good linearity; data on the 1:1 proportion between complex and peroxide was not used to build this model due to the condition of  $[t\text{BuOOH}](t) \approx [t\text{BuOOH}]_0$  not being valid for this composition of the solution. The kinetic parameters calculated using this model on reactions 1 and 2 are reported in Table 3.5.

**Table 3.5** Kinetic parameters obtained for reactions 1 and 2. The reaction schemes are not in stoichiometric balance and do not necessarily include all reactants and products, but only involve the detected species in the spectrokinetic study. L = 6,6'-dimethyl-2,2'-bipyridyl.

Reaction scheme	Reaction order	Rate constant
$[\text{Cu}(\text{L})_2]\text{PF}_6 + t\text{BuOOH} \rightarrow \text{PC1}$	1 for $[\text{Cu}(\text{L})_2]\text{PF}_6$ 0.5 for $t\text{BuOOH}$	$k_1 = (1.4 \pm 0.1) \cdot 10^{-3} \text{ Hz} \cdot \text{M}^{-0.5}$
$\text{PC1} + t\text{BuOOH} \rightarrow \text{PC2}$	1 for PC1 0.67 for $t\text{BuOOH}$	$k_2 = (4.0 \pm 0.4) \cdot 10^{-4} \text{ Hz} \cdot \text{M}^{-0.67}$

From the kinetic data obtained, both reactions appear to have a first-order dependence on the reactant containing Cu ( $[\text{Cu}(6,6'\text{-dimethyl-2,2'\text{-bipyridyl)}_2]\text{PF}_6$  and PC1 for reactions 1 and 2, respectively), while fractional

reaction orders were registered for *t*BuOOH in both cases, suggesting a more complex reaction mechanism involving multiple elementary steps. This agrees with i) the fact that the formation of PC2 is observed even in 1:1 proportion between complex and *t*BuOOH (suggesting that the complex is the limiting reagent) and ii) the absence of detectable residual organic radicals in the EPR spectra. In particular, point ii) is consistent with an overall complex:peroxide stoichiometry of 2:1 (where complex may refer to either Cu(6,6'-dimethyl-2,2'-bipyridyl)PF<sub>6</sub> or PC1): supposing that homolytic cleavage of some moiety of *t*BuOOH is involved, the 1-electron oxidation of Cu(I) to Cu(II) would leave one of the free radicals in solution, possibly detectable by EPR (at least in the case of Reaction 1). Consistently with those semi-quantitatively determined by the MCR concentration profiles, the rate constants for both reactions are quite low, in a  $k_1 \approx 3.5k_2$  proportion. The rate constant for the first reaction, involving oxidation of N-ligated Cu(I), is in line with similar reactions already proposed in the literature.<sup>52</sup> The reliability of this model, however, is based on the supposition that:

1. Reaction 1 goes to completion before reaction 2 starts (*i.e.*,  $[PC1]_0 = [Cu^+]_0$ ).
2. No side reactions occur that consume *t*BuOOH.
3. The concentration of *t*BuOOH at the start of reaction 2 is  $0.5 \cdot [Cu]_0$ .

Although condition 1) is approximately verified, as confirmed by UV-Vis spectrokinetic profiles, conditions 2) and 3) remained unchecked at this point. Moreover, the choice of the solvent was found to be important: in the absence of CH<sub>2</sub>Cl<sub>2</sub>, adding *t*BuOOH to a solution of complex did not result in any detectable reaction, as reported in Figure 3.19.

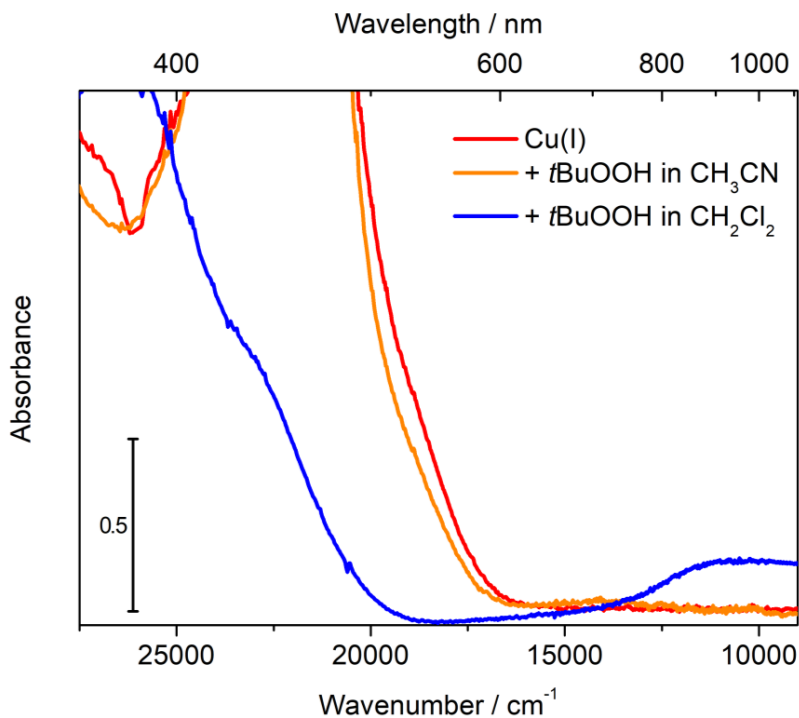


**Figure 3.19** UV-Vis spectra of a 1 mM solution of  $[\text{Cu}(6,6'\text{-dimethyl-2,2'\text{-bipyridyl)}_2]\text{PF}_6$  in  $\text{CH}_2\text{Cl}_2$  and  $\text{CH}_3\text{CN}$  after 70h of reaction with  $t\text{BuOOH}$  (in 1:5 proportion of complex:peroxide). The spectrum of the solution in  $\text{CH}_3\text{CN}$  before reaction with  $t\text{BuOOH}$  is reported in red. Spectra were acquired using fibre optics in a 1.0 cm cuvette.

The spectrum of the starting solution in  $\text{CH}_3\text{CN}$  of  $[\text{Cu}(6,6'\text{-dimethyl-2,2'\text{-bipyridyl)}_2]\text{PF}_6$  is not reported in Figure 3.19 since it shows the same features as the one in  $\text{CH}_2\text{Cl}_2$  (*i.e.*, the starting Cu(I) form of the complex is the same regardless of the solvent). After 70h of reaction with a 5-fold excess of  $t\text{BuOOH}$ , the spectrum of the solution in  $\text{CH}_2\text{Cl}_2$  is consistent with the formation of PC2, while the one for the solution in  $\text{CH}_3\text{CN}$  remains practically unchanged; addition of small amounts of  $\text{CH}_2\text{Cl}_2$  to the latter solution promotes the start of the reaction. This behaviour seems to suggest a role of the chlorinated solvent in the reaction: if  $\text{CH}_3\text{CN}$  was somehow responsible for quenching the reaction, small additions of  $\text{CH}_2\text{Cl}_2$  would likely not be able to start it.

While UV-Vis and EPR spectroscopy provided specific, consistent information on the metallic centre, the evolution of  $t\text{BuOOH}$  along reaction could be

probed via *in situ* transmission IR spectroscopy. Since the detector for the IR spectrophotometer needs to be cooled with liquid N<sub>2</sub> every 6h, the series was collected with a 100-fold *t*BuOOH excess over 4h to ensure peak concentration of PC1 at ca. 30 min and PC2 at ca. 4h. A full-range IR spectrum of the starting [Cu(6,6'-dimethyl-2,2'-bipyridyl)<sub>2</sub>]PF<sub>6</sub> solution prior to oxidation is shown in Figure 3.20.

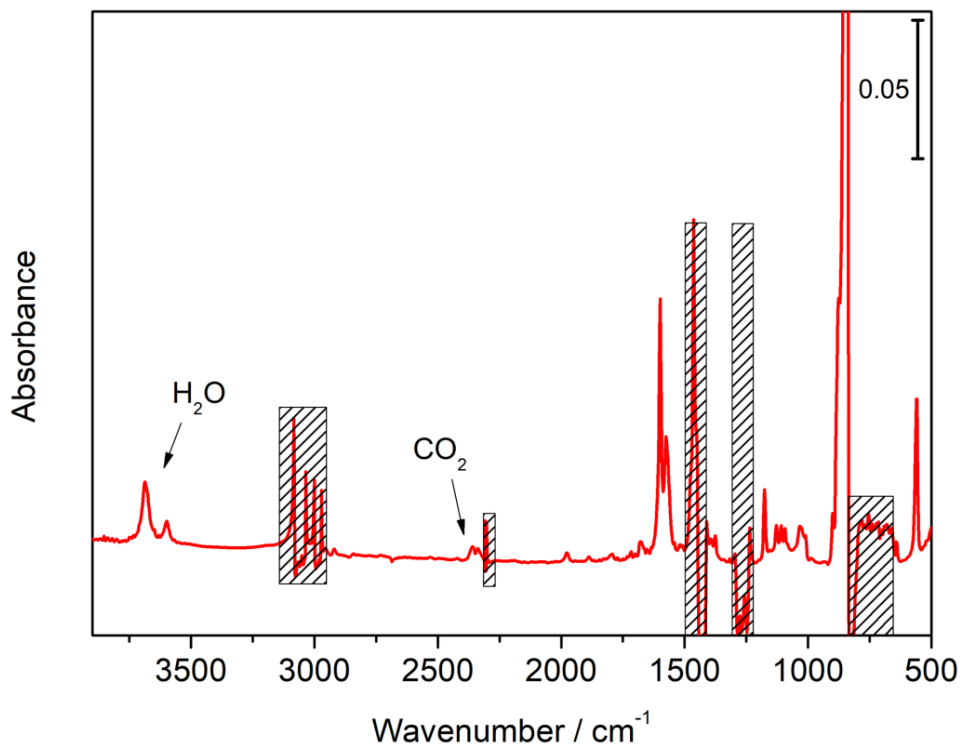


**Figure 3.20** Transmission IR spectra of a 2 mM solution of [Cu(6,6'-dimethyl-2,2'-bipyridyl)<sub>2</sub>]PF<sub>6</sub> in CH<sub>2</sub>Cl<sub>2</sub>. The signals marked in the spectra are due to liquid H<sub>2</sub>O impurities in the solvent or windows and gaseous CO<sub>2</sub> in the measurement chamber. Zones covered in dashed rectangles are blind windows due to absorption of the solvent.

The spectrum of the complex in solution in its Cu(I) form is consistent with both spectra of the pure ligand<sup>53</sup> and spectra of Cu-complexes bearing similar ligands,<sup>54</sup> with intense absorptions due to stretching modes of the rings (1599 and 1575 cm<sup>-1</sup>) and bending modes of the backbone (847 cm<sup>-1</sup>). Some notable interferences can be noted in the spectrum, namely stretching vibrations of H<sub>2</sub>O (at 3686 and 3600 cm<sup>-1</sup>) present in the solvent and/or KBr windows and CO<sub>2</sub> (at 2359 and 2338 cm<sup>-1</sup>) present as gas in the sample chamber and

dissolved in the liquid phase; moreover, strong absorptions from the solvent completely preclude the acquisition of reliable data in some spectral intervals (marked with dashed rectangles in Figure 3.20). To aid interpretation and check kinetic behaviour, the MCR-ALS was run on the time series of IR spectra; the resulting spectral and concentration profiles are portrayed in Figure 3.21.

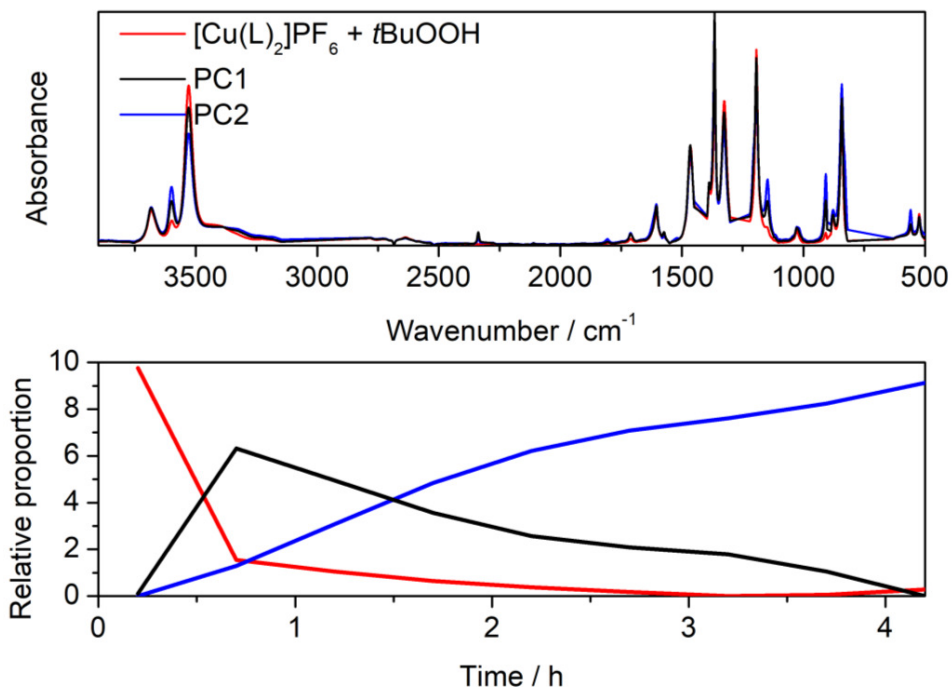


**Figure 3.21** Pure spectral (top) and concentration (bottom) profiles retrieved by the MCR-ALS algorithm applied to the IR reaction profiles of  $[\text{Cu}(6,6'\text{-dimethyl-2,2'}\text{-bipyridyl})_2]\text{PF}_6$  and  $t\text{BuOOH}$ . Blind zones due to intense solvent absorption were removed from the input to aid convergence.

The algorithm successfully assigns 3 pure components to the dataset, identifying the starting point (the signals due to the combination of  $[\text{Cu}(6,6'\text{-dimethyl-2,2'}\text{-bipyridyl})_2]\text{PF}_6$  and  $t\text{BuOOH}$ ) and two additional components. Even with some confusion due to the continuous generation of reaction products, the concentration profiles reflect the kinetic behaviour described by UV-Vis spectrokinetic analysis, confirming that i) the last two components correspond to PC1 and PC2 (together with a mixture of reaction products) and ii) the reaction proceeded consistently with what was previously observed with no detectable interference from the IR setup. The IR spectra in the high

wavenumber zone collected during reaction of  $[\text{Cu}(6,6'\text{-dimethyl-2,2'\text{-bipyridyl)}_2]\text{PF}_6$  with  $t\text{BuOOH}$  (along with reference spectra of  $\text{H}_2\text{O}$  and  $t\text{BuOOH}$ ) are shown in Figure 3.22.

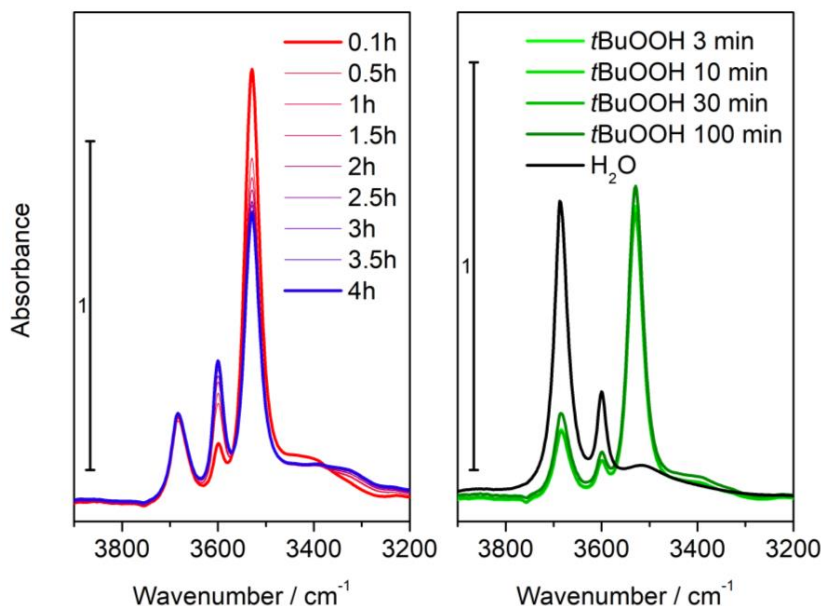


**Figure 3.22** Left: transmission IR spectra (high wavenumbers) of a 2 mM solution of  $[\text{Cu}(6,6'\text{-dimethyl-2,2'\text{-bipyridyl)}_2]\text{PF}_6$  in  $\text{CH}_2\text{Cl}_2$  during reaction with  $t\text{BuOOH}$ . Right: transmission IR spectra (high wavenumbers) of a 150 mM solution of in  $\text{CH}_2\text{Cl}_2$   $t\text{BuOOH}$  (green curves) and a saturated solution of  $\text{H}_2\text{O}$  in  $\text{CH}_2\text{Cl}_2$  (black curve).

The experimental spectra during the oxidation reaction (Figure 3.22, left panel) showed the evolution of three main signals at 3683 (practically unchanged), 3600 (with an increasing trend) and  $3529\text{ cm}^{-1}$  (with a decreasing trend). In order to assign these signals, the IR spectra of  $t\text{BuOOH}$  and  $\text{H}_2\text{O}$  in  $\text{CH}_2\text{Cl}_2$  in the same experimental conditions are shown in Figure 3.22 (right panel). Since signals at the same wavenumbers were retrieved in this control experiment, these features can be assigned to  $\nu_{\text{asym}}$  and  $\nu_{\text{sym}}$  of  $\text{H}_2\text{O}$  ( $3683$  and  $3600\text{ cm}^{-1}$ , respectively) and  $\nu_{\text{OH}}$  of  $t\text{BuOOH}$  ( $3529\text{ cm}^{-1}$ ); furthermore, the spectrum of  $t\text{BuOOH}$  in the absence of Cu shows no significant decrease in intensity of the signal at  $3529\text{ cm}^{-1}$  as a function of time. Comparison of the two sets of spectra leads to the conclusion that i) some amount of  $\text{H}_2\text{O}$  was already present in the  $t\text{BuOOH}$  solution and ii) the peroxide is stable in a  $\text{CH}_2\text{Cl}_2$  solution for more than 1 h. The amount of water present at the start of the oxidation experiment



is thus likely to come from the addition of *t*BuOOH. Although the signal at 3683  $\text{cm}^{-1}$  remained unchanged during the oxidation reaction (hinting that the amount of  $\text{H}_2\text{O}$  in the solution remained constant), the signal at 3600  $\text{cm}^{-1}$  significantly increased over time: this trend can be explained in terms of the formation of *t*BuOH as reaction product, with the signal at 3600  $\text{cm}^{-1}$  being compatible with its  $\nu_{\text{OH}}$ ,<sup>55</sup> other signals due to *t*BuOH grew with the same trend along the oxidation series (*vide infra*). The formation of this co-product was accompanied by a consumption of *t*BuOOH, as testified by the significant decrease in the signal at 3529  $\text{cm}^{-1}$ ; this decrease, corresponding to more than 30% of the signal of the peroxide, is not explainable in terms of the sole reaction with  $[\text{Cu}(6,6'\text{-dimethyl-2,2'\text{-bipyridyl)}_2]\text{PF}_6$  in a 100-fold excess of *t*BuOOH, and has to be due to side reactions involving this molecule. The reaction order on *t*BuOOH and reaction rates retrieved from the UV-Vis spectrokinetic study must be taken with care after this finding. Since *t*BuOOH was observed to be stable in the absence of the complex, and the oxidation reaction was observed not to start in the absence of  $\text{CH}_2\text{Cl}_2$ , a possible hypothesis is that the Cu(I) centre is able to catalyze the degradation of *t*BuOOH, with a role of  $\text{CH}_2\text{Cl}_2$  as a possible co-catalyst or as a free radical propagator. IR spectra in the lower wavenumber zone corresponding to the ones shown in Figure 3.22 (left panel) are reported in Figure 3.23.

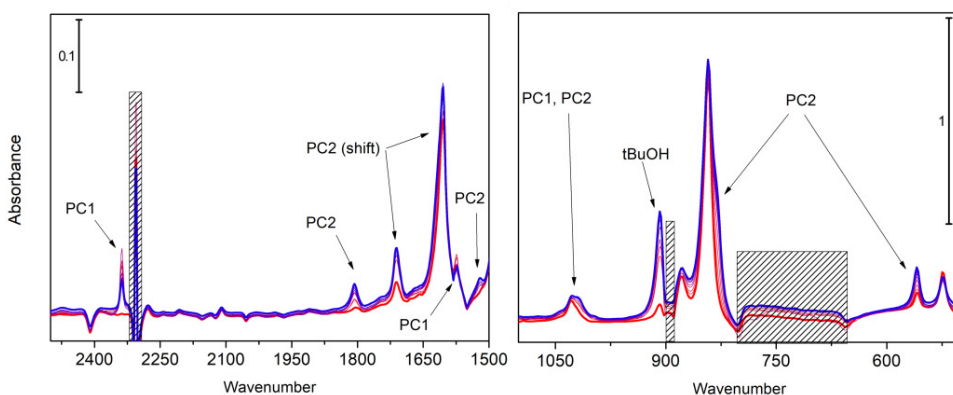


**Figure 3.23** Transmission IR spectra (low wavenumbers) of a 2 mM solution of  $[\text{Cu}(6,6'\text{-dimethyl-2,2'\text{-bipyridyl)}_2]\text{PF}_6$  in  $\text{CH}_2\text{Cl}_2$  during reaction with *t*BuOOH. The spectra correspond to the ones shown in Figure 3.22 (left panel) with the same time scale (curves from red to blue). Zones covered in dashed rectangles are blind windows due to absorption of the solvent. Components assigned to PC1, PC2 or *t*BuOH are marked in the figure together with the presence of significant shifts in the bands.

As can be noticed, not many vibrations that can be directly associated with PC1 were observed upon reaction; this may be due to i) inaccessibility of vibrational features (due to spectral interference from other species, blind windows from the solvent, IR inactivity of some modes, modes under  $500\text{ cm}^{-1}$ ) or ii) an intrinsically low number of new vibrations in PC1 compared to  $[\text{Cu}(6,6'\text{-dimethyl-2,2'}\text{-bipyridyl})_2]\text{PF}_6$ ; the latter hypothesis would be consistent with the UV-Vis and EPR data indicating a small, neutral molecule ( $\text{H}_2\text{O}$ ,  $t\text{BuOH}$ ) or a  $\text{Cl}^-$  anion as additional ligand. Acquisition of spectra in a solution obtained from 1:1 molar ratios of complex:peroxide did not result in the detection of additional signals possibly covered by the intense signals of  $t\text{BuOOH}$  and  $t\text{BuOH}$  in the 1:100 proportion; obtaining reliable signals in the OH stretching zone with this method is, however, very difficult due to spectral interference of trace amounts of  $\text{H}_2\text{O}$  from the solvent or KBr windows, making it impossible to exclude the formation of adducts with  $\text{H}_2\text{O}$  or  $t\text{BuOH}$  completely. The features associated with the formation of PC2 seem to suggest a more complex structure, since more absorptions appeared in the spectra at reaction times consistent with its formation; although a univocal assignment is difficult to make, the vibrational features are at least consistent with reports in the literature on  $[\text{CuOOR}]^+$  species (with  $\text{R} = \text{H}$  or  $\text{C}_n\text{H}_m$ ) with reported signals for  $\nu_{\text{O-O}}$  and  $\nu_{\text{Cu-O}}$  in the  $800\text{-}900$  and  $500\text{-}650\text{ cm}^{-1}$  ranges, respectively. Assignment of PC2 to one of these species is certainly not plausible on the basis of this comparison alone, but it is at least consistent with EXAFS, UV-Vis and EPR data suggesting an  $\text{R}(\text{O})\text{O}^-$  species as the most compatible ligand within the explored pool of species.

This multitechnique, computationally aided study on the oxidation reaction of  $[\text{Cu}(6,6'\text{-dimethyl-2,2'}\text{-bipyridyl})_2]\text{PF}_6$  by  $t\text{BuOOH}$  showed how an apparently simple chemical problem could require unpredictable effort in its study. The one-electron  $\text{Cu(I)}/\text{Cu(II)}$  conversion, the apparently easy two-reactants system and the slow kinetics allowing to characterize most species involved in the reaction all suggested that identification of such species and the reaction mechanism would not be such a challenging task; yet, several complications such as the rapid degradation of  $t\text{BuOOH}$  (only detected by IR) and the detection of two separate  $\text{Cu(II)}$  species (as highlighted by EPR spectroscopy) revealed how *in situ* multitechnique characterization can be often necessary to

disentangle even apparently trivial problems. Furthermore, the role of multivariate algorithms to disentangle complex dataset comprised of mixtures of spectra was found to be fundamental to obtain fine details on the species that form, with the added benefit of retrieving concentration profiles of the system under investigation. Although a definitive assignment of the chemical identity of PC1 and PC2 is still somewhat ambiguous, many possible species were excluded and general geometrical/electronic requirements for the remaining candidates have been established.

### 3.4 Tetradentate Cu complexes

Enzymatic systems that are able to selectively cleave the C-H bond with relatively simple metal-based active sites usually manage to do so in relatively mild conditions.<sup>56</sup> It is no surprise that synthetic efforts that aim to replicate such exceptional reactivity often try to reproduce the same coordination motifs around the metal centre of choice in an easier to control environment (like an organometallic complex or a sterically constrained solid material).<sup>57-60</sup> Since full replication of the intricate and large biological system is neither feasible nor desired, the focus of bioinspired efforts is directed at reproducing the electronic and geometrical features of the active site. This is the case for the complexes characterized in this section, that employ a bis(imine)-bis(imidazole) coordinating pattern that can tightly bind the Cu site in a structural motif that can still be flexible and reactive towards redox reactions. Air stability of the complex in solid form allowed to safely characterize the starting Cu(I) form in which it was synthesized: extensive characterization was performed on the Cu(I) state of this complex in a previous study,<sup>5</sup> comprising NMR spectroscopy, X-ray diffraction, X-ray absorption/emission spectroscopies and DFT; current developments on these systems are ongoing, focusing on their catalytic performance for C-H selective activation. Since catalytic tests on the selective oxidation of cyclohexane and cyclohexene using peroxides as oxidizing agents and these complexes as catalysts involve the Cu(I)/Cu(II) redox cycle, further characterization was employed to study the species responsible for this reactivity. As a starting point, the Cu(I) form of the complex was exposed to H<sub>2</sub>O and H<sub>2</sub>O<sub>2</sub> as possible oxidizing agents for the Cu centre, with subsequent

re-reduction of the metal via L-ascorbic acid (HAsc); the XAS spectra corresponding to these states are shown in Figure 3.24.

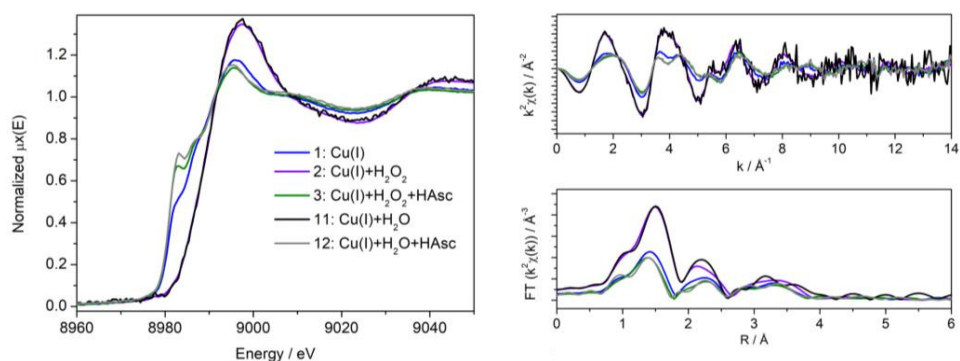


**Figure 3.24** Cu K-edge XAS spectra of species obtained after reaction of a 7.5 mM solution of IG01 (Cu(I) form) in dimethylformamide with different reactants. Left panel: normalized XANES spectra. Right panel:  $k^2\chi(k)$  EXAFS spectra (top) and magnitude of FT-EXAFS spectra (bottom). The Fourier transform of the EXAFS spectra was applied in the 2.48–11.1 Å<sup>-1</sup> range.

The XANES spectrum of the initial state of IG01 (1) confirmed a Cu(I) species is the major component, in agreement with previous studies on the powder form of the sample:<sup>5</sup> this can be inferred by both the edge position (8990 eV) and the presence of the Cu(I) dipole-allowed 1s→4p transition at ca. 8983 eV. The relatively low intensity of this transition suggested either/both a relatively high coordination number (3-4) or/and a bent angle (*i.e.*, a non-linear configuration) in case of low coordination.<sup>47</sup> As a comparison, single-crystal XRD data found the sample in solid form to present a tetracoordinated Cu site with similar Cu-N bond lengths 2.05 Å on average. Upon addition of H<sub>2</sub>O or H<sub>2</sub>O<sub>2</sub>, the XANES spectra are consistent with a complete oxidation to a Cu(II) state: this is confirmed by the shift in the edge position to higher energies (8990.9 eV), the absence of the Cu(I) 1s→4p transition and the formation of the weak dipole-forbidden Cu(II) 1s→3d transition at ca. 8978 eV. The spectral quality of the sample oxidized in H<sub>2</sub>O (11) was found to be poor compared to the one oxidized in H<sub>2</sub>O<sub>2</sub> (2), probably because of the formation of bubbles and/or precipitates in the reaction mixture. Although the XANES spectrum is still interpretable, this interference made it difficult to extract good-quality FT-EXAFS spectra from (11). As expected for a Cu(II) state, the coordination number on Cu seemed to increase: this is noticeable both from the higher

intensity of the white line and on the overall increase of the intensity of the first- and second-shell contribution on the FT-EXAFS for (2) and (11). From what can be observed from XAS spectroscopy only, the two states obtained after oxidation using H<sub>2</sub>O<sub>2</sub> and H<sub>2</sub>O are practically indistinguishable. It also has to be considered that contact with H<sub>2</sub>O<sub>2</sub> necessarily implies a major fraction of H<sub>2</sub>O in the reaction environment, as water is the solvent (if not also a byproduct of reaction) of H<sub>2</sub>O<sub>2</sub>. Upon reaction of the oxidized states with L-ascorbic acid, the Cu(II) species converted back to a Cu(I) state (as confirmed by the XANES spectra), though this time small but significant differences can be noticed in the white line region and especially in the 1s→4p transition compared to the original spectrum (1). Considering the FT-EXAFS is affected in shape but not much in intensity compared to (1), a change in the coordination environment/electronic structure without significant change in coordination number may explain the differences in these data. A possibility is the formation of a relatively low amount of linear Cu(I) species (*e.g.*, Cu coordinated by fragments of partial hydrolysis of the ligand) that would contribute significantly to the XANES but only weakly to changes in the EXAFS. A third possibility, considering also that preliminary mass spectrometry data suggest additional O atoms retained in the Cu(I) states after an oxidation-reduction, is that OH<sup>-</sup> groups formed during the oxidation are coordinating the Cu(I) as additional/substitutive ligands (*e.g.*, N-Cu<sup>+</sup>-N + OH<sup>-</sup> → N + N-Cu<sup>+</sup>-OH<sup>-</sup>). The initial Cu(I) form presents a triflate as counterion, and when the sample is oxidized to a Cu(II) state an additional counterion is needed to balance the charge: this could be possibly supplied by an OH<sup>-</sup> formed during the reaction, that could then be retained (after re-reduction using L-ascorbic acid) by the Cu(I) as counterion due to the low coordination ability of the triflate anion compared to an OH<sup>-</sup>.

To explore the possible configuration of these Cu(I) states, a series of DFT optimizations were carried out on the geometry of the complex. The structure obtained using the hybrid B3LYP functional for IG01 is reported in Figure 3.25.

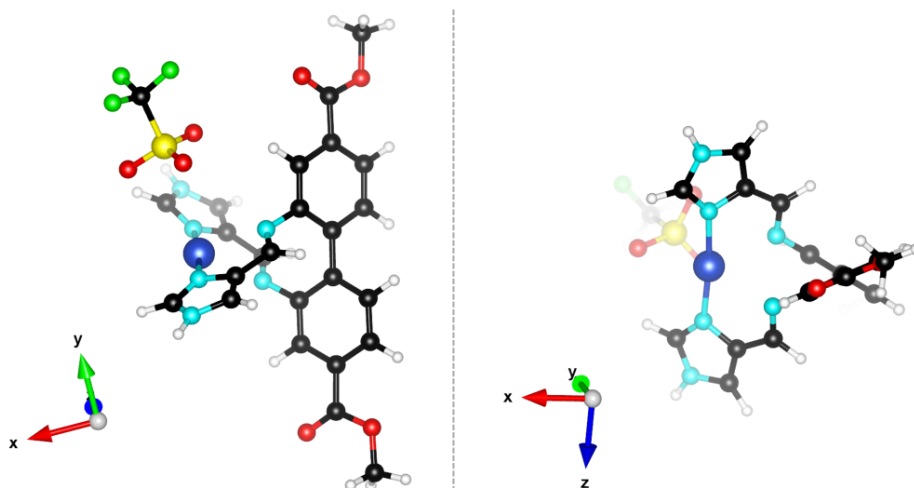


**Figure 3.25** Optimized B3LYP structure of IG01 from two different viewpoints. Colour code: H in white, C in black, N in cyan, O in red, F in green, S in yellow, Cu in blue.

As can be seen, the DFT minimum using the B3LYP functional converges to an almost perfect linear coordination for Cu(I), with a  $N_{\text{imidazole}}\text{-Cu-N}_{\text{imidazole}}$  angle of  $175^\circ$ . This functional is widely used in the literature for geometry optimizations (including the previous study on this same complex) and is typically regarded as appropriate for this purpose. However, similar coordination patterns usually give rise to a very intense  $1s \rightarrow 4p$  transition (as shown in Section 2.2), in contrast with the experimental feature being relatively low in this case. Since such a coordination geometry would also be at odds with the structure found for the solid, that also presents an experimental XANES spectrum similar to the one found for the solution, this discrepancy could be due to an incorrect computational description of the system. Indeed, by using a range-separated hybrid functional (CAM-B3LYP) two minimum structures with similar energy can be obtained: while one of them is very similar to the B3LYP minimum point, the other displays a bent  $N_{\text{imidazole}}\text{-Cu-N}_{\text{imidazole}}$  angle ( $155^\circ$  instead of  $175^\circ$ ), in which the two  $N_{\text{imine}}$  atoms are also involved in the coordination of Cu. A comparison between the two minima is displayed in Figure 3.26.

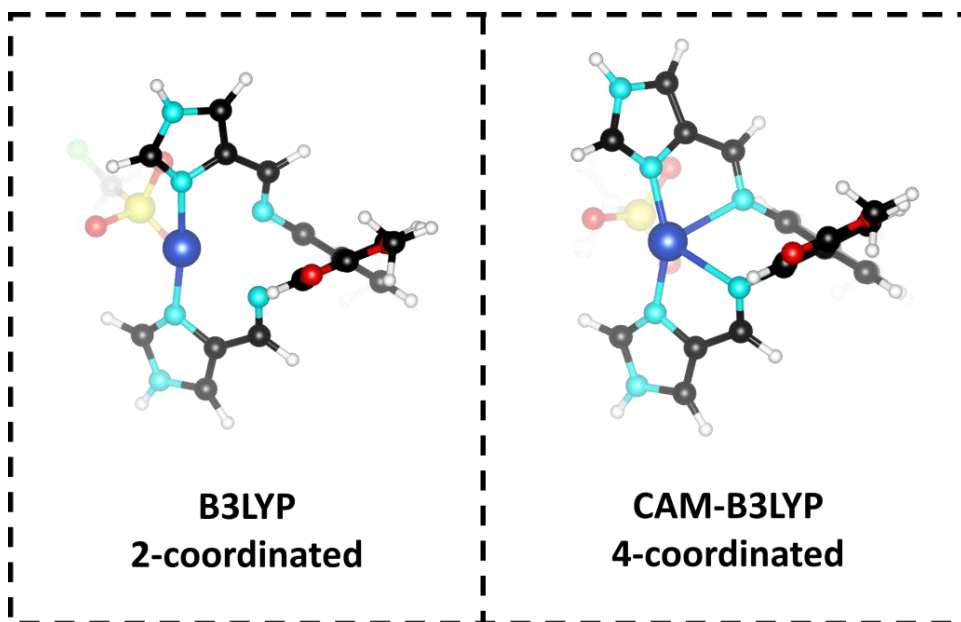


**Figure 3.26** Optimized B3LYP (left) and CAM-B3LYP (right) structures of IG01 from the same viewpoint. The structure labelled as “CAM-B3LYP” refer to the bent structure minimum found for the complex. Colour code: H in white, C in black, N in cyan, O in red, F in green, S in yellow, Cu in blue.

The structure obtained using the CAM-B3LYP functional was found to be more similar to the structure in the solid sample, with average Cu-N<sub>imidazole</sub> and Cu-N<sub>imine</sub> distances of 1.97 and 2.36 Å, respectively. Simulation of XANES spectra for these two geometries confirms that such a decrease in the N<sub>imidazole</sub>-Cu-N<sub>imidazole</sub> bite angle would give rise to a less intense 1s→4p transition in the case of these structures, as shown in Figure 3.27.

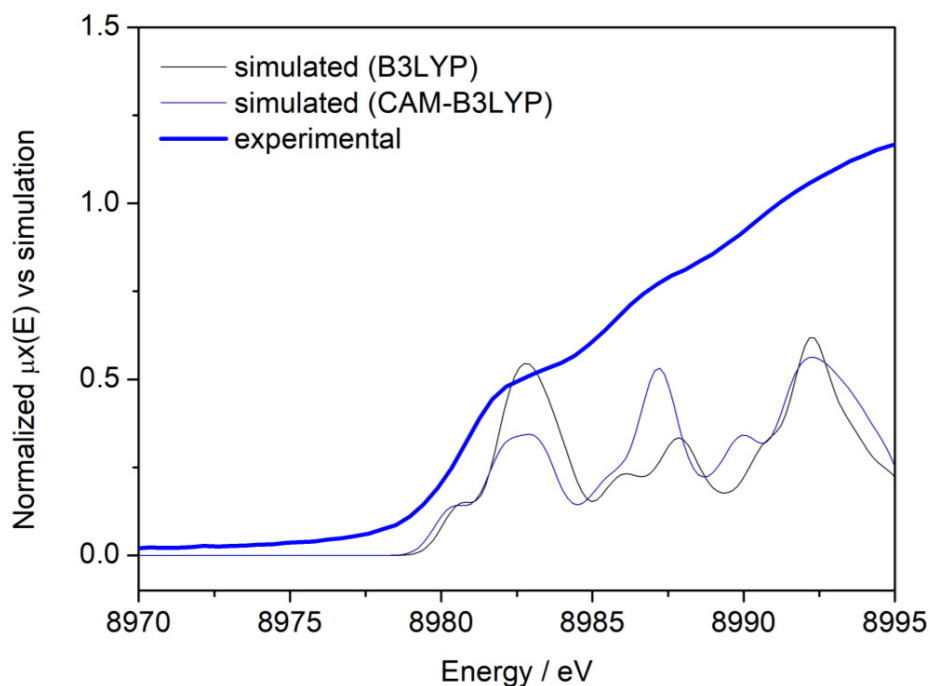


**Figure 3.27** Normalized pre-edge and rising edge XANES spectra of IG01 in solution (thick blue) corresponding to sample (1) in Figure 3.24 along with TD-DFT simulated spectra of the structures shown in Figure 3.26 optimized using the B3LYP (thin black) and the CAM-B3LYP (thin blue) functionals. Calculated spectra are displayed with an energy shift of -6 eV and Gaussian lineshape width of 2.3 eV.

Such a striking dependency of the geometry on the choice of the functional, resulting in very different simulated spectra, was not expected initially; in order to rationalize this discrepancy, relaxed PES scans along the  $N_{\text{imidazole}}\text{-Cu-N}_{\text{imidazole}}$  angle for the two functionals were run. The resulting curves are shown for the two functionals in Figure 3.28.



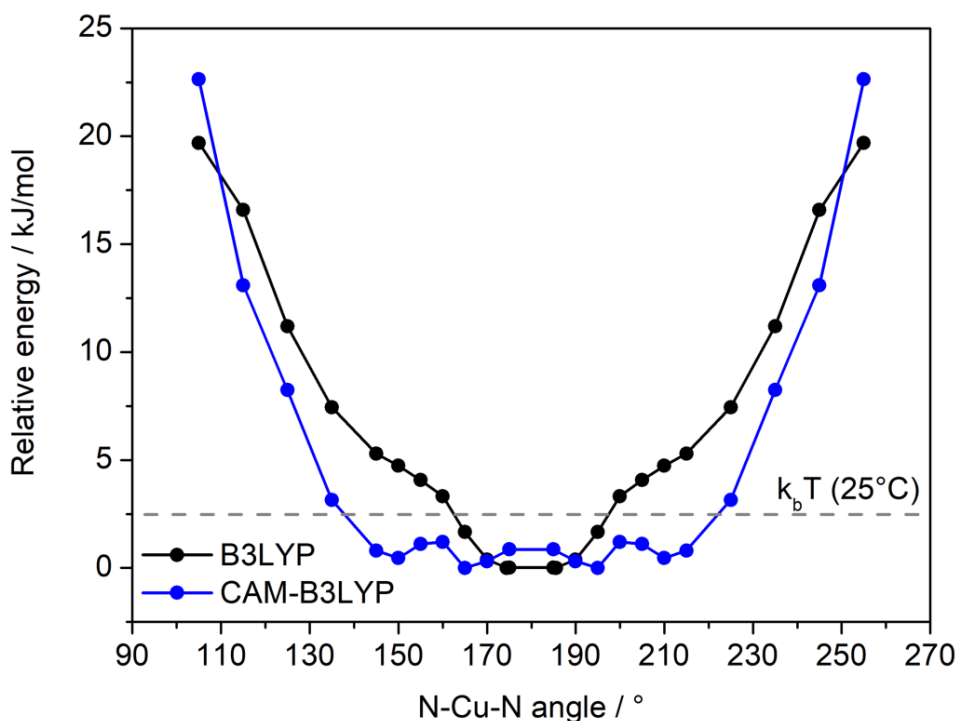


**Figure 3.28** Relaxed PES scans (electronic energies) of IG01 along the reaction coordinate consisting of the *N*imidazole-Cu-*N*imidazole angle using the B3LYP (black) and CAM-B3LYP (blue) functionals. The dashed grey line indicates thermally accessible geometries at 25°C. Relative energies are referred to the minimum point in each PES.

The calculation of these PES scans turned out to be quite computationally expensive because of the general flatness of the PES around these angle values which, in turn, reflects a remarkable flexibility of this structure; such a flat PES profile is consistent with what was already observed on this complex in the solid form.<sup>5</sup> Essentially all angles in the range 135-180° are calculated to be thermally accessible at room temperature. As a comparison, the PES around the same angle in the case of Cu(II) (IG01b complex, *vide infra*) is reported in Figure 3.29.

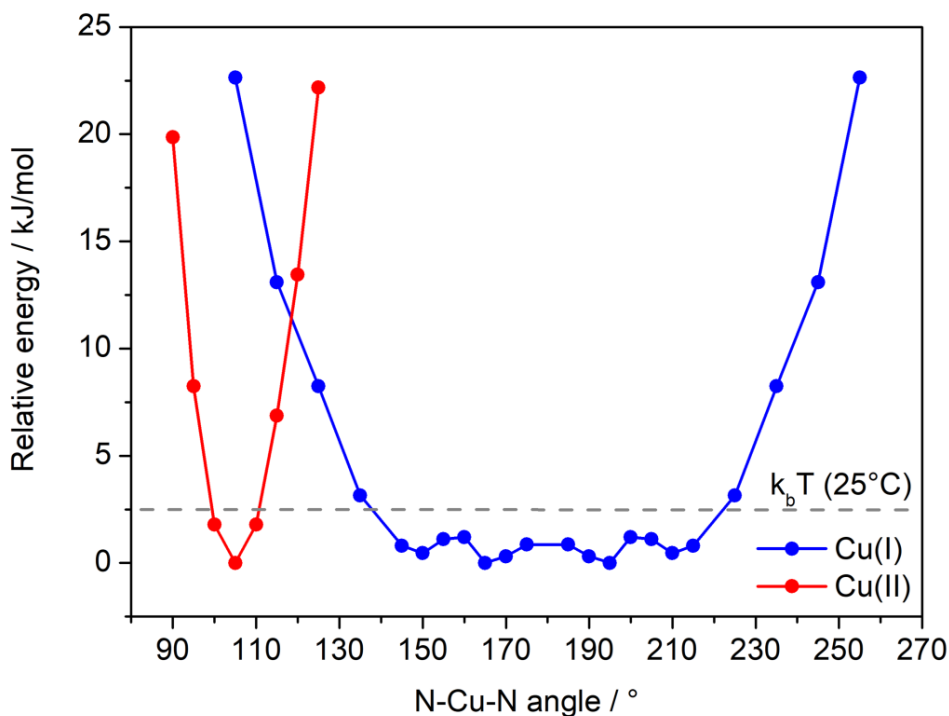


**Figure 3.28** Relaxed PES scans (electronic energies) of IG01 (blue) and IG01b (red) along the reaction coordinate consisting of the  $N_{\text{imidazole}}\text{-Cu-}N_{\text{imidazole}}$  angle using the CAM-B3LYP functional. The dashed grey line indicates thermally accessible geometries at 25°C. Relative energies are referred to the minimum point in each PES.

The Cu(II) structure showed no particular dependence on the functional and displayed a more common, harmonic-like flexibility (accessible angles between 100-110°). Preliminary molecular dynamics (MD) simulations on the Cu(I) state showed that the triflate counterion is displaced when explicit solvent molecules are introduced, and the structure is confirmed to be very flexible: angles oscillated in the same range found by DFT and the equilibrium position settled around 155°. With this new picture in mind, a possibility is for this system to display such a strong flexibility that the resulting XANES spectrum could be an average of several geometries that fall in this wide range of angles. This would be consistent with the experimental XANES, in which a simple linear coordination geometry approaching 180° would be unlikely to reproduce the spectrum of (1). Furthermore, the displacement of the triflate in the MD simulations could be indicative of a very weakly bound ionic couple, in which

implicit solvation through the CPCM model could lead to an overestimation of the interaction between the complex cation and the triflate anion.

Another possible explanation for the unusual intensity of the  $1s \rightarrow 4p$  transition after reduction with L-ascorbic acid could be partial hydrolysis of the ligand after introduction of  $H_2O_2$  or  $H_2O$  in the system: in both cases of Cu(I) ligation by (i) a partially hydrolysed ligand or (ii) two 4-imidazolecarboxaldehydes resulting from complete hydrolysis of the ligand, the geometry around Cu(I) was found to be more linear; the structures corresponding to these hypotheses along with the corresponding simulated XANES spectra are shown in Figure 3.29.

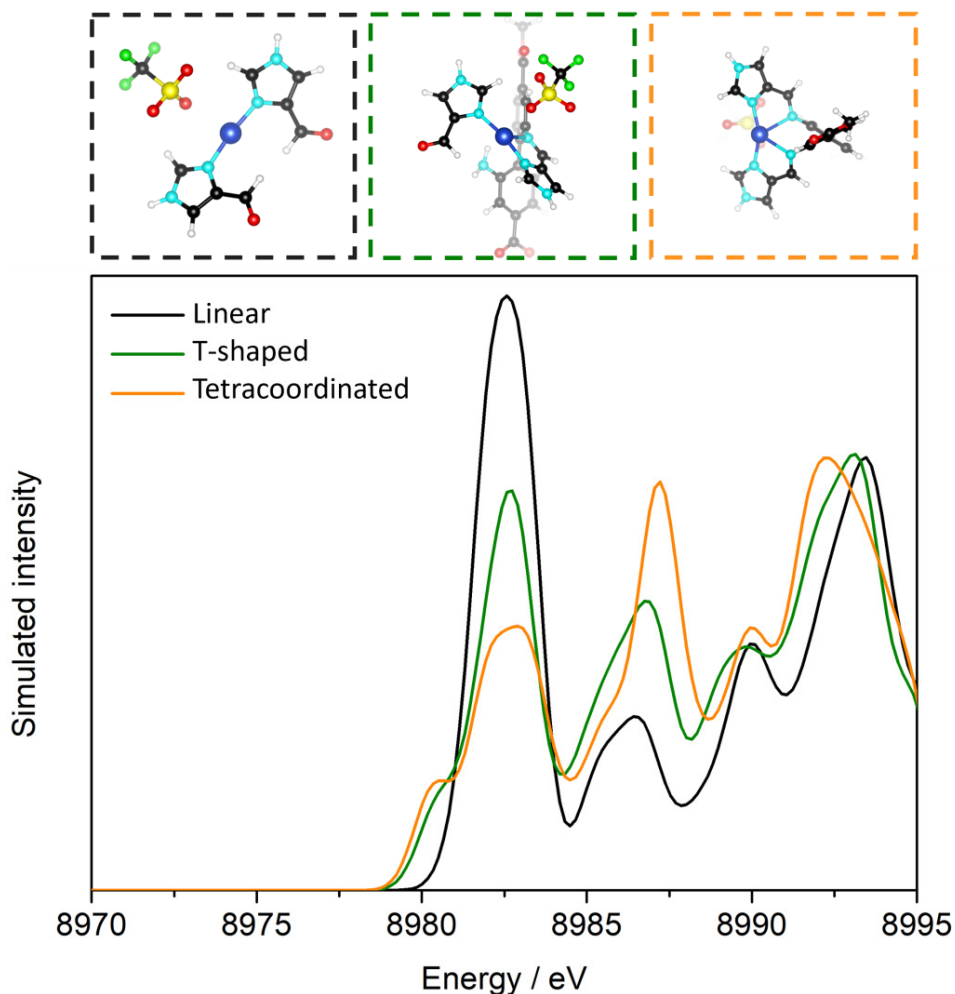


**Figure 3.29** Calculated pre-edge and rising edge XANES spectra of possible Cu(I) complexes (shown on the right) resulting from partial hydrolysis of the ligand. Calculated spectra are displayed with an energy shift of -6 eV and Gaussian lineshape width of 2.3 eV.

In both the case of linear and T-shaped coordination, the resulting Cu(I)  $1s \rightarrow 4p$  transition was predicted to be more intense than in the tetracoordinated case. Mass spectrometry of the solution after introduction of  $H_2O_2$  or  $H_2O$  found minor fragments consistent with 4-imidazolecarboxaldehyde, showing that at least part of the ligand is hydrolysed at the imine site after introduction of the oxidizing agent.

XAS spectra corresponding to species obtained using a solution of IG01b as the starting point are depicted in Figure 3.30.

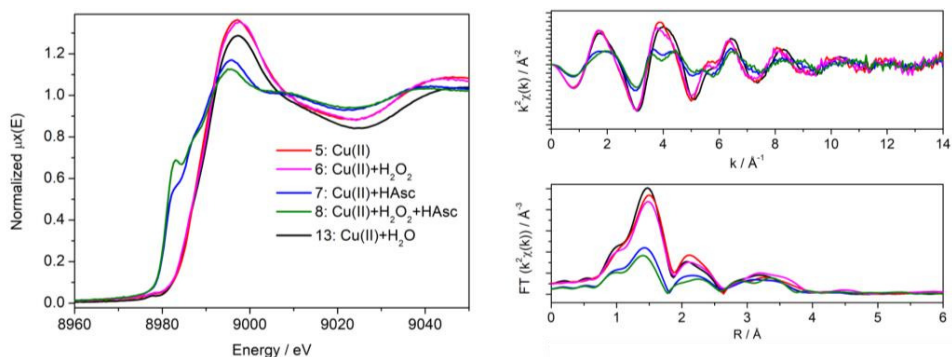


**Figure 3.30** Cu K-edge XAS spectra of species obtained after reaction of a 7.5 mM solution of IG01b (Cu(II) form) in dimethylformamide with different reactants. Left panel: normalized XANES spectra. Right panel:  $k^2\chi(k)$  EXAFS spectra (top) and magnitude of FT-EXAFS spectra (bottom). The Fourier transform of the EXAFS spectra was applied in the 2.48–11.1 Å<sup>-1</sup> range.

The as-prepared material (5) showed XAS spectra consistent with the general shape of a Cu(II) species (*e.g.*, Figures 3.9 and 3.24) and was found to be very similar to the oxidized states previously discussed (spectra 2 and 11 in Figure 3.24) in both the XANES and EXAFS parts. When IG01b was directly reduced using L-ascorbic acid, the resulting XANES spectrum (7) was extremely similar to the one obtained for IG01 (1), with a relatively weak Cu(I) 1s→4p transition: this fact, together with NMR and MS data, suggest that this species corresponds to a simple reduction to the as-synthesized Cu(I) complex (IG01). When H<sub>2</sub>O<sub>2</sub> was added to the solution of IG01b (6), the spectral shape was mainly unaffected in both the XANES and EXAFS regions, although some differences could be spotted in the rising edge and white line region; something similar seemed to occur after the addition of H<sub>2</sub>O (13). These differences appear even more significant when considering that after reduction on a sample that was exposed to H<sub>2</sub>O<sub>2</sub> (8) the final Cu(I) state was found to show significant differences compared to (7), and resembled in fact the other Cu(I) states obtained starting from IG01 (spectra 3 and 12 in Figure 3.24). This seems to suggest that addition of H<sub>2</sub>O<sub>2</sub>/H<sub>2</sub>O already had an effect on the Cu(II) state (IG01b). Unfortunately, as already commented in Section 3.3, Cu K-edge XAS is a very powerful technique to spot differences in Cu(I) states, but a bit less direct when Cu(II) states are involved: the edge profile is generally “flatter” and presents less features, leading to simulations that are usually undecisive and can be less useful for interpretation; as an example of this, the

experimental and simulated XANES spectra for IG01b are reported in Figure 3.31.

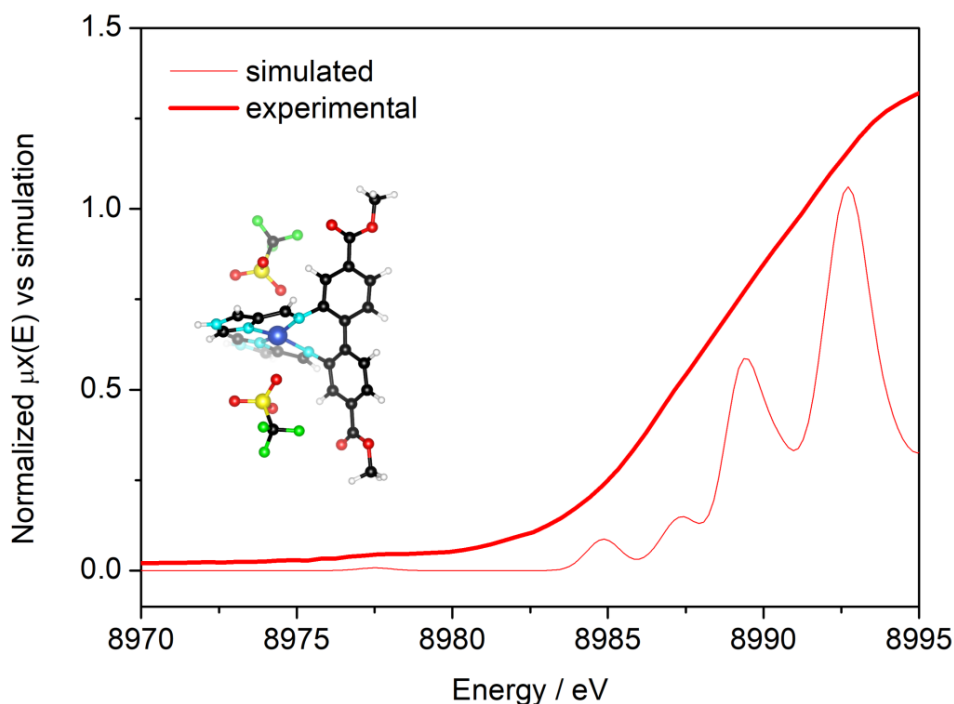


**Figure 3.31** Normalized pre-edge and rising edge XANES spectra of IG01b in solution (thick line) corresponding to sample (5) in Figure 3.30 along with the TD-DFT simulated spectrum of its calculated structure (shown in overlay). Calculated spectra are displayed with an energy shift of -6 eV and Gaussian lineshape width of 2.3 eV.

As can be seen, the calculated spectrum is certainly consistent with the experimental one; nonetheless, virtually any Cu(II) structure similar to the one displayed in Figure 3.31 could produce similar spectra with no significant features to correlate to the experimental spectrum apart from the Cu(II) 1s→3d transition at ca. 8978 eV.

This DFT-assisted XAS study on the Cu(I) and Cu(II) forms of imine/imidazole tetracoordinated complexes and their interaction with oxidizing/reducing agents was further proof that relatively smaller structures (compared to the ones shown in Chapter 2) do not necessarily imply simpler characterization. Subtle differences in speciation and structural flexibility can lead to challenging situations in which the combination of experimental and computational tools

can make the difference. XANES showed that there is additional reactivity other than plain oxidation when H<sub>2</sub>O<sub>2</sub> is added to these Cu complex; however, because Cu(I) states are generally richer in features compared to Cu(II) in Cu K-edge XAS, these changes were best observed indirectly after reduction. UV-Vis and EPR studies are ongoing on these systems to better characterize the Cu(II) part of these materials.

## References

1. Constable, E. C. & Housecroft, C. E. The Early Years of 2,2'-Bipyridine—A Ligand in Its Own Lifetime. *Mol.* 2019, Vol. 24, Page 3951 24, 3951 (2019).
2. Kohn, F. E. et al. Octahedral Bipyridine and Bipyrimidine Dioxomolybdenum(vi) Complexes: Characterization, Application in Catalytic Epoxidation, and Density Functional Mechanistic Study. doi:10.1002/1521-3765(20020517)8:10.
3. Giordano, M. et al. Methoxy-substituted copper complexes as possible redox mediators in dye-sensitized solar cells. *New J. Chem.* 45, 15303–15311 (2021).
4. Hall, J. R., Litzow, M. R. & Plowman, R. A. Coordination compounds of substituted 1,10-Phenanthrolines and related dipyritydyls. VI. Complexes of copper(II) and 4,6,4',6'-Tetramethyl-2,2'-bipyridine. *Aust. J. Chem.* 18, 1331–1338 (1965).
5. Gerz, I. et al. Structural Elucidation, Aggregation, and Dynamic Behaviour of N,N,N,N-Copper(I) Schiff Base Complexes in Solid and in Solution: A Combined NMR, X-ray Spectroscopic and Crystallographic Investigation. *Eur. J. Inorg. Chem.* 2021, 4762–4775 (2021).
6. Gerz, I. Bioinspired Copper Complexes for Incorporation into UiO-67. (2022).
7. Lieberman, R. L. & Rosenzweig, A. C. Crystal structure of a membrane-bound metalloenzyme that catalyses the biological oxidation of methane. *Nat.* 2005 4347030 434, 177–182 (2005).

8. Bissaro, B. et al. Oxidative cleavage of polysaccharides by monocopper enzymes depends on H<sub>2</sub>O<sub>2</sub>. *Nat. Chem. Biol.* 2017 1310 13, 1123–1128 (2017).
9. Kracher, D. et al. Extracellular electron transfer systems fuel cellulose oxidative degradation. *Science* (80-. ). 352, 1098–1101 (2016).
10. Bissaro, B., Kommedal, E., Røhr, Å. K. & Eijsink, V. G. H. Controlled depolymerization of cellulose by light-driven lytic polysaccharide oxygenases. *Nat. Commun.* 2020 111 11, 1–12 (2020).
11. Chylenski, P. et al. Lytic Polysaccharide Monooxygenases in Enzymatic Processing of Lignocellulosic Biomass. *ACS Catal.* 9, 4970–4991 (2019).
12. Signorile, M., Bonino, F., Damin, A. & Bordiga, S. A Novel Raman Setup Based on Magnetic-Driven Rotation of Sample. *Top. Catal.* 61, 1491–1498 (2018).
13. Cammack, R. & Cooper, C. E. [12] Electron paramagnetic resonance spectroscopy of iron complexes and iron-containing proteins. *Methods Enzymol.* 227, 353–384 (1993).
14. Weyhermüller, T., Paine, T. K., Bothe, E., Bill, E. & Chaudhuri, P. Complexes of an aminebis(phenolate) [O,N,O] donor ligand and EPR studies of isoelectronic, isostructural Cr(III) and Mn(IV) complexes. *Inorganica Chim. Acta* 337, 344–356 (2002).
15. Stoll, S. & Schweiger, A. EasySpin, a comprehensive software package for spectral simulation and analysis in EPR. *J. Magn. Reson.* 178, 42–55 (2006).
16. Aasa, R. & Vänngård, tore. EPR signal intensity and powder shapes: A reexamination. *J. Magn. Reson.* 19, 308–315 (1975).
17. Ravel, B. & Newville, M. ATHENA, ARTEMIS, HEPHAESTUS: data analysis for X-ray absorption spectroscopy using IFEFFIT. *urn:issn:0909-0495* 12, 537–541 (2005).
18. Neese, F. & Wiley, J. The ORCA program system. *Wiley Interdiscip. Rev. Comput. Mol. Sci.* 2, 73–78 (2012).



19. Neese, F. Software update: The ORCA program system—Version 5.0. *Wiley Interdiscip. Rev. Comput. Mol. Sci.* 12, e1606 (2022).
20. Neese, F., Wennmohs, F., Becker, U. & Riplinger, C. The ORCA quantum chemistry program package. *J. Chem. Phys.* 152, 224108 (2020).
21. Becke, A. D. A new mixing of Hartree–Fock and local density-functional theories. *J. Chem. Phys.* 98, 1372–1377 (1993).
22. Weigend, F. & Ahlrichs, R. Balanced basis sets of split valence, triple zeta valence and quadruple zeta valence quality for H to Rn: Design and assessment of accuracy. *Phys. Chem. Chem. Phys.* 7, 3297–3305 (2005).
23. Weigend, F. Accurate Coulomb-fitting basis sets for H to Rn. *Phys. Chem. Chem. Phys.* 8, 1057–1065 (2006).
24. Helmich-Paris, B., de Souza, B., Neese, F. & Izsák, R. An improved chain of spheres for exchange algorithm. *J. Chem. Phys.* 155, (2021).
25. Grimme, S., Ehrlich, S. & Goerigk, L. Effect of the damping function in dispersion corrected density functional theory. *J. Comput. Chem.* 32, 1456–1465 (2011).
26. Barone, V. & Cossi, M. Quantum calculation of molecular energies and energy gradients in solution by a conductor solvent model. *J. Phys. Chem. A* 102, 1995–2001 (1998).
27. Cossi, M., Rega, N., Scalmani, G. & Barone, V. Energies, structures, and electronic properties of molecules in solution with the C-PCM solvation model. *J. Comput. Chem.* 24, 669–681 (2003).
28. Yanai, T., Tew, D. P. & Handy, N. C. A new hybrid exchange–correlation functional using the Coulomb-attenuating method (CAM-B3LYP). *Chem. Phys. Lett.* 393, 51–57 (2004).
29. Reiher, M. Douglas-Kroll-Hess theory: A relativistic electrons-only theory for chemistry. *Theor. Chem. Acc.* 116, 241–252 (2006).

30. Pantazis, D. A., Chen, X. Y., Landis, C. R. & Neese, F. All-electron scalar relativistic basis sets for third-row transition metal atoms. *J. Chem. Theory Comput.* 4, 908–919 (2008).
31. Angeli, C., Cimiraglia, R., Evangelisti, S., Leininger, T. & Malrieu, J. P. Introduction of n-electron valence states for multireference perturbation theory. *J. Chem. Phys.* 114, 10252–10264 (2001).
32. Angeli, C., Cimiraglia, R. & Malrieu, J. P. N-electron valence state perturbation theory: a fast implementation of the strongly contracted variant. *Chem. Phys. Lett.* 350, 297–305 (2001).
33. Angeli, C., Cimiraglia, R. & Malrieu, J. P. n-electron valence state perturbation theory: A spinless formulation and an efficient implementation of the strongly contracted and of the partially contracted variants. *J. Chem. Phys.* 117, 9138–9153 (2002).
34. Van Lenthe, E., Snijders, J. G. & Baerends, E. J. The zero-order regular approximation for relativistic effects: The effect of spin–orbit coupling in closed shell molecules. *J. Chem. Phys.* 105, 6505–6516 (1996).
35. Brémond, E. & Adamo, C. Seeking for parameter-free double-hybrid functionals: The PBE0-DH model. *J. Chem. Phys.* 135, 24106 (2011).
36. Drosou, M., Mitsopoulou, C. A., Orio, M. & Pantazis, D. A. EPR Spectroscopy of Cu(II) Complexes: Prediction of g-Tensors Using Double-Hybrid Density Functional Theory. *Magnetochemistry* 8, 36 (2022).
37. Perdew, J. P. & Wang, Y. Accurate and simple analytic representation of the electron-gas correlation energy. *Phys. Rev. B* 45, 13244 (1992).
38. Hedegård, E. D., Kongsted, J. & Sauer, S. P. A. Optimized basis sets for calculation of electron paramagnetic resonance hyperfine coupling constants: Aug-cc-pVTZ-J for the 3d atoms Sc-Zn. *J. Chem. Theory Comput.* 7, 4077–4087 (2011).
39. Gómez-Piñeiro, R. J., Pantazis, D. A. & Orio, M. Comparison of Density Functional and Correlated Wave Function Methods for the Prediction of Cu(II) Hyperfine Coupling Constants. *ChemPhysChem* 21, 2667–2679 (2020).

40. Jaumot, J., Gargallo, R., De Juan, A. & Tauler, R. A graphical user-friendly interface for MCR-ALS: a new tool for multivariate curve resolution in MATLAB. *Chemom. Intell. Lab. Syst.* 76, 101–110 (2005).
41. Kaes, C., Katz, A. & Hosseini, M. W. Bipyridine: The most widely used ligand. A review of molecules comprising at least two 2,2'-bipyridine units. *Chem. Rev.* 100, 3553–3590 (2000).
42. Munakata M., Kitagawa S., Asahara A. & Masuda H. Crystal Structure of Bis(2,2'-bipyridine)copper(I) Perchlorate. <https://doi.org/10.1246/bcsj.60.1927> 60, 1927–1929 (2006).
43. Harrison, W. D., Hathaway, B. J. & IUCr. Bis(2,2'-bipyridyl)-catena- $\mu$ -tetrathionato-copper(II). *urn:issn:0567-7408* 34, 2843–2845 (1978).
44. Itoh, S., Kishikawa, N., Suzuki, T. & Takagi, H. D. Syntheses, structural analyses and redox kinetics of four-coordinate [CuL<sub>2</sub>]<sup>2+</sup> and five-coordinate [CuL<sub>2</sub>(solvent)]<sup>2+</sup> complexes (L = 6,6'-dimethyl-2,2'-bipyridine or 2,9-dimethyl-1,10-phenanthroline): completely gated reduction reaction of [Cu(dmp)<sub>2</sub>]<sup>2+</sup> in nitromethane. *Dalt. Trans.* 0, 1066–1078 (2005).
45. Kavan, L. et al. Electrochemical Properties of Cu(II/I)-Based Redox Mediators for Dye-Sensitized Solar Cells. *Electrochim. Acta* 227, 194–202 (2017).
46. Saygili, Y. et al. Liquid State and Zombie Dye Sensitized Solar Cells with Copper Bipyridine Complexes Functionalized with Alkoxy Groups. *J. Phys. Chem. C* 124, 7071–7081 (2020).
47. Kau, L.-S. et al. X-ray Absorption Edge Determination of the Oxidation State and Coordination Number of Copper: Application to the Type 3 Site in *Rhus vernicifera* Laccase and Its Reaction with Oxygen. *JACS* 109, 113–121 (1987).
48. Garribba, E., Micera, G., Sanna, D. & Strinna-Erre, L. The Cu(II)-2,2'-bipyridine system revisited. *Inorganica Chim. Acta* 299, 253–261 (2000).

49. Garribba, E. & Micera, G. The determination of the geometry of Cu(II) complexes. An EPR spectroscopy experiment. *J. Chem. Educ.* 83, 1229–1232 (2006).
50. Qiu, S. R. et al. Origins of optical absorption characteristics of Cu 2+ complexes in aqueous solutions. *Phys. Chem. Chem. Phys.* 17, 18913–18923 (2015).
51. Miessler P. J.; Tarr, D. A., *Inorganic Chemistry*. (Pearson, 2013).
52. Elwell, C. E. et al. Copper-Oxygen Complexes Revisited: Structures, Spectroscopy, and Reactivity. *Chem. Rev.* 117, 2059–2107 (2017).
53. Seyfi, S., Alizadeh, R., Ganji, M. D. & Amani, V. Molecular, electronic structure and spectroscopic properties of 6,6'-dimethyl-2,2'-bipyridine and Hg<sup>2+</sup> complex: Experimental and DFT investigations. *Vacuum* 139, 9–22 (2017).
54. Balaiah, B., Sastry, B. A., Chary, M. N., Ponticelli, G. & Massacesi, M. IR, EPR and optical absorption studies of some 2,2'-bipyridine complexes of Copper(II). *J. Mol. Struct.* 78, 289–297 (1982).
55. Korppi-Tommola, J. Tert-butyl alcohol—matrix i.r. spectra and vibrational assignment. *Spectrochim. Acta Part A Mol. Spectrosc.* 34, 1077–1085 (1978).
56. Ciano, L., Davies, G. J., Tolman, W. B. & Walton, P. H. Bracing copper for the catalytic oxidation of C–H bonds. *Nat. Catal.* 2018 18 1, 571–577 (2018).
57. Baek, J. et al. Bioinspired Metal-Organic Framework Catalysts for Selective Methane Oxidation to Methanol. *J. Am. Chem. Soc.* 140, 18208–18216 (2018).
58. Rebilly, J. N., Colasson, B., Bistri, O., Over, D. & Reinaud, O. Biomimetic cavity-based metal complexes. *Chem. Soc. Rev.* 44, 467–489 (2014).
59. Patel, R. N., Singh, N., Shukla, K. K., Gundla, V. L. N. & Chauhan, U. K. Synthesis, structure and biomimetic properties of Cu(II)–Cu(II) and Cu(II)–Zn(II) binuclear complexes: possible models for the chemistry of Cu–Zn superoxide dismutase. *J. Inorg. Biochem.* 99, 651–663 (2005).

60. Wang, Y., DuBois, J. L., Hedman, B., Hodgson, K. O. & Stack, T. D. P. Catalytic galactose oxidase models: Biomimetic Cu(II)-phenoxyl-radical reactivity. *Science* (80-. ). 279, 537–540 (1998).

## Conclusions

The rather wide scope of this thesis work described some of the characterization tools that can be developed and used to study systems that exploit the rich redox chemistry of Cu, with a special focus on Cu-exchanged zeolites and tetracoordinated Cu-based metallorganic complexes. Although the specific discussion topics were diverse and widely different from one another, several common threads can be found throughout this work as general conclusions. The Cu(I)/Cu(II) redox couple can at first be thought of as a “simple”, even textbook-like system: compared to other transition metals, for instance, one would think that the relatively simple  $d^{10}/d^9$  electron configuration (resulting in singlet or doublet spin states) would give rise to repetitive, easily identifiable and interpretable patterns in electronic and EPR spectra. Depending on the level of detail that is required for the specific problem, however, this thesis is at least a testament to the complexity that can arise even in this apparently straightforward case. Special care should be taken when connecting trends that were established in solid materials and systems in solution, as these connections can be underestimated or overestimated depending on the case. If there is one, single *fil rouge* connecting all the studies discussed in this thesis, it is undoubtedly that multitechnique, *in situ* characterization is today a strict requirement to answer complex questions on apparently simple problems. A single, cutting-edge technique may be able to give precious and unprecedented information on a system, but comprehensive understanding can often only be reached by simultaneously looking at it from different perspectives – or with different wavelengths. Similarly, there is arguably no good reason not to employ theoretical tools (in the form of quantum chemistry and multivariate methods) to make sense of the enormous and possibly ambiguous data that is collected experimentally: most (if not all)

data in this work could not be processed or understood without such methods, which become more inexpensive and approachable by the day.

## Acknowledgements

My PhD project, as well as the preparation of this thesis work, was only possible because of the many people that were present through this long journey; this small space is dedicated to acknowledging their help and support.

I would like to express my gratitude to my supervisors Silvia and Matteo, who introduced me to the world of spectroscopy and helped me to grow professionally, scientifically and personally along the way. I learned different lessons from you two that I will always carry with me.

My heartfelt thank you goes to all my colleagues and friends in Via Quarello and Via Giuria, who always welcomed me and made me feel part of a team. To Natale, who was always there to support me and bear with me, for his exceptional ability to make things work out in and out of the lab. To Alberto, both slow and precise to a fault, my safety net for an overly detailed but scientifically bulletproof opinion. To Alessia, Michele, Paolo, Francesca, Virginia, Melodj, Margherita, Valeria, Sergio, Andrea, Vasco, Chiara, Guillermo, Beatrice, Edoardo, Barbara, Eleonora, Luz, Valentino. To Dr. Andrea Martini at the Fritz Haber Institute for his unvaluable scientific insight and his role in one of humanity's greatest feasts.

A big thank you goes to Lowik Dewek-Raszka, Daniele Bonavia and Flavie Le Rai, which in the development of their master's thesis project help me develop my own project. I know they are on their way to become great scientists and I hope we can cross ways in the future.

A special thank you goes to the staff of the beamlines I visited for X-ray-related activities, especially Dr. Kirill Lomachenko, Dr. Cesare Atzori and Dr. Davide Salusso at BM23 (ESRF), who gave substantial contributions to all the experiments I took a part in at their facility.

I acknowledge the CuBE project (Horizon 2020 Excellence Science ERC-Synergy program 2019-CuBE: “Unravelling the secrets of Cu-based catalysts for C–H activation”, grant agreement no. 856446) for funding my research activity in all its aspects, and I am deeply indebted to all the CuBE staff in Torino and abroad for their unvaluable help. I thank Prof. Claudia Barolo, Prof. Gloria Berlier, Prof. Francesca Bonino, Prof. Elisa Borfecchia, Barbara Centrella, Dr. Valentina Crocellà, Dr. Alessandro Damin, Valeria Finelli, Beatrice Garetto, Dr. Stefano Nejrotti, Dr. Carlotta Pontremoli, and Natale Porcaro from the UniTO team. A special acknowledgement goes to the staff at the MPI-CEC that welcomed me and helped me during my period abroad in Mülheim: my supervisors Prof. Serena DeBeer and Dr. Sergio Jannuzzi, who guided me during my stay and taught me so much in so little time; Dr. Isabelle Gerz and Ashish Tamhankar who gave me constant and unconditional support, in science and in daily life in Germany; Christian Feike, Fabian Otto and Derya Demirbas who had the patience to bear with my constant requests and helped me with experimental activities; Zach, Tiago, Isis, Ilmari, Chris, Derek, Kushal, Olivia, Daniel and all the people at the institute with which I had the pleasure to share many lunch breaks with. I thank all the CuBE staff at the UiO and NMBU in Norway, especially Prof. Unni Olsbye, Dr. Erlend Aunan, Dr. Sebastian Prodingler and Mouhammad Abu Rasheed; I would also like to extend my gratitude to Prof. Stian Svelle, Dr. Pablo Beato, Dr. Izar Berdiell, Dr. Karoline Kvande and Bjørn Solemsli for sharing results and fruitful discussions in the context of the iCSI project.

I acknowledge support from the Project CH4.0 under the MUR program "Dipartimenti di Eccellenza 2023–2027" (CUP: [D13C22003520001](#)).





# Appendix A1

The development of reliable experimental setups to perform *in situ* and *operando* spectroscopy has been one of the objectives of this PhD project; although no specific case for UV-Vis spectroscopy on solid materials has been reported in the main text, the development of one such setup is reported in Figure 2.3. The reason for interest in setups of this kind should be evident from the many examples of *in situ* spectroscopy reported throughout the document: studies of the materials that go beyond basic characterization of the as synthesized form but inspect them in their working conditions are of paramount importance. Some of the main arguments for the characterization of materials by means of *in situ* spectroscopies include:

- 1) Residual components from synthesis or previous treatment may still be present in the material (*e.g.*, templating agents in zeolites or porous materials) that influence the properties of the catalyst.
- 2) The formation (or degradation) of certain species may be promoted by the reaction conditions (*e.g.*, temperature or pressure) as opposed to *ex situ* studies.
- 3) The experimental technique itself may be sensitive to changes in reaction conditions, which can lead to the formation of artifacts.

Even though the formation of a specific species is identified with *in situ* spectroscopy, and supposing the concentration of said species decreases when the reactant is introduced, deducing that the observed species is responsible for catalysis is technically not correct. Quantitative assessment of the productivity and selectivity towards a specific product or class of products should be provided if a claim on the aforementioned species as an active site wants to be proposed, *i.e.*, *operando* spectroscopy should be performed; if this is not the case, disappearance of said species after introduction of the reagent could be equally ascribable to degradation of the catalyst, introduction of pollutants along with the reagent, or more complex mechanisms if selectivity is not controlled. A specific note should be pointed out while discussing *ex situ/in situ/operando* spectroscopy. *In situ* spectroscopy should specifically refer to spectroscopy performed in reaction conditions, whatever the specifics of such reaction may be in terms of reaction temperature, pressure, chemical environment or other relevant variables. In case the performance of the catalyst is simultaneously evaluated by analytical measurements of products in

a quantitative manner (*i.e.*, productivity and selectivity are assessed), this methodology may be called *operando* spectroscopy. All labels akin to *simil-operando*, *quasi-operando* or such are at the least of questionable value, since catalyst performance is either measured simultaneously (*operando*) or it is not (*in situ*). That being said, the development of *operando* (and *in situ*) experimental setups is surely not trivial, since conditions for optimal acquisition of spectra can often be partially or completely incompatible with the reaction conditions that need to be reproduced; further complications may arise when connecting product analysers that may be sensitive to specific thermochemical conditions. Figure A1.1 reports an example of the first version of an *operando* setup for DR-UV-Vis spectroscopy system developed in the context of the author's master thesis project.

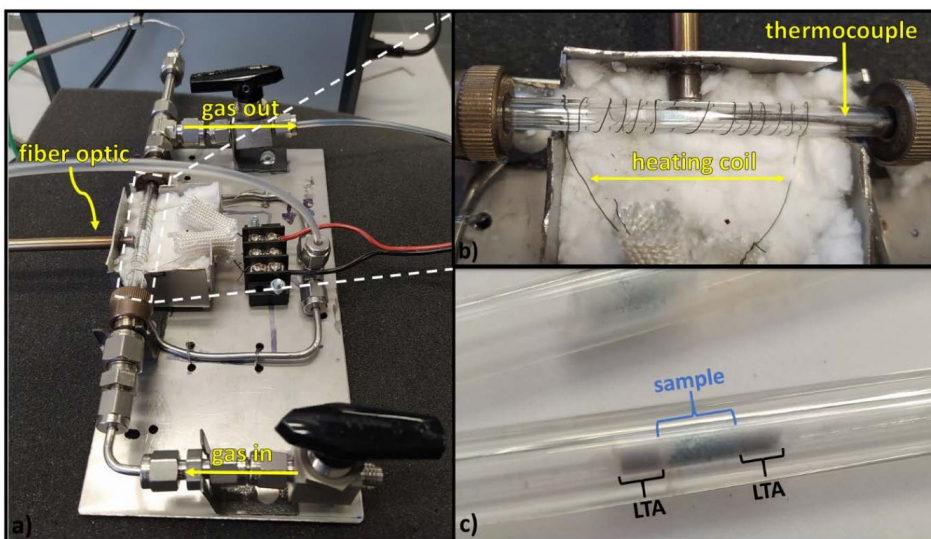


**Figure A1.1** First version of experimental setup for *operando* DR-UV-Vis spectroscopy. LTA zeolite traps positioned as water traps.

In this first version of the setup, the sample was pressed and sieved into a high purity sapphire reactor to allow for collection of both UV-Vis and Raman spectra. Heating was achieved via a NiCr coil powered through a low-voltage supply system and connected to a PID device for accurate temperature ramp control; gaseous reactants were connected to the reactor via Swagelok stainless steel connectors, and effluents were directed towards analytics (mass spectrometer) via the same type of connections. The fibre optics for UV-Vis

light irradiation and collection, as described in section 2.1, was in direct contact with the reactor window. An example on data collected with this setup on a Cu-ZSM-5 sample is shown in Figure A1.2.

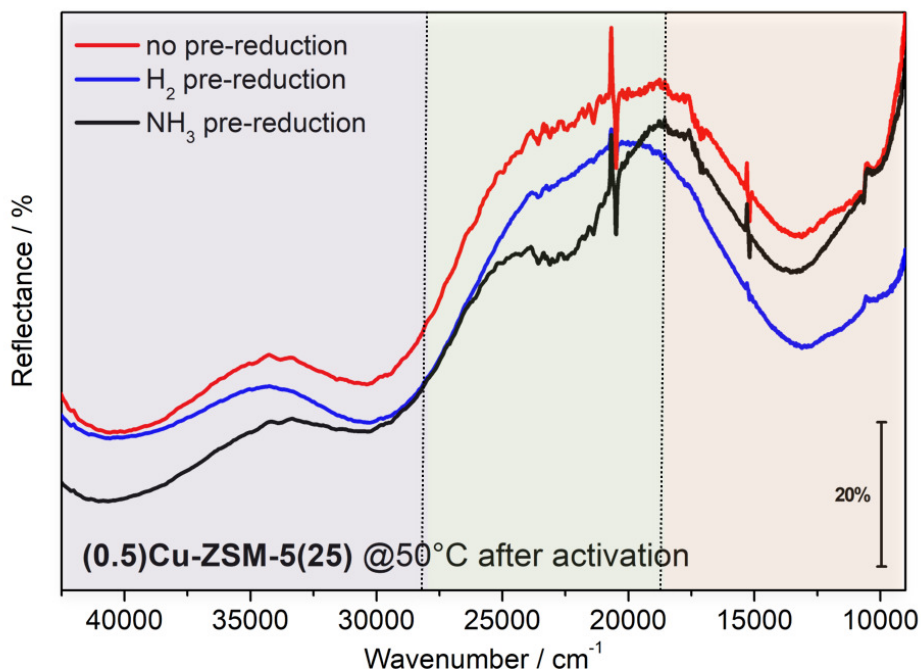


**Figure A1.2** In situ DR-UV-Vis data collected on a Cu-ZSM-5 sample in He at 50°C.

As can be noticed from the spectra (which show some variability depending on pre-treatment) systematic significant interferences were present in the 20000-25000  $\text{cm}^{-1}$  zone, which could be attributed to spurious reflections of the cylindrical sapphire reactor and small differences in the position of the fibre optics with respect with the measurement on the blank. This case specifically testifies to the inconvenience of such distortions on the spectra in the assessment of the band at ca. 22700  $\text{cm}^{-1}$  that forms depending on pretreatment conditions. Furthermore, non-perfect fitting of the Swagelok components with the reactor sometimes led to small air leaks; although these were confirmed to be only traces amounts by online mass spectrometry, the enormous sensitivity of these materials to even minute amounts of  $\text{H}_2\text{O}$  was enough to severely reduce the productivity of the catalyst (testifying again on the importance of *operando* spectroscopy). In order to reduce both the spectral interference and air pollution effects on this setup, a new version was

developed according to Figure 2.3. A significant improvement on both airtightness and spectral quality was achieved, as testified by the spectra shown in Figure A1.3.

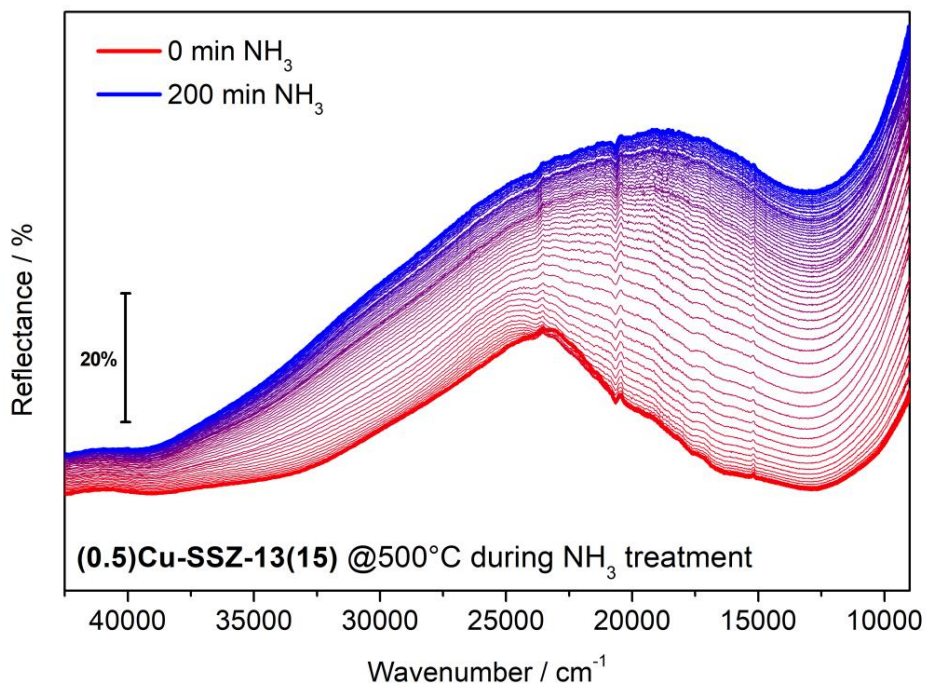


**Figure A1.3** In situ DR-UV-Vis data collected on a Cu-SSZ-13 sample during treatment in NH<sub>3</sub> at 500°C.

Although some minor interferences are still present, the spectral quality of the spectrum was significantly enhanced it was possible to reliably monitor spectral features in all zones of the spectra. A key factor in this upgrade was played by the new quartz reactor cell with increased diameter compared to the sapphire one, providing a flatter surface of the reactor wall which led to less spurious reflections, as well as a tighter slot for the fibre optics that allowed for more reproducible positioning of the probe. Depending on the specific reaction, though, a reactor with a smaller internal diameter may be needed to properly reproduce experimental conditions; this fact once again testifies to the dilemma of optimal conditions for spectroscopy vs reactivity in the development of setups for *operando* characterization.

# Appendix A2

## Copper Speciation

How to cite: *Angew. Chem. Int. Ed.* **2021**, *60*, 25891–25896

International Edition: doi.org/10.1002/anie.202109705

German Edition: doi.org/10.1002/ange.202109705

# Copper Pairing in the Mordenite Framework as a Function of the Cu<sup>I</sup>/Cu<sup>II</sup> Speciation

Gabriele Deplano<sup>+</sup>, Andrea Martini<sup>+</sup>, Matteo Signorile,<sup>\*</sup> Elisa Borfecchia, Valentina Crocellà, Stian Svelle, and Silvia Bordiga

**Abstract:** A series of gas-phase reactants is used to treat a Cu-exchanged mordenite zeolite with the aim of studying the influence of the reaction environment on the formation of Cu pairs. The rearrangement of Cu ions to form multimetric sites as a function of their oxidation state was probed by X-ray absorption spectroscopy (XAS) and also by applying advanced analysis through wavelet transform, a method able to specifically locate Cu–Cu interactions also in the presence of overlapping contributions from other scattering paths. The nature of the Cu-oxo species formed upon oxidation was further crosschecked by DFT-assisted fitting of the EXAFS data and by resonant Raman spectroscopy. Altogether, the Cu<sup>I</sup>/Cu<sup>II</sup> speciation clearly correlates with Cu proximity, with metal ion pairs quantitatively forming under an oxidative environment.

## Introduction

Within the paradigm of an improved use of fossil resources, strategies facilitating the exploitation of many small/remote natural gas sources (including biogas) is of utmost importance.<sup>[1,2]</sup> In particular, chemical processes able to transform methane (the main constituent of natural gas) into liquid analogues are desirable for a simplified handling and transportation. The presently implemented syngas-based

technologies are energy intensive processes, thus economically viable only for large-scale applications.<sup>[3]</sup> As an alternative, the direct conversion of methane to methanol (DMTM) via partial oxidation represents a promising route. In analogy to biological systems (e.g. methanotrophic bacteria hosting the pMMO enzymes),<sup>[4–6]</sup> several Cu-based catalysts for DMTM have been developed and studied.<sup>[7]</sup> Among them, Cu-exchanged zeolites have received much attention after the discovery of their activity in DMTM by Schoonheydt's group in 2005.<sup>[8]</sup> Many different topologies and compositions (in terms of Si/Al and Cu/Al ratios) have been explored, aiming at finding structure–activity relationships.<sup>[9]</sup> A combination of experimental and theoretical techniques has been applied to identify the active species responsible for this reactivity, and many mechanisms have been proposed to explain their formation and outstanding selectivity. Moreover, different reaction conditions heavily impact the speciation of Cu inside the zeolite framework, thus influencing DMTM.<sup>[10]</sup> Overall, the Cu<sup>I</sup>/Cu<sup>II</sup> redox cycle and the local coordination environment around Cu sites are the key features for understanding these complex systems.

In this context, opportune gas-phase reactants (e.g. NH<sub>3</sub>) affect both Cu speciation and framework distribution when used prior to oxidation, as the coordinative nature of NH<sub>3</sub> enhances the Cu cations' mobility.<sup>[11]</sup> Accordingly, the Cu speciation in the framework changes,<sup>[12]</sup> as well as the average Cu–Cu distance, in turn conditioning the formation of active species. Indeed, these are supposedly multinuclear Cu sites bridged by O atoms; different Cu–Cu distances could affect oxidation pathways and drive towards different speciation. Thereby, understanding the effect of the redox history of a Cu-zeolite on the final speciation of Cu sites (including Cu-oxo species) is relevant for optimizing both DMTM catalysts and reaction protocols. Accordingly, a selection of reducing agents has been used to activate a Cu-MOR sample subsequently characterized through XAS, aiming at probing the oxidation state and local environment of the resulting species. Furthermore, the application of Wavelet Transform (WT) Analysis<sup>[13]</sup> on these data allowed us correlating the existence of Cu–Cu interactions with the fraction of reduced/oxidized Cu species. Through DFT-supported fitting of the EXAFS data, specific Cu-oxo species were identified.



## Results and Discussion


In this work, we focus on an ad hoc synthesized Cu-MOR (Si/Al = 8.22 and Cu/Al = 0.27, atomic ratios from EDX),

[\*] G. Deplano,<sup>[+]</sup> Dr. A. Martini,<sup>[+]</sup> Dr. M. Signorile, Dr. E. Borfecchia, Dr. V. Crocellà, Prof. S. Bordiga  
 Department of Chemistry, NIS and INSTM Reference Centre  
 Università di Torino  
 Via G. Quarello 15, I-10135 and Via P. Giuria 7, I-10125, Torino (Italy)  
 E-mail: matteo.signorile@unito.it

Dr. A. Martini<sup>[+]</sup>  
 Smart Materials, Research Institute, Southern Federal University  
 Sladkova Street 174/28, 344090 Rostov-on-Don (Russia)  
 Prof. S. Svelle  
 Department of Chemistry  
 SMN Centre for Materials Science and Nanotechnology  
 University of Oslo  
 N-0315, Oslo (Norway)

[\*] These authors contributed equally to this work.

 Supporting information and the ORCID identification number(s) for the author(s) of this article can be found under:  
 <https://doi.org/10.1002/anie.202109705>.

 © 2021 The Authors. *Angewandte Chemie International Edition* published by Wiley-VCH GmbH. This is an open access article under the terms of the Creative Commons Attribution License, which permits use, distribution and reproduction in any medium, provided the original work is properly cited.

prepared and characterized as described in Section S1 of the Supporting Information (SI). Basic characterization data (powder XRD and N<sub>2</sub> adsorption isotherm at 77 K) are provided in Figure S1 of the SI. We relied on a home-made material rather than on a commercial one, since Cu-MOR samples we previously studied<sup>[14]</sup> have been proved to contain traces of TiO<sub>2</sub> (anatase polymorph), as shown in Figure S2 of the SI, making it unsuitable for Raman and optical characterization. Figure 1 a and c shows the ex situ XAS data collected at RT for the Cu-MOR treated according to Section S1.1. Each sample was subjected to a specific gas-phase redox treatment. Reduction in NH<sub>3</sub>, H<sub>2</sub>, CO and CH<sub>4</sub> was performed at 250 °C. A sample deeply reduced in NH<sub>3</sub> at 500 °C was also prepared. Regardless the reduction treatment, each sample was subsequently outgassed at 500 °C to ensure complete desorption of species possibly coordinating the Cu ions. Oxidized samples were produced by exposing the sample, possibly pre-reduced in NH<sub>3</sub> at 500 °C, to pure O<sub>2</sub> at 500 °C. Finally, a sample that just underwent vacuum dehydration (thus triggering self-reduction) was considered. Given the edge energy position and the observed XANES features, any contributions from metallic Cu, even in the form of small Cu<sup>0</sup> clusters, can be safely ruled out over the whole set of investigated samples (see also Figure S3). The XANES spectrum in Figure 1 a, belonging to the sample reduced at 500 °C in the presence of NH<sub>3</sub>, shows no traces of the pre-edge 1s→3d transition arising at ca. 8978 eV (see the inset in Figure 1 a), typical of Cu<sup>II</sup> ions. Conversely, it is characterized by a prominent 1s→4p rising-edge peak located at ca. 8983 eV and by a low intensity in the white line (WL) region, typical of a site with a low coordination number. In the limit

of the energy resolution, these spectral features infer the existence of a quasi-linear pure Cu<sup>I</sup> site, in accordance with previous studies, also involving model compounds.<sup>[2,10,14–19]</sup> This interpretation is in line with the phase-uncorrected FT-EXAFS spectrum (Figure 1b): the first-shell maximum is observed at 1.5 Å, with a shoulder extending within 1.8–2.6 Å. The low intensity of the first-shell peak agrees with a twofold coordinated Cu<sup>I</sup> center, most likely with framework oxygen atoms. The XANES spectra of the samples treated in NH<sub>3</sub> and in H<sub>2</sub> at 250 °C are still dominated by a Cu<sup>I</sup> species, but the presence a minor fraction of Cu<sup>II</sup> sites is indicated by the appearance of the Cu<sup>II</sup> 1s→4p transition at ca. 8987 eV. Subtle modifications are also noted in the pre-edge range, pointing to a trace of the Cu<sup>II</sup> 1s→3d peak. Yet, within the available energy resolution, we cannot conclusively comment about this inherently weak spectral feature in samples 2 and 3. Consistently, if compared to the NH<sub>3</sub> 500 °C state, the EXAFS spectrum exhibits a more intense first-shell peak and a structured second-shell peak, consistent with the presence of Cu<sup>II</sup> sites interacting with the framework and having a higher coordination number. The XANES spectra corresponding to the samples reduced in CO, CH<sub>4</sub> and self-reduced (SR) are almost mutually identical.

From these profiles an increase in the relative contribution from Cu<sup>II</sup> centers is clear, determining the abatement of the Cu<sup>I</sup> 1s→4p transition and causing the increase of the Cu<sup>II</sup> 1s→3d and 1s→4p ones. Overall, XANES indicates an almost equal Cu<sup>I</sup>/Cu<sup>II</sup> fraction with a potential slight preference for Cu<sup>II</sup> in these samples. The related EXAFS spectra show the same first- and second-shell features described before, but more intense due to the larger fraction of Cu<sup>II</sup> sites.

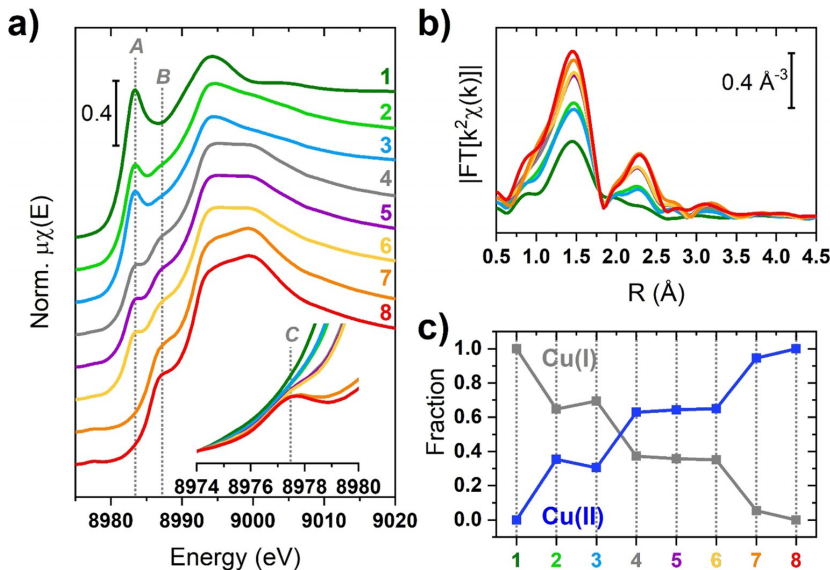


**Figure 1.** a) XANES spectra and b)  $k^2$ -weighted module of FT-EXAFS for Cu-MOR; c) linear combination fit of XANES spectra (samples 1 and 8 taken as references): 1) reduced in NH<sub>3</sub> at 500 °C; 2) reduced in NH<sub>3</sub> at 250 °C; 3) reduced in H<sub>2</sub> at 250 °C; 4) reduced in CO at 250 °C; 5) reduced in CH<sub>4</sub> at 250 °C; 6) self-reduced by vacuum dehydration at 500 °C; 7) directly oxidized in O<sub>2</sub> at 500 °C; and 8) pre-reduced in NH<sub>3</sub> and oxidized in O<sub>2</sub> at 500 °C. In the inset of (a), the magnification of the weak Cu<sup>II</sup> 1s→3d transition is reported. Vertical dotted lines highlight the Cu<sup>I</sup> 1s→4p (A); Cu<sup>I</sup> 1s→4p (B); and Cu<sup>II</sup> 1s→3d (C) transitions. The errors affecting the Cu<sup>I</sup>/Cu<sup>II</sup> fractions obtained from LCF are as low as 0.01.



Finally, in agreement with the literature,<sup>[10,14,19–23]</sup> the XANES spectra of the samples oxidized at 500 °C account for a largely dominant Cu<sup>II</sup> oxidation state. The Cu<sup>I</sup> 1s→4p transition is absent in the XANES of both oxidized samples, inferring a pure Cu<sup>II</sup> state. The corresponding EXAFS spectra are consistent with three/fourfold O-ligated Cu<sup>II</sup>, located at well-defined ion-exchange sites in the zeolite framework.<sup>[10,12]</sup> The second shell appears well-structured and it stems mainly from the Cu–Al/Si and Cu–Cu single scattering (SS) contributions.

The amount of Cu<sup>I</sup> and Cu<sup>II</sup> species in each XANES spectrum was obtained by linear combination fit (LCF)<sup>[24]</sup> on the normalized XANES (Figure 1a), in the 8975–9020 eV range. The number of chemical species was defined through a Principal Component Analysis<sup>[25–27]</sup> (see Figure S4 of the SI) and set to two. The XANES spectra of samples reduced in NH<sub>3</sub> (sample 1) and pre-reduced in NH<sub>3</sub> and then oxidized in O<sub>2</sub> at 500 °C (sample 8) were chosen as standards for the least-square procedure.<sup>[28]</sup> The XANES LCF provided a very small  $R_{\text{factor}}$  (0.04 %) concerning the reconstruction of the experimental XANES, indicating that the selected references are

suitable to reproduce each single XANES spectrum of the dataset; a direct comparison between experimental and LCF curves can be found in Figure S5. The Cu<sup>I</sup>–Cu<sup>II</sup> fraction, retrieved by this approach, is reported in Figure 1c. The samples treated with NH<sub>3</sub> and H<sub>2</sub> at 250 °C show an almost equivalent larger abundance (about 65 %) of Cu<sup>I</sup> sites. Instead, the self-reduced sample and the ones treated with CO or CH<sub>4</sub> show a lower fraction of Cu<sup>I</sup> sites (below 40 %), becoming closely nil in the sample directly oxidized at 500 °C (<5 %). Due to its sensitivity to the chemical nature of the scatterers surrounding the absorbing atom, we employed the WT approach to provide a more robust description of high  $R$  EXAFS features.<sup>[13,29]</sup> All the WT representations show a main lobe at low  $R$  values ( $\Delta k$ : 0.0–12.5 Å<sup>-1</sup> and  $\Delta R$ : 0.5–2.0 Å), as observed on the full two dimensional ( $k, R$ ) maps in Figure S6. As previously described, this feature is due to the SS contributions arising from the (extra-)framework oxygen atoms located in the first coordination shell of the Cu centers. Figure 2 shows, for each treatment, the region of the WT map involving the EXAFS second- and third-shells ( $\Delta k$ : 0.0–12.5 Å<sup>-1</sup> and  $\Delta R$ : 2.0–4.0 Å), where Cu–Cu contributions are

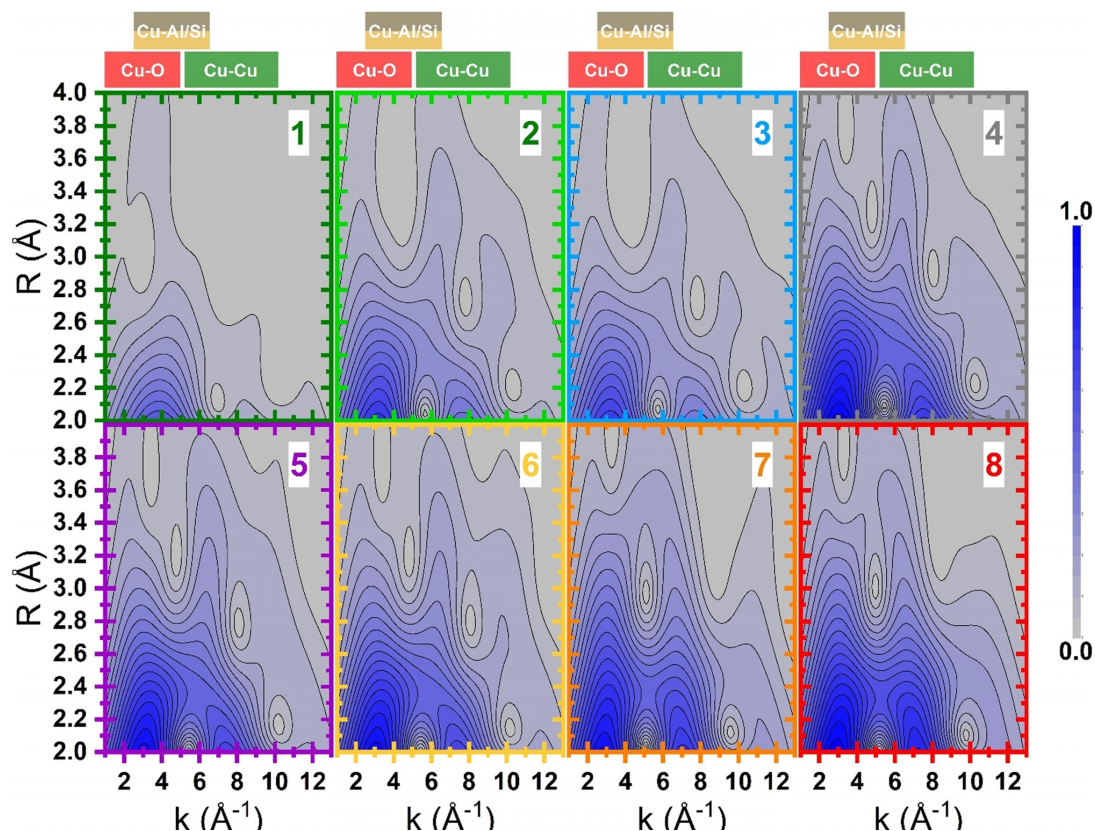


**Figure 2.** Wavelet transform representation of the EXAFS signal for Cu-MOR: 1) reduced in NH<sub>3</sub> at 500 °C; 2) reduced in NH<sub>3</sub> at 250 °C; 3) reduced in H<sub>2</sub> at 250 °C; 4) reduced in CO at 250 °C; 5) reduced in CH<sub>4</sub> at 250 °C; 6) self-reduced by vacuum dehydration at 500 °C; 7) directly oxidized in O<sub>2</sub> at 500 °C; and 8) pre-reduced in NH<sub>3</sub> and oxidized in O<sub>2</sub> at 500 °C. Boxes in the upper part of the figure highlight the region of maximum intensity in  $k$  for Cu–O, Cu–Si/Al and Cu–Cu scattering paths. Vertical lines highlight the position of maximum in  $k$  for Cu–Cu scattering path.

expected. The WT map of the sample reduced in  $\text{NH}_3$  at  $500^\circ\text{C}$  only shows a weak lobe at  $k$  values around  $4.0 \text{ \AA}^{-1}$ . In this region, the backscattering amplitude factor terms for Cu–O and Cu–Al/Si SS have their maxima, largely overlapped (see Figure S7). The WT map confirms that the shoulder appearing in the FT-EXAFS for this sample derives from weak scattering paths involving the farther framework O and Si/Al atoms of the low coordinated  $\text{Cu}^{\text{I}}$  site. In the WT maps of samples reduced at  $250^\circ\text{C}$  in  $\text{NH}_3$  and  $\text{H}_2$ , the low  $k$ -region becomes more structured. A second lobe appears at higher  $k$  values ( $\Delta k$ :  $5.0\text{--}7.0 \text{ \AA}^{-1}$  and  $\Delta R$ :  $2.0\text{--}4.0 \text{ \AA}$ ), arising from intensified contributions of scattering paths among Si/Al and  $\text{Cu}^{\text{II}}$  sites, superimposed to contributions from the lattice O farther from Cu centers. The presence of a small Cu–Cu contribution cannot be excluded, albeit overshadowed by signal from the framework atoms. In fact, a weak ridge is observed at  $7.0 \text{ \AA}^{-1}$ , where the backscattering amplitude factor for a Cu–Cu SS has its maximum. The latter presents increased intensity in the WT maps of samples reduced in  $\text{CO}$ ,  $\text{CH}_4$  and SR. Finally, this feature reaches its maximum intensity for both samples oxidized in  $\text{O}_2$  at  $500^\circ\text{C}$ , that is, when the content of  $\text{Cu}^{\text{II}}$  sites is the highest.<sup>[13,30]</sup> At its maximum development, this sub-lobe extends over a rather broad  $R$ -space range, pointing to a relatively high level of structural disorder in the Cu–Cu interatomic distance distribution. In order to comparatively assess the presence of Cu–Cu scattering contributions through the investigated states, similarly to some previous reports,<sup>[13,30,31]</sup> we computed the power density function  $\Phi^R(k)$  of each WT representation. This quantity was obtained integrating the squared modulus of the WT over the  $R$  range within  $2.0$  and  $4.0 \text{ \AA}$ , which ensures the inclusion, if present, of whatever Cu–Cu path contribution. Figure 3 a shows the results of these calculations. Herein, a first peak is located for all the states between  $0.0\text{--}5.5 \text{ \AA}^{-1}$ , ascribed to the WT low- $k$  sub-lobes, which collectively account for the contribution due to O, Si and Al atomic neighbors surrounding the Cu centers. The second, weaker peak ( $6.0\text{--}8.0 \text{ \AA}^{-1}$ ) is ascribable to Cu–Cu contributions, reflecting the high- $k$  sub-lobe in the WT maps discussed before. The intensity of this peak, as measured at its maximum at  $6.8 \text{ \AA}^{-1}$  for each of the considered states, nicely correlates with the  $\text{Cu}^{\text{II}}$  fraction as previously determined by XANES LCF. Such a result, depicted in Figure 3 b, quantitatively confirms the preference of  $\text{Cu}^{\text{II}}$  toward the formation of multimeric species, whereas  $\text{Cu}^{\text{I}}$  ions remain preferentially separated. The approach of Cu ions in their oxidized form, coherently observed in an oxidative environment, is most probably accompanied by the formation of Cu-oxo species, supposedly active in DMTM. Thus, their exact identification is of utmost interest toward a better understanding of the methane oxidation process (despite not explicitly investigated here). Furthermore, the observation of fingerprints of specific Cu-oxo species also supports the qualitative analysis of Cu–Cu distances as inferred by EXAFS data obtained via Fourier or Wavelet transform. Thereby, an EXAFS fitting procedure was carried out. In particular, we focused our analysis on the two extreme cases: i) at the most reduced sample, that is, treated at  $500^\circ\text{C}$  in  $\text{NH}_3$  (sample 1 in Figure 1); and ii) further oxidized in pure  $\text{O}_2$  at  $500^\circ\text{C}$  (sample 8 in Figure 1). As

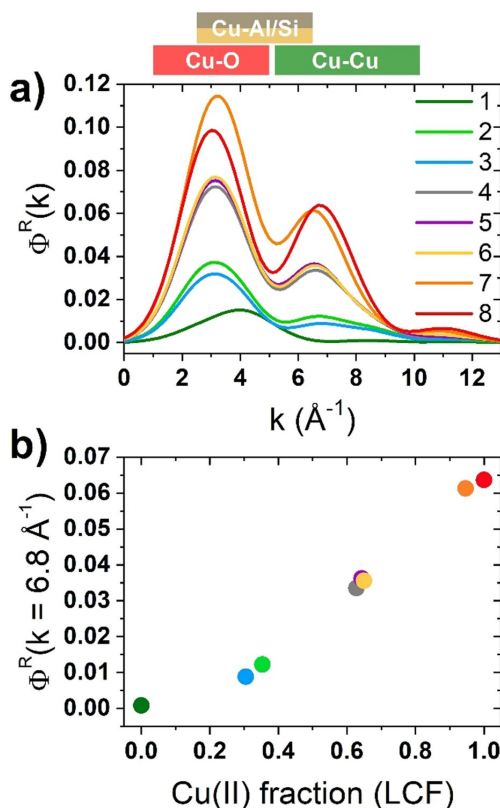


**Figure 3.** a) Power density function  $\Phi^R$  of each WT representation, integrated over the  $2.0\text{--}4.0 \text{ \AA}$  range, for Cu-MOR: 1) reduced in  $\text{NH}_3$  at  $500^\circ\text{C}$ ; 2) reduced in  $\text{NH}_3$  at  $250^\circ\text{C}$ ; 3) reduced in  $\text{H}_2$  at  $250^\circ\text{C}$ ; 4) reduced in  $\text{CO}$  at  $250^\circ\text{C}$ ; 5) reduced in  $\text{CH}_4$  at  $250^\circ\text{C}$ ; 6) self-reduced by vacuum dehydration at  $500^\circ\text{C}$ ; 7) directly oxidized in  $\text{O}_2$  at  $500^\circ\text{C}$ ; and 8) pre-reduced in  $\text{NH}_3$  and oxidized in  $\text{O}_2$  at  $500^\circ\text{C}$ . b) Value of  $\Phi^R$  at  $k = 6.8 \text{ \AA}^{-1}$  (highlighted by the vertical dotted line in (a)) as a function of the  $\text{Cu}^{\text{II}}$  fraction as obtained from LCF of XANES spectra (see Figure 1 c). Boxes in the upper part of the Figure highlight the region of maximum intensity in  $k$  for Cu–O, Cu–Si/Al and Cu–Cu scattering paths. Vertical lines highlight the position of maximum in  $k$  for Cu–Cu scattering path.

structural guess we created, on the basis of the recent literature,<sup>[10,13,14,17,22,32]</sup> four DFT models as described in detail in the Section S5 of SI. The Cu(-oxo) models were hosted in the eight-membered rings of the side pocket of MOR structure, where the siting of Al atoms (i.e. the anchoring site for the Cu ions) was selected on the basis of a systematic prescreening of all possible configurations (see Figure S8 for the considered Al substitutional sites and Table S1 for main outcomes). Four Cu(-oxo) structures were considered (graphically represented in Figure S9): a couple of  $\text{Cu}^{\text{I}}$  ions (labeled  $2[\text{Cu}^{\text{I}}]^+$ ), a mono- $\mu$ -oxo dicopper site ( $[\text{Cu}^{\text{II}}\text{-O-Cu}^{\text{II}}]^{2+}$ ) and two peroxo dicopper sites, owning a different spatial configuration ( $[\text{Cu}^{\text{II}}\text{-OO-Cu}^{\text{II}}]^{2+}_{\text{sideon}}$  and  $[\text{Cu}^{\text{II}}\text{-OO-Cu}^{\text{II}}]^{2+}_{\text{endon}}$ ). The fit on the reduced sample was performed considering the  $2[\text{Cu}^{\text{I}}]^+$ , whereas that for the oxidized state was attempted

with all the aforementioned Cu-oxo models. Nonetheless, only the fit based on the  $[\text{Cu}^{\text{II}}\text{-O-Cu}^{\text{II}}]^{2+}$  structure was sufficiently in agreement with the experimental data (see Section S6 of the SI) and will be discussed herein. The EXAFS fit results, summarized in Figure 4 and Table S2 of the SI (fixed coordination numbers for the  $2[\text{Cu}^{\text{I}}]^+$  and the  $[\text{Cu}^{\text{II}}\text{-O-Cu}^{\text{II}}]^{2+}$  DFT models are given in Table S3 and S4, respectively) and the in Table, properly reproduce the experimental spectra ( $R_{\text{factor}}$  lower than 1% in both the cases) and provided a set of physically reliable optimized parameters. Results obtained for a fit attempt performed with the  $[\text{Cu}^{\text{II}}\text{-OO-Cu}^{\text{II}}]^{2+}_{\text{sideon}}$  structural model are reported in Table S5 (fixed coordination numbers in Table S6), though some physically inconsistent parameters were obtained. The fitting strategies and parametrization adopted are described in Section S6.1 of the SI, while the individual EXAFS path contributions are shown in Figure S10 and S11. Raw data and best-fit in  $k$ -space are shown in Figure S12.

Focusing on the sample reduced in  $\text{NH}_3$  at  $500^\circ\text{C}$ , the EXAFS first-shell feature mostly originates from the SS paths involving the framework oxygen atoms sited close to the Cu absorbers. The latter were found to be approximately in phase (see Figure S10) with an average  $\text{Cu-O}_{\text{fw1}}$  distance refined at  $1.93 \pm 0.01 \text{ \AA}$ . The broadening of the first-shell peak toward longer distances can be ascribed to a second type of O framework atoms at a slightly longer distance from the absorber (i.e.  $\text{Cu-O}_{\text{fw2}}$ ). The contribution from farther framework atoms (O, Al and Si) is instead weak since, due to the high heterogeneity of the Cu-sites, these paths are in antiphase to each other, causing the abatement of their EXAFS signals (see Figure S10). Indeed, high  $R$ -values features are absent, in accordance with the related WT

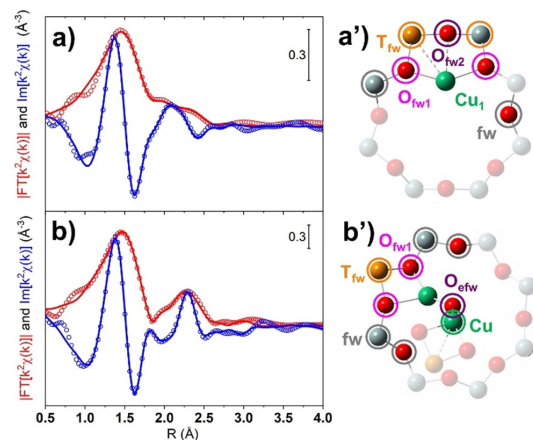


**Figure 4.** Phase-uncorrected (red) modulus and imaginary part (blue) of the experimental and best-fit FT EXAFS spectra for a) the most reduced sample (i.e. treated at  $500^\circ\text{C}$  in  $\text{NH}_3$ , sample 1 in Figure 1); and b) further oxidized in pure  $\text{O}_2$  at  $500^\circ\text{C}$  (sample 8 in Figure 1). Experimental data are shown as open circles, the best fits as solid lines. The structural models adopted in the fit are shown in (a') ( $2[\text{Cu}^{\text{I}}]^+$ , only one Cu ion of the pair showed here for clarity) and (b') ( $[\text{Cu}^{\text{II}}\text{-O-Cu}^{\text{II}}]^{2+}$ ). Atoms color code: Cu, green; Si, gray; Al, yellow; O, red. The atoms included in the fitting model are shown in bright colors. The entire structure of the models is reported in Figure S9a,b.

representation (see Figure 2, panel 1). Finally, the interaction involving the Cu–Cu path was not included in the fit, since the interatomic distance among the two  $\text{Cu}^{\text{I}}$  atoms in the  $2[\text{Cu}^{\text{I}}]^+$  DFT model is  $> 5.0 \text{ \AA}$ , that is, outside the limit of detectability of FT-EXAFS analysis for this case. Considering the EXAFS spectrum of Cu-MOR activated in  $\text{O}_2$  at  $500^\circ\text{C}$  after pre-reduction in  $\text{NH}_3$  at  $500^\circ\text{C}$ , the first-shell of the experimental FT-profile is successfully reproduced considering two sub-shell of O neighbors in the first-coordination sphere, involving framework ( $\text{O}_{\text{fw1}}$ ) and extraframework ( $\text{O}_{\text{efw}}$ , that is, involved in the formation of Cu-oxo species) O atoms. These two families of O atoms contribute in partial antiphase (see Figure S11) at  $1.93 \pm 0.02$  and  $1.97 \pm 0.02 \text{ \AA}$ , respectively. The second maximum of the FT-EXAFS is effectively modelled by the SS contribution of a single  $\text{T}_{\text{fw}}$  (Al) atom at a distance of  $2.68 \pm 0.01 \text{ \AA}$  from the Cu absorber. In the high- $R$  range, the contribution from farther framework O and Si atoms (fw) is observed too. Finally, a Cu–Cu contribution is refined at  $3.28 \pm 0.08 \text{ \AA}$  (ca.  $2.88 \text{ \AA}$  in the phase uncorrected FT-EXAFS plot), consistent with previous WT-EXAFS fitting results on oxidized Cu-MOR,<sup>[13]</sup> as well as conventional EXAFS fitting on Cu-CHA.<sup>[10,30]</sup> Based on a more symmetrical mono- $\mu$ -oxo dicopper site model, Sushkevich et al.<sup>[29]</sup> reported instead shorter Cu–Cu separations around  $2.85 \text{ \AA}$ , yet associated with minority Cu-species, as indicated by coordination numbers of ca. 0.3. Not surprisingly, our EXAFS analysis revealed a relatively high Debye–Waller factor associated with Cu–Cu scattering path, properly reflecting the broad intensity distribution observed for the Cu–Cu sub-lobe in the WT maps (Figure 2). The small deviation (ca.  $-0.02 \text{ \AA}$ ) of the fitted  $R_{\text{Cu}}$  from the DFT distance fully supports the choice of this structure for the EXAFS fitting refinement, in line with the occurrence of such type of  $[\text{Cu}^{\text{II}}\text{-O-Cu}^{\text{II}}]^{2+}$  cores as a dominant, although not exclusive, configuration under the adopted pretreatment conditions.

## Conclusion

In summary, a sample of Cu-mordenite was systematically treated with a broad set of gas-phase reactants to gain specific information on the influence of different redox-active molecules on Cu pairing. XAS was employed to simultaneously probe the oxidation state and the proximity of the Cu sites as a function of different redox treatments. In addition, the WT approach (augmented by the power density function analysis) was demonstrated being an irreplaceable tool toward the selective assessment of Cu–Cu contributions in the XAS dataset, showing a relation between the oxidation state of the metal center and the proximity of Cu sites. For the first time, the presence of Cu pairs was quantitatively correlated to the fraction of oxidized  $\text{Cu}^{\text{II}}$  sites present in the sample. DFT-assisted EXAFS fitting further allowed identifying the fingerprints of the Cu-oxo species formed after oxidative treatment as due to dimeric Cu–O–Cu sites (also confirmed by resonant Raman spectroscopy, see Figure S13). As multiple Cu sites have been proved to work cooperatively through the redox pathways that lead both to activation of the material and reaction with methane, reliably monitoring the specific

interactions between the metal sites is essential to understand the mechanism underlying these processes. In addition, exploring how different reactants interact with these materials help in identifying relationships between the activation protocol and the reaction performances. Exploring in a rational way the range of variability that characterizes these systems (topology, composition, reactants, temperatures) with tools capable to detect such specific features and trends will be the key to a better understanding of selective DMTM process, pointing toward ad hoc engineering of catalysts and reaction protocols that could maximize selectivity and productivity.

## Acknowledgements

The authors acknowledge funding from Horizon 2020 Excellence Science ERC-Synergy program 2019-CUBE: “Unravelling the secrets of Cu-based catalysts for C–H activation” (grant agreement No. 856446). This publication forms a part of the iCSI (industrial Catalysis Science and Innovation) Centre for Research-based Innovation, which receives financial support from the Research Council of Norway under Contract No. 237922. Access to the XAS facilities at the Elettra synchrotron was granted through proposal no. 20200065. We acknowledge the Sigma2 Norwegian High Performance Computing program (project no. NN4683K). The authors acknowledge Dr. Luca Olivi (XAFS beamline at Elettra Sincrotrone Trieste) for the support during measurements, A. Bellia for synthesizing the Cu-MOR sample, and Prof. G. Berlier and Dr. C. Negri for fruitful discussions. Open Access Funding provided by Università degli Studi di Torino within the CRUI-CARE Agreement.

## Conflict of Interest

The authors declare no conflict of interest.

**Keywords:** copper · EXAFS · methane-to-methanol conversion · mordenite · wavelet transform · XANES

- [1] “Hydrogen and Synthesis Gas by Steam- and CO<sub>2</sub> Reforming”: J. R. Rostrup-Nielsen, J. Sehested, J. Nørskov in *Advances in Catalysis*, Vol. 47, Academic Press, New York, 2002, pp. 65–139.
- [2] A. Holmen, *Catal. Today* **2009**, 142, 2–8.
- [3] W. Taifan, J. Baltrusaitis, *Appl. Catal. B* **2016**, 198, 525–547.
- [4] M. O. Ross, F. MacMillan, J. Wang, A. Nisthal, T. J. Lawton, B. D. Olafson, S. L. Mayo, A. C. Rosenzweig, B. M. Hoffman, *Science* **2019**, 364, 566–570.
- [5] B. Bissaro, Å. K. Røhr, G. Müller, P. Chylenski, M. Skaugen, Z. Forsberg, S. J. Horn, G. Vaaje-Kolstad, V. G. H. Eijssink, *Nat. Chem. Biol.* **2017**, 13, 1123–1128.
- [6] J. A. Hangasky, A. T. Iavarone, M. A. Marletta, *Proc. Natl. Acad. Sci.* **2018**, 115, 4915–4920.
- [7] M. Ravi, M. Ranocchiarri, J. A. van Bokhoven, *Angew. Chem. Int. Ed.* **2017**, 56, 16464–16483.
- [8] M. H. Groothaert, P. J. Smeets, B. F. Sels, P. A. Jacobs, R. A. Schoonheydt, *J. Am. Chem. Soc.* **2005**, 127, 1394–1395.
- [9] M. A. Newton, A. J. Knorpp, V. L. Sushkevich, D. Palagin, J. A. van Bokhoven, *Chem. Soc. Rev.* **2020**, 49, 1449–1486.
- [10] D. K. Pappas, E. Borfecchia, M. Dyballa, I. A. Pankin, K. A. Lomachenko, A. Martini, M. Signorile, S. Teketel, B. Arstad, G. Berlier, C. Lamberti, S. Bordiga, U. Olsbye, K. P. Lillerud, S. Svelle, P. Beato, *J. Am. Chem. Soc.* **2017**, 139, 14961–14975.
- [11] C. Paolucci, I. Khurana, A. A. Parekh, S. Li, A. J. Shih, H. Li, J. R. Di Iorio, J. D. Albarracin-Caballero, A. Yezerets, J. T. Miller, W. N. Delgass, F. H. Ribeiro, W. F. Schneider, R. Gounder, *Science* **2017**, 357, 898–903.
- [12] E. Borfecchia, K. A. Lomachenko, F. Giordano, H. Falsig, P. Beato, A. V. Soldatov, S. Bordiga, C. Lamberti, *Chem. Sci.* **2015**, 6, 548–563.
- [13] A. Martini, M. Signorile, C. Negri, K. Kvande, K. A. Lomachenko, S. Svelle, P. Beato, G. Berlier, E. Borfecchia, S. Bordiga, *Phys. Chem. Chem. Phys.* **2020**, 22, 18950–18963.
- [14] D. K. Pappas, A. Martini, M. Dyballa, K. Kvande, S. Teketel, K. A. Lomachenko, R. Baran, P. Glatzel, B. Arstad, G. Berlier, C. Lamberti, S. Bordiga, U. Olsbye, S. Svelle, P. Beato, E. Borfecchia, *J. Am. Chem. Soc.* **2018**, 140, 15270–15278.
- [15] P. Vanelderen, B. E. R. Snyder, M. L. R. G. Hadt, F. Vancanwenbergh, O. Coussens, R. A. Schoonheydt, B. F. Sels, E. I. Solomon, *J. Am. Chem. Soc.* **2015**, 137, 6383–6392.
- [16] M. L. Tsai, R. G. Hadt, P. Vanelderen, B. F. Sels, R. A. Schoonheydt, R. E. I. Solomon, *J. Am. Chem. Soc.* **2014**, 136, 3522–3529.
- [17] C. Buono, A. Martini, I. A. Pankin, D. K. Pappas, C. Negri, K. Kvande, K. A. Lomachenko, E. Borfecchia, *Radiat. Phys. Chem.* **2020**, 175, 108111.
- [18] F. Giordano, E. Borfecchia, K. A. Lomachenko, A. Lazzarini, G. Agostini, E. Gallo, A. V. Soldatov, P. Beato, S. Bordiga, C. Lamberti, *J. Phys. Chem. Lett.* **2014**, 5, 1552–1559.
- [19] M. A. Newton, A. J. Knorpp, A. B. Pinar, V. L. Sushkevich, D. Palagin, J. A. van Bokhoven, *J. Am. Chem. Soc.* **2018**, 140, 10090–10093.
- [20] I. A. Pankin, A. Martini, K. A. Lomachenko, A. V. Soldatov, S. Bordiga, E. Borfecchia, *Catal. Today* **2020**, 345, 125–135.
- [21] E. M. C. Alayon, M. Nachttegaal, A. Bodi, M. Ranocchiarri, J. A. van Bokhoven, *Phys. Chem. Chem. Phys.* **2015**, 17, 7681–7693.
- [22] G. Turnes Palomino, P. Fiscaro, S. Bordiga, A. Zecchina, V. Giuria, E. Giamello, C. Lamberti, *J. Phys. Chem. B* **2000**, 104, 4064–4073.
- [23] V. L. Sushkevich, J. A. van Bokhoven, *Chem. Commun.* **2018**, 54, 7447–7450.
- [24] A. Martini, E. Borfecchia, *Crystals* **2020**, 10, 664.
- [25] M. Fernandez-Garcia, C. Marquez Alvarez, G. L. Haller, *J. Phys. Chem.* **1995**, 99, 12565–12569.
- [26] S. Beauchemin, D. Hesterberg, M. Beauchemin, *Soil Sci. Soc. Am. J.* **2002**, 66, 83–91.
- [27] A. Martini, S. A. Guda, A. A. Guda, G. Smolentsev, A. Algasov, O. Usoltsev, M. A. Soldatov, A. Bugaev, Y. Rusalev, C. Lamberti, A. V. Soldatov, *Algorithms. Comput. Phys. Commun.* **2020**, 250, 107064.
- [28] S. Calvin, *XAFS for Everyone*, 1<sup>st</sup> ed., CRC, Boca Raton, **2013**.
- [29] V. L. Sushkevich, O. V. Safonova, D. Palagin, M. A. Newton, J. A. van Bokhoven, *Chem. Sci.* **2020**, 11, 5299–5312.
- [30] C. Negri, T. Sella, E. Borfecchia, A. Martini, K. A. Lomachenko, T. V. W. Janssens, M. Cutini, S. Bordiga, G. Berlier, *J. Am. Chem. Soc.* **2020**, 142, 15884–15896.
- [31] H. Funke, M. Chukalina, A. C. A. Scheinost, *J. Synchrotron Radiat.* **2007**, 14, 426–432.
- [32] A. Martini, E. Borfecchia, K. A. Lomachenko, I. A. Pankin, C. Negri, G. Berlier, P. Beato, H. Falsig, S. Bordiga, C. Lamberti, *Chem. Sci.* **2017**, 8, 6836–6851.

Manuscript received: July 20, 2021

Accepted manuscript online: September 28, 2021

Version of record online: November 2, 2021

# Appendix A3

# Titration of Cu(I) Sites in Cu-ZSM-5 by Volumetric CO Adsorption

Gabriele Deplano, Matteo Signorile,\* Valentina Crocellà, Natale Gabriele Porcaro, Cesare Atzori, Bjørn Gading Solemsli, Stian Svelle, and Silvia Bordiga\*



Cite This: *ACS Appl. Mater. Interfaces* 2022, 14, 21059–21068



Read Online

ACCESS |



Metrics & More



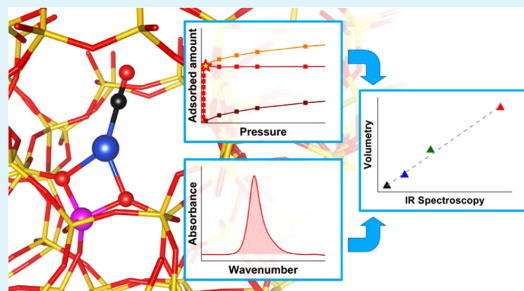
Article Recommendations



Supporting Information

**ABSTRACT:** Cu-exchanged zeolites are widely studied materials because of their importance in industrial energetic and environmental processes. Cu redox speciation lies at the center of many of these processes but is experimentally difficult to investigate in a quantitative manner with regular laboratory equipment. This work presents a novel technique for this purpose that exploits the selective adsorption of CO over accessible Cu(I) sites to quantify them. In particular, isothermal volumetric adsorption measurements are performed at 50 °C on a series of opportunely pre-reduced Cu-ZSM-5 to assess the relative fraction of Cu(I); the setup is fairly simple and only requires a regular volumetric adsorption apparatus to perform the actual measurement. Repeatability tests are carried out on the measurement and activation protocols to assess the precision of the technique, and the relative standard deviation (RSD) obtained is less than 5%. Based on the results obtained for these materials, the same CO adsorption protocol is studied for the sample using infrared spectroscopy, and a good correlation is found between the results of the volumetric measurements and the absorbance of the peak assigned to the Cu(I)–CO adducts. A linear model is built for this correlation, and the molar attenuation coefficient is obtained, allowing for spectrophotometric quantification. The good sensitivity of the spectrophotometric approach and the precision and simplicity of the volumetric approach form a complementary set of tools to quantitatively study Cu redox speciation in these materials at the laboratory scale, allowing for a wide range of Cu compositions to be accurately investigated.

**KEYWORDS:** Cu-ZSM-5, zeolites, redox speciation, Cu(I) titration, carbon monoxide, adsorption volumetry, Cu(I) monocarbonyls



## 1. INTRODUCTION

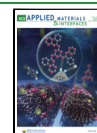
Cu-exchanged zeolites have received increasing attention in the last decades for their performance as heterogeneous redox catalysts. The ability of these materials to perform environmentally and industrially crucial reactions, like NH<sub>3</sub>-mediated selective catalytic reduction (SCR) for NO<sub>x</sub> abatement<sup>1</sup> and direct conversion of methane to methanol (DMTM),<sup>2</sup> led the scientific community to study the mechanisms underlying the peculiar reactivities involved; moreover, the peculiar structural properties of Cu zeolites impart astounding selectivities to these catalysts,<sup>2</sup> thus encouraging the development of new porous materials also featuring enhanced productivity (e.g., Cu-MOFs).<sup>3–5</sup> Studying these materials under conditions that are relevant to the reaction they perform is, however, a very difficult task, and many experimental and computational techniques have been exploited in the years to tackle this problem.<sup>6–17</sup> In particular, the assessment of the oxidation state of the Cu in these materials is of paramount importance, as the Cu(I)/Cu(II) cycle lies at the base of both NH<sub>3</sub>-SCR and DMTM reactions. The techniques that are most frequently applied for this investigation are electronic spectroscopies, such as diffuse reflectance (DR) UV–vis spectroscopy and X-ray absorption spectroscopy (XAS); however, only the latter is

applicable for quantitative studies as in the case of UV–vis the molar attenuation coefficient of the species is unknown. Although XAS is currently the gold standard for quantitative Cu redox speciation analysis in these materials,<sup>18</sup> performing the experiment calls for exploiting large-scale facilities, making it costly, time-consuming, and effectively limiting a thorough understanding of this variable when access to a synchrotron is not feasible. Moreover, quantitative XAS analysis introduces further issues: for example, widely used methods like linear combination fit (LCF) need the spectra of the pure species as input, which are very difficult to obtain for these materials. In this work, the development and validation of a quantitative technique to monitor the amount of Cu(I) based on the selective interaction of CO with Cu(I) in the zeolite framework is presented. By exploiting volumetric isothermal

Received: February 24, 2022

Accepted: April 18, 2022

Published: April 28, 2022



adsorption of CO on a series of Cu-ZSM-5 materials, the amount of accessible Cu(I) after a reductive treatment is assessed with a laboratory adsorption apparatus; furthermore, repeatability tests are carried out to measure the precision of the technique, both in terms of the uncertainty due to the instrumental measurement itself and the one introduced by the pretreatment procedure. The results are used to calculate the molar attenuation coefficient of the IR fingerprint of the Cu(I)-CO adducts, to allow for semiquantitative IR studies in the same context. Other indirect techniques are available for studying Cu(II)/Cu(I) speciation; one of the most frequently used, especially in studies concerning NH<sub>3</sub>-SCR, is temperature-programmed reduction (TPR) with a mixture of NH<sub>3</sub> and NO.<sup>19,20</sup> This technique has been successfully applied to titrate the amount of Cu(II) in Cu zeolites, and is thus complementary to the ones proposed herein that aim at titrating Cu(I) sites. When performing NH<sub>3</sub>-NO TPR, the Cu(I) fraction is usually retrieved via mass balance, supposing that no other oxidation states are present other than Cu(I) and Cu(II). In this context, the approach developed in this work has several advantages. First of all, it allows directly measuring the amount of Cu(I), avoiding mass balance in cases where other oxidation states may be present (e.g., Cu(0)); moreover, it can be coupled with NH<sub>3</sub>-NO TPR to retrieve the possible fraction of Cu that is present in states other than Cu(II) and Cu(I) via mass balance. Another advantage of the proposed techniques is the relative ease of use, both in terms of operating conditions (e.g., near-room-temperature measurements) and required instrumentation (adsorption apparatus and/or IR spectrophotometer). Chemisorption of probe molecules and IR spectroscopy have been extensively applied for studying Cu speciation in Cu zeolites,<sup>21–23</sup> and a recent contribution from Xie et al. applies a complementary experimental and theoretical study to find key indicators for the formation of Cu dimers in Cu-ZSM-5 materials and their relationship with catalytic activity.<sup>24</sup>

The choice of Cu-ZSM-5 materials for this study was based on two main reasons: (i) sharp and narrow IR bands associated with the Cu(I)-CO<sub>x</sub> adducts, due to the homogeneity of the environment surrounding Cu species in ZSM-5, (ii) full accessibility of the cations by the probe molecule as all of the substitutional positions for cations are exposed in the channels in the MFI framework. Evidence from IR spectroscopy clearly suggests an irreversible, species-selective chemisorption of CO on Cu(I) sites at 50 °C and at a pressure < 10<sup>-3</sup> mbar. On the basis of previous reports<sup>9,27</sup> and as further supported by density functional theory (DFT) investigation reported herein, the stable species are Cu(I) monocarbonyls; thus, the amount of irreversibly adsorbed CO directly titrates the fraction of Cu(I) in the zeolite host. A quantitative approach was developed based on these observations, with the aim of producing an accurate and precise technique for Cu redox speciation studies in these materials.

The same approach could be applied to Cu zeolites belonging to different framework types, obtaining analogous results. However, different topologies are characterized by a less homogeneous environment of Cu species that cause the formation of slightly different Cu-CO<sub>x</sub> adducts, implying larger bandwidths and small shifts in the band position.<sup>25–29</sup> Moreover, in the case of some topologies, Cu location can hamper the accessibility of some Cu species that are consequently hardly probed by CO. Examples are the cations

located inside the sodalite cavities in FAU or LTA<sup>30–35</sup> or in the side pockets of MOR.<sup>36,37</sup>

## 2. EXPERIMENTAL SECTION

**2.1. Materials.** Two commercial ZSM-5 samples were used for this study: CBV 2314 (Zeolyst International, Si/Al ratio: 11.5, nominal cation form: ammonium, Na<sub>2</sub>O weight %: 0.05, data from producer) and CBV 5524G (Zeolyst International, Si/Al ratio: 25, nominal cation form: ammonium, Na<sub>2</sub>O weight %: 0.05, data from producer). Initially, the NH<sub>4</sub>-ZSM-5 samples were exchanged by a 1 M NH<sub>4</sub>NO<sub>3</sub> solution at 70 °C for 6 h, to obtain the sample in a purely ammonium form. The exchange procedure was repeated three times, supplying fresh NH<sub>4</sub>NO<sub>3</sub> solution at each stage. At the end of the third repetition, the sample was washed with abundant distilled water and dried at 70 °C for 2 h. Finally, the amount of Cu(II) acetate monohydrate (Sigma-Aldrich, 99.99%) required to obtain a concentration of 1 and 20 mM (for lower and higher Cu loadings, respectively) was dissolved in water and the ammonium form of the zeolite was added to the solution (250 mL per zeolite gram). The mixture was stirred at room temperature for 48 h and then the obtained Cu zeolite was filtered and washed. The procedure was repeated twice for selected samples, to approach stoichiometric exchange (Cu/Al = 0.5). Finally, the exchanged zeolite as recovered by filtration was dried at 100 °C overnight and calcined at 550 °C for 5 h to remove the residual acetate. In all cases, the solution was buffered with acetic acid in the 4–5 pH range, to avoid the formation of extraframework CuO<sub>x</sub> species. The Cu loading of the materials, expressed as Cu/Al ratios, was evaluated by inductively coupled plasma optical emission spectroscopy (ICP-OES): the composition of the obtained materials is summarized in Table 1.

**Table 1. List of Cu Zeolites Used in This Work<sup>a</sup>**

name	Si/Al <sup>b</sup>	Cu/Al <sup>b</sup>
(0.07)Cu-MFI(11.5)	11.5	0.07
(0.35)Cu-MFI(11.5)	11.5	0.35
(0.45)Cu-MFI(11.5)	11.5	0.45 <sup>c</sup>
(0.05)Cu-MFI(25)	25	0.05
(0.48)Cu-MFI(25)	25	0.48 <sup>c</sup>

<sup>a</sup>(a) Si/Al ratio supplied by the producer (Zeolyst International). (b) Cu/Al ratios measured by ICP-OES. All Si/Al and Cu/Al are reported as molar ratios. (c) Exchange procedure repeated twice.

**2.2. Methods.** Carbon monoxide (supplied by Sapio SRL, 99.99998% purity grade) adsorption isotherms were measured on a commercial volumetric apparatus (Micromeritics ASAP 2020, Norcross GA) at 50 °C. This specific temperature was selected since it is estimated for a sample exposed to an IR beam during an IR experiment, where precise Cu-carbonyl stability is expected (vide infra). The samples were ground in a mortar and pelleted, to prevent any powder residues from moving out of the cell while exposed to gas/vacuum treatment. The pellets were then inserted in a custom adsorption cell (Figure S1) consisting of a quartz burette with connections that allow for vacuum and thermochemical treatment; the cell is equipped with a plug-in thermal jacket for measurements in thermostatic fluid.<sup>38</sup> The sample temperature was kept constant using an external isothermal liquid bath (Julabo F25-EH). Prior to the measurements, Cu zeolite pellets were treated at a high temperature on a vacuum line equipped with a turbomolecular pump; full details on the treatment can be found in the next section. The sample is usually measured in the form of pellet fragments, to avoid possible damage to the instrumentation; depending on the amount of sample and cell volume, the finer part of a powder could escape the cell if the pressure is abruptly changed (e.g., if evacuating starting from a high pressure). If the measurement strictly needs to be performed on a powder (e.g., if there is proof that the form of the sample may influence the composition, or if it is directly sampled out of a catalytic bed), the instrumental parameters can be tuned to perform safe

experiments; for instance, the outgassing can be performed with smaller, more frequent steps.

Transmission IR spectra were acquired using an Invenio R spectrophotometer from Bruker, equipped with a mercury cadmium telluride (MCT) cryodetector, a resolution of  $2\text{ cm}^{-1}$  and averaging 32 scans (64 for background spectrum, collected with an empty measurement chamber). The samples were sieved and pressed into self-supporting pellets, placed in a gold envelope, and inserted in a quartz cell equipped with KBr windows (optical path: 2 mm); to be able to calculate the molar attenuation coefficients, the area and the weight of the pellets were measured. For transmission IR spectrophotometry, the sample needs to be pressed into a pellet form to guarantee uniform thickness and to minimize scattering effects; this implies that samples in powder form cannot be measured as such by employing this technique.

**2.3. Activation Protocol.** For the coupled IR/volumetry experiments on all samples, the activation protocol was performed as follows. The sample cell was heated from room temperature to  $550\text{ }^\circ\text{C}$  with a ramp of  $5\text{ }^\circ\text{C}/\text{min}$  in dynamical vacuum.  $\text{O}_2$  (100 mbar) was then dosed and kept in contact with the sample at the same temperature for 30 min. The sample was then outgassed at the same temperature for 40 min. Under these conditions, most of the Cu in the samples was converted to Cu(II), as suggested by the almost absent (within the detection limit of conventional XANES)  $1s > 4p$  transition due to Cu(I) (8983 eV) in the XAS spectrum of the material (see Figure S2). Then, a controlled  $\text{NH}_3$  treatment was performed to maximize the amount of Cu(I). Previous data showed that prolonged treatment in  $\text{NH}_3$  at a high temperature (i.e.,  $500\text{ }^\circ\text{C}$ ) can reduce 75–90% of the total Cu to Cu(I).<sup>39</sup> This result is qualitatively supported by XANES data collected for the (0.45)Cu-MFI(11.5) sample (Figure S2). Accordingly, 100 mbar of  $\text{NH}_3$  was dosed on the sample at  $550\text{ }^\circ\text{C}$  for 30 min. Finally, outgassing was performed at the same temperature until a residual pressure of  $5 \times 10^{-4}$  mbar was achieved, then the sample was cooled down to room temperature. This procedure aimed to maximize the amount of highly uncoordinated Cu(I) that would have been probed by CO.

For both repeatability tests, the activation protocol was performed as follows. The sample was heated from room temperature to  $500\text{ }^\circ\text{C}$  with a ramp of  $5\text{ }^\circ\text{C}/\text{min}$  in dynamical vacuum.  $\text{O}_2$  was then dosed and kept in contact with the sample at the same temperature for 1 h. The sample was then outgassed at the same temperature for 40 min.  $\text{NH}_3$  was dosed on the sample at  $500\text{ }^\circ\text{C}$  for 1 h. Finally, outgassing was performed at the same temperature for 1 h and the sample was cooled down to room temperature. The only difference between the two activation protocols was the partial pressure of the gases (300 vs 100 mbar) to take into account the different amounts of sample used (ca. 300 vs 80 mg per replica).

**2.4. Computational Details.** The (co-)adsorption of CO and  $\text{NH}_3$  on Cu-ZSM-5 was simulated at the DFT level of theory by means of the CRYSTAL17 periodic code.<sup>40</sup> ZSM-5 models and computational parameters were adapted from the previous report by Morra et al.<sup>41</sup> In brief, Cu(I) substitution was investigated at three different sites, i.e., those with Al occupying the T7, T8, and T10 tetrahedral positions in the MFI framework. The Al siting has been chosen on the basis of occupancies experimentally obtained by X-ray diffraction (XRD) on Cs-ZSM-5 samples.<sup>42</sup> The calculations were carried out with the hybrid GGA B3LYP functional.<sup>43,44</sup> Dispersive interaction has been included empirically through the Grimme D3 scheme.<sup>45</sup> Concerning the basis set, the framework atoms have been described through a double- $\zeta$  quality basis set; in detail, the basis set proposed by Nada and co-workers was adopted for Si and O atoms,<sup>46</sup> whereas the Al was described with the basis set from Catti et al.;<sup>47</sup> such choice provides a good description of zeolitic frameworks at a reasonable computational cost.<sup>41,48–50</sup> Concerning the extraframework Cu cations, as well as atoms of sorbed molecules, these have been described through the Ahlrichs TZVP basis.<sup>51</sup> The truncations for the mono- and bielectronic integral (TOLINTEG) were set to {7 7 7 25}. The sampling in the reciprocal space (SHRINK) was set to {2 2}, for a total of 8 k points. The maximum order of shell multipoles in the long-range zone for the electron–electron Coulomb interaction

(POLEORDR keyword) was chosen to be 6. All of the other parameters were set to default values according to the CRYSTAL17 manual.<sup>52</sup>

Each Cu(I) model was geometry optimized and, upon screening, T10 was revealed to be significantly more stable than T7/T8, accounting for 99% of the substituted sites on a Boltzmann population basis. Accordingly, the adsorption processes were simulated only for the T10 site. Molecular adducts were manually built and further optimized. The following adducts were considered: Cu(I)(CO), Cu(I)(CO)<sub>2</sub>, Cu(I)(NH<sub>3</sub>), and Cu(I)(NH<sub>3</sub>)(CO). The main geometrical parameters for each structure are given in Table S1. To evaluate the vibrational properties and the thermodynamic functions describing the Cu adducts (enthalpies and Gibbs free energies), harmonic frequencies were computed for a subset of atoms including the Cu(I) cation; the sorbed molecule(s); and the Al framework atom and its neighbors up to the second coordination shell (namely, 4 O and 4 Si atoms).

The variation of electronic energy ( $\Delta E$ ), enthalpy ( $\Delta H$ ), and Gibbs free energy ( $\Delta G$ ) associated with the formation of an adduct, evaluated under experimentally relevant  $p$ ,  $T$  conditions, were computed as follows

$$\Delta X = \sum X_{\text{products}} - \sum X_{\text{reagents}}, \text{ with } X = E, H \text{ or } G$$

The relevant processes for which formation/dissociation energetics have been computed, selected on the basis of experimental evidence, are summarized in Table 2.

**Table 2. Relevant Processes of Cu(I) Adduct Formation/Dissociation Investigated by DFT**

#		process
1	Cu(I)(CO) formation	$\text{ZCu(I)} + \text{CO} \rightarrow \text{ZCu(I)(CO)}$
2	Cu(I)(CO) <sub>2</sub> formation	$\text{ZCu(I)(CO)} + \text{CO} \rightarrow \text{ZCu(I)(CO)}_2$
3	Cu(I)(NH <sub>3</sub> ) formation	$\text{ZCu(I)} + \text{NH}_3 \rightarrow \text{ZCu(I)(NH}_3)$
4	Cu(I)(CO)(NH <sub>3</sub> ) formation	$\text{ZCu(I)(NH}_3) + \text{CO} \rightarrow \text{ZCu(I)(CO)(NH}_3)$

### 3. RESULTS AND DISCUSSION

**3.1. CO Adsorption on Cu Zeolites.** Detailed characterization of the interaction of CO with Cu-exchanged zeolites has been available for more than 20 years.<sup>9,27,53,54</sup> In particular, IR and X-ray spectroscopies highlight how the interaction of CO with Cu(I) sites is heavily dependent on the temperature and the partial pressure of CO, while interaction with Cu(II) is generally negligible at ambient conditions. At  $50\text{ }^\circ\text{C}$ , and generally near room temperature, increasing pressures of CO favor the formation of Cu(I)CO and Cu(I)(CO)<sub>2</sub> adducts in a subsequent manner, as is evident from IR spectra of CO dosed on a pre-reduced material (Figure 1). For Cu-ZSM-5 materials, as already reported in the literature, an absorption band is first formed at  $2157\text{ cm}^{-1}$  corresponding to the CO stretching frequency in the Cu-monocarbonyl adducts; when pressure is increased, this band starts decreasing in intensity in correspondence with the appearance of two bands at  $2178$  and  $2151\text{ cm}^{-1}$ , assigned to the symmetric and antisymmetric stretching of the CO molecules in Cu-dicarbonyl adducts (along with the rotovibrational profile of the CO in the gaseous phase) (Figure 1a).<sup>54</sup> An additional weak band can be noticed at  $2108\text{ cm}^{-1}$  when the CO is first dosed and when the sample is outgassed: this has been assigned to the stretching mode of Cu(I)<sup>13</sup>CO adducts, based on the relative intensity and position of this band (matching the expected isotopic shift,



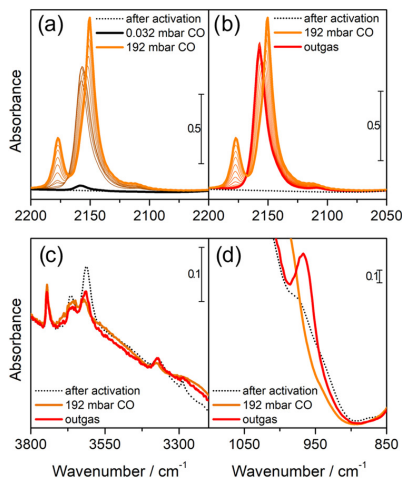


**Figure 1.** Interaction of CO over the pre-reduced (0.35)Cu-MFI(11.5) sample. (a) Effect of increasing pressure of CO (from black to orange). (b) Effect of outgassing of the sample exposed to 192 mbar of CO (from orange to red). (c) Effect of CO on the OH stretching modes. (d) Effect of CO on the perturbation of framework modes by Cu.

as estimated via harmonic oscillator model, of  $-48\text{ cm}^{-1}$ ) with respect to the  $\text{Cu(I)}^{12}\text{CO}$  one.<sup>55–58</sup> The spectra are very well defined with bands characterized by a small bandwidth, very similar to what would be expected in the case of a homogeneous complex. This suggests the formation of uniform complexes characterized by a very similar structure.<sup>53</sup> If the sample is evacuated, the trend is reversed and the single band corresponding to the Cu-monocarbonyls is restored (Figure 1b); thanks to the depletion of Cu dicarbonyls, the intensity of the monocarbonyls band reaches its maximum intensity. Further evacuation does not change the band intensity even at long time scales (several hours), suggesting an irreversible interaction between the Cu(I) and the adsorbed CO.

The high stability of the  $\text{Cu(I)CO}$ , together with its unusually high CO stretching frequencies have been explained in terms of  $\text{Cu(I)CO}$  bonds where electrostatic and  $\sigma$ -donative covalent contributions are predominant, as well as contribution from  $\pi$ -back-donation.<sup>29</sup>

After activation, the material presents three main peaks in the  $3800\text{--}3500\text{ cm}^{-1}$  region (Figure 1c), assigned, respectively, to the O–H stretching modes of isolated silanols on the surface ( $3745\text{ cm}^{-1}$ ), partial extraframework AlOH species ( $3664\text{ cm}^{-1}$ ), and Al(OH)Si Brønsted sites ( $3610\text{ cm}^{-1}$ ).<sup>59,60</sup> Upon CO dosages at room temperature, we do not expect any erosion of the Brønsted sites, due to the low proton affinity of the probe;<sup>61</sup> conversely, as soon as CO is introduced, both signals associated with the stronger acidic protons (i.e., AlOH and Al(OH)Si) are partially consumed. This unexpected fact can be explained considering the presence of traces of  $\text{NH}_3$  coordinated to Cu sites, that are displaced once CO is admitted in the cell and can further react with the acidic proton sites and form some  $\text{NH}_4^+$  species. The formation of  $\text{NH}_4^+$  explains the decrease in intensity of the band peaked at ca.  $3300\text{ cm}^{-1}$  (assigned to a N–H stretching of residual  $\text{NH}_3$ ), as well as the growth of broad bands centered at  $2963$ ,  $2800$ , and  $2598\text{ cm}^{-1}$  and the peak at  $1450\text{ cm}^{-1}$ , due to the

ammonium bending mode<sup>62</sup> (Figure S3). A direct interaction of CO with the Brønsted acid sites is thus excluded, based on the absence of any characteristic peak associated with this adduct ( $1169\text{--}1175\text{ cm}^{-1}$ ); furthermore, the literature agrees that this interaction is only present at significantly lower temperatures (e.g., liquid  $\text{N}_2$  temperature).<sup>63</sup> The displacement of  $\text{NH}_3$  from Cu sites appears quantitative upon CO dosage; thus, the residual fraction of coordinated ammonia is not affecting the Cu(I) titration by CO.

This vision is further confirmed by inspecting the  $1050\text{--}850\text{ cm}^{-1}$  zone of the IR spectra (Figure 1d): for Cu-exchanged zeolites in which the cation can interact strongly with the framework (i.e., it is barely screened by ligands) the appearance of one or more peaks associated to the cation-perturbed framework modes is expected.<sup>53</sup> As can be seen, only a small absorption at  $979\text{ cm}^{-1}$  is present after activation; when a high pressure of CO is introduced, this shoulder disappears, and a stronger and sharper contribution appears at  $967\text{ cm}^{-1}$  after the sample is outgassed. This is consistent with an initial coordination of Cu by  $\text{NH}_3$  molecules that are readily displaced by CO, which coordinates the Cu sites upon increasing pressure as Cu dicarbonyls; when the sample is outgassed, the Cu(I) reverts to stable monocarbonyl complexes without further coordination by  $\text{NH}_3$  (suggested by the appearance of the strong peak at  $967\text{ cm}^{-1}$  and the fact that the Brønsted protons in the high-frequency zone do not recover their initial intensity).

A similar trend was observed in all of the samples, apart from the appearance of an additional component at  $2133\text{ cm}^{-1}$  when CO pressure is increased, mainly visible in the case of the (0.48)Cu-MFI(25) material. This peak has been assigned to a mixed ligand  $[\text{Cu}(\text{NH}_3)(\text{CO})]^+$  complex,<sup>53</sup> testifying that for this sample, the removal of  $\text{NH}_3$  was less effective (Figures S4 and S5). However, the presence of some  $\text{NH}_3$  does not invalidate the measurement with CO, due to the stronger interaction of CO that displaces  $\text{NH}_3$ . For the sake of completeness, the data obtained on this sample are reported in the supporting.

**3.2. Description of Volumetric Methodology and Validation.** Based on the phenomenon described above, isothermal volumetric adsorption measurements of CO at  $50\text{ }^\circ\text{C}$  (i.e., the temperature of the sample under the IR beam) can be exploited to quantify the amount of Cu(I) accessible by this gaseous probe. The procedure works as follows. A primary CO adsorption isotherm is collected for the treated sample: when the gas is dosed, the probe is adsorbed on the Cu sites with a species distribution dictated by the pressure (as detected by IR spectroscopy). When a plateau is reached, most of the CO is adsorbed on Cu(I) sites as dicarbonyls; upon evacuation, these revert to Cu(I) monocarbonyls; thus, only the fraction of irreversibly adsorbed CO is retained. Subsequently, a secondary CO adsorption isotherm is collected; since the Cu(I) sites are already bonding a CO molecule each, the secondary isotherm only accounts for the reversible CO fraction (i.e., Cu dicarbonyls). By subtracting the two isotherms, the value at the elbow point represents the amount of CO irreversibly bound to the catalyst (in mmol/g); since the composition of the catalyst is known and the irreversibly bound CO is in a 1:1 ratio with the Cu(I) sites, the percentage of Cu(I) over the total amount of Cu can be easily calculated. An example of this measurement for a Cu-ZSM-5 sample is shown in Figure 2. The complete dataset of isotherms for all considered materials is reported in Figure S6.

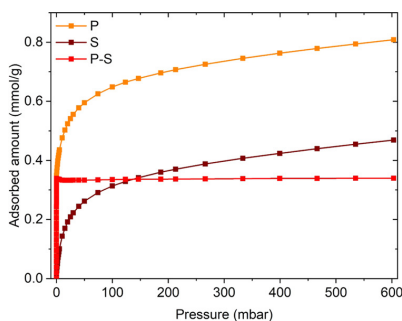


**Figure 2.** CO adsorption isotherms performed at 50 °C on the pre-reduced (0.35)Cu-MFI(11.5) sample. Orange: primary isotherm (P); brown: secondary isotherm (S); red: difference between the primary and secondary isotherm (P–S), used to calculate the amount of irreversibly bound CO.

The concentration of reduced Cu detected by the volumetric technique is in line with XAS results (see Figure S2), so repeatability tests were performed to assess the precision of this method for quantitative purposes; the (0.35)Cu-MFI(11.5) material was used for all of these tests. Two main sources of uncertainty for this technique were identified, being the uncertainty intrinsic to the volumetric measurement itself and the one associated with the treatment procedure, and two separate sets of experiments were devised to calculate them.

Since errors associated with the pretreatment were estimated to be higher than the ones related to the measurement itself, all possible interferences from the activation procedure were excluded for the first step. This was done by activating a large batch of the sample and storing it in an Ar-filled glovebox (residual O<sub>2</sub> and H<sub>2</sub>O concentrations < 0.5 ppm); an adequate portion of this identical sample was taken time after time for three replica measurements, which were compared to check instrumental repeatability. The results are summarized in Table 3.

**Table 3. Results of the Instrumental Repeatability Tests on the (0.35)Cu-MFI(11.5) Sample**

replica	irreversibly adsorbed CO (mmol/g)	Cu(I) concentration (%)
1	0.3389	75.2
2	0.3231	71.7
3	0.3110	69.0

As can be noticed, the amount of adsorbed CO shows a decreasing trend in time, which is reflected in the Cu(I) concentration. Each measurement can take up to 24 h, so this decrease could be ascribed to small amounts of pollutants inside the glovebox. For instance, very small amounts of water inside the inert environment could potentially lead to Cu(I) oxidation to Cu(II) over long periods of time, as has been already reported in the literature.<sup>64</sup> It has been also shown that introducing H<sub>2</sub>O in such materials when CO is interacting with Cu(I) (i.e., when monocarbonyls are present) can lead to mixed ligand H<sub>2</sub>O/CO adduct,<sup>53</sup> which are, however, reversible in vacuum and do not seem to be able to oxidize Cu(I). Regardless of the source of the pollution, it has to be stressed that under normal operating conditions (i.e., not in conditions similar to this test, in which a sensitive sample has been stocked for a long time because of the way the

experiment had to be performed), the sample is measured in the same cell in which it is activated, and so possible pollutants are unlikely to reach the material during transfer from the vacuum line to the instrument. It should also be noted that the standard measurement procedure does not include any transfer in the glovebox, so this particular interference is not an issue for the actual measurements. The calculated RSD of the results from this test is 4.3%, although if a systematic error is present in this case due to sample pollution over time, this may not be an accurate indicator for measurement uncertainty. Nonetheless, the sources of uncertainty strictly related to the measurement procedure should include instrumental parameters that are set or measured by the instrument. In particular, supposing repeated measurements on samples that have the same exact composition (in terms of Cu(I) amount), errors can arise from weighing the sample in the cell (as well as the empty cell before the sample is introduced), dosing and measuring the gas pressure (done automatically by the volumetric instrument), equilibration times, small drifts in the isothermal bath and other similar effects. Overall, each of these sources of uncertainty is reported and certified for the instruments (balances, volumetric apparatus, thermocouples, etc.) and can, in principle, be used to calculate a total measurement-related uncertainty through the propagation of error. The actual value for this kind of uncertainty will depend on the specific instruments adopted, and it is outside the scope of this work to extensively discuss these aspects.

The uncertainty associated with the treatment was subsequently calculated; the procedure involved the activation and measurements of three separate replicas of the same sample that were prepared and measured one after the other in separate cells. The results are reported in Table 4.

**Table 4. Results of the Treatment Repeatability Tests on the (0.35)Cu-MFI(11.5) Sample**

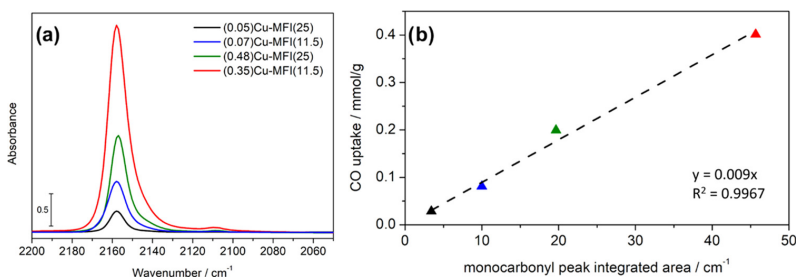
replica	irreversibly adsorbed CO (mmol/g)	Cu(I) concentration (%)
1	0.4123	91.5
2	0.4115	91.4
3	0.3801	84.4

As expected, the uncertainty related to the treatment is slightly higher (relative standard deviation: 4.58%); this can be ascribed to small differences in the activation procedure such as gas pressures not being exactly the same, slight differences in the temperature and exposition time, different times between disconnecting the cell from the vacuum lines and connecting it to the volumetric apparatus, and so on. Overall, though the error is not very high, it is advisable to operate in replicas when possible. The higher Cu(I) content detected by this experiment compared to the previous one can be ascribed to different effects, namely, (i) the overall simpler and shorter procedure, (ii) the smaller volume of the cell, and (iii) the lower amount of pelletized sample. It should be noted, however, that both of these experiments aimed at assessing the repeatability of their respective step of the procedure, i.e., calculating the variance of the different replicas; differences in the mean value for the two experiments are thus expected, as the procedure for the two experiments is different.

**3.3. Insights from Periodic DFT Calculations.** Table 5 lists the energetic values obtained for the formation of simulated adducts from DFT calculations.

**Table 5.**  $\Delta E$ ,  $\Delta H$ , and  $\Delta G$  Values (in kJ/mol) Computed for the Formation of Cu(I)-CO/NH<sub>3</sub> Adducts Listed in Table 2 ( $T = 50\text{ }^{\circ}\text{C}$ )

adduct #	$\Delta E$	$\Delta H$		$\Delta G$	
		$p = 0.001\text{ mbar}$	$p = 100\text{ mbar}$	$p = 0.001\text{ mbar}$	$p = 100\text{ mbar}$
1	-169.3	-163.1	-163.1	-80.3	-111.2
2	-65.8	-72.5	-63.6	12.2	-9.9
3	-203.2	-192.9	-192.9	-107.6	-138.5
4	-81.3	-78.8	-78.8	6.6	-24.3

**Figure 3.** CO adsorbed on the four reference Cu-ZSM-5 samples. (a) IR spectra of the samples after interaction with 200 mbar CO and outgassing (spectra have been normalized, and the spectrum of material prior to CO dosage has been subtracted). (b) Uptake of irreversibly bound CO on the samples versus integrated area of the Cu(I) monocarbonyl species. The intercept has been fixed to 0.

All of the adsorption events simulated here do not cause any significant deformation of the MFI framework, as testified by the negligible modification of the cell parameters and, consequently, of the cell volume; the local surrounding of Cu(I) is, instead, significantly affected (see Figures S7, S8 and Table S1). The subsequent adsorption of two CO molecules brings the Cu(I) from its original bipodal coordination to the framework O atoms toward a quasi-tetrahedral coordination environment, passing through a planar, triligated structure upon the adsorption of a single CO molecule.<sup>65</sup> The adsorption of a NH<sub>3</sub> molecule induces an even more severe deformation, with Cu(I) coordinated in an almost linear geometry between a single-framework O and the adsorbed molecule, as already proposed for other Cu-CHA during NH<sub>3</sub>-temperature programmed desorption (TPD) experiments.<sup>17</sup> By adsorbing a further CO molecule, the coordination turns back to a more regular quasi-tetrahedral environment. Thermodynamic functions were evaluated at conditions relevant for the sake of experiments interpretation, i.e., at a temperature of 50 °C and at values of pressure representative for a complete adsorption (100 mbar) and for a full desorption of reversible fractions (0.001 mbar). Overall, all of the simulated processes are exothermic, with a large dependence of the evolved heat on the number of coordinated molecules (i.e., significantly lower in the event of the adsorption of a second molecule); the computed values are in good agreement with calorimetric data previously reported in the literature.<sup>66</sup> Furthermore, the variation of the pressure has a limited effect on  $\Delta H$  values. Instead, this impacts much more in the  $\Delta G$  values: as a matter of fact, most of the processes are exoergonic, but some turn to endoergonic at the lower pressure value. In detail, the monocarbonyl adduct (1) is always stable, regardless of the considered pressure. Conversely, the dicarbonyl adduct (2) is stable only at high pressures, whereas it is expected to easily desorb as the pressure is decreased, in line with experimental observations. The same behavior commented for 1 is also observed for the

ammonia adduct (3) that exhibits the highest stability among the considered structures. Finally, the formation of a mixed NH<sub>3</sub>-CO adduct (4), where a CO molecule is adsorbed on a preexisting ammonia adduct (3), is favored at a high pressure, whereas it turns slightly unstable upon pressure decrease. The overall description by DFT fully supports the experimental observations: the superior stability of monocarbonyls against dicarbonyls enforces the assumptions at the basis of the volumetric titration method. Also, the polluting effect of residual ammonia is highlighted, as in the case of isolated Cu(I) sites: (i) the NH<sub>3</sub> adduct is more stable than the CO one, inferring the CO adsorption event could not in principle displace a preadsorbed ammonia molecule; and (ii) the stability of the mixed adduct is not achieved at a low pressure. Thereby, Cu(I) sites interacting with residuals of NH<sub>3</sub>, not desorbed during the material activation, cannot be titrated by CO within the proposed experimental conditions, thus constituting a relevant contribution to the treatment-related uncertainty. However, the residual amount of NH<sub>3</sub> is small (as from IR measurements); thus, the untitrated Cu(I) fraction is most probably contributing to the error of the method. Furthermore, IR spectroscopy experimentally shows that part of the NH<sub>3</sub> is displaced to the Brønsted acid sites through a mechanism not described by our simplified DFT model. The contribution of NH<sub>3</sub> pollution is then even lower than expected from the bare simulation results.

#### 3.4. Calculation of Molar Attenuation Coefficient.

Once the precision of the volumetric methodology was assessed, the same protocol was used to measure the amount of accessible Cu(I) in all Cu-ZSM-5 samples. All of the materials show a total Cu(I) content of around 85% after NH<sub>3</sub> reduction at 550 °C and are in very good correlation with the IR data collected on samples treated under the same conditions and exposed to CO (Figure 3).

The spectra reported in Figure 3a show the interaction of CO with the reduced samples, and have been treated to obtain comparable data; full information on the normalization

procedure can be found in the SI (Section S6). As can be seen in Figure 3b, the correlation with the volumetric data acquired on the four samples is very good. This agreement suggests that IR spectrophotometry can be used as a semiquantitative tool for the same purpose if the molar attenuation coefficient of the Cu(I) monocarbonyl vibration is known. The application of the Beer–Lambert law to solid materials is not trivial, and one should be aware that scattering effects and differences between the geometrical and the optical thickness can lead to incorrect results.<sup>67</sup> These conditions must be checked *a posteriori* (see Section S7, Figures S9 and S10 in the SI for the complete statistical analysis), and the molar attenuation coefficient can be obtained by applying the following equation:

$$A \text{ (cm}^{-1}\text{)} = \varepsilon \left( \frac{\text{cm}}{\mu\text{mol}} \right) \frac{C \left( \frac{\mu\text{mol}}{\text{g}} \right) w \text{ (g)}}{S \text{ (cm}^2\text{)}}$$

where  $A$  is the integrated area of the band of interest,  $\varepsilon$  represents the integrated molar attenuation coefficient of the band,  $C$  is the concentration of the species (in this case, the concentrations resulting from the volumetric technique were used), and  $S$  and  $w$  are the geometrical area and the weight of the sample pellet, respectively. By plotting  $A$  vs  $Cw/S$ , the molar attenuation coefficient of the band is the slope of the line, as shown for this case in Figure 4.

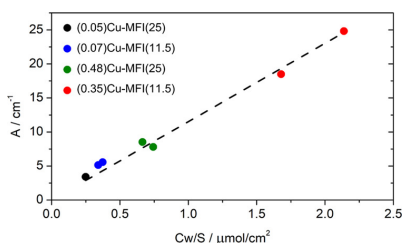


**Figure 4.** Linear model for quantifying the molar attenuation coefficient relative to the Cu(I) monocarbonyl adducts. For the (0.07)Cu-MFI(11.5), (0.35)Cu-MFI(11.5), and (0.48)Cu-MFI(25) samples, two replicas were measured. The intercept has been fixed to 0.

To retain the quantitative aspect of this analysis, the integrated areas of the monocarbonyl peaks are calculated on the non-normalized spectra after subtraction of the spectra of the corresponding activated material. The model is linear in a range corresponding to a large spectrum of possible compositions of Cu-ZSM-5 materials and Cu zeolites in general (0.16–2.6 Cu wt %), and the molar attenuation coefficient obtained with this method corresponds to  $11.5 \pm 0.3 \text{ cm}^2/\mu\text{mol}$ ; details on the statistical analysis can be found in the SI. In 2012, Góra-Marek et al.<sup>25</sup> performed a similar analysis on one sample of Cu-ZSM-5 and used the results to determine Cu speciation in Cu zeolites of different topologies. In their study, they decided to use the absorbance instead of the integral of the peak, so the two molar attenuation coefficients cannot be directly compared, also because of the likely difference in pellet weight. By fitting the data obtained in the present work using a model that employs absorbance instead of the integral of the peak, a similar (not integral) molar attenuation coefficient is obtained (1.2 instead of 1.3  $\text{cm}^2/\mu\text{mol}$ ); this discrepancy is most likely due to a different

sample set (i.e., a wider range of Cu(I) concentrations) and the decision not to include the origin point (0,0) explicitly in the dataset. As a matter of fact, using the equation proposed in the present work allows comparison between materials with different compositions and, most importantly, bandwidth is somehow taken into account by the use of the integrated molar attenuation coefficient. In particular, the same interaction on zeolites that bear different topologies may show different bandwidths and band symmetries due to the relative inhomogeneity of the sites; this, in turn, may lead to inaccurate quantitative results if the absorbance value is used instead of the peak integral. Finally, it is important to note how the value for the integrated molar attenuation coefficient is rather high; as a comparison, the integrated molar attenuation coefficient for pyridine adsorbed on Brønsted acid sites on zeolites is  $\varepsilon(\text{B})_{1545} = 1.02 \text{ cm}^2/\mu\text{mol}$ . This confirms the high sensitivity of the technique, making its application advantageous even when the Cu(I) content is low (low Cu content of the sample and/or low reduced fraction). For very high Cu(I) contents, the absorbance may exceed the limit in which the Beer–Lambert law can be safely applied; the volumetric approach is, however, an accurate technique even for these cases. In this sense, the two techniques can be thought of as complementary since volumetric measurements may not be as accurate for samples that show too low adsorption.

## CONCLUSIONS

The selective interaction of CO with Cu(I) has been exploited to develop a novel technique to quantitatively assess the amount of accessible Cu(I) sites in Cu zeolites, using a set of Cu-ZSM-5 with variable composition as reference materials. This volumetric adsorption technique allows us to access Cu redox speciation, a key variable in many catalytic processes based on this class of materials, by means of common laboratory instrumentation; in addition, repeatability tests on the measurements further reported a good precision for this methodology (relative error < 5%). This quantification, applied to a selected range of Cu-ZSM-5 materials, nicely correlates with the area of the IR band associated with Cu(I) monocarbonyl species; by modeling this correlation with the Beer–Lambert law, the molar attenuation coefficient for this peak has been calculated, allowing for easily accessible semiquantitative IR studies on these materials. Future work will expand this concept toward different zeolites, to explore the applicability of these methods to materials with more complex topology (e.g., featuring potentially inaccessible Cu(I) sites) but more relevant for their catalytic activity.

## ASSOCIATED CONTENT

### Supporting Information

The Supporting Information is available free of charge at <https://pubs.acs.org/doi/10.1021/acsami.2c03370>.

Volumetric apparatus; XANES spectra of oxidized and reduced (0.45)Cu-MFI(11.5) material; mixed ligand  $\text{NH}_3/\text{CO}$  complex from IR spectroscopy; CO adsorption isotherms; DFT optimized structures; normalization of the IR spectra of the materials interacting with CO; and statistical analysis of the spectrochemical linear model (PDF)

## AUTHOR INFORMATION

## Corresponding Authors

**Matteo Signorile** – Department of Chemistry, NIS and INSTM Reference Centre, Università di Torino, 10135 Torino, TO, Italy; [orcid.org/0000-0003-0521-3702](https://orcid.org/0000-0003-0521-3702); Email: [matteo.signorile@unito.it](mailto:matteo.signorile@unito.it)

**Silvia Bordiga** – Department of Chemistry, NIS and INSTM Reference Centre, Università di Torino, 10135 Torino, TO, Italy; [orcid.org/0000-0003-2371-4156](https://orcid.org/0000-0003-2371-4156); Email: [silvia.bordiga@unito.it](mailto:silvia.bordiga@unito.it)

## Authors

**Gabriele Deplano** – Department of Chemistry, NIS and INSTM Reference Centre, Università di Torino, 10135 Torino, TO, Italy

**Valentina Crocellà** – Department of Chemistry, NIS and INSTM Reference Centre, Università di Torino, 10135 Torino, TO, Italy; [orcid.org/0000-0002-3606-8424](https://orcid.org/0000-0002-3606-8424)

**Natale Gabriele Porcaro** – Department of Chemistry, NIS and INSTM Reference Centre, Università di Torino, 10135 Torino, TO, Italy

**Cesare Atzori** – Department of Chemistry, NIS and INSTM Reference Centre, Università di Torino, 10135 Torino, TO, Italy; Present Address: European Synchrotron Radiation Facility, 71 Avenue des Martyrs, 38000 Grenoble, France; [orcid.org/0000-0002-3227-7421](https://orcid.org/0000-0002-3227-7421)

**Bjørn Gading Solemsli** – SMN Centre for Materials Science and Nanotechnology, Department of Chemistry, University of Oslo, N-0315 Oslo, NO, Norway

**Stian Svelle** – SMN Centre for Materials Science and Nanotechnology, Department of Chemistry, University of Oslo, N-0315 Oslo, NO, Norway; [orcid.org/0000-0002-7468-5546](https://orcid.org/0000-0002-7468-5546)

Complete contact information is available at:  
<https://pubs.acs.org/10.1021/acsami.2c03370>

## Author Contributions

The manuscript was written through contributions of all authors. All authors have given approval to the final version of the manuscript.

## Funding

The work was financially supported by the European Research Council (ERC), under the Horizon 2020 research and innovation program: CuBE ERC-Synergy project (Grant agreement no. 856446).

## Notes

The authors declare no competing financial interest.

## ACKNOWLEDGMENTS

The authors acknowledge the European Research Council (ERC), under the Horizon 2020 research and innovation program: CuBE ERC-Synergy project (Grant agreement no. 856446). This work forms a part of the iCSI (industrial Catalysis Science and Innovation) Centre for Research-based Innovation, which receives financial support from the Research Council of Norway under Contract No. 237922. The authors acknowledge the Sigma2 Norwegian High Performance Computing program (project no. NN4683K) and thank Lowik Dewez-Raska for having synthesized the Cu-ZSM-5 samples within his master's thesis work.

## REFERENCES

- (1) Mohan, S.; Dinesha, P.; Kumar, S. NO<sub>x</sub> Reduction Behaviour in Copper Zeolite Catalysts for Ammonia SCR Systems: A Review. *Chem. Eng. J.* **2020**, *384*, No. 123253.
- (2) Newton, M. A.; Knorpp, A. J.; Sushkevich, V. L.; Palagin, D.; van Bokhoven, J. A. Active Sites and Mechanisms in the Direct Conversion of Methane to Methanol Using Cu in Zeolitic Hosts: A Critical Examination. *Chem. Soc. Rev.* **2020**, *49*, 1449–1486.
- (3) Baek, J.; Rungtaweeworanit, B.; Pei, X.; Park, M.; Fakra, S. C.; Liu, Y.; Alshimri, S. A.; Alshihri, S.; Trickett, C. A.; Somorjai, G. A.; Yaghi, O. M. Bioinspired Metal–Organic Framework Catalysts for Selective Methane Oxidation to Methanol Bioinspired Metal–Organic Framework Catalysts for Selective Methane Oxidation to Methanol. *J. Am. Chem. Soc.* **2018**, *140*, 18208–18216.
- (4) Zheng, J.; Ye, J.; Ortun, M. A.; Fulton, J. L.; Gutie, O. Y.; Camaioni, D. M.; Motkuri, R. K.; Li, Z.; Webber, T. E.; Mehdi, B. L.; Browning, N. D.; Penn, R. L.; Farha, O. K.; Hupp, J. T.; Truhlar, D. G.; Cramer, C. J.; Lercher, J. A. Selective Methane Oxidation to Methanol on Cu–Oxo Dimers Stabilized by Zirconia Nodes of an NU-1000 Metal–Organic Framework. *J. Am. Chem. Soc.* **2019**, *141*, 9292–9304.
- (5) Ikuno, T.; Zheng, J.; Vjunov, A.; Sanchez-sanchez, M.; Ortun, M. A.; Pahls, D. R.; Fulton, J. L.; Camaioni, D. M.; Li, Z.; Ray, D.; Mehdi, B. L.; Browning, N. D.; Farha, O. K.; Hupp, J. T.; Cramer, C. J.; Gagliardi, L.; Lercher, J. A. Methane Oxidation to Methanol Catalyzed by Cu–Oxo Clusters Stabilized in NU-1000 Metal–Organic Framework. *J. Am. Chem. Soc.* **2017**, *139*, 10294–10301.
- (6) Tyrsted, C.; Borfecchia, E.; Berlier, G.; Lomachenko, K. A.; Lamberti, C.; Bordiga, S.; Vennestrom, P. N. R.; Janssens, T. V. W.; Falsig, H.; Beato, P.; Puig-Molina, A. Nitrate–Nitrite Equilibrium in the Reaction of NO with a Cu-CHA Catalyst for NH<sub>3</sub>-SCR. *Catal. Sci. Technol.* **2016**, *6*, 8314–8324.
- (7) Marberger, A.; Petrov, A. W.; Steiger, P.; Elsener, M.; Kröcher, O.; Nachttegaal, M.; Ferri, D. Time-Resolved Copper Speciation during Selective Catalytic Reduction of NO on Cu-SSZ-13. *Nat. Catal.* **2018**, *1*, 221–227.
- (8) Oord, R.; Schmidt, J. E.; Weckhuysen, B. M. Methane-to-Methanol Conversion over Zeolite Cu-SSZ-13, and Its Comparison with the Selective Catalytic Reduction of NO<sub>x</sub> with NH<sub>3</sub>. *Catal. Sci. Technol.* **2018**, *8*, 1028–1038.
- (9) Lamberti, C.; Bordiga, S.; Salvalaggio, M.; Spoto, G.; Zecchina, A.; Geobaldo, F.; Vlaic, G.; Bellatreccia, M. XAFS, IR, and UV–Vis Study of the CuI Environment in CuI-ZSM-5. *J. Phys. Chem. B* **1997**, *101*, 344–360.
- (10) Borfecchia, E.; Lomachenko, K. A.; Giordanino, F.; Falsig, H.; Beato, P.; Soldatov, A. V.; Bordiga, S.; Lamberti, C. Revisiting the Nature of Cu Sites in the Activated Cu-SSZ-13 Catalyst for SCR Reaction. *Chem. Sci.* **2015**, *6*, 548–563.
- (11) Borfecchia, E.; Beato, P.; Svelle, S.; Olsbye, U.; Lamberti, C.; Bordiga, S. Cu-CHA-a Model System for Applied Selective Redox Catalysis. *Chem. Soc. Rev.* **2018**, *47*, 8097–8133.
- (12) Andersen, C. W.; Bremholm, M.; Ravnborg, N.; Blichfeld, B.; Lundegaard, F. Location of Cu<sup>2+</sup> in CHA zeolite investigated by X-ray diffraction using the Rietveld/maximum entropy method. *IUCr* **2014**, *5*, 382–386.
- (13) Moreno-González, M.; Palomares, A. E.; Chiesa, M.; Boronat, M.; Giamello, E.; Blasco, T. Evidence of a Cu<sup>2+</sup>–Alkane Interaction in Cu-Zeolite Catalysts Crucial for the Selective Catalytic Reduction of NO<sub>x</sub> with Hydrocarbons. *ACS Catal.* **2017**, *7*, 3501–3509.
- (14) Song, J.; Wang, Y.; Walter, E. D.; Washton, N. M.; Mei, D.; Kovarik, L.; Engelhard, M. H.; Proding, S.; Wang, Y.; Peden, C. H. F.; Gao, F. Toward Rational Design of Cu/SSZ-13 Selective Catalytic Reduction Catalysts: Implications from Atomic-Level Understanding of Hydrothermal Stability. *ACS Catal.* **2017**, *7*, 8214–8227.
- (15) Thommes, M.; Kaneko, K.; Neimark, A. V.; Olivier, J. P.; Rodriguez-reinoso, F.; Rouquerol, J.; Sing, K. S. W. Physisorption of Gases, with Special Reference to the Evaluation of Surface Area and Pore Size Distribution (IUPAC Technical Report). *Pure Appl. Chem.* **2015**, *87*, 1051–1069.

- (16) Paolucci, C.; Verma, A. A.; Bates, S. A.; Kispersky, V. F.; Miller, J. T.; Gounder, R.; Delgass, W. N.; Ribeiro, F. H.; Schneider, W. F. Isolation of the Copper Redox Steps in the Standard Selective Catalytic Reduction on Cu-SSZ-13. *Angew. Chem., Int. Ed.* **2014**, *53*, 11828–11833.
- (17) Paolucci, C.; Khurana, I.; Parekh, A. A.; Li, S.; Shih, A. J.; Li, H.; Di Iorio, J. R.; Albarracin-Caballero, J. D.; Yezerets, A.; Miller, J. T.; Delgass, W. N.; Ribeiro, F. H.; Schneider, W. F.; Gounder, R. Dynamic Multinuclear Sites Formed by Mobilized Copper Ions in NO<sub>x</sub> Selective Catalytic Reduction. *Science* **2017**, *357*, 898–903.
- (18) Groothaert, M. H.; van Bokhoven, J. A.; Battiston, A. A.; Weckhuysen, B. M.; Schoonheydt, R. A. Bis( $\mu$ -Oxo)Dicopper in Cu-ZSM-5 and Its Role in the Decomposition of NO: A Combined in Situ XAFS, UV–Vis–Near-IR, and Kinetic Study. *J. Am. Chem. Soc.* **2003**, *125*, 7629–7640.
- (19) Negri, C.; Martini, A.; Deplano, G.; Lomachenko, K. A.; Janssens, T. V. W.; Borfecchia, E.; Berlier, G.; Bordiga, S. Investigating the Role of Cu-Oxo Species in Cu-Nitrate Formation over Cu-CHA Catalysts. *Phys. Chem. Chem. Phys.* **2021**, *23*, 18322–18337.
- (20) Villamaina, R.; Liu, S.; Nova, I.; Tronconi, E.; Ruggeri, M. P.; Collier, J.; York, A.; Thompson, D. Speciation of Cu Cations in Cu-CHA Catalysts for NH<sub>3</sub>-SCR: Effects of SiO<sub>2</sub>/AlO<sub>3</sub> Ratio and Cu-Loading Investigated by Transient Response Methods. *ACS Catal.* **2019**, *9*, 8916–8927.
- (21) Modén, B.; Da Costa, P.; Fonfe, B.; Lee, D. K.; Iglesia, E. Kinetics and Mechanism of Steady-State Catalytic NO Decomposition Reactions on Cu-ZSMS. *J. Catal.* **2002**, *209*, 75–86.
- (22) Valyon, J.; Hall, W. K.; Bell, A. T.; Panayotov, D.; Iwamoto, M.; Horterra, C.; Hums, G.; Nam, I. S.; Dejong, K. P.; Hightower, J. W. An infrared study of an active NO decomposition catalyst. *Stud. Surf. Sci. Catal.* **1993**, *75*, 1339–1350.
- (23) Bell, V. A.; Feeley, J. S.; Deeba, M.; Farrauto, R. J. In-situ high-temperature FTIR studies of NO<sub>x</sub> reduction with propylene over Cu/ZSM-5 catalysts. *Catal. Lett.* **1994**, *29*, 15–26.
- (24) Xie, P.; Pu, T.; Aranovich, G.; Guo, J.; Donohue, M.; Kulkarni, A.; Wang, C. Bridging Adsorption Analytics and Catalytic Kinetics for Metal-Exchanged Zeolites. *Nat. Catal.* **2021**, *4*, 144–156.
- (25) Góra-Marek, K.; Palomares, A. E.; Glanowska, A.; Sadowska, K.; Datka, J. Copper Sites in Zeolites—Quantitative IR Studies. *Microporous Mesoporous Mater.* **2012**, *162*, 175–180.
- (26) Tarach, K. A.; Jablonska, M.; Pyra, K.; Liebau, M.; Reiprich, B.; Glaser, R.; Góra-Marek, K. Effect of Zeolite Topology on NH<sub>3</sub>-SCR Activity and Stability of Cu-Exchanged Zeolites. *Appl. Catal., B* **2021**, *284*, No. 119752.
- (27) Yamashita, H.; Matsuo, M.; Tsuji, K.; Shioya, Y.; Anpo, M.; Che, M. In-Situ XAFS, Photoluminescence, and IR Investigations of Copper Ions Included within Various Kinds of Zeolites. Structure of Cu(I) Ions and Their Interaction with CO Molecules. *J. Phys. Chem. A* **1996**, *100*, 397–402.
- (28) Giordanino, F.; Vennestrøm, P. N. R.; Lundegaard, L. F.; Stappen, F. N.; Mossin, S.; Beato, P.; Bordiga, S.; Lamberti, C. Characterization of Cu-Exchanged SSZ-13: A Comparative FTIR, UV-Vis, and EPR Study with Cu-ZSM-5 and Cu- $\beta$  with Similar Si/Al and Cu/Al Ratios. *Dalton Trans.* **2013**, *42*, 12741–12761.
- (29) Lamberti, C.; Zecchina, A.; Groppo, E.; Bordiga, S. Probing the Surfaces of Heterogeneous Catalysts by in Situ IR Spectroscopy. *Chem. Soc. Rev.* **2010**, *39*, 4951–5001.
- (30) Fitch, A. N.; Jobic, H.; Renouprez, A. Localization of Benzene in Sodium-Y-Zeolite by Powder Neutron Diffraction. *J. Phys. Chem. B* **1986**, *90*, 1311–1318.
- (31) Mortier, W. J. *Compilation of Extra Framework Sites in Zeolites*; Butterworth & Co.: Guildford, 1982; Vol. 19–31, pp 41–48.
- (32) Hunger, M.; Engelhardt, G.; Koller, H.; Weitkamp, J. Characterization of Sodium Cations in Dehydrated Faujasites and Zeolite EMT by <sup>23</sup>Na DOR, 2D Nutation, and MAS NMR. *Solid State Nucl. Magn. Reson.* **1993**, *2*, 111–120.
- (33) Tsyganenko, A. A.; Escalona Platero, E.; Otero Areán, C.; Garrone, E.; Zecchina, A. Variable-temperature IR Spectroscopic Studies of CO Adsorbed on Na-ZSM-5 and Na-Y Zeolites. *Catal. Lett.* **1999**, *61*, 187–192.
- (34) Montanari, T.; Salla, I.; Busca, G. Adsorption of CO on LTA Zeolite Adsorbents: An IR Investigation. *Microporous Mesoporous Mater.* **2008**, *109*, 216–222.
- (35) Kuterasiński, Ł.; Podobinski, J.; Rutkowska-Zbik, D.; Datka, J. IR Studies of the Cu Ions in Cu-Faujasites. *Molecules* **2019**, *24*, No. 4250.
- (36) Maurin, G.; Bell, R. G.; Devautour, S.; Henn, F.; Giuntini, J. C. Modeling the Effect of Hydration in Zeolite Na<sup>+</sup>-Mordenite. *J. Phys. Chem. B* **2004**, *108*, 3739–3745.
- (37) Geobaldo, F.; Lamberti, C.; Ricchiardi, G.; Bordiga, S.; Zecchina, A.; Palomino, G. T.; Areat, C. O. N<sub>2</sub> Adsorption at 77 K on H-Mordenite and Alkali-Metal-Exchanged Mordenites: An IR Study. *J. Phys. Chem. C* **1995**, *99*, 11167–11177.
- (38) Crocellà, V.; Atzori, C.; Latini, G.; Signorile, M. A Kit for Volumetric Measurements of Gas Adsorption. PCT/IB2021/051769, WO2021/181211A12021.
- (39) Deplano, G.; Martini, A.; Signorile, M.; Borfecchia, E.; Crocellà, V.; Svelle, S.; Bordiga, S. Copper Pairing in the Mordenite Framework as a Function of the CuI/CuII Speciation. *Angew. Chem., Int. Ed.* **2021**, *60*, 25891–25896.
- (40) Erba, A.; Baima, J.; Bush, I.; Orlando, R.; Dovesi, R. Large-Scale Condensed Matter DFT Simulations: Performance and Capabilities of the CRYSTAL Code. *J. Chem. Theory Comput.* **2017**, *13*, 5019–5027.
- (41) Morra, E.; Signorile, M.; Salvadori, E.; Bordiga, S.; Giamello, E.; Chiesa, M. Nature and Topology of Metal–Oxygen Binding Sites in Zeolite Materials: <sup>17</sup>O High-Resolution EPR Spectroscopy of Metal-Loaded ZSM-5. *Angew. Chem., Int. Ed.* **2019**, *58*, 12398–12403.
- (42) Kim, C. W.; Heo, N. H.; Seff, K. Framework Sites Preferred by Aluminum in Zeolite ZSM-5. Structure of a Fully Dehydrated, Fully Cs<sup>+</sup>-Exchanged ZSM-5 Crystal (MFI, Si/Al = 24). *J. Phys. Chem. C* **2011**, *115*, 24823–24838.
- (43) Becke, A. D. A New Mixing of Hartree–Fock and Local Density-functional Theories. *J. Chem. Phys.* **1993**, *98*, 1372–1377.
- (44) Lee, C.; Yang, W.; Parr, R. G. Development of the Colle-Salvetti Correlation-Energy Formula into a Functional of the Electron Density. *Phys. Rev. B* **1988**, *37*, 785–789.
- (45) Grimme, S.; Antony, J.; Ehrlich, S.; Krieg, H. A Consistent and Accurate Ab Initio Parametrization of Density Functional Dispersion Correction (DFT-D) for the 94 Elements H–Pu. *J. Chem. Phys.* **2010**, *132*, No. 154104.
- (46) Nada, R.; Nicholas, J. B.; McCarthy, M. I.; Hess, A. C. Basis Sets for Ab Initio Periodic Hartree-Fock Studies of Zeolite/Adsorbate Interactions: He, Ne, and Ar in Silica Sodalite. *Int. J. Quantum Chem.* **1996**, *60*, 809–820.
- (47) Catti, M.; Valerio, G.; Dovesi, R.; Causà, M. Quantum-Mechanical Calculations of the Solid-State Equilibrium MgO + Alpha-Al<sub>2</sub>O<sub>3</sub> MgAl<sub>2</sub>O<sub>4</sub> (Spinel) versus Pressure. *Phys. Rev. B* **1994**, *49*, 14179–14187.
- (48) Signorile, M.; Braglia, L.; Crocellà, V.; Torelli, P.; Groppo, E.; Ricchiardi, G.; Bordiga, S.; Bonino, F. Titanium Defective Sites in TS-1: Structural Insights by Combining Spectroscopy and Simulation. *Angew. Chem., Int. Ed.* **2020**, *59*, 18145–18150.
- (49) Signorile, M.; Damin, A.; Bonino, F.; Crocellà, V.; Lamberti, C.; Bordiga, S. The Role of Dispersive Forces Determining the Energetics of Adsorption in Ti Zeolites. *J. Comput. Chem.* **2016**, *37*, 2659–2666.
- (50) Signorile, M.; Damin, A.; Bonino, F.; Crocellà, V.; Ricchiardi, G.; Lamberti, C.; Bordiga, S. Computational Assessment of Relative Sites Stabilities and Site-Specific Adsorptive Properties of Titanium Silicalite-1. *J. Phys. Chem. C* **2018**, *122*, 1612–1621.
- (51) Schäfer, A.; Huber, C.; Ahlrichs, R. Fully Optimized Contracted Gaussian Basis Sets of Triple Zeta Valence Quality for Atoms Li to Kr. *J. Chem. Phys.* **1994**, *100*, 5829–5835.
- (52) Dovesi, R.; Saunders, V. R.; Roetti, C.; Orlando, R.; Zicovich-Wilson, C. M.; Pascale, F.; Civalleri, B.; Doll, K.; Harrison, N. M.; Bush, I. J.; D’Arco, Ph.; Llunel, M.; Causà, M.; Noël, Y.; Maschio, L.; Erba, A.; Rérat, M.; Casassa, S. CRYSTAL17 User’s Manual, 2017. <https://www.crystal.unito.it/Manuals/crystal17.pdf>.

(53) Zecchina, A.; Bordiga, S.; Palomino, G. T.; Scarano, D.; Lamberti, C.; Salvalaggio, M. Mono-, Di-, and Tricarbonylic Species in Copper(I)-Exchanged Zeolite ZSM-5: Comparison with Homogeneous Copper(I) Carbonylic Structures. *J. Phys. Chem. B* **1999**, *103*, 3833–3844.

(54) Bordiga, S.; Turnes Palomino, G.; Arduino, D.; Lamberti, C.; Zecchina, A.; Otero Areán, C. Well Defined Carbonyl Complexes in Ag<sup>+</sup>- and Cu<sup>+</sup>-Exchanged ZSM-5 Zeolite: A Comparison with Homogeneous Counterparts. *J. Mol. Catal. A: Chem.* **1999**, *146*, 97–106.

(55) Sárkány, J. Effects of Water and Ion-Exchanged Counterion on the FTIR Spectra of ZSM-5. II. (Cu<sup>+</sup>-CO)-ZSM-5: Coordination of Cu<sup>+</sup>-CO Complex by H<sub>2</sub>O and Changes in Skeletal T-O-T Vibrations. *Top. Catal.* **2002**, *18*, 271–277.

(56) Sárkány, J. Effects of Water and Ion-Exchanged Counterion on the FT-IR Spectra of ZSM-5: Part III. Cu<sup>+</sup>(CO)<sub>2</sub>-ZSM-5: Interaction of Cu(CO)<sub>2</sub> Complex with H<sub>2</sub>O and Changes in Skeletal T-O-T Vibrations. *Appl. Catal., A* **2002**, *229*, 291–312.

(57) Miessner, H.; Landmesser, H.; Jaeger, N.; Richter, K. Surface Carbonyl Species of Copper Supported on Dealuminated Y Zeolite. *J. Chem. Soc., Faraday Trans.* **1997**, *93*, 3417–3422.

(58) Bulánek, R. Investigation of IR Vibrational Band of C–O Bond of Carbonyl Species in Cu+-MFI Zeolites. *Phys. Chem. Chem. Phys.* **2004**, *6*, 4208–4214.

(59) Holm, M. S.; Svelle, S.; Joensen, F.; Beato, P.; Christensen, C. H.; Bordiga, S.; Bjørgen, M. Assessing the Acid Properties of Desilicated ZSM-5 by FTIR Using CO and 2,4,6-Trimethylpyridine (Collidine) as Molecular Probes. *Appl. Catal., A* **2009**, *356*, 23–30.

(60) Armaroli, T.; Gutiérrez Alejandro, A.; Bevilacqua, M.; Trombetta, M.; Milella, F.; Ramirez, J.; Busca, G. 13-P-25-FTIR Studies of the Interaction of Aromatic and Branched Aliphatic Compounds with Internal, External and Extraframework Sites of MFI-Type Zeolite Materials. In *Zeolites and Mesoporous Materials at the Dawn of the 21st Century*, Galarnau, A.; Fajula, F.; Di Renzo, F.; Vedrine, J., Eds.; Studies in Surface Science and Catalysis; Elsevier, 2001; Vol. 135, p 346.

(61) Pazé, C.; Bordiga, S.; Lamberti, C.; Salvalaggio, M.; Zecchina, A.; Bellussi, G. Acidic Properties of H-β Zeolite As Probed by Bases with Proton Affinity in the 118–204 kcal mol<sup>-1</sup> Range: A FTIR Investigation. *J. Phys. Chem. B* **1997**, *101*, 4740–4751.

(62) Zecchina, A.; Marchese, L.; Bordiga, S.; Pazé, C.; Gianotti, E. Vibrational Spectroscopy of NH<sub>4</sub><sup>+</sup> Ions in Zeolitic Materials: An IR Study. *J. Phys. Chem. B* **1997**, *101*, 10128–10135.

(63) Wakabayashi, F.; Kondo, J. N.; Domen, K.; Hirose, C. Direct comparison of N<sub>2</sub> and CO as IR-spectroscopic probes of acid sites in H-ZSM-5 zeolite. *J. Phys. Chem. D* **1995**, *99*, 10573–10580.

(64) Park, S. K.; Kurshev, V.; Luan, Z. H.; Lee, C. W.; Kevan, L. Reaction of NO with Copper Ions in Cu(II)-Exchanged ZSM-5 Zeolite: Electron Spin Resonance, Electron Spin Echo Modulation and Fourier Transform Infrared Spectroscopy. *Microporous Mesoporous Mater.* **2000**, *38*, 255–266.

(65) Lamberti, C.; Palomino, G. T.; Bordiga, S.; Berlier, G.; Acapito, F. D.; Zecchina, A. Structure of Homoleptic CuI(CO)<sub>3</sub> Cations in CuI-Exchanged ZSM-5 Zeolite: An X-Ray Absorption Study. *Angew. Chem., Int. Ed.* **2000**, *12*, 2138–2141.

(66) Bolis, V.; Barbaglia, A.; Bordiga, S.; Lamberti, C.; Zecchina, A. Heterogeneous Nonclassical Carbonyls Stabilized in Cu(I)- and Ag(I)-ZSM-5 Zeolites: Thermodynamic and Spectroscopic Features. *Spectrochim. J. Phys. Chem. B* **2004**, *108*, 9970–9983.

(67) Morterra, C.; Garrone, E.; Bolis, V.; Fubini, B. An Infrared Spectroscopic Characterization of the Coordinative Adsorption of Carbon Monoxide on TiO<sub>2</sub>. *Spectrochim. Acta, Part A* **1987**, *43*, 1577–1581.

## Recommended by ACS

### Structure of Selective and Nonselective Dicopper (II) Sites in CuMFI for Methane Oxidation to Methanol

Mikalai A. Artsiusheuski, Vitaly L. Sushkevich, et al.

DECEMBER 06, 2022

ACS CATALYSIS

READ 

### Tuning Copper Active Site Composition in Cu-MOR through Co-Cation Modification for Methane Activation

Dieter Plessers, Bert F. Sels, et al.

JANUARY 18, 2023

ACS CATALYSIS

READ 

### Assessing the Influence of Zeolite Composition on Oxygen-Bridged Diamino Dicopper(II) Complexes in Cu-CHA DeNO<sub>x</sub> Catalysts by Machine Learning-Assisted X-ray A...

Andrea Martini, Elisa Borfecchia, et al.

JUNE 28, 2022

THE JOURNAL OF PHYSICAL CHEMISTRY LETTERS

READ 

### Rate Controlling in Low-Temperature Standard NH<sub>3</sub>-SCR: Implications from Operando EPR Spectroscopy and Reaction Kinetics

Yiqing Wu, Feng Gao, et al.

MAY 23, 2022

JOURNAL OF THE AMERICAN CHEMICAL SOCIETY

READ 

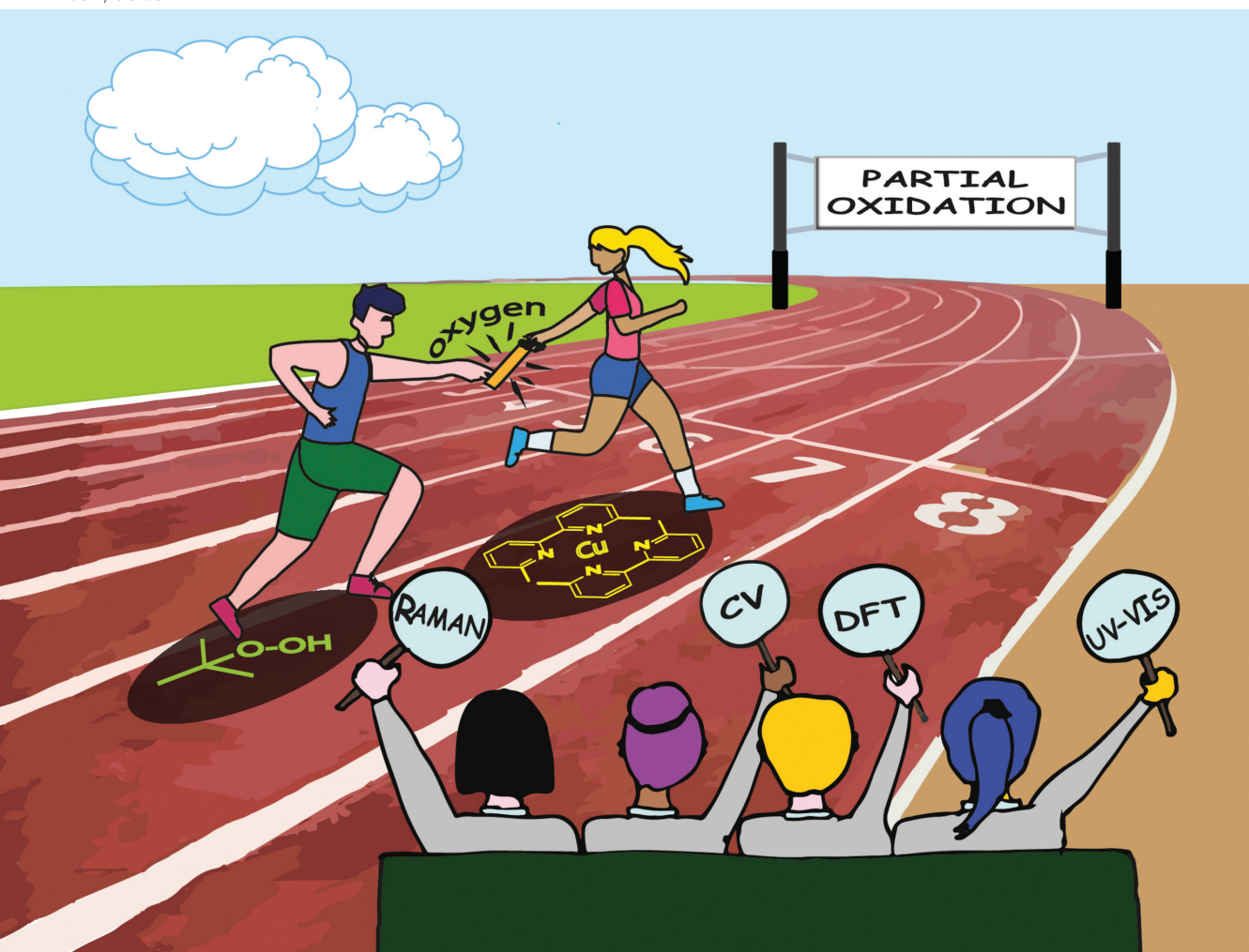
Get More Suggestions >

# Appendix A4



# Dalton Transactions

An international journal of inorganic chemistry  
rsc.li/dalton



ISSN 1477-9226

**PAPER**

Matteo Bonomo, Silvia Bordiga *et al.*  
A multi-technique approach to unveil the redox behaviour  
and potentiality of homoleptic Cu<sup>I</sup> complexes based on  
substituted bipyridine ligands in oxygenation reactions

Cite this: *Dalton Trans.*, 2022, **51**,  
14439

# A multi-technique approach to unveil the redox behaviour and potentiality of homoleptic Cu<sup>I</sup> complexes based on substituted bipyridine ligands in oxygenation reactions†

Barbara Centrella,<sup>‡a</sup> Gabriele Deplano,<sup>‡a</sup> Alessandro Damin,<sup>a</sup>  
Matteo Signorile,<sup>‡a</sup> Mariagrazia Tortora,<sup>‡b,c</sup> Claudia Barolo,<sup>‡a,d</sup>  
Matteo Bonomo,<sup>‡a\*</sup> and Silvia Bordiga,<sup>‡a\*</sup>

The effect of differently substituted 2,2'-bipyridine ligands (*i.e.* 6,6'-dimethyl-2,2'-bipyridine, 5,5'-dimethyl-2,2'-bipyridine, 6,6'-dimethoxy-2,2'-bipyridine and 2,2'-bipyridine) on the reversible oxidation of the resulting Cu<sup>I</sup> homoleptic complexes is investigated by means of a multi-technique approach (electronic and vibrational spectroscopies, DFT, electrochemistry). Among the four tested complexes, [Cu<sup>I</sup>(6,6'-dimethyl-2,2'-bipyridine)<sub>2</sub>](PF<sub>6</sub>) shows a peculiar behavior when oxidized with an organic peroxide (*i.e.* *tert*-butyl hydroperoxide, tBuOOH). The simultaneous use of UV-Vis-NIR and Raman spectroscopy methods and cyclic voltammetry, supported by DFT based calculations, allowed identifying (i) the change in the oxidation state of the copper ion and (ii) some peculiar modification in the local structure of the metal leading to the formation of a [Cu<sup>II</sup>OH]<sup>+</sup> species. The latter, being able to oxidize a model molecule (*i.e.* cyclohexene) and showing the restoration of the original Cu<sup>I</sup> complex and the formation of cyclohexanone, confirms the potential of these simple homoleptic Cu<sup>I</sup> complexes as model catalysts for partial oxygenation reactions.

Received 20th April 2022,  
Accepted 19th July 2022

DOI: 10.1039/d2dt01234k

rsc.li/dalton

## Introduction

Copper is one of the most available transition metals in the Earth's crust and seawater;<sup>1,2</sup> it is usually produced in a relatively high quantity (19.7 Mtons in 2017) and low cost (6\$ per kg).<sup>3</sup> Moreover, Cu requires lower energy for its production compared to other metals (cradle-to-gate LCA),<sup>4</sup> and a straightforward recycling could further decrease the CO<sub>2</sub>-eq. emissions for its life cycle.<sup>5</sup> Copper is a redox active metal that, beside the metallic state (Cu<sup>0</sup>), can reach three different oxidation states (Cu<sup>I</sup>, Cu<sup>II</sup> and Cu<sup>III</sup>). Nature, as well as and synthetic and industrial chemistry, takes advantage of its one-electron (Cu<sup>I</sup> to Cu<sup>II</sup>) or two-electron (Cu<sup>I</sup> to Cu<sup>III</sup>) redox chemistry to

carry out a plethora of chemical reactions, from oxygenation to hydroxylation and from C–C to C–N bond formation.<sup>6</sup>

To be effectively exploited as a redox catalyst, Cu<sup>n</sup> needs to be stabilized by molecular ligands<sup>7</sup> or supramolecular structures (*e.g.* zeolites or metal organic frameworks<sup>8–10</sup>) preferring the former for homogeneous and the latter for heterogeneous reactions. Focusing on homogeneous complexes, an almost infinite library of ligands able to form stable complexes with both Cu<sup>I</sup> and Cu<sup>II</sup> centres have been designed and synthesized.<sup>11</sup> Among them, a central role has been played by 2,2'-bipyridine (bpy), mainly due to its low cost and synthetic easiness; indeed, bpy has been described as “the most widely used ligand”<sup>12</sup> in both homoleptic and heteroleptic fashions. The bpy ligands show excellent behaviour to firmly complex both Cu<sup>I</sup> and Cu<sup>II</sup>, enabling, when appropriately substituted, the reversibility of the oxidation state of the metal. As a matter of fact, the redox potential of the Cu<sup>I</sup>/Cu<sup>II</sup> couple, and thus the reversibility of the conversion, is affected by the steric hindrance nearby the metal centre.<sup>13,14</sup> Besides the energy required for the electron transfer, one should also consider the reorganization energy required for the conformational change, as tetra-coordinated Cu<sup>I</sup> is stabilized in a tetrahedral symmetry, while Cu<sup>II</sup> prefers a square planar one.<sup>15</sup> The energy required for the conformational change is usually relatively

<sup>a</sup>Department of Chemistry and NIS Interdepartmental Center and INSTM reference center, University of Turin, via Pietro Giuria 7, I-10125 Turin, Italy.

E-mail: matteo.bonomo@unito.it, silvia.bordiga@unito.it

<sup>b</sup>AREA SCIENCE PARK, Padriciano, 99, 34149 Trieste, Italy

<sup>c</sup>Eletra-Sincrotrone Trieste, S.S. 114 km 163.5, Basovizza, 34149 Trieste, Italy

<sup>d</sup>ICxT Interdepartmental Centre, Università degli Studi di Torino, Lungo Dora Sena 100, 10153 Torino, Italy

† Electronic supplementary information (ESI) available. See DOI: <https://doi.org/10.1039/d2dt01234k>

‡ These two authors equally contributed to the paper.



high, but it could be lowered by modulating the steric hindrance around the metal centre.<sup>16</sup> With opportune hindrance constraints the Cu<sup>I</sup> complex can be forced toward a distorted tetrahedral geometry that can easily switch to a Cu<sup>II</sup> square planar one.<sup>17</sup> At the same time, the square planar geometry of Cu<sup>II</sup> will be distorted as well,<sup>18</sup> facilitating the back-reduction to the Cu<sup>I</sup> state.<sup>19</sup> These features allowed the successful exploitation of Cu(bpy)<sub>1/2</sub> complexes in different fields dealing with the redox process, such as Dye-Sensitized Solar Cells (DSSCs)<sup>20–25</sup> and Light-emitting Electrochemical Cells (LECs)<sup>26,27</sup> and also as asymmetric catalysts<sup>28</sup> and as linkers in MOFs.<sup>29</sup>

Cu<sup>I</sup> systems (constructed *in situ* using a Cu-salt as the copper source and bpy as the ligand, in a 1 : 1 stoichiometric ratio) in oxidation reactions of organic compounds have been extensively studied, among the others, by Stahl and coworkers.<sup>30–33</sup> In 2011,<sup>30</sup> they reported the oxidation of primary alcohols using a mixture of Cu<sup>I</sup>(ACN)<sub>4</sub> as the copper source, bpy (1 eq.) and NMI (*N*-methylimidazole, 2 eq.) as ligands, molecular oxygen as the oxidant and a nitroxyl source (*i.e.* TEMPO) as the co-catalyst to regenerate Cu<sup>I</sup>, thereby increasing the low catalytic efficiency previously reported.<sup>34</sup> They proved that this Cu<sup>I</sup> mixture leads to an almost quantitative yield only if the Cu source is a Br<sup>−</sup> salt, whereas very poor yields are obtained in the presence of Cl<sup>−</sup> salts. A couple of years later, Stahl<sup>31</sup> successfully tested similar mixtures for the oxidation of secondary alcohols (with ABNO as the nitroxyl radical): the decoration of the bpy ligand with methoxyl groups at the 4-4' position provided a higher yield, whereas no oxidation was detected using 6,6'-dimethylbipyridine. The same group also investigated the oxidation of amines to imines<sup>32</sup> and the lactonization of diols<sup>33</sup> using analogous systems. They tested different substituents at the 4,4' position (*i.e.* methyl, methoxyl or *tert*butyl) showing comparable yields; indeed, replacing NMI with DMAP (in a 2 : 1 ratio with respect to the Cu source) further improves the reaction yield, especially in coordinating solvents (*e.g.* THF, DMSO...). A similar approach (a mixture of CuBr : 6,6'-Bubpy : DMAP 1 : 1 : 3 in ACN) has also been reported by Oisaki and Kanai,<sup>35</sup> for the oxidation of amines to imines and C–C couplings: in this case, <sup>t</sup>Bu-substituted bpy outperforms bpy. Chiba reported the incorporation of atmospheric oxygen in activated *N*-alkylamidines leading to the oxidation of a tertiary C–H bond.<sup>36</sup> In this case, phen-based mixtures lead to better yields than bpy-based systems.

It should be recalled that bpy-based Cu<sup>II</sup> supramolecular systems (*i.e.* MOFs<sup>37,38</sup>) as well as other Cu<sup>I/II</sup> mixtures<sup>39–42</sup> based on *N*-chelating ligands (in a 1 : 1 ratio) have been exploited in oxidation, oxygenation or hydroxylation reactions, but their discussion falls outside the aim of the present paper. On the other hand, the literature on Cu : bpy 1 : 2 mixtures for oxygenation reactions is extremely scarce. To the best of our knowledge, the only report on Cu<sup>I</sup> systems by Sawyer dates back to 1993:<sup>43</sup> the bpy ligand was mixed in a 2 : 1 ratio with a Cu<sup>I</sup> source in the ACN/pyridine system using H<sub>2</sub>O<sub>2</sub> or *t*BuOOH as the oxidant; cyclohexane or cyclohexene was oxidized to the

corresponding peroxides and ketones with a relatively low yield (that is three times higher for the unsaturated substrate). They proposed (but not validated) different reaction patterns initiated by the deprotonation of the peroxide reactant mediated by pyridine that leads to the formation of a reactive Cu–OOR intermediate. Similarly, Repo *et al.*<sup>44</sup> reported the use of a Cu<sup>II</sup> : bpy 1 : 2 mixture for the oxidation of 2,2'-biphenol proving that the substitution of the bipyridine ligand is of pivotal importance in the tuning of the catalytic activity.

In all the described approaches, the main proposed reaction mechanism involves the formation of hydroperoxide species bound to the metallic center, as also proved by the production of ROOH (where R is an aliphatic substrate) as the main product.<sup>41</sup> However, Cu(bpy)<sub>1/2</sub>(L)<sub>0/2</sub> complexes are always obtained *in situ* by mixing a stoichiometric amount of the ligand and Cu source in ACN. Although this methodology leads to the product formation and avoids an additional synthetic step, it has a major drawback: as brilliantly evidenced by Tuzek,<sup>45</sup> the one-pot approach does not allow controlling the real chemical structure of the catalyst; as a matter of fact, apart from the desired (or proposed) one, other species (involving both homoleptic systems and heteroleptic ones and also including the solvent as the possible ligand<sup>46,47</sup>) are likely to form. Indeed, ACN has a recognized coordination power<sup>48</sup> and could induce ligand exchange (especially if present in a very large excess, as occurring when it is adopted as a solvent); this equilibrium is further complicated if pyridine (as a base) is added,<sup>49</sup> due to its even higher coordination ability. To avoid this issue, two approaches could be followed: (i) the *ex situ* synthesis (and characterization) of the complexes to be used as catalysts and/or (ii) the development of an accessible experimental method to follow the chemical modification of the complexes during the reaction. A first step toward (i) has been recently made by Shul'pin *et al.* synthesizing both Cu<sup>I</sup> and Cu<sup>II</sup> phenanthroline-based homoleptic complexes (possibly modified with an additional ancillary ligand) having a fair activity (in the Cu<sup>II</sup> form) for the oxidation of cyclohexene by H<sub>2</sub>O<sub>2</sub> in ACN. Nevertheless, it should be pointed out that, even in this case, the integrity of the complexes after the dissolution in ACN has not been proved.

Throughout this paper, we select and synthesize four different homoleptic Cu<sup>I</sup>(bpy)<sub>2</sub> complexes aiming at investigating the effect of the nature and position of the substituent of 2,2'-bipyridine on the redox behaviour of the Cu center. A multi-technique approach (electronic and vibrational spectroscopies and electrochemistry) supported by computational analyses is exploited to investigate the chemical modification of Cu complexes undergoing a redox cycle by exploiting a combination of different solvents and oxidants. We highlight that the 6,6'-dimethyl-2,2'-bipyridyl Cu<sup>I</sup> complex shows a peculiar reversibility, strongly differing from its homologues. Thus, a more detailed dynamic analysis (simultaneous time-resolved UV-Vis-NIR and Raman analyses) of this system, conducted at Elettra synchrotron, proved almost quantitative reversibility of the redox cycle and the ability to easily oxidize a targeted molecule (*i.e.* cyclohexene).



## Results and discussion

### Design of modified 2,2'-bipyridine ligands and selection of oxidation conditions

Among the various modifiers to decorate the 2,2'-bipyridine skeleton, methyl was selected as the simplest substituent bound both at the 6,6' and 5,5' positions leading to 6,6'-dimethyl-2,2'-bipyridine (coded BPA) and 5,5'-dimethyl-2,2'-bipyridine (BPB), respectively; as a modifier impacting both the electronic properties and the steric hindrance of the ligand, methyl was replaced by a methoxy moiety (6,6'-dimethoxy-2,2'-bipyridine, BPC). To have a comparison with literature data,<sup>43</sup> the unsubstituted 2,2'-bipyridine (BPD) was also considered. To obtain the complexes, the ligands were reacted with tetrakis(acetonitrile)Cu(I) hexafluorophosphate as both a copper and counterion source (see Scheme 1 and the Experimental section for further details); indeed, the ligand exchange reaction was promoted by the higher coordination strength of the bipyridine ligands: as a result, [Cu(6,6'-dimethyl-2,2'-bipyridine)<sub>2</sub>] (PF<sub>6</sub>) (CuBPA), [Cu(5,5'-dimethyl-2,2'-bipyridine)<sub>2</sub>] (PF<sub>6</sub>) (CuBPB), [Cu(6,6'-dimethoxy-2,2'-bipyridine)<sub>2</sub>] (PF<sub>6</sub>) (CuBPC) and [Cu(2,2'-bipyridine)<sub>2</sub>] (PF<sub>6</sub>) (CuBPD) were obtained with almost quantitative yields. It is noteworthy that complex formation reactions are fast and easy to reproduce, making the process inexpensive and scalable.

Aiming at driving a homogeneous redox reaction, the choice of both the solvent and oxidant (to be used in conjunction with the Cu complexes) is crucial, and it could seriously impact the effectiveness of the reaction. In this context, the most exploited solvent in the literature is ACN, that is also valuable for its (electro)chemical inertness and its well-known simple spectroscopic fingerprint, that allows one to predict the signals of the sample.<sup>50</sup> Unfortunately, when dissolved in ACN, all the complexes, but CuBPA, tend to degrade quickly, as proved by the loss of color of the solution (Fig. S1†). This was attributed to a ligand exchange between all of the three BPB, BPC, and BPD and ACN, ascribable to the large excess of the latter.

To further prove this instability, we dissolved Cu<sup>I</sup>(bpy)<sub>2</sub> complexes in degassed ACN; even in this case, a colorless solution is obtained proving the loss of the MLCT band (*vide infra*); very interestingly, when the solvent is allowed to slowly evaporate (under nitrogen), a more and more reddish solution is obtained, and when all the solvent is removed, a dark red powder is obtained, proving that the instauration of a ligand

exchange equilibrium is the main reason for instability. A partial oxidation of Cu<sup>I</sup> due to atmospheric oxygen could not be completely excluded. These results match well with the evidence found in a previous paper by some of us<sup>51</sup> and with the results of Sawyer *et al.*<sup>43</sup> The kinetics of the ligand exchange reaction is sensibly influenced by the nature of the substituent and its position on the bipyridine ligand;<sup>52</sup> specifically, it is really fast for CuBPB and CuBPD and a bit slower for CuBPC; on the other hand, only limited reaction (tested by mass spectrometry, not shown) occurred with CuBPA, ascribable to the higher steric hindrance of the methyl moieties (at the 6,6' position).

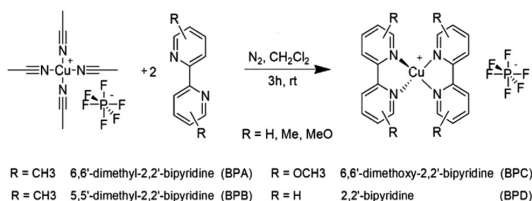
Thus, we were forced to change the solvent, and we resolved to dichloromethane (DCM), which ensures a high solubility of Cu<sup>I</sup> complexes coupled with a well-known spectroscopic fingerprint. Unfortunately, Cu<sup>II</sup> counterparts are insoluble in DCM, preventing us to propose a comparison with the reduced complexes. A possible strategy to improve the solubility of [Cu<sup>II</sup>(bpy)<sub>2</sub>]<sup>2+</sup> complexes consists of the use of ancillary ligands (*i.e.* Cl<sup>-</sup>), but this will seriously impact the complexes' geometry, making a comparison unreliable.

With respect to the oxidant, both hydrogen peroxide (H<sub>2</sub>O<sub>2</sub>) and *tert*-butyl hydroperoxide (*t*BuOOH) have been tested relying on the literature.<sup>43,50,53</sup> The former is more reactive<sup>54</sup> but it has a high water content, whereas the latter's reaction, a milder oxidant,<sup>55</sup> could be more easily controlled. Hydrogen peroxide (30% w/w in water) is just partially soluble in DCM; therefore, when the oxidation reaction occurs, the resulting Cu<sup>II</sup> complex is mainly observed in water, as proved by the greenish color of the aqueous phase; only traces were found in the organic phase. Thus, we resolved to *t*BuOOH, assuring a homogeneous organic phase. The milder reactivity of *t*BuOOH could be fairly considered as a valuable point in order to finely tune the reactivity of CuPBX by the ligand design. To precisely follow the redox processes and to detect the involved species, we exploited a multi-technique approach (*i.e.* cyclic voltammetry, Raman, UV-Vis-NIR). Indeed, it will be immediately concluded that the nature of the ligands complexing Cu<sup>I</sup> heavily impacts the oxidation process.

### Electrochemical characterization of pristine and oxidized complexes

Cyclic voltammetry, more generally electrochemistry, is one of the techniques of election to investigate the oxidation state of metal complexes due to the high electroactivity of the metal centre.<sup>56</sup> This also implies that the redox potential of the complexes could be dramatically influenced by the nature of the ligands accounting for both electronic and steric effects. In the present case, the ligand could influence the accessibility of oxidant species to the copper centre. The voltammograms of the pristine and oxidized (with *t*BuOOH) complexes are reported in Fig. 1.

All the complexes show good electrochemical stability in DCM (no changes are highlighted upon continuous cycling), and the voltammograms are characterized by a reversible redox peak, the position of which strongly depends on the



Scheme 1 Scheme of synthetic procedure.



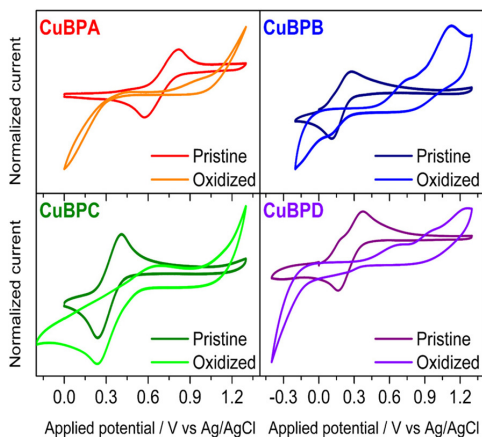


**Fig. 1** Cyclovoltammograms of pristine complexes (darker lines) and after 50 cycles from the addition of *t*BuOOH (0.1 ml of *t*BuOOH 5.5 M *n*-decane solution) as oxidant (lighter lines). Complexes were dissolved (5 mM) in a solution of DCM containing TBAPF<sub>6</sub> (0.1 M) as a supporting electrolyte. CV's starting potential has been set to 0 V vs. Ag/AgCl and the scan is conducted toward positive values.

nature of the ligand.  $E_{1/2}$  of the unsubstituted bipyridyl complex (CuBPD) is located at 269 mV vs. Ag/AgCl; the insertion of methyl in position 5 (CuBPB) just slightly influences the electrochemical behaviour of the complex leading to a more easily oxidizable copper atom ( $E_{1/2} = 190$  mV). The insertion of methoxy moieties in the ligands at positions 6 and 6' (CuBPC) leads to a less easily oxidizable system ( $E_{1/2} = 324$  mV); this could be due to a higher hindrance of the methoxy group. Recently, Giordano *et al.*<sup>51</sup> pointed out that the oxygen could partially coordinate the copper atom reducing its proneness to oxidation. According to the literature,<sup>57</sup> CuBPA shows the highest redox potential ( $E_{1/2} = 697$  mV) due to the steric hindrance of the methyl group that likely causes more severe distortion of the oxidized complex geometry (see  $\tau$  parameter in Table S1†). This trend is in good agreement with the one calculated using DFT (Table S1†). Indeed, the higher potential of CuBPA could also be an indicator of a more energetic-costly Cu<sup>I</sup> → Cu<sup>II</sup> transition. CVs could also give some insights into the Cu<sup>I</sup> → Cu<sup>II</sup> redox kinetics, with  $\Delta E_p$  (*i.e.* the voltage difference between the oxidation and reduction peaks) being directly related to the latter;<sup>58</sup> the higher  $\Delta E_p$ , the lower the kinetic of the electronic oxidation. Within the analysed complexes, CuBPA shows a higher  $\Delta E_p$  (0.24 V) followed by CuBPD (0.21 V), CuBPC (0.17 V) and CuBPB (0.16 V), that are comparable to that of the Fe/Fc<sup>+</sup> couple (0.27 V).

The effect of substituents is even clearer after the addition of the oxidant (*t*BuOOH): as soon as the latter was added, the voltammograms evolved differently as a consequence of the substitution on the pyridine rings. No matter the complex involved, the electrochemical oxidation is always faster compared to the simple addition of an oxidant. This proves that

the oxidation is (partially) assisted by potential cycling. After 50 cycles from the addition of *t*BuOOH, the voltammogram of CuBPA is almost flat, proving that the concentration of the reduced form of the complex is close to zero, as also evidenced by UV-Vis-NIR (*vide infra*). A small shoulder could still be detected at *ca.* 1 V, which could be ascribed to the presence of *meta*-stable species generated throughout the oxidation process: indeed, this shoulder tends to vanish at longer times. As expected, CuBPB and CuBPD behave similarly; the voltammograms of both the complexes are completely flat in the oxidation scan up to 0.6 V, but they present a more pronounced shoulder at 740 mV and 640 mV, respectively. Very interestingly, an irreversible oxidation process could be evidenced at a potential higher than 0.9 V, which could be likely ascribed to the oxidation of the ligand.

This process seems to be catalyzed by the presence of a metal; as a matter of fact, the sole ligands (Fig. S2†) do not show any oxidation process at  $V < 1.2$  V even after the addition of *t*BuOOH. Another interesting point could be evidenced: while CuBPA's voltammogram is almost flat throughout the reduction cycle, CuBPD and (even more) CuBPB show an irreversible, very broad reduction peak; the latter is placed at the same potential of the Cu<sup>II</sup> → Cu<sup>I</sup> reduction, well correlating with literature reports.<sup>43</sup> This is a fair hint that the addition of *t*BuOOH leads (at least partially) to pure electronic oxidation, the result of which is a Cu<sup>II</sup> complex that does not involve the presence of any oxo-species. This feature is even more evident when CuBPC is oxidized, for which a sharp and irreversible peak (0.27 V vs. Ag/AgCl) is recorded. The absence of an associated oxidation peak is due to the presence of *t*BuOOH (added in excess) in the solution that chemically re-oxidizes the Cu<sup>I</sup> complex as soon as the latter is electrochemically produced.

### Characterization of electronic transitions of the pristine and oxidized complexes

Before going into detail with the description of the effect of the oxidation/oxygenation process on different complexes, a precise assignment of the electronic transitions observed experimentally has been conducted supported by DFT. Indeed, the simulated results are in good and qualitative agreement with the experimental ones (Fig. S3–S5† and related discussion), thus making them valuable support for the interpretation of the data-set presented hereafter. The UV-Vis spectra of the four Cu complexes, both in their pristine state and in two different oxidation pathways (*i.e.* using NOPF<sub>6</sub> or *t*BuOOH), are reported in Fig. 2 (top frame). The choice of *t*BuOOH was discussed above, whereas NOPF<sub>6</sub> was also tested as an alternative oxidizing agent because of the suspicion of oxygenated species formed. It is reported in the literature that the NO<sup>+</sup> species is able to oxidize metal centres with a single electron transfer mechanism, releasing gaseous NO.<sup>19,22</sup> However, due to the good coordination ability of nitrosyl molecules,<sup>59,60</sup> the formation of a Cu<sup>II</sup>-pentacoordinate species could not be *a priori* excluded. Therefore, *t*BuOOH could likely lead to the formation of a Cu<sup>II</sup>-O(bpy)<sub>2</sub><sup>+</sup>/Cu<sup>II</sup>-OH(bpy)<sub>2</sub><sup>+</sup>(PF<sub>6</sub><sup>-</sup>) species, whereas NOPF<sub>6</sub> would preferably form Cu<sup>II</sup>(PF<sub>6</sub>)<sub>2</sub> with likely a



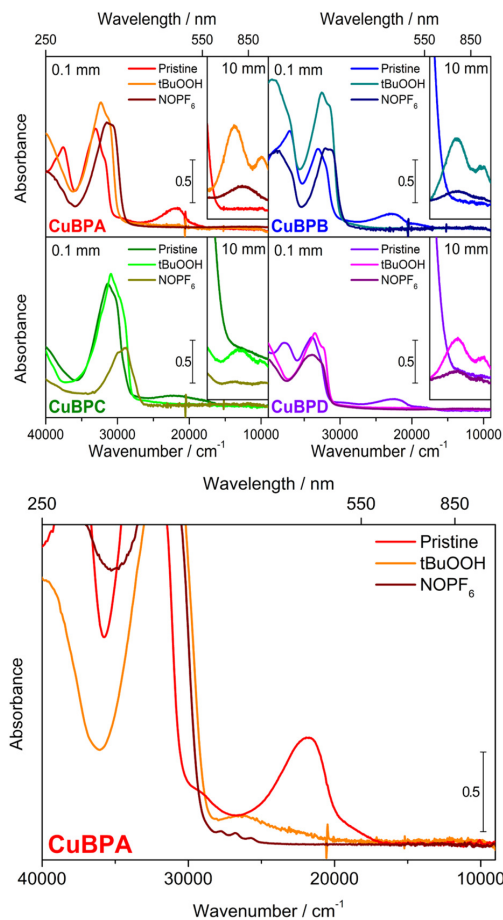


**Fig. 2** Top: UV-Vis spectra of the four complexes in their pristine form and after reaction with *t*BuOOH and NOPF<sub>6</sub>. Solutions were prepared with a concentration of 5 mM (DCM). Data in the inset show the spectra in the region 17 500–9 000 cm<sup>-1</sup>, in correspondence with the *x*-scale in the main panels. Main panel: 1 mm optical path. Inset: 10 mm optical path. The spectra for the two cuvette thicknesses were registered simultaneously on the same sample solution recirculating between the two and a reservoir. Spectra are reported in absorbance without any additional treatment. Bottom: Zoom of UV-Vis to highlight the occurrence of the band at 26 500 cm<sup>-1</sup> (377 nm) after the oxidation with *t*BuOOH. Optical path: 1 mm.

NO ancillary ligand. By comparing the final state of the complexes that reacted with the two oxidants, one could discriminate electronic oxidation from oxygenation since the two possible outcomes should present different electronic structures and geometries.

In their pristine form, the complexes show two main peaks located around 28 000 cm<sup>-1</sup> and 22 000 cm<sup>-1</sup> (Fig. S3†). On the basis of a natural transition orbital (NTO, see Fig. S6† for Cu<sup>I</sup>BPA) analysis of the simulated electronic transitions, this peculiar band is ascribed to a metal to ligand charge transfer

(MLCT) from the Cu *d*<sub>yz</sub> orbital (hybridized with some N sp<sup>2</sup> orbitals) to the π\* orbitals of the ligands.<sup>61</sup> The differences between the complexes in the region above 28 000 cm<sup>-1</sup> are mainly due to the differences in the structure of the ligands (Fig. S7†). The high energy contribution, represented by the simulated transition at 35 000 cm<sup>-1</sup>, is instead due to a second MLCT from the Cu *d*<sub>xy</sub> orbital to the π\* orbitals of the ligands. The identified MLCT is of particular interest since they can be exploited to achieve resonant Raman conditions with opportune excitation wavelengths, thus allowing a preferential enhancement of vibrational modes having the same symmetry as that for the electronic transition (thus strictly related to the Cu<sup>II</sup> cation). One should note that this evidence is not consistent with the UV-Vis spectra of CuBPD (obtained *in situ* in ACN) reported by Sawyer *et al.*,<sup>43</sup> they showed a spectrum without any transition in the visible region. This observation could suggest that the effective formation of a Cu<sup>I</sup>(bpy)<sub>2</sub><sup>+</sup> complex is not occurring under these conditions.

Meaningful changes appear in this region for all complexes upon oxidation: they arise from a combination of structural and electronic effects, as they result from both perturbation of the ligand transitions and differences in the MLCT transitions. On the other hand, the band around 22 000 cm<sup>-1</sup> differs slightly between the complexes, but disappears completely for all of them upon oxidation, with a subsequent appearance of one or two bands in the region between 17 500 and 9 000 cm<sup>-1</sup> (Fig. 2, top frame insets); the latter is assigned to d-d transitions on the metal centre. Interestingly, most complexes show two distinct bands at around 13 700 and 10 000 cm<sup>-1</sup>, likely indicating a geometrical distortion of the d<sup>9</sup> system; the only exception in this trend is that CuBPA is oxidized using NOPF<sub>6</sub>, suggesting differences in the coordination structure of this sample for the two oxidation pathways.

As can be seen in Fig. 2 (bottom frame), CuBPA is also characterized by a peculiar absorption at 26 500 cm<sup>-1</sup> (377 nm) after oxidation with *t*BuOOH (absent when treated with NOPF<sub>6</sub>); the intensity of this peak is five times more intense than the main d-d transition. This band could be fairly attributed to the formation of an oxygenated species (*i.e.* Cu<sup>II</sup>-O(bpy)<sub>2</sub><sup>+</sup>, Cu<sup>II</sup>-OH(bpy)<sub>2</sub><sup>+</sup> or Cu<sup>II</sup>-OOH(bpy)<sub>2</sub><sup>+</sup>, *vide infra*) and it accounts for the different coloration of the *t*BuOOH-oxidized solutions (see Fig. S8†). On the other hand, the spectra of the other samples seem to be very similar, no matter the nature of the oxidant; this could be fairly ascribed to the lower protection offered by the ligands other than BPA. Interestingly, a sizeable drop in the intensity of the d-d transition is observed upon oxidation with NOPF<sub>6</sub>: this is most probably due to solubility issues (bare Cu<sup>2+</sup> complexes are less soluble in DCM than Cu<sup>+</sup> ones), also causing precipitation (*i.e.* a blue precipitate could be detected) and the formation of suspensions, decreasing the collected signal as a consequence of scattering phenomena.

#### Characterization of vibrational modes of the pristine and oxidized complexes

The reaction of Cu complexes in DCM solutions with the *t*BuOOH oxidizing agent has also been followed by Raman



Spectroscopy, adopting the experimental set-up described in the Experimental section and choosing a 244 nm exciting laser line to fully exploit the resonance conditions, thus overcoming possible scarce sensitivity due to the adopted concentration. It is worth mentioning here that DFT calculations are able to properly reproduce the position of the peaks in the Raman spectra of the parent solid powders thus making them valuable support for the interpretation of the data-set presented hereafter. A more detailed analysis is provided in the SI (Fig. S9–S11† and related discussion).

The results are reported in Fig. 3, where the spectra obtained for the pristine/oxidized complexes (solid colored lines) are compared with those obtained for the respective parent ligands (solid grey lines) and bare DCM (solid black line). For the sake of comparison, the Raman spectra obtained for the pristine/oxidized complexes are normalized at the DCM peak falling at 1425  $\text{cm}^{-1}$ . As it can be seen from the reported data, the reaction with *t*BuOOH causes just small variations in the Raman spectra of the complexes when compared to those obtained for the pristine ones; this suggests that the original structure of the Cu containing complexes is maintained after the reaction (also testified by the fact that no clear bands ascribable to bare ligands appear after *t*BuOOH addition), further highlighting the peculiarity of our approach.

However, a closer inspection of the spectra of the CuBPA (see also Fig. S12†) and CuBPD complexes reveals a blue-shift ( $\Delta\nu_1 = +10 \text{ cm}^{-1}$  for both complexes, and  $+20 \text{ cm}^{-1}$  with respect to the bare ligands in the *trans* configuration) of the peaks at 1014  $\text{cm}^{-1}$  and 1028  $\text{cm}^{-1}$  ( $\nu_1^{\text{Cu}}$ ), respectively, after interaction with *t*BuOOH; this shift is very faint in CuBPC and not observable for CuBPB. Furthermore, with respect to the CuBPA complex, a blue-shift of the peak at 1324  $\text{cm}^{-1}$  ( $\nu_2^{\text{Cu}}$ )

can be observed ( $\Delta\nu_2 \sim +10 \text{ cm}^{-1}$ ). From the reported data, it can be concluded that Raman Spectroscopy can be fruitfully used to follow the reactivity of such complexes with respect to oxidizing agents.

### Evidence from the proposed multi-technique approach

The proposed multi-technique approach allows us to highlight a dramatic influence of the nature and the position of a substituent on the oxidation (oxygenation) reaction of 2,2'-bipyridine-based  $\text{Cu}^{\text{I}}$  complexes. As a matter of fact, each technique provides interesting but sometimes partial insights. UV-Vis-NIR spectroscopy shows, after the addition of an appropriate oxidant, the formation of a  $\text{Cu}^{\text{II}}$  species as proved by the occurrence of d-d transitions at higher wavelengths (the inset in the top frame of Fig. 2). Indeed, for CuBPA, the choice of the oxidizing agent seems to be particularly meaningful, leading to different spectra when NOPF<sub>6</sub> is employed in place of *t*BuOOH. Indeed, the peculiar behaviour of CuBPA could be clearly evidenced by the presence of an additional peak at 26 500  $\text{cm}^{-1}$  (CuBPA treated with *t*BuOOH). This unique behaviour of CuBPA could be rationalized by referring to the electrochemical data of all the complexes: CuBPA shows remarkably higher redox potential and, once oxidized, it becomes electrochemically inactive in the investigated potential window; this is a fair evidence that, on the one hand,  $\text{Cu}^{\text{II}}$ BPA is not the (main) result of the oxidation and, on the other hand, the product of the oxidation is stable and does not immediately react with other species or incur in self-oxidation reactions. The other complexes seem to have a different fate as a results of the addition of *t*BuOOH; CuBPC tends to be oxidized to its initial  $\text{Cu}^{2+}$  form as proved by the persistence of the electrochemical reduction peak at 0.27 V and  $\text{Cu}^{\text{II}}$ BPC is particularly stable due to the effect of the methoxy groups close to the copper site. CuBPB and CuBPD, instead, seem to incur in a (partial) self-oxidation reaction as proved by the appearance of an additional oxidation peak at  $V > 0.5 \text{ V}$ .<sup>43</sup> In this context, Raman analyses are very meaningful to highlight that the reaction with *t*BuOOH does not significantly impact the vibrational transitions characteristic of each system, proving that the oxidation process neither dramatically changes the chemical environment of the metal centre nor destroys the ligand.

The findings mentioned above prove that CuBPA shows a peculiar behaviour, likely giving rise to stable oxygenated  $\text{Cu}^{\text{II}}(\text{bpy})_2^+$  species. To further investigate the nature of such species, we performed DFT simulation of the UV-Vis and Raman spectra for some hypothetical structures (whose optimized geometries are reported in Fig. S13†). The outcomes, compared with experimental results, are reported in Fig. 4. By qualitative comparison of the experimental UV-vis spectrum of CuBPA oxidized by *t*BuOOH with the simulated spectra of  $\text{Cu}^{\text{II}}\text{-O}(\text{bpy})_2^+$  and  $\text{Cu}^{\text{II}}\text{-OH}(\text{bpy})_2^+$ , both the models show electronic transitions in the 25 000–30 000  $\text{cm}^{-1}$  region.

In detail, the CuBPA–OH structure better reproduces the experimental profile, with a well-distinguished band peaking at 29 000  $\text{cm}^{-1}$ . This assignment is further confirmed by the good agreement of the calculated d–d transitions for  $\text{Cu}^{\text{II}}\text{-OH}$

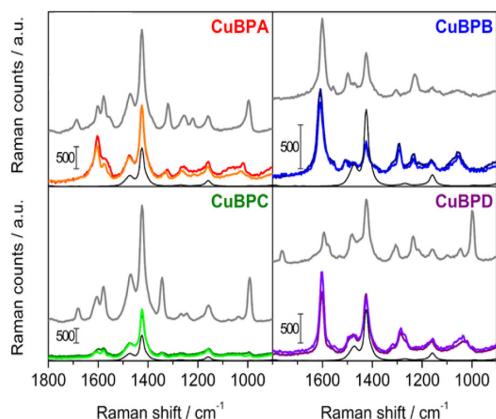
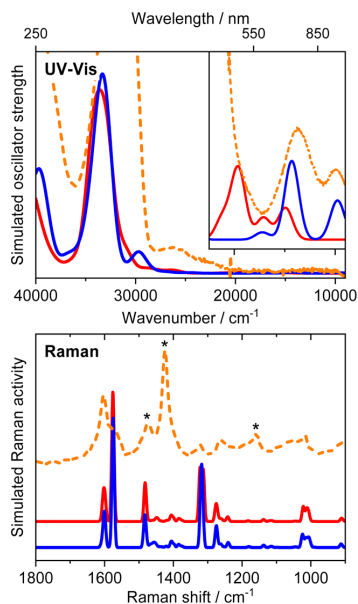


Fig. 3 Raman spectra of DCM solutions of ligands (grey curves), pristine complex and oxidized complexes for CuBPA (red panel), CuBPB (blue panel), CuBPC (green panel), CuBPD (violet panel). In all the panels, darker colour refers to the solution after the addition of *t*BuOOH. DCM spectrum (in black) is reported for the sake of clarity (black curves).





**Fig. 4** Computed (solid lines) UV-Vis (top frame) and Raman (bottom frame) spectra vs. experimental ones (dashed lines) for CuBPA bearing a Cu–O<sub>x</sub> specie: oxy- (red lines) and hydroxo- (blue lines). Experimental UV-Vis has been collected with an optical path of 1 mm. Experimental Raman has been collected with a 244 nm excitation wavelength (asterisks highlight the features of DCM). Simulated spectra have been convoluted with Gaussian functions (FWHM set to 5 cm<sup>-1</sup> for Raman, to 1000 cm<sup>-1</sup> for UV-Vis). Computed vibrational frequencies have been scaled by a multiplicative factor (0.978).

(bpy)<sub>2</sub><sup>+</sup> with those experimentally observed. Other options, such as Cu<sup>II</sup>-OOH(bpy)<sub>2</sub><sup>+</sup> or Cu<sup>II</sup>(bpy)<sub>2</sub><sup>+</sup> (Fig. S14†) seem to be unlikely, showing simulated spectra that sizeably differ from the experimental ones (especially when electronic transitions are considered). One should note that the selected functional and basic set are in line with the ones conventionally exploited in the literature (Table S2†).

This assignment is also supported by the thermodynamic stability of the species, as the Gibbs free energy of formation (calculated according to the reactions shown in Scheme S1†) for Cu<sup>II</sup>-OH(bpy)<sub>2</sub><sup>+</sup> is lower than that of Cu<sup>II</sup>-O(bpy)<sub>2</sub><sup>+</sup> or Cu<sup>II</sup>-OOH(bpy)<sub>2</sub><sup>+</sup> (26.9 kJ mol<sup>-1</sup> vs. 36.3 kJ mol<sup>-1</sup> or 214.8 kJ mol<sup>-1</sup>, respectively). In the case of Raman spectroscopy, unfortunately, specific Cu–O modes are not detectable under the adopted experimental conditions. Nonetheless, the simulated spectra for Cu<sup>II</sup>-O(bpy)<sub>2</sub><sup>+</sup>, Cu<sup>II</sup>-OOH(bpy)<sub>2</sub><sup>+</sup> and Cu<sup>II</sup>-OH(bpy)<sub>2</sub><sup>+</sup> show a shift for the  $\nu_{1}^{\text{Cu}}$  mode observed between +25 and +32 cm<sup>-1</sup> with respect to *trans*-BPA, in line with experimental results. This result confirms that the models correctly account for the screening effect of the O/OH group on the Cu<sup>II</sup> ion, as the  $\Delta\nu_{1}^{\text{Cu}}$  value obtained for an isolated Cu<sup>II</sup> is +38 cm<sup>-1</sup> from simulation (Table S3†). A further confirmation could be obtained from the quite good correlation between *q/r* (the

elementary charge/ionic radius ratio of M<sup>m+</sup>) and computed  $\Delta\nu_{1}$  between pristine *trans*-BPA and *cis*-BPA in the M<sup>+</sup> complex (Fig. S15†) for the calculation performed on M<sup>m+</sup>(*cis*-BPA)<sub>2</sub> (where M<sup>m+</sup> = Li<sup>+</sup>, Na<sup>+</sup>, K<sup>+</sup>, Cu<sup>+</sup>, Be<sup>2+</sup>, Mg<sup>2+</sup> or Ca<sup>2+</sup>); indeed,  $\Delta\nu_{1}^{\text{M}^{m+}} > 0$  has been observed for the BPD interacting with the surface species of SiO<sub>2</sub> and Al<sub>2</sub>O<sub>3</sub>.<sup>62</sup>

Aiming at proving the reversibility of the oxygenation reaction experimented by the Cu site, we treated the oxidized solution with a common oxidizable substrate (*i.e.* cyclohexene); after the addition, the solution of oxidized CuBPA turns to a dark orange solution (*i.e.* the same as pristine CuBPA, *vide infra*). This reversibility is even more clear when the reaction between activated CuBPA and cyclohexene is followed by CV (Fig. S16†): indeed, after the addition, the voltammogram evolves towards the characteristic redox peaks of Cu<sup>I</sup>BPA. Complementary findings have been obtained by coupling Raman (@Elettra synchrotron) and UV-Vis spectroscopy with an *in situ* approach (*vide infra*). However, other complexes, namely CuBPB, CuBPC and CuBPD, do not show the same behaviour: indeed, no remarkable modifications could be evidenced after the addition of cyclohexene, proving that the oxygenated species, if obtained and stable, are not reactive enough (or not able) to promote the oxidation of cyclohexene.

#### Exploitation of the *in situ* synchrotron-based Raman/UV-Vis simultaneous set-up

As proved in the previous section, CuBPA shows a peculiar behaviour compared to the other complexes tested within this work. Electrochemistry proved that once oxidized, CuBPA is able to return to its Cu<sup>I</sup> state when an appropriate reductant is added. This observation is supported by the fact that the most probable species, *i.e.* Cu<sup>II</sup>-OH(bpy)<sub>2</sub><sup>+</sup>, has a slightly positive formation energy (*i.e.* 23.3 kJ mol<sup>-1</sup>), and thus the hydroxyl moiety is potentially reactive toward a reductant. It should be noted that electrochemistry gives meaningful insights into the electroactive species only and, thus, eventual degradation of the complexes or the formation of products of interest could be hardly detectable. Moreover, the continuous supply of electrons (due to the CV approach) could have no trivial effect on reduction reaction catalysis.

To further shed light on the reactivity of the selected complex during its redox cycle, we resolved to joint and simultaneous monitoring of the reaction solution by means of both vibrational and electronic spectroscopy. This allows us to finely detect some modification of the different substrates in the reaction solution. Following this idea, it clearly appears that the adopted exciting laser line (*i.e.* 244 nm) can suffer from sensitivity problems (Fig. 3, red panel): in fact,  $\nu_{1}^{\text{Cu}}$ , even if still visible, undergoes a drastic loss in intensity after CuBPA reacts with *t*BuOOH. This is mainly ascribable to a change in energy for reaching resonance conditions in the reacted system, limiting our ability to finely follow the redox cycle. To avoid this, at the synchrotron facility Elettra, we finely screened the excitation wavelengths (*i.e.* 226 nm, 244 nm and 266 nm) and by selecting the 266 nm line we were able to obtain clear spectra for all the tested solutions. The major drawback in the





employment of synchrotron radiation is the relatively low intensity of the incident radiation in the exploited range, forcing us to use relatively long acquisition times and to average the measurements on 3 scans at least. It was possible to record one Raman spectrum every 30 minutes, much slower than the time resolution ensured by the UV-Vis-NIR set-up (one spectrum each minute). The effect of oxidant (*i.e.* *t*BuOOH) and (then) reductant (*i.e.* cyclohexene) addition could be finely followed by means of UV-Vis-NIR spectroscopy (Fig. S17<sup>†</sup>); as soon as *t*BuOOH is added to a 1 mM solution of CuBPA, the intensity of the characteristic absorption peak starts to slowly but constantly decrease and simultaneously a broad peak (at 26 500  $\text{cm}^{-1}$ ) grows. After 150 minutes, the electronic spectrum of oxidized CuBPA is invariant. At this stage, the Raman spectrum of the same solution (green profile in Fig. 5) presents two main differences compared to the spec-

trum recorded at  $t = 0$  (red profile in Fig. 5): a clear shift toward a lower Raman shift of the band at 1050  $\text{cm}^{-1}$  and a broadening of the peak at 1600  $\text{cm}^{-1}$ . The former is directly related to the change in the coordination of the metal ion, and it is consistent with the formation of a  $\text{Cu}^{\text{II}}\text{-OH}(\text{bpy})_2^+$  species (*vide supra*), whereas the latter is directly related to the vibrational modes of the bipyridine ring and, thus, less sensitive to the charge state of the metal. This could be ascribable both to a change in the geometry of the ligand and to the irreversible oxidation of the latter. To check this and to eventually prove the reversibility of the oxidation process of the Cu centre, we added an equimolar (with respect to *t*BuOOH) amount of cyclohexene. Following this addition, the UV-Vis-NIR (Raman) spectrum of the solution starts to rapidly evolve, and the recovery of the peak centred at 22 000  $\text{cm}^{-1}$  can be easily detected. After only 90 minutes from the addition ( $t =$

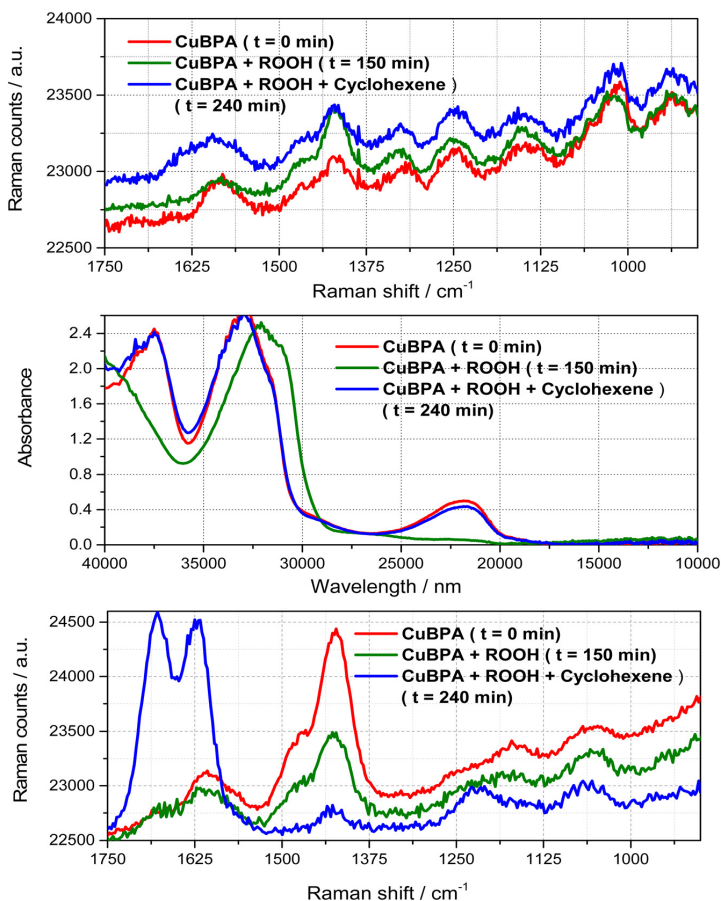


Fig. 5 Synchrotron Raman (top) and UV-Vis-NIR (middle) spectra of pristine CuBPA solution (1 mM in DCM, red lines) and after the addition of *t*BuOOH (green lines) and cyclohexene (blue lines). Measurements are made simultaneously on the same solution exploiting the custom-made set-up described above (Raman exciting wavelength = 266 nm). Synchrotron Raman spectrum recorded with an exciting wavelength of 226 nm (bottom) in the same conditions.



240 minutes), the peak is completely recovered (the discrepancy in the absorbance value is due to the dilution of the solution caused by the addition of oxidant and reductant solutions). After 240 minutes, the Raman spectrum (blue curves in Fig. 5) also shows the same vibrational mode of the pristine solution. The only difference is due to the rise of a broad contribution in the 1688–1620  $\text{cm}^{-1}$  range, *i.e.* at frequencies quite different from that characterizing C=C stretching in cyclohexene (1651  $\text{cm}^{-1}$ ), thereby suggesting that new species are formed; unfortunately, resonance conditions obtained for CuBPA employing exciting light falling at 266 nm prevent the obtaining of much more clear signals. For this reason, the same reaction has been followed by adopting exciting light at 226 nm: the results are reported in the bottom panel of Fig. 5. It is worth noting here that under such conditions the broad signal is substituted by two narrower peaks centred at 1680 and 1620  $\text{cm}^{-1}$  respectively, the highest one witnessing for the presence of a carboxylic species (*i.e.* C=O stretching) and the lowest for a conjugated C=C, probably the cyclohexanone that is one of the oxidation products of cyclohexene.<sup>10,30,43</sup> The presence of both cyclohexanone and cyclohexen-2-one (compatible with the vibration at 1620  $\text{cm}^{-1}$ ) has been further confirmed by GC-MS analyses (Fig. S18†). It should be noted that the MS spectrum of cyclohexanone is slightly more complicated than expected due to the dynamic equilibrium with cyclohex-1-en-1-ol (its enolic tautomer). We would like to stress that GC-MS spectra were collected as a control to justify the arising spectroscopic features. A more detailed analysis of the obtained products and the extension of the reaction scope will be discussed in a forthcoming paper.

## Experimental

### Materials and methods

All chemicals and solvents used were purchased from Merck (if not differently specified) and employed without further purification. 5,5'-Dimethyl-2,2'-bipyridine, 6,6'-dimethyl-2,2'-bipyridine and *tert*-butyl hydroperoxide were purchased from TCI. Copper complexes were synthesized under a  $\text{N}_2$  atmosphere to prevent the oxidation of the metal centre and were obtained in excellent yield (>95%), according to a literature procedure. To oxidize the metal centre to  $\text{Cu}^{\text{II}}$ , hydrogen peroxide (30% in water), nitrosium hexafluorophosphate and *tert*-butyl hydroperoxide (5.5 M in decane) were employed in appropriate ratios; cyclohexene was then used as an oxidizable substrate to verify the reversibility of the oxidation/oxygenation of the metal centre. A multi-technique approach was used to follow the redox cycle: cyclic voltammetry, Raman and UV-Vis-NIR.

### Synthetic procedures

**Synthesis of the ligand 6,6'-dimethoxy-2,2'-bipyridyl (BPC).** The 6,6'-dimethoxy-2,2'-bipyridyl ligand was synthesized under a  $\text{N}_2$  atmosphere to minimize the presence of water in the reaction mixture, according to a literature procedure.<sup>26</sup> A white

solid was obtained with 80% yield (0340 g).  $^1\text{H}$  NMR ( $\text{CDCl}_3$ ):  $\delta$  = 8.02 (2H, d), 7.68 (2H, dd), 6.75 (2H, d), 4.04 (6H, s).

**General synthesis of copper(i) complexes.** Copper complexes were synthesized following the literature reports<sup>51</sup> by mixing tetrakis(acetonitrile)copper(i) hexafluorophosphate and the bipyridine ligand (1 : 2 ratio) in anhydrous  $\text{CH}_2\text{Cl}_2$ . The solution was stirred under a  $\text{N}_2$  atmosphere for three hours and, after stripping the solvent, the product was obtained as a coloured powder in excellent yield.

**[Cu(6,6'-dimethyl-2,2'-bipyridyl)]<sub>2</sub> (PF<sub>6</sub>) (CuBPA).** Following the above-mentioned general procedure, 0.98 g of the desired complex was obtained as a red powder with a yield of 98%.  $^1\text{H}$  NMR (600 MHz,  $(\text{CD}_3)_2\text{CO}$ )  $\delta$  8.55 (d,  $J$  = 8 Hz, 1H), 8.20 (t,  $J$  = 8 Hz, 1H), 7.69 (d,  $J$  = 8 Hz, 1H), 2.35 (s, 3H), 2.09 (solvent residual peak).

**[Cu(5,5'-dimethyl-2,2'-bipyridyl)]<sub>2</sub> (PF<sub>6</sub>) (CuBPB).** Following the above-mentioned general procedure, 0.95 g of the desired complex was obtained as a violet powder with a yield of 95%.  $^1\text{H}$  NMR (600 MHz,  $(\text{CD}_3)_2\text{CO}$ )  $\delta$  8.62 (d,  $J$  = 8 Hz, 1H), 8.58 (s, 1H), 8.13 (d,  $J$  = 8 Hz, 1H), 2.45 (s, 3H), 2.09 (solvent residual peak).

**[Cu(6,6'-dimethoxy-2,2'-bipyridyl)]<sub>2</sub> (PF<sub>6</sub>) (CuBPC).** Following the above-mentioned general procedure, 0.97 g of the desired complex was obtained as a dark powder with a yield of 97%.  $^1\text{H}$  NMR (600 MHz,  $(\text{CD}_3)_2\text{CO}$ )  $\delta$  8.27 (m, 2H), 7.32 (d,  $J$  = 7 Hz, 1H), 3.76 (s, 3H), 2.09 (solvent residual peak).

**[Cu(2,2'-bipyridyl)]<sub>2</sub> (PF<sub>6</sub>) (CuBPD).** Following the above-mentioned general procedure, 0.97 g of the desired complex was obtained as a brown powder with a yield of 97%.  $^1\text{H}$  NMR (600 MHz,  $(\text{CD}_3)_2\text{CO}$ )  $\delta$  8.81 (s, 1H), 8.35 (s, 1H), 7.82 (s, 1H), 2.09 (solvent residual peak).

**NMR spectra details.** The NMR spectra were recorded on a Jeol ECZ-R 600 MHz instrument, in  $(\text{CD}_3)_2\text{CO}$ , using the residual solvent peak as an internal reference ( $(\text{CD}_3)_2\text{CO}$ ,  $^1\text{H}$ : 2.09 ppm).<sup>63</sup> All the chemical shifts are reported in delta ( $\delta$ ) units. Coupling constants are reported in Hertz (Hz). Multiplicity is reported as follows: s (singlet), d (doublet), t (triplet), and m (multiplet). For each experiment, 8 scans were used with 5 s of relaxation and an acquisition time of 2.9 s. The spectra were recorded at  $-40$  °C (Fig. S19–S22†).

**Computational details.** DFT simulations on Cu-complexes were performed with the Gaussian G16 (rev. B.01) code<sup>64</sup> by exploiting the hybrid B3LYP functional.<sup>65</sup> Unrestricted wavefunctions were adopted for all calculations, also when considering singlet states. Spin multiplicity was set to 1 (singlet state) for the initial  $\text{Cu}^{\text{I}}$  structures, whereas it was set to 2 (doublet) for  $\text{Cu}^{\text{II}}$  and hydro(pero)xo or 3 (triplet) for  $\text{Cu}^{\text{II}}$  oxyl models. The def2-TZVP basis set developed by Ahlrichs and co-workers<sup>66</sup> was adopted in the description of all atoms. Dispersive forces were included in the calculation through the Grimme D3 empirical scheme with Becke–Johnson damping.<sup>67</sup> The effect of solvation was implicitly accounted for *via* the polarizable conductor calculation model (CPCM) method.<sup>68,69</sup>

Fig. S3† shows the structure of the structural models adopted in the calculations of the starting  $\text{Cu}^{\text{I}}$  complexes. Their structure was manually constructed by positioning the



two bipyridyl ligands, oriented with the N atoms tetrahedrally coordinating the Cu atom at a distance of 2.0 Å. Counterion(s) were not included in the structural model. These initial models were geometrically optimized, and vibrational frequencies (including IR and Raman intensities) were computed. The absence of imaginary frequencies confirmed that minimum structures were obtained. From the optimized structures of the Cu<sup>I</sup> complexes, Cu<sup>II</sup> models were constructed by imposing the correct charge-spin, further optimized and adopted in frequency calculations. For the only CuBPA complex, we also simulated some hypothetical structures of Cu–O<sub>x</sub> species, as expected to form upon interaction with *t*BuOOH, namely: Cu<sup>II</sup>–O(bpy)<sub>2</sub><sup>+</sup> (oxyl), Cu<sup>II</sup>–OH(bpy)<sub>2</sub><sup>+</sup> (hydroxo) and Cu<sup>II</sup>–OOH(bpy)<sub>2</sub><sup>+</sup> (hydroperoxyl). Their optimized structures are shown in Fig. S13.† The main geometrical parameters for each model and their computed Cu<sup>I</sup>/Cu<sup>II</sup> oxidation potentials are reported in Tables S1 and S2.†

**UV-Vis spectroscopic characterization.** UV-Vis-NIR spectroscopy was performed on the samples with an Avantes AvaSpec-ULS2048XL-EVO fibre optics spectrometer (25 μm slits), coupled to an Avantes AvaLight-DH-S light source (equipped with a deuterium and a halogen lamp). Fibre optics with a high-OH fused silica core of 100 μm in diameter were used. Integration times and averaging were optimized for each sample to guarantee the best compromise between spectral and time resolution. The solutions were examined using Hellma flow-through high-performance quartz glass (QS grade) cuvettes with screw connections; depending on the concentration, a cuvette with an appropriate optical path length was selected between 0.1, 1 and 10 mm. The flow was regulated between the cuvette (s) and the liquid reservoir by means of a peristaltic pump using FEP (fluorinated ethylene propylene), PTFE (polytetrafluoroethylene) and fluorinated rubber connections.

**Raman spectra of the solid powders of the Cu complexes.** The whole set of Cu-based [2-2'-Bpy] homoleptic complexes in the form of solid powders were investigated through Raman Spectroscopy in order to obtain their major vibrational features. For the sake of comparison, all the parent [2-2'-Bpy] based ligands were also measured. Two different exciting laser lines (hereafter ELL) were adopted, emitting respectively at 785 nm (12 739 cm<sup>-1</sup>) and 244 nm (40 984 cm<sup>-1</sup>). Measurements were performed on a Renishaw Raman microscope equipped respectively with an Olympus 20× ULWD (NA = 0.40) and a Thorlabs UV-B 15× (NA = 0.31) objective through which the EEL was focused on the sample. The resulting back-scattered light (collected through the objectives described above) was then analysed respectively through 1200 l mm<sup>-1</sup> and 3600 l mm<sup>-1</sup> gratings. In order to prevent the possible thermal degradation of the investigated samples induced by the focused ELL, custom-made apparatus which allows holder movement (rotation) during measurements was adopted.<sup>70</sup> The presented spectra were obtained by averaging 3 consecutive measurements (from which the stability of the sample during the measurement was confirmed), each one resulting from the sum of 10 acquisitions of 20 s (ELL = 785 nm) or the sum of 20 acquisitions of 20 s each (ELL = 244 nm).

### Raman spectra of the DCM solutions of the Cu complexes.

Raman spectroscopy was adopted, as a complement to other techniques, to characterize, from a vibrational point of view, the whole set of Cu based [2,2'-bpy] homoleptic complexes (and, for the sake of comparison, their parent 2,2'-bpy based ligands) in the form of DCM solutions (a nominal concentration of 1 mM). Furthermore, a deep analysis of the obtained Raman spectra helped to get insights into the species formed when *tert*-butyl hydroperoxide was added in preparing the DCM solutions of such complexes. To overcome the possible drawbacks due to the low concentration, the 244 nm (40 984 cm<sup>-1</sup>) ELL was adopted in order to exploit as much as possible the Resonant conditions. Measurements were performed on a Renishaw Raman Microscope equipped with a 15× (NA = 0.31) objective through which the ELL was focused on the sample. The resulting back-scattered light (collected through the objective) was then analysed by 3600 l mm<sup>-1</sup> grating. Measurements were performed on the DCM solutions of the complexes placed in UV-Vis Hellma quartz (QS grade) cuvettes: the solutions were magnetically stirred continuously during the measurement thanks to the apparatus already described.<sup>70</sup> The presented spectra were obtained by averaging 3 consecutive measurements (from which the stability of the sample along the measurement was confirmed), each one resulting from the sum of 20 acquisitions of 20 s each.

### Electrochemical characterization (cyclic voltammetry).

Electrochemical characterization (cyclic voltammetry, CV) was performed by means of a BioLogic sp150 potentiostat. A three-electrode set-up was employed with a Pt disc (diameter = 5 mm) as the working electrode, a Pt wire as the counter-electrode and Ag/AgCl as the reference electrode. For the analysis of the Cu<sup>I</sup> species, the complexes were dissolved (5 mM) in a solution of DCM containing tetrabutylammonium hexafluorophosphate (TBAPF<sub>6</sub>, 0.1 M) as the supporting electrolyte. CVs were recorded at 100 mV s<sup>-1</sup>. Before each measurement, the electrolyte was degassed with Argon to avoid the presence of oxygen. To analyse the oxidized sample, 0.1 ml of the *t*BuOOH solution was added to the Cu<sup>I</sup> solution. A similar approach was employed when the effect of the cyclohexene as a reductant was investigated.

**Raman spectra of the DCM solutions of the Cu complexes at the IUVS beamline.** *In situ* Raman measurements on the systems described above were also performed by exploiting the facilities available at the BL10.2-IUVS beamline of Elettra Sincrotrone Trieste (Italy).<sup>71</sup> After the initial screening of some of the available exciting wavelengths, we resolved to use 266 nm (4.66 eV, 37 594 cm<sup>-1</sup>) by regulating the undulator gap and using a Czerny-Turner monochromator (Acton SP2750, Princeton Instruments, Acton, MA, USA) equipped with a holographic grating at 1800 l mm<sup>-1</sup> to monochromatize the incoming synchrotron radiation. Raman spectra were obtained in a back-scattered geometry by using a triple-stage spectrometer (Trivista, Princeton Instruments, Acton, MA, USA) with a spectral resolution of 2.3 cm<sup>-1</sup> per pixel. Calibration of the spectrometer was standardized using cyclohexane. The possible photo/thermal damage effect due to the prolonged exposure of



the sample to exciting radiation was reduced by continuously moving the sample cell (UV-Vis Hellma quartz glass cuvette, QS grade) during the measurements. Each measurement consists of 30 scans of 30 seconds each, and then it is averaged between three successive scans.

**UV-Vis/Raman simultaneous analyses at synchrotron.** To provide simultaneous evidence on both the electronic transitions (UV-Vis-NIR) and vibrational modes (Raman, 266 or 226 nm exciting wavelength) of the selected complex undergoing a redox cycle, *i.e.* oxidation and reduction, a custom-made set-up was also employed (see Fig. S23†). This consists of a three-necked flask within which the investigated solution was allowed to recirculate thanks to a peristaltic pump. Two of the necks are closed with a PTFE stopper with two holes for the inlet and outlet tubes (1/16 inches diameter, in PTFE). The former goes from the flask (behaving as a reservoir) to the Raman (or UV-Vis-NIR) cuvette, whereas the latter makes the opposite. This system allows one to obtain a continuous flow of the solution. The reservoir is located halfway between the Raman and UV-Vis-NIR cuvettes to ensure the simultaneity between the two measurements. One should note that UV-Vis-NIR spectra were recorded each minute, whereas Raman spectra were recorded with a lower time resolution (each 15 minutes). The addition of the oxidant (and then of the reductant) was performed directly within the flask.

**Gas chromatography/mass spectroscopy coupled analyses.** GC-MS analyses were carried out on a trace Polaris q (by ThermoFischer), implemented with an Rxi 5Sil MS column (30 mm 0.25 mm 0.25 $\mu$ m) with a Splitless injector using Helium (1 ml min<sup>-1</sup>) as the gas carrier. The oven was initially set at 35 °C and the temperature was increased up to 150 °C (ramp 10 °C min<sup>-1</sup>). The gas was detected by using an EI-Mass Spectrometer ( $T_{\text{source}} = 200$  °C) working in the scan mode ( $m/z = 40\text{--}150$ ) by means of an ionic trap analyser.

## Conclusions

Throughout this paper, the redox behaviour of homoleptic copper 2,2'-bipyridine-based complexes toward the reaction with specific oxidants has been investigated by means of a multi-technique approach coupling electrochemistry and vibrational/electronic spectroscopy and supported by computational data. The selected complexes differ in the nature and the position of the substituent on the ligand skeleton. This has a dramatic influence on both the stability and the redox potential of the resulting complexes. Indeed, only CuBPA (*i.e.* [Cu(6,6'-dimethyl-2,2'-bipyridyl)<sub>2</sub>](PF<sub>6</sub>) complex) exhibits a peculiar behaviour in the reaction with specific oxidants (*i.e.* *t*BuOOH or NOPF<sub>6</sub>); indeed, the spectroscopic and electrochemical characterization of CuBPA gave some evidence of the formation of a (stable) Cu<sup>II</sup> hydroxyl-species when reacted with *t*BuOOH, as proved by the appearance of an absorption peak at *ca.* 26 500 cm<sup>-1</sup> (UV-Vis-NIR) and a marked shift of the peak located at 1014 cm<sup>-1</sup> (Raman). By means of DFT calculations, this relatively stable oxygen-containing species was identified

as Cu<sup>II</sup>-OH(bpy)<sub>2</sub><sup>+</sup>. These findings push us to further investigate the redox reactivity of CuBPA by means of a simultaneous UV-Vis-NIR/Raman experiment taking advantage of synchrotron facilities at Elettra: the formation of an oxygen-modified Cu<sup>II</sup> species after the reaction with *t*BuOOH has been confirmed. Additionally, the latter could oxidize relatively fast a target compound (*i.e.* cyclohexene) and quantitatively form back the Cu<sup>I</sup> complex, as also confirmed by electrochemical measurements. It should be noted that the specific reaction mechanism of the redox cycle is still under investigation taking advantage of both laboratories and synchrotron light-based experiments, but some oxygenated products have been already detected. The above-reported results open the way toward the application of Cu(BPA) as a precursor of a class of properly designed (homoleptic) copper bipyridine complexes in oxygenation reactions among which the Direct Methane to Methanol reaction is the most challenging one.

## Author contributions

Conceptualization: C.B., M.B., and S.B. Data curation: B.C., G. D., A.D., M.S., and M.B. Formal analysis: B.C., G.D., A.D., M.S., and M.B. Funding acquisition: S.B. and C.B. Investigation: B. C., G.D., A.D., M.S., and M.B. Methodology: A.D., M.S., M.T., C.B., M.B., and S.B. Project administration: S.B. Resources: A. D., M.S., C.B., M.B. and S.B. Software: A.D. and M.S. Supervision: S.B., C.B., and M.B. Validation: B.C., G.D., A.D., M.S., and M.B. Visualization: B.C., G.D., A.D., and M.S., M.B. Writing - original draft: B.C., G.D., A.D., and M.B. Writing - review & editing: B.C., G.D., M.B., C.B., and S.B.

## Conflicts of interest

The authors have no conflict of interest to declare.

## Acknowledgements

The authors acknowledge the funding from Horizon 2020 Excellence Science ERC-Synergy program 2019-CUBE: "Unravelling the secrets of Cu-based catalysts for C-H activation" (grant agreement no. 856446). The authors acknowledge the CERIC-ERIC Consortium (project number 20207012, "Redox chemistry of model Cu complexes for direct alkane to alcohol conversion investigated by *in situ/operando* UV-Raman spectroscopy) for access to IUVS beamline facility at Elettra and financial support. The authors acknowledge the C3S consortium for granting computational resources on the OCCAM cluster, funded by the Compagnia di San Paolo. The authors thank the European Regional Development Fund and Interreg V-A Italy Austria 2014-2020 through the Interreg Italy-Austria project ITAT 1059 InCIMA4 "InCIMA for Science and SMEs". The authors are strongly indebted to Dr Alessandro Gessini and Dr Barbara Rossi (IUVS beamline staff) for technical support and to Dr Roberto Buscaino for the GC-MS measure-



ments. Dr Natale Porcaro is acknowledged for his help in the laboratory.

## Notes and references

- V. M. Goldschmidt, *J. Chem. Soc.*, 1937, 655–673.
- Copper – Element information, properties and uses | Periodic Table, <https://www.rsc.org/periodic-table/element/29/copper>, (accessed 11 July 2021).
- U.S. Geological Survey, <https://minerals.usgs.gov/minerals/>.
- P. Nuss and M. J. Eckelman, *PLoS One*, 2014, **9**, e101298.
- M. Soulier, S. Glöser-Chahoud, D. Goldmann and L. A. Tercero Espinoza, *Resour., Conserv. Recycl.*, 2018, **129**, 143–152.
- R. Trammell, K. Rajabimoghdam and I. Garcia-Bosch, *Chem. Rev.*, 2019, **119**, 2954–3031.
- C. E. Elwell, N. L. Gagnon, B. D. Neisen, D. Dhar, A. D. Spaeth, G. M. Yee and W. B. Tolman, *Chem. Rev.*, 2017, **117**, 2059–2107.
- Y. S. Wei, M. Zhang, R. Zou and Q. Xu, *Chem. Rev.*, 2020, **120**, 12089–12174.
- J. Baek, B. Rungtaweeworanit, X. Pei, M. Park, S. C. Fakra, Y. S. Liu, R. Mathew, S. A. Alshimri, S. Alshehri, C. A. Trickett, G. A. Somorjai and O. M. Yaghi, *J. Am. Chem. Soc.*, 2018, **140**, 18208–18216.
- X. Feng, Y. Song, J. S. Chen, Z. Xu, S. J. Dunn and W. Lin, *J. Am. Chem. Soc.*, 2021, **143**, 1107–1118.
- L. Marais, H. C. M. Vosloo and A. J. Swarts, *Coord. Chem. Rev.*, 2021, **440**, 213958.
- C. Kaes, A. Katz and M. W. Hosseini, *Chem. Rev.*, 2000, **100**, 3553–3590.
- M. Magni, A. Colombo, C. Dragonetti and P. Mussini, *Electrochim. Acta*, 2014, **141**, 324–330.
- D. B. Rorabacher, *Chem. Rev.*, 2004, **104**, 651–697.
- S. Hattori, Y. Wada, S. Yanagida and S. Fukuzumi, *J. Am. Chem. Soc.*, 2005, **127**, 9648–9654.
- C.-W. Lee and F. C. Ansen, *J. Phys. Chem.*, 1983, **87**, 3360–3362.
- R. K. Kokal, S. Bhattacharya, L. S. Cardoso, P. B. Miranda, V. R. Soma, P. Chetti, D. Melepurath and S. S. K. Raavi, *Sol. Energy*, 2019, **188**, 913–923.
- S. Maity, S. Kundu, T. Weyhermüller and P. Ghosh, *Inorg. Chem.*, 2015, **54**, 1300–1313.
- L. Kavan, Y. Saygili, M. Freitag, S. M. Zakeeruddin, A. Hagfeldt and M. Grätzel, *Electrochim. Acta*, 2017, **227**, 194–202.
- E. Tanaka, H. Michaels, M. Freitag and N. Robertson, *J. Mater. Chem. A*, 2020, **8**, 1279–1287.
- A. Glinka, M. Gierszewski, B. Gierczyk, G. Burdziński, H. Michaels, M. Freitag and M. Ziółek, *J. Phys. Chem. C*, 2020, **124**, 2895–2906.
- Y. Saygili, M. Stojanovic, H.-S. Kim, J. Teuscher, R. Scopelliti, M. Freitag, S. M. Zakeeruddin, J.-E. Moser, M. Grätzel and A. Hagfeldt, *J. Phys. Chem. C*, 2020, **124**, 7071–7081.
- Y. Saygili, M. Söderberg, N. Pellet, F. Giordano, Y. Cao, A. B. Munoz-García, S. M. Zakeeruddin, N. Vlachopoulos, M. Pavone, G. Boschloo, L. Kavan, J. E. Moser, M. Grätzel, A. Hagfeldt and M. Freitag, *J. Am. Chem. Soc.*, 2016, **138**, 15087–15096.
- C. Barolo, J. H. Yum, E. Artuso, N. Barbero, D. Dicenso, M. G. Lobello, S. Fantacci, F. Deangelis, M. Grätzel, M. K. Nazeeruddin and G. Viscardi, *ChemSusChem*, 2013, **6**, 2170–2180.
- E. C. Constable, A. H. Redondo, C. E. Housecroft, M. Neuburger and S. Schaffner, *J. Chem. Soc., Dalton Trans.*, 2009, 6634–6644.
- E. Fresta, G. Volpi, M. Milanese, C. Garino, C. Barolo and R. D. Costa, *Inorg. Chem.*, 2018, **57**, 10469–10479.
- M. D. Weber, C. Garino, G. Volpi, E. Casamassa, M. Milanese, C. Barolo and R. D. Costa, *Dalton Trans.*, 2016, **45**, 8984–8993.
- H. L. Kwong, W. S. Lee, H. F. Ng, W. H. Chiu and W. T. Wong, *J. Chem. Soc., Dalton Trans.*, 1998, 1043–1046.
- X. Li, B. Zhang, R. Van Zeeland, L. Tang, Y. Pei, Z. Qi, T. W. Goh, L. M. Stanley and W. Huang, *Catal. Lett.*, 2018, **148**, 940–945.
- J. M. Hoover and S. S. Stahl, *J. Am. Chem. Soc.*, 2011, **133**, 16901–16910.
- J. E. Steves and S. S. Stahl, *J. Am. Chem. Soc.*, 2013, **135**, 15742–15745.
- J. Kim and S. S. Stahl, *ACS Catal.*, 2013, **3**, 1652–1656.
- X. Xie and S. S. Stahl, *J. Am. Chem. Soc.*, 2015, **137**, 3767–3770.
- P. Gamez, I. W. C. E. Arends, J. Reedijk and R. A. Sheldon, *Chem. Commun.*, 2003, **3**, 2414–2415.
- T. Sonobe, K. Oisaki and M. Kanai, *Chem. Sci.*, 2012, **3**, 3249–3255.
- Y. F. Wang, H. Chen, X. Zhu and S. Chiba, *J. Am. Chem. Soc.*, 2012, **134**, 11980–11983.
- T. Toyao, K. Miyahara, M. Fujiwaki, T. H. Kim, S. Dohshi, Y. Horiuchi and M. Matsuoka, *J. Phys. Chem. C*, 2015, **119**, 8131–8137.
- D. Jiang, T. Mallat, D. M. Meier, A. Urakawa and A. Baiker, *J. Catal.*, 2010, **270**, 26–33.
- B. Louis, C. Detoni, N. M. F. Carvalho, C. D. Duarte and O. A. C. Antunes, *Appl. Catal., A*, 2009, **360**, 218–225.
- G. B. Shul'pin, Y. N. Kozlov and L. S. Shul'pina, *Catalysts*, 2019, **9**, 1046.
- I. Garcia-Bosch and M. A. Siegler, *Angew. Chem., Int. Ed.*, 2016, **55**, 12873–12876.
- K. Choroba, B. Machura, S. Kula, L. R. Raposo, A. R. Fernandes, R. Kruszynski, K. Erfurt, L. S. Shul'Pina, Y. N. Kozlov and G. B. Shul'Pin, *Dalton Trans.*, 2019, **48**, 12656–12673.
- A. Sobkowiak, A. Qui, X. Liu, A. Llobet and D. T. Sawyer, *J. Am. Chem. Soc.*, 1993, **115**, 609–614.
- H. Korpi, V. Sippola, I. Filpponen, J. Sipilä, O. Krause, M. Leskelä and T. Repo, *Appl. Catal., A*, 2006, **302**, 250–256.



- 45 B. Herzigkeit, B. M. Flöser, T. A. Engesser, C. Näther and F. Tuczek, *Eur. J. Inorg. Chem.*, 2018, **2018**, 3058–3069.
- 46 V. Leandri, Q. Daniel, H. Chen, L. Sun, J. M. Gardner and L. Kloo, *Inorg. Chem.*, 2018, **57**, 4556–4562.
- 47 F. Xu, T. Tao, K. Zhang, X. X. Wang, W. Huang and X. Z. You, *Dalton Trans.*, 2013, **42**, 3631–3645.
- 48 M. Munakata, S. Kitagawa and M. Miyazima, *Inorg. Chem.*, 1985, **24**, 1638–1643.
- 49 L. Palacios, A. Di Giuseppe, R. Castarlenas, F. J. Lahoz, J. J. Pérez-Torrente and L. A. Oro, *Dalton Trans.*, 2015, **44**, 5777–5789.
- 50 L. S. Shul'pina, M. M. Vinogradov, Y. N. Kozlov, Y. V. Nelyubina, N. S. Ikonnikov and G. B. Shul'pin, *Inorg. Chim. Acta*, 2020, **512**, 119889.
- 51 M. Giordano, G. Volpi, M. Bonomo, P. Mariani, C. Garino and G. Viscardi, *New J. Chem.*, 2021, **45**, 15303–15311.
- 52 L. Aronne, B. C. Dunn, J. R. Vyvyan, C. W. Souvignier, M. J. Mayer, T. A. Howard, C. A. Salhi, S. N. Goldie, L. A. Ochrymowycz and D. B. Rorabacher, *Inorg. Chem.*, 1995, **34**, 357–369.
- 53 M. Salavati-Niasari, P. Salemi and F. Davar, *J. Mol. Catal. A: Chem.*, 2005, **238**, 215–222.
- 54 C. J. Marzocco, *J. Chem. Educ.*, 1999, **76**, 1517.
- 55 Y. Lu, D. Ng and M. S. Mannan, *Ind. Eng. Chem. Res.*, 2011, **50**, 1515–1522.
- 56 G. A. Mabbott, *J. Chem. Educ.*, 1983, **60**, 697.
- 57 F. Brunner, Y. M. Klein, S. Keller, C. D. Morris, A. Prescimone, E. C. Constable and C. E. Housecroft, *RSC Adv.*, 2015, **5**, 58694–58703.
- 58 N. Elgrishi, K. J. Rountree, B. D. McCarthy, E. S. Rountree, T. T. Eisenhart and J. L. Dempsey, *J. Chem. Educ.*, 2018, **95**, 197–206.
- 59 F. Roncaroli, M. Videla, L. D. Slep and J. A. Olabe, *Coord. Chem. Rev.*, 2007, **251**, 1903–1930.
- 60 C. M. Gallego, C. Gaviglio, Y. Ben-David, D. Milstein, F. Doctorovich and J. Pellegrino, *Dalton Trans.*, 2020, **49**, 7093–7108.
- 61 S. Keller, E. C. Constable, C. E. Housecroft, M. Neuburger, A. Prescimone, G. Longo, A. Pertegás, M. Sessolo and H. J. Bolink, *Dalton Trans.*, 2014, **43**, 16593–16596.
- 62 S. A. Bagshaw and R. P. Cooney, *J. Mater. Chem.*, 1994, **4**, 557–563.
- 63 H. E. Gottlieb, V. Kotlyar and A. Nudelman, *J. Org. Chem.*, 1997, **62**, 7512–7515.
- 64 M. J. Frisch, G. W. Trucks, H. B. Schlegel, G. E. Scuseria, M. A. Robb, J. R. Cheeseman, G. Scalmani, V. Barone, G. A. Petersson, H. Nakatsuji, X. Li, M. Caricato, A. V. Marenich, J. Bloino, B. G. Janesko, R. Gomperts, B. Mennucci, H. P. Hratchian, J. V. Ortiz, A. F. Izmaylov, J. L. Sonnenberg, D. Williams-Young, F. Ding, F. Lipparini, F. Egidi, J. Goings, B. Peng, A. Petrone, T. Henderson, D. Ranasinghe, V. G. Zakrzewski, J. Gao, N. Rega, G. Zheng, W. Liang, M. Hada, M. Ehara, K. Toyota, R. Fukuda, J. Hasegawa, M. Ishida, T. Nakajima, Y. Honda, O. Kitao, H. Nakai, T. Vreven, K. J. A. Throssell, Jr. Montgomery, J. E. Peralta, F. Ogliaro, M. J. Bearpark, J. J. Heyd, E. N. Brothers, K. N. Kudin, V. N. Staroverov, T. A. Keith, R. Kobayashi, J. Normand, K. Raghavachari, A. P. Rendell, J. C. Burant, S. S. Iyengar, J. Tomasi, M. Cossi, J. M. Millam, M. Klene, C. Adamo, R. Cammi, J. W. Ochterski, R. L. Martin, K. Morokuma, O. Farkas, J. B. Foresman and D. J. Fox, *Gaussian G16 (rev. B.01)*, 2016.
- 65 A. D. Becke, *J. Chem. Phys.*, 1993, **98**, 1372–1377.
- 66 F. Weigend and R. Ahlrichs, *Phys. Chem. Chem. Phys.*, 2005, **7**, 3297–3305.
- 67 S. Grimme, S. Ehrlich and L. Goerigk, *J. Comput. Chem.*, 2011, **32**, 1456–1465.
- 68 V. Barone and M. Cossi, *J. Phys. Chem. A*, 1998, **102**, 1995–2001.
- 69 M. Cossi, N. Rega, G. Scalmani and V. Barone, *J. Comput. Chem.*, 2003, **24**, 669–681.
- 70 M. Signorile, F. Bonino, A. Damin and S. Bordiga, *Top. Catal.*, 2018, **61**, 1491–1498.
- 71 B. Rossi, C. Bottari, S. Catalini, F. D'Amico, A. Gessini and C. Masciovecchio, in *Molecular and Laser Spectroscopy*, Elsevier, 2020, pp. 447–482.



# Appendix A5



## Reducibility of Cu-zeolites and stability of Cu<sup>+</sup> monocarbonyl adducts: Qualitative and quantitative relationships from MCR-XAS and DFT

Gabriele Deplano<sup>a</sup>, Matteo Signorile<sup>a,\*</sup>, Cesare Atzori<sup>b</sup>, Davide Salusso<sup>b</sup>, Elisa Borfecchia<sup>a</sup>, Valentina Crocellà<sup>a</sup>, Silvia Bordiga<sup>a</sup>

<sup>a</sup> Department of Chemistry, NIS and INSTM Reference Centre, Università di Torino, Via P. Giuria 7, 10125 and Via G. Quarello 15/A, 10135 Torino, TO, Italy

<sup>b</sup> European Synchrotron Radiation Facility, 71 Avenue des Martyrs, CS 40220, 38043 Cedex 9 Grenoble, France

### ARTICLE INFO

#### Keywords:

Cu zeolites  
Cu<sup>+</sup> titration  
Cu-carbonyls  
XAS, volumetry  
DFT

### ABSTRACT

A series of Cu-exchanged zeolites differing in framework topology and composition are studied through in situ X-ray Absorption Spectroscopy (XAS) to highlight differences in reducibility depending on the characteristics of the different samples. After reduction at high temperature in NH<sub>3</sub>, the samples are exposed to CO at 50 °C followed by a temperature-programmed desorption to study the different stability of carbonyl species forming on the Cu<sup>+</sup> sites. Multivariate Curve Analysis applied to the XAS data allows extracting concentration profiles and pure spectral profiles on the species involved during several steps of the reaction. While all the samples are quantitatively reduced after treatment in NH<sub>3</sub>, the stability of the [Cu(CO)]<sup>+</sup> sites shows a dependence on the topology of the materials. DFT calculations on possible sites occupied by Cu in the different frameworks are consistent with the stability trends observed experimentally and, together with isothermal volumetric CO adsorption data, confirm the particular instability of the Cu<sup>+</sup>-monocarbonyls formed in the CHA framework.

### 1. Introduction

Cu-exchanged zeolites are widely studied materials for their performance on several relevant reactions, such as the direct conversion of methane to methanol (DMTM) [1] and the NH<sub>3</sub>-mediated selective catalytic reduction (SCR) of NO<sub>x</sub> in Diesel engine exhaust [2]. The reactivity of such materials as catalysts is usually based on the Cu<sup>2+</sup>/Cu<sup>+</sup> redox cycle [3] as a means to promote redox reactions on the respective substrate. To better understand (and possibly enhance) the performance of these materials, in-depth investigation of their properties in conditions as close as possible to the ones involved in the reaction is of paramount importance. For this task, several techniques have been developed and applied, comprising in situ and *operando* spectroscopies [4–9], computational modelling [10–15], diffraction [1,16,17], electron microscopy [18] and more [19,20]. Due to the importance of the Cu redox cycle in the catalytic activity, the quantification of the relative amount of Cu<sup>2+</sup>/Cu<sup>+</sup> species at any moment of the reaction is a key information for mechanistic elucidation. While Cu<sup>2+</sup> can be detected by several experimental techniques, Cu<sup>+</sup> can be more challenging to quantitatively assess: for instance, the d [10] electronic configuration of such species excludes the use of EPR spectroscopy, and the absence of

d-d transition bands in UV-Vis spectroscopy also hinders the characterization. Even when Cu<sup>+</sup> sites are not directly involved in the reactions under study (for instance, in DMTM the proposed active species most often involve Cu<sup>2+</sup> adducts), the reducibility of the Cu (and thus the reversibility of the redox cycle) has been correlated with catalytic performance [21]. X-ray Absorption Spectroscopy (XAS) is widely used as the main spectroscopic technique for quantitative assessment in this field, due to its sensitivity, element-selectivity and the possibility to perform in situ and *operando* experiments with relative ease. Data treatment procedures such as Linear Combination Fit (LCF) can then be used to extract the relative amounts of Cu components in different oxidation states and coordination environment based on previously acquired spectra of standard materials. While quantification through LCF is often challenging for solid materials, due to the lack of representative and/or easily reproducible standards, statistical approach such as Multivariate Curve Resolution (MCR) have been successfully applied to several cases [22–24], showing good performance also for difficult cases. One of the main drawbacks of this technique is, however, the fact that it is still mostly accessible through large scale facilities (i.e., synchrotron sources). Recently, some attempts have been made to find an alternative approach to obtain the same information; a recent

\* Corresponding author.

E-mail address: [matteo.signorile@unito.it](mailto:matteo.signorile@unito.it) (M. Signorile).

<https://doi.org/10.1016/j.cattod.2023.114403>

Received 20 July 2023; Received in revised form 2 October 2023; Accepted 5 October 2023

Available online 6 October 2023

0920-5861/© 2023 The Author(s). Published by Elsevier B.V. This is an open access article under the CC BY license (<http://creativecommons.org/licenses/by/4.0/>).



publication from our group provided a simple way to titrate Cu<sup>+</sup> in Cu-ZSM-5 materials by means of broadly available lab instrumentation (such as isothermal volumetric adsorption and/or infrared spectroscopy), exploiting CO as a probe molecule at room temperature and low partial pressure [25]. It has been widely proved that under such conditions, CO selectively and irreversibly binds Cu<sup>+</sup> to form stable monocarbonyl adducts [26–29], that can then be used to titrate the amount of Cu<sup>+</sup> in the materials.

In this work, we investigate the reduction behaviour of a series of Cu-exchanged zeolites by high temperature (500 °C) reduction in the presence of NH<sub>3</sub> via MCR-assisted XAS. The pre-reduced materials are then cooled down to 50 °C and exposed to CO as a probe molecule, to directly assess the reversibility of the interaction of CO with these materials. A TPD protocol is subsequently applied on the materials to check the stability range of these adducts and how the decomposition takes place. Six Cu-zeolites of different topologies that are relevant for catalytic applications (e.g., CHA, MOR and MFI) and with different compositions in terms of Al and Cu content are explored in order to highlight framework- and composition-specific trends. The data are then compared with volumetric results and DFT calculations to validate and rationalize these specific differences.

## 2. Experimental

### 2.1. Materials

All the materials mentioned in this paper have been synthesised and characterized in previous studies. Details about the synthetic procedures, composition and characterization methodologies can be found in the respective references listed in Table 1, in which the Si/Al and Cu/Al ratios are also reported for all samples.

### 2.2. Methods

#### 2.2.1. X-ray absorption spectroscopy

The in situ XAS data were collected at the BM23 beamline [33] of the European Synchrotron Radiation Facility (ESRF), under the beamtime awarded through the CH-6264 proposal [34]. The Microtomo [35] reactor cell, developed by the ESRF sample environment group, was chosen as sample environment. The powdered Cu-zeolites were prepared in the form of self-supporting pellets of 1.3 cm diameter with masses optimized for transmission-mode XAS measurements (ca. 40 mg, resulting in  $\Delta\mu x =$  in the range 0.6–1.0 with total absorption after the edge of less than  $\mu x = 2.5$  for all samples) and placed inside the reactor cell. The temperature of the sample was controlled by the heating system integrated in the Microtomo cell. The total gas flow rate and the composition of the feed were adjusted by a set of mass flow controllers controlled by a remote terminal. The in situ Cu K-edge spectra were acquired in transmission mode, employing a double-crystal Si(111) monochromator to scan the incident energy, and ionization chambers to detect incident ( $I_0$ ) and transmitted photons ( $I_1$ ). A Cu metal foil was measured simultaneously with all the collected XAS spectra by means of a third ionization chamber ( $I_2$ ), for energy calibration purposes. [36,37] The chambers were filled with a He/Ar mixture up to 2 bar with Ar partial pressure of 0.1 and 0.3 bar for  $I_0$  and  $I_{1,2}$  chambers, respectively.

**Table 1**

List of Cu-zeolites used in this work. All Si/Al and Cu/Al are reported as molar ratios.

Name	Si/Al	Cu/Al	Reference
(0.48)Cu-CHA(15)	15	0.48	[30]
(0.35)Cu-CHA(5)	5	0.35	[30]
(0.32)Cu-MOR(11)	11	0.36	[31]
(0.21)Cu-MOR(6.5)	6.5	0.21	[32]
(0.48)Cu-MFI(25)	25	0.48	[25]
(0.35)Cu-MFI(11.5)	11.5	0.35	[25]

The XAS signal was monitored as a function of time/temperature during the treatment steps, with acquisitions of ca. 2 min/scan in the 8830–9800 eV energy range. Spectra were collected in continuous mode with energy step of 0.3 eV, then were rebinned with constant energy steps of 5 eV in the pre-edge region (8928 – 8960 eV) and 0.3 eV in the XANES region (8960 – 9050 eV); a uniform sampling step in k-space of 0.08 Å<sup>-1</sup> was adopted in the extended region of the spectra. The energy ranges in the XANES scans analysed in this work were aligned using the simultaneously measured data for the Cu metal foil and normalized to unity edge jump. A custom Python-based script based on the Larch library [38] was employed for data alignment and normalization.

#### 2.2.2. XANES statistical analysis and multivariate curve resolution

All the analysed XANES datasets comprised a range of spectra in the range 8070–9020 eV, with the number of spectra depending on the considered treatment step (vide infra). The XANES spectra collected throughout this work were analysed sample-wise via a Multivariate Curve Resolution (MCR) approach. [22,39,40] This technique involves the decomposition of experimental data in a set of pure spectra and concentration profiles, which can be used as qualitative and quantitative descriptive tools when a mixture of several species is present. An initial guess was generated via a Principal Component Analysis (PCA) of the experimental data, which provides a set of pure spectra based on the selected number of Principal Components (PC); the PCs are then used to initialize the Alternating Least Squares (ALS) algorithm, an iterative process that provides the spectra and concentration profiles upon convergence. The number of relevant PCs ( $n$ ) for each instance was selected by locating the elbow point of the relative Scree plot (corresponding to the  $k^{\text{th}}$  PC), visually inspecting the residual variances and evaluating the goodness of fit in the interval  $k-1 \leq n \leq k+1$ . The convergence tolerance on the Lack of Fit (LOF) parameter for two successive iterations was set to 0.1%. After selection of the PCs, the MCR-ALS routine was initialized using the SIMPLISMA method [40]. XANES spectra are particularly suited for MCR-ALS analysis, since the element-selective characteristic of this technique allows to exploit some constraint that greatly enhance the efficiency of the algorithm, i.e., non-negativity of both spectral and concentration profiles, as well as closure for concentration profiles (i.e., summing to 1) can be employed to drive the algorithm toward a stable solution. [41] Indeed, in all cases convergence was achieved in less than 25 iterations, with final LOF values < 0.5%. Quality of reproduction of the experimental data was evaluated through the  $\%R_{\text{Factor}}$ , defined as:

$$\%R_{\text{Factor}} = \frac{\sum_{i,j} |D - D^{\text{PCA}}|}{\sum_{i,j} |D|}$$

where  $D$  and  $D^{\text{PCA}}$  are the original and the PCA reconstructed dataset, while the subscripts  $i$  and  $j$  are the respective rows and columns. For every dataset, the  $\%R_{\text{Factor}}$  was > 99.999%.

#### 2.2.3. Isothermal volumetric adsorption measurements

Carbon monoxide (supplied by Sapio SRL, 99.99998% purity grade) adsorption isotherms were measured on a commercial volumetric apparatus (Micromeritics ASAP 2020) at 50 °C.

The samples were mortar ground and pelleted, in order to prevent any powder residues from moving out of the cell, while exposing to gas/vacuum treatment. The pellets were then inserted in a custom adsorption cell (Fig. S1) [42]. The sample temperature was kept constant by using an external isothermal liquid bath (Julabo F25-EH). Prior to the measurements, Cu-zeolite pellets were treated at high temperature on a vacuum line equipped with a turbomolecular pump; full details on the treatment can be found in the next section. After treatment, a primary CO adsorption measurement was performed on the sample, followed by an outgassing time interval of 2 h and a secondary CO adsorption run. As described in a previous publication [25], the difference between the primary and the secondary adsorption isotherms yields the amount of

irreversibly bound CO per gram of material, which can then be converted (supposing a 1:1 ratio between  $\text{Cu}^+$  and CO) to the amount of  $\text{Cu}^+$  through the equation:

$$\text{Cu}^+(\%) = \text{CO uptake} \left( \frac{\text{mmol}_{\text{CO}}}{\text{g}} \right) * \text{formula weight} \left( \frac{\text{g}}{\text{mmol}_{\text{Cu}}} \right) * 100$$

### 2.3. Treatment protocols

For the in situ XAS measurements, the same treatment procedure was applied to all samples, as shown in Fig. S2 and briefly described in the following. The gas employed for the experiments was supplied to the ESRF and consisted of the following:  $\text{NH}_3$ , 0.4 mol% in He (Air Products); CO, 5 mol% in He (Air Liquide);  $\text{O}_2$ , pure (Air Liquide); He, pure (Air Products). The sample was heated in a pure  $\text{O}_2$  flow from room temperature to 500 °C with a ramp of 5 °C/min and kept at the same temperature for 10 min. After a He flush for 15 min, the sample was exposed to  $\text{NH}_3$  (0.4 mol% mixture in He) at the same temperature for 40 min. He was dosed again to the sample for 80 min at 500 °C; the inert environment was kept while ramping down to 50 °C, after which the sample was kept in isothermal conditions for 10 more minutes. The sample was then exposed to CO (5 mol% mixture in He) for 15 min, and subsequently flushed with He for 120 min. Finally, the temperature was raised from 50 °C to 500 °C in He with a ramp of 5 °C/min. Mass flow controllers were calibrated for each mixture and used to keep a constant gas flow of 30 ml/min for each step of the procedure.

For all volumetric experiments, the following activation protocol was employed. The sample cell was heated from room temperature to 500 °C with a ramp of 5 °C/min under dynamic vacuum (residual pressure  $< 10^{-3}$  mbar).  $\text{O}_2$  (100 mbar) was then dosed and kept in contact with the sample at the same temperature for 30 min. The sample was then outgassed at the same temperature for 40 min. In this way, we brought all the samples to their most oxidized state. Then, a controlled  $\text{NH}_3$  treatment was performed in order to maximize the amount of  $\text{Cu}^+$  species. Previous studies on the topic showed that high temperature treatment in the presence of  $\text{NH}_3$  leads to a  $\text{Cu}^+$  content in the 75–92% range; [25,32] this is further confirmed in the present study (vide infra). Accordingly, 100 mbar of  $\text{NH}_3$  were dosed on the sample at 500 °C for 30 min. Finally, outgassing was performed at the same temperature until a residual pressure of  $< 10^{-3}$  mbar was achieved, then the sample was cooled down to room temperature. This procedure aims at maximizing the amount of highly uncoordinated  $\text{Cu}^+$  that can be probed by CO.

### 2.4. Computational details

The adsorption of CO on the different Cu-zeolites studied experimentally was simulated at DFT level of theory by means of the CRYSTAL17 periodic code [43]. For each framework,  $\text{Cu}^+$  substitution was studied at different positions, aiming at accounting for the possible heterogeneity of the CO adsorption sites as a function of the ring system hosting the cation. In detail, two sites, placed respectively in a large and a small ring, were investigated herein. Nomenclature and sites labelling used hereafter for defining the ring-systems refers to that proposed by the International Zeolites Association on the Database of Zeolite Structures [44]. For CHA,  $\text{Cu}^+$  was positioned in the 6-membered ring (-MR) of the *d6r* cage or within the 8-MR window of the *cha* cage, maintaining the same position for the framework Al that is charge-balanced by the extraframework ion. The same strategy was adopted for MOR, where Al was placed in the T4 crystallographic site and the  $\text{Cu}^+$  inside the 8-MR “side pocket” or in the 12-MR main channel. Finally, MFI models were adapted from previous report by the authors [25], with  $\text{Cu}^+$  located near an Al positioned in the T8 site ( $\text{Cu}^+$  in a 6-MR on channel wall) or in the T10 site ( $\text{Cu}^+$  exposed on a 10-MR ring at channels intersection). The local structure of  $\text{Cu}^+$  in each model is shown in Fig. 1.

The calculations were carried out with parameters from a previous work involving Cu-MFI, i.e., the hybrid GGA B3LYP functional [45,46]. Dispersive interaction have been included empirically through the Grimme D3 scheme [47]. The basis set by Nada et al. was adopted for describing Si and O atoms [48], whereas that by Catti et al. [49] was used in for Al. Extraframework Cu cations and atoms belonging to sorbed carbon monoxide (C and O) have been described by the Ahlrichs TZVP basis [50]. The truncations for the mono- and bi-electronic integral (TOLINTEG) were set to {7 7 7 25}. The sampling in the reciprocal space (SHRINK) was set to {2 2} ({3 3} for CHA), providing a total of 8 k points sampled in MFI and MOR (14 in CHA). The maximum order of shell multipoles in the long-range zone for the electron-electron Coulomb interaction (POLEORDR keyword) was chosen to be 6. All the other parameters were set to default values according to the CRYSTAL17 manual [51].

Each  $\text{Cu}^+$  model was geometry optimized, then molecular adducts with carbon monoxide (mono- and di-carbonyls) were built and further optimized. The periodic models are provided in Appendix A of SI in cif format. Finally, the thermodynamic functions describing the Cu adducts (enthalpies and Gibbs free energies) were evaluated by computing harmonic frequencies over a subset of atoms including: the  $\text{Cu}^+$  cation; the sorbed molecule(s); the Al framework atom and its neighbours up to

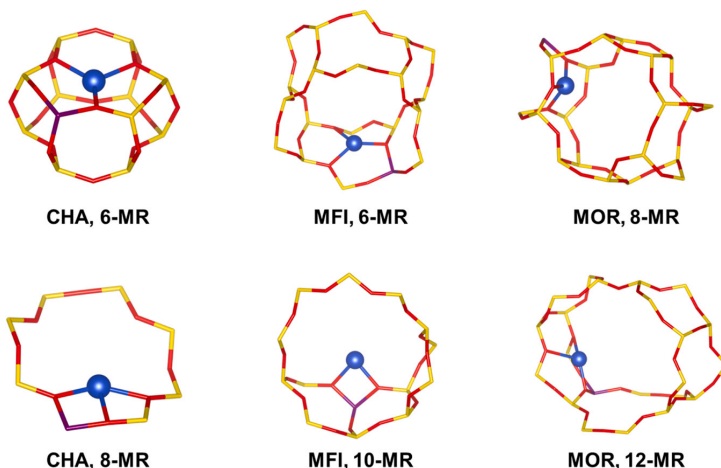


Fig. 1. Representation of the local structure of  $\text{Cu}^+$  models considered in this work. Atoms colour code: red, O; purple, Al; yellow, Si; blue, Cu.

the 2nd coordination shell (namely 4 O and 4 Si atoms, possibly including additional atoms to fully include small 4-MR rings, if applicable).

The variation of electronic energy ( $\Delta E$ ), enthalpy ( $\Delta H$ ) and Gibbs free energy ( $\Delta G$ ) associated to the formation of an adduct, evaluated at experimentally relevant p,T conditions, were computed as it follows:

$$\Delta X = \sum X_{\text{products}} - \sum X_{\text{reagents}}, \text{ with } X = E, H \text{ or } G$$

### 3. Results and discussion

#### 3.1. Effect of topology and composition on stationary states

X-ray spectroscopy has been extensively used as a tool to study Cu-exchanged zeolites, due to its unique ability to probe the electronic and geometric structure of the Cu sites in an element selective fashion. *In situ* and *operando* experiments are more and more practicable, and general trends and features can be described in operating conditions with good time resolution. XAS spectra in both the XANES and EXAFS regions were collected during the whole treatment for all samples. For the sake of brevity, only the XANES spectra corresponding to the stationary states for each reaction step are described in the following. Fig. 2 (left panel) shows the materials after exposure to O<sub>2</sub> at 500 °C. The well-known features of oxidized Cu-zeolites are present for all samples in a very similar way, namely the Cu<sup>2+</sup> 1 s→3d and 1 s→4p transitions at ca. 8978 and 8987 eV, respectively, as well as the high intensity of the white line. After exposure to NH<sub>3</sub> (Fig. 2, central panel), the Cu<sup>2+</sup> 1 s→3d transition vanishes and an intense feature at 8983 eV, corresponding to the Cu<sup>+</sup> 1 s→4p transition, appears. In agreement with the literature, and as confirmed by MCR-ALS (vide infra), the shape of the spectra for all materials are consistent with the presence of a major fraction of 2-coordinated Cu<sup>+</sup> species; in particular, the formation of [Cu(NH<sub>3</sub>)<sub>2</sub>]<sup>+</sup> linear complexes has been described in similar conditions for related samples. [3] Interestingly, the Cu-CHA samples show differences in the rising edge region compared to the other materials; (0.35)Cu-CHA(5) in particular shows a lower intensity of the Cu<sup>+</sup> 1 s→4p transition and a structured white line. This could be indicative of a lower amount of Cu<sup>+</sup>

involved in the formation of [Cu(NH<sub>3</sub>)<sub>2</sub>]<sup>+</sup> complexes or, alternatively, in a distorted geometry of such complexes due to framework/composition-dependent steric constraints. After NH<sub>3</sub> is removed at the same temperature (Fig. 2, right panel), the spectra of the materials change and group in correspondence to the topology. In both Cu-CHA samples the intensity of the Cu<sup>+</sup> 1 s→4p transition decreases and the rising edge/white line region is severely modified; this seems to imply a significative structural modification of the Cu sites after NH<sub>3</sub> is removed. Nonetheless, also referring to previous literature, the different resulting spectrum (with respect to the other frameworks) does not infer the over-reduction of Cu to the metallic state. In fact, both the XANES and the corresponding EXAFS spectra for Cu-CHA samples does not exhibit common features with those of a reference Cu metal foil, as reported in Fig. S3. A decrease in the Cu<sup>+</sup> 1 s→4p transition intensity also occurs for the Cu-MFI samples, with only a slight modification in the white line region; the spectra of the Cu-MOR materials are the least affected by the removal of NH<sub>3</sub>. The variation upon flushing with He could be rationalized in terms of the calculated structure for the framework-coordinated Cu<sup>+</sup> sites shown in Fig. 1: in particular, for both Cu-MOR sites the metal is ligated in a quasi-linear fashion by two of the coordinated oxygen atoms compared to the other frameworks, which would lead to an enhanced intensity of the 1 s→4p transition. For the sake of brevity, MCR-ALS decomposition of this part of the reaction is reported in the SI (Figs. S4 and S5). The NH<sub>3</sub> desorption rate for the three materials follows the order CHA > MOR > MFI (from faster to slower) as retrieved from MCR-ALS decomposition (Fig. S6). This trend is likely induced by the small cage structure of the CHA topology: diffusion problems can be excluded due to the small kinetic diameter of NH<sub>3</sub>. [52].

Upon cooling down to 50 °C, all samples retain a similar spectral shape, as shown in Fig. 3 (left panel), though the white line region for both Cu-CHA samples is slightly modified again; this peculiar behaviour could be related to the possibility of the Cu atoms to move from their initial equilibrium positions inside the zeolitic host upon interaction with NH<sub>3</sub>, as suggested in the recent literature. [53,54] The central panel of Fig. 3 shows the interaction of CO with the samples at the same temperature. The interaction is very quick, as it will be described in

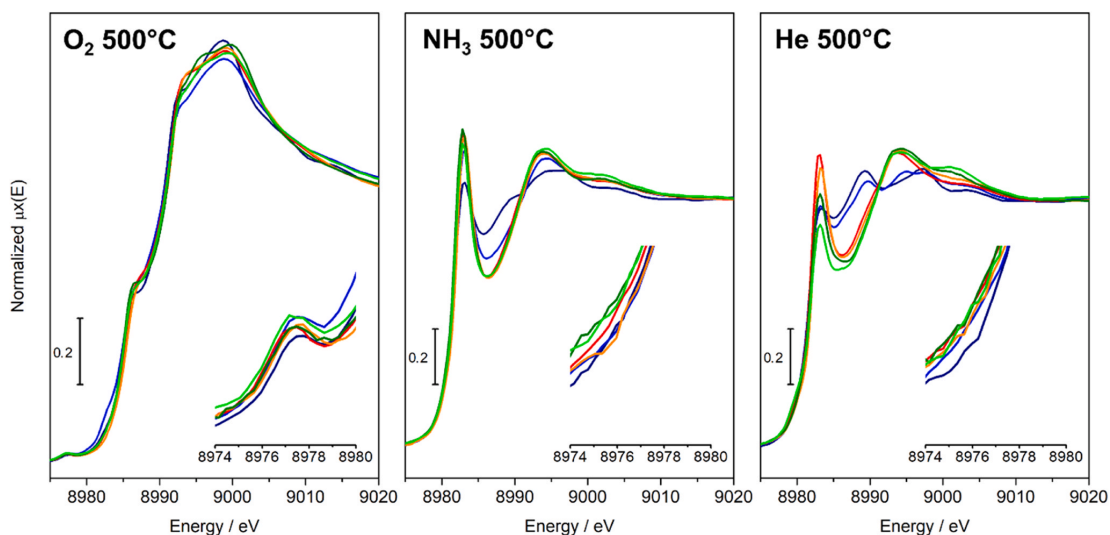
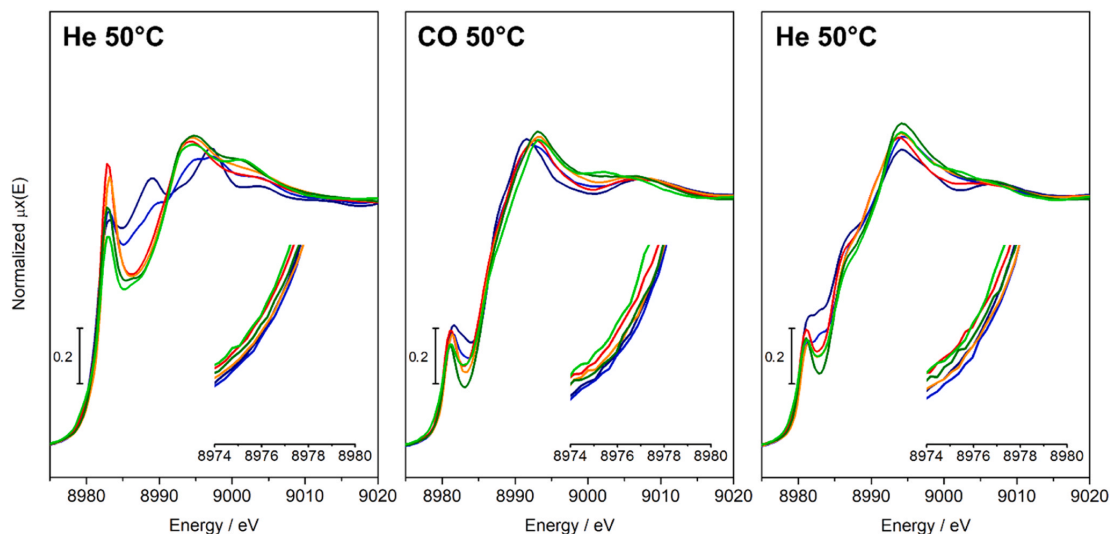


Fig. 2. Cu K-edge XANES spectra for the six Cu-zeolite samples at key reaction steps (500 °C). Insets: zoom on the 1 s→3d transition zone of the edge. Left panel: oxidized in O<sub>2</sub> at 500 °C. Middle panel: reduced in NH<sub>3</sub> at 500 °C after oxidation and He flush. Right panel: flushed with He at 500 °C after reduction in NH<sub>3</sub>. Colour code: blue, (0.48)Cu-CHA(15); navy, (0.35)Cu-CHA(5); red, (0.32)Cu-MOR(11); orange, (0.21)Cu-MOR(6.5); light green, (0.48)Cu-MFI(25); olive, (0.35)Cu-MFI(11.5).



**Fig. 3.** Cu K-edge XANES spectra for the six Cu-zeolite samples at key reaction steps (50 °C). Insets: zoom on the 1 s-3d transition zone of the edge. Left panel: flushed in He and cooled at 50 °C. Middle panel: exposed to CO at 50 °C. Right panel: flushed with He at 50 °C after exposure to CO. Colour code: blue, (0.48)Cu-CHA(15); navy, (0.35)Cu-CHA(5); red, (0.32)Cu-MOR(11); orange, (0.21)Cu-MOR(6.5); light green, (0.48)Cu-MFI(25); olive, (0.35)Cu-MFI(11.5).

detail in the next section, and the spectral profiles drastically change leading to a similar shape for all materials. The  $\text{Cu}^+$  1 s $\rightarrow$ 4p transition dramatically decreases, and a sharp feature at ca. 8981 eV appears, together with a shoulder on the rising edge at ca. 8987 eV. After the CO is removed from the cell by flushing with He, the spectra reach a new equilibrium as shown in Fig. 3 (right panel). In these conditions the peak at 8987 eV becomes more evident, and the feature at 8981 eV decreases in intensity for some samples (mainly the Cu-CHAs) with a simultaneous partial recovery of the  $\text{Cu}^+$  1 s $\rightarrow$ 4p transition. A key point is that the spectral profiles of the samples after a prolonged He flushing do not correspond to those before exposure to CO; this is in agreement with the formation of at least a fraction of irreversible adducts between the  $\text{Cu}^+$  sites and the carbon monoxide. According to the literature [28,29,55–57], and as shown by our group in a recent publication for Cu-MFI zeolites [25], interaction of CO at 50 °C with Cu sites in the zeolitic host leads to the formation of a series of carbonyl complexes (i.e.,  $[\text{Cu}(\text{CO})_2]^+$ ,  $[\text{Cu}(\text{CO})]^+$  and  $[\text{Cu}(\text{CO})_2]^{2+}$ ). When the CO partial pressure is lowered (e.g., when vacuum is applied/CO is removed from the gaseous feed) the only stable species are the  $\text{Cu}^+$  monocarbonyls; in the case of Cu-MFI samples,  $[\text{Cu}(\text{CO})]^+$  accounted for up to 89% of total Cu species, according to volumetric measurements. A reasonable explanation for the spectral sequence shown in Fig. 3 is then the formation of multiple carbonyl species upon exposure to CO at relatively high partial pressure, followed by a partial decomplexation when the CO partial pressure is set to zero, i.e., during He flushing; the only carbonyl complex that is retained after this step is  $[\text{Cu}(\text{CO})]^+$  (i.e., the  $\text{Cu}^+$  monocarbonyl), while a fraction of the total Cu may still be present as  $\text{Cu}^+$  or  $\text{Cu}^{2+}$  sites coordinated to the framework. This picture is further confirmed by calculations and MCR analysis (vide infra). Interestingly, the peak at 8983 eV corresponding to the  $\text{Cu}^+$  1 s $\rightarrow$ 4p transition that is partially restored after flushing likely corresponds to a fraction of  $\text{Cu}^+$  not coordinated by CO; this seems to happen more prominently for the CHA topology, and this transition is in fact partly visible for (0.35)Cu-CHA(5), even in the presence of CO in gas phase. Since the  $\text{Cu}^+$  1 s $\rightarrow$ 4p peak only partially overlaps with the characteristic transitions of CO-bound  $\text{Cu}^+$  (i.e., the ones at 8981 and 8987 eV), it can be fortuitously used to qualitatively and semi-quantitatively assess the amount of  $\text{Cu}^+$  that is not coordinated by CO. From the spectra portrayed in Fig. 3 (right

panel), the trend seems to be CHA>MOR>MFI in decreasing order of untitrated  $\text{Cu}^+$ , in good agreement with volumetric data on the same series of samples reported in Table 2.

Finally, all materials were heated up to 500 °C in He flow to study the desorption behaviour of CO and its influence on the Cu sites: the XANES spectra of all materials at the final point of this treatment are reported in Fig. 4. Though a more detailed discussion of the transient states will be presented in the next section, it is already apparent that the majority of Cu in this stationary state is present as  $\text{Cu}^+$  species; in fact, a comparison with the spectra of the samples in He at 500 °C after treatment in  $\text{NH}_3$  (see Fig. 2) confirms a striking similarity between the two situations. Specific differences on the samples may be due to residual  $[\text{Cu}(\text{NH}_3)_2]^+$  complexes in the latter (which present a more intense  $\text{Cu}^+$  1 s $\rightarrow$ 4p transition, as already discussed) or a slightly different positioning of the Cu sites in the two cases. This information, together with the MCR profiles presented in the next section, suggest that the  $[\text{Cu}(\text{CO})]^+$  complexes simply decompose to framework-bound  $\text{Cu}^+$  and gaseous CO after thermal treatment; this phenomenon can thus be described as a simple desorption and does not involve a change of Cu oxidation state nor a decomposition of CO.

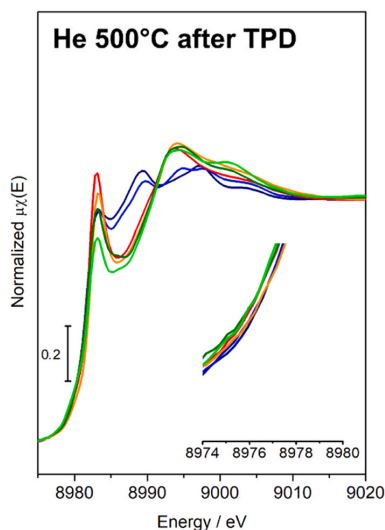
### 3.2. Quantitative analysis using MCR-ALS

Fig. 5 portrays the MCR-ALS reconstruction on the spectral series shown in Fig. 3 consisting of the steps at 50 °C for an example material for each framework, namely (0.35)Cu-CHA(5), (0.32)Cu-MOR(11) and (0.35)Cu-MFI(11.5); the same reconstruction for the other materials is reported in Fig. S7. The spectra extracted for the 3 identified components are consistent with a bare  $\text{Cu}^+$  species, a  $\text{Cu}^+$  dicarbonyl and a  $\text{Cu}^+$  monocarbonyl adduct. As already discussed in the previous section, the

**Table 2**

$\text{Cu}^+$  concentrations measured by isothermal volumetric adsorption of CO at 50 °C on the 3 samples discussed in the previous section.

Sample	CO uptake (mmol/g)	$\text{Cu}^+$ concentration (%)
(0.35)Cu-CHA(5)	0.480	60.6
(0.32)Cu-MOR(11)	0.322	74.6
(0.35)Cu-MFI(11.5)	0.401	89.1



**Fig. 4.** Cu K-edge XANES spectra for the six Cu-zeolite samples at 500 °C after temperature programmed desorption of CO in He. Inset: zoom on the 1 s-3d transition zone of the edge. Colour code: blue, (0.48)Cu-CHA(15); navy, (0.35)Cu-CHA(5); red, (0.32)Cu-MOR(11); orange, (0.21)Cu-MOR(6.5); light green, (0.48)Cu-MFI(25); olive, (0.35)Cu-MFI(11.5).

spectrum of the bare  $\text{Cu}^+$  is characterized by an intense pre-edge 1 s $\rightarrow$ 4p transition centred at 8983 eV and by an unstructured white line of comparable intensity (except in the case of Cu-CHA). This spectral shape nicely matches the PC1 component shown in Fig. 5. PC2 presents its higher concentration when CO is present at high partial pressure in the gaseous feed, thus can be reasonably assigned to a high-coverage situation, i.e. to the formation of  $[\text{Cu}(\text{CO})_2]^+$  adducts. Finally, PC3 is consistent with the presence of  $[\text{Cu}(\text{CO})]^+$  adducts, as it is found to be stable at 50 °C under a negligible CO partial pressure, as expected from previous reports. Interestingly, though the shape of the white line region for the CHA topology is again confirmed, the spectra of the carbonyl adducts are similar across the three framework types. This fact suggests a lower involvement of the zeolitic framework in determining the local structure of the Cu-carbonyl adducts. Although some error stemming from the algorithm is to be expected, useful information about the relative proportion of the species can be extracted from the concentration profiles (bottom panels of Fig. 5). In all cases, the conversion from bare  $\text{Cu}^+$  to  $[\text{Cu}(\text{CO})_2]^+$  adducts is quantitative, but for the CHA topology a complete formation of  $[\text{Cu}(\text{CO})]^+$  species after flushing He is never achieved: the conversion of  $[\text{Cu}(\text{CO})_2]^+$  to  $[\text{Cu}(\text{CO})]^+$  is not quantitative for (0.35)Cu-CHA(5) (c.a. 95%) and is readily accompanied by the formation of a fraction of bare  $\text{Cu}^+$  species (c.a. 5% for CHA samples) in less than 45 min, in agreement with what was previously described (vide supra). The reversibility of these adducts is observed also for the other materials, but it appears to be enhanced for the CHA topology, possibly due to the steric constraints imposed by the small cage system (and the relative abundance of Cu for the (0.35)Cu-CHA(5) material). In the case of (0.35)Cu-CHA(5) the desorption was registered for a longer time during the experiment (full range in Fig. S8), and the MCR concentration profile shows a very clean distinction between the different species with almost 10% of residual unbound  $\text{Cu}^+$  species after 65 min.

The MCR-ALS reconstruction performed on the TPD step is shown in Fig. 6 for the selected samples; the reconstruction for the other samples is reported in Fig. S9. In this case, although not immediately evident from the experimental spectra, 3 components are retrieved for all

materials. From the concentration profiles (bottom panels in Fig. 6), it is apparent that the initial monocarbonyl species first convert to an intermediate species at lower temperatures, which then yields the final species upon further heating. Since the final state highly resembles the spectrum of the reduced material at 500 °C after  $\text{NH}_3$  removal, the intermediate state is probably indicative of a bare  $\text{Cu}^+$  species bound to the framework in a different equilibrium position than the one at 500 °C. For the MOR and MFI framework, this species bears a striking similarity to the bare  $\text{Cu}^+$  species at 50 °C shown in Fig. 3 (left panel), so the spectral series can be described in terms of two subsequent events: the thermally-induced desorption of CO from the  $[\text{Cu}(\text{CO})]^+$  complex, leading to the formation of a low-temperature bare  $\text{Cu}^+$  species reaching maximum concentration at ca. 300 °C, and the geometrical rearrangement of this species at higher temperatures. In the case of CHA, however, the intermediate state resembles more the intermediates of the other framework than the state before exposure to CO in Fig. 3 (right panel); a possible explanation for this difference is a mobilization of the Cu in the CHA framework due to treatment in  $\text{NH}_3$ , with a subsequent repositioning after interaction with CO and/or thermal treatment. This species is also formed at lower temperatures compared to the other frameworks, and reaches maximum concentration at a temperature of ca. 250 °C and 150 °C for (0.48)Cu-CHA(15) and (0.35)Cu-CHA(5), respectively. An overall lower thermal stability of Cu-carbonyls in the CHA framework is in accordance with DFT calculations (vide infra), and is already apparent from the presence of ca. 10% of the intermediate species at the starting point of the TPD for (0.35)Cu-CHA(5). It has to be noted, though, that the Cu density in the framework for (0.35)Cu-CHA(5) is higher compared to the MOR and MFI samples (0.87 compared to 0.47 and 0.45, respectively), so that concentration-dependent effects may also play a role in such a striking difference. Still, the same method applied to the (0.48)Cu-CHA(15) sample (with a 0.45 Cu density) yields a maximum for the formation of the low-temperature  $\text{Cu}^+$  species at 250 °C, still lower than all other non-CHA samples. Together with the peculiar speciation of  $\text{Cu}^+$  species in the CHA framework and the results from DFT calculations (vide infra), framework-dependent properties (especially in the case of CHA) appear to play the major role in this case.

### 3.3. Isothermal volumetric CO adsorption

Results for isothermal volumetric CO adsorption measurements on the samples described in the previous sections are reported in Table 2 (full isotherms shown in Fig. S10). The amount of  $\text{Cu}^+$  measured on the samples is in line with the results obtained via MCR-ALS, showing a slow, but measurable, decomposition of the  $[\text{Cu}(\text{CO})]^+$  adducts over time in the order CHA >> MOR > MFI. The longer desorption times employed during the volumetric experiments, compared to the XAS measurements, can justify the lower amounts of  $\text{Cu}^+$  computed by this experimental tool, especially for the CHA topology, where the presence of a significant fraction of uncoordinated  $\text{Cu}^+$  is already observable in the spectra (Fig. 3, right panel). The lower stability of the  $[\text{Cu}(\text{CO})]^+$  adducts in the CHA framework was also confirmed by DFT calculation, as shown in the next section.

### 3.4. Insights from simulation

The formation of  $[\text{Cu}(\text{CO})_2]^+$  adducts on  $\text{Cu}^+$  at 50 °C in the presence of CO and the subsequent decomposition to  $[\text{Cu}(\text{CO})]^+$  when the CO partial pressure is decreased were observed for all the investigated samples; specific differences were found depending on the framework type, and especially in the case of CHA, the monocarbonyl complex appeared to be less stable than in the other topologies. In the view of getting an atomistic description of the adsorption/desorption processes, DFT simulations were performed on a set of representative structures for each topology investigated in this work. As shown in Fig. 1, depending on the framework topology/ring structure where  $\text{Cu}^+$  is sitting, various coordination geometries are possible for the ion toward the framework.

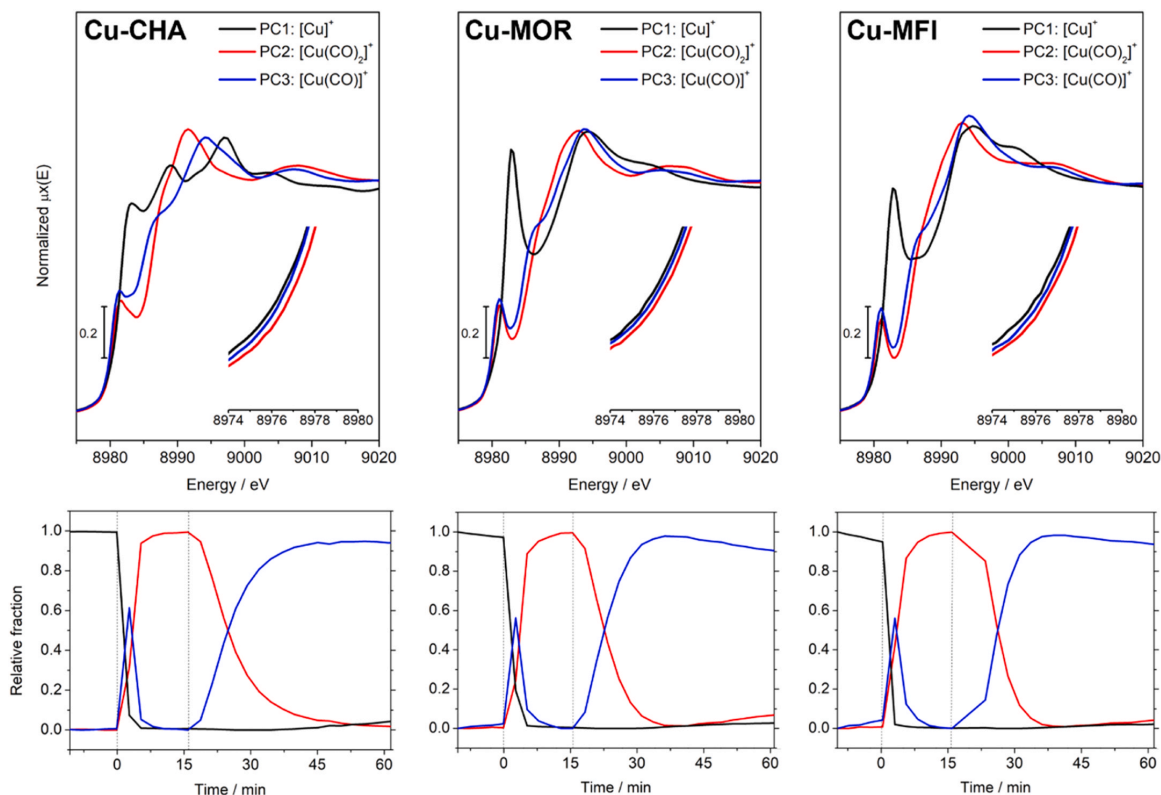


**Fig. 5.** Pure spectral (top) and concentration (bottom) profiles extracted by MCR-ALS on a sample of each framework type during the steps at 50 °C described in Fig. 3 (vide supra). Insets: zoom on the 1 s-3 d transition zone of the edge. Colour code: black,  $\text{Cu}^+$  coordinated to the framework; red,  $[\text{Cu}(\text{CO})_2]^+$  complex coordinated to the framework; blue,  $[\text{Cu}(\text{CO})]^+$  complex coordinated to the framework.

The main coordination motifs can be identified are: i) a T-shaped geometry, with  $\text{Cu}^+$  bridging across two equidistant framework O atoms, with the contribution of a third framework O at slightly longer distance, typical of  $\text{Cu}^+$  sitting in large pores; ii) a trigonal geometry, with  $\text{Cu}^+$  coordinated by three closely equivalent framework O atoms, observed in smaller pores/more constrained cavities. An exception to this trend is represented by  $\text{Cu}^+$  positioned in the 10-MR of MFI, grafted to two non-collinear, Al-bound O framework atoms. Upon interaction with the first CO molecule (see graphical representation of optimized structures in Figs. S11–13), regardless the considered  $\text{Cu}^+$  site, the adsorption event causes the detachment of the metal ion from the framework, now assuming a quasi-trigonal coordination with two framework O and the C atom from the adsorbate. The adsorption of a second CO molecule expands the  $\text{Cu}^+$  coordination sphere to a quasi-tetrahedral one, with the only exception of the  $\text{Cu}^+$  site hosted in the 8-MR that is unable to coordinate a second CO molecule, as due to the steric constraint imposed by the confined environment in the MOR side pocket.

Table 3 lists the electronic energy, enthalpy and Gibbs free energy variations computed for the formation of  $[\text{Cu}(\text{CO})]^+$  and  $[\text{Cu}(\text{CO})_2]^+$  adducts starting from a bare  $\text{Cu}^+$  site in different positions inside each framework.

In all cases, the formation of the carbonyl adducts is thermodynamically favoured (except for the  $[\text{Cu}(\text{CO})_2]^+$  in the 8-membered ring for the MOR topology, that is not formed in practice). Both in terms of enthalpy and Gibbs free energy, the MFI topology shows the highest stability among the series for the formation of  $[\text{Cu}(\text{CO})]^+$  adducts, consistently with experimental observations. On the other hand, the

CHA framework presents the lowest difference in energies between the mono- and dicarbonyl species, as well as the highest energy ( $-38.6$  kJ/mol) for the  $[\text{Cu}(\text{CO})]^+$  adduct in the 6-membered ring position. This difference is likely the reason for the strikingly different behaviour of the samples of this topology (especially (0.35)Cu-CHA(5)) upon prolonged CO desorption.

Finally, calculated phase diagrams showing the stability of  $[\text{Cu}(\text{CO})_2]^+$  and  $[\text{Cu}(\text{CO})]^+$  adducts as a function of temperature and pressure are portrayed in Fig. 7.

Although the pressure gauge in the volumetric instrument can accurately read pressure down to  $10^{-3}$  mbar (which has been used as the lower bound for the phase diagrams), the actual pressure in the sample cell is likely to be lower than this value since a turbomolecular pump is used to evacuate the cell; this is also consistent with the MCR reconstruction, in which no evidence of residual Cu-dicarbonyls (except in the case of Cu-CHA) is found. As can be observed, the average temperature for the decomposition of the  $[\text{Cu}(\text{CO})]^+$  to a bare  $\text{Cu}^+$  species at  $10^{-3}$  mbar (that well approximates a negligible partial pressure of CO in flow experiments) in the case of CHA (162 °C) is much lower than that for the other two frameworks (275 °C and 340 °C for MOR and MFI, respectively), especially in the case of Cu located in the 6-membered rings. Supposing an unequal occupancy of the Cu sites in the different rings, the trend in terms of framework topology is still respected. These average temperatures are in perfect agreement with what was found from MCR-ALS during the TPD steps for the three samples (see Fig. 6, bottom panels) confirming the general trend in desorption kinetics and overall stability for the three topologies.

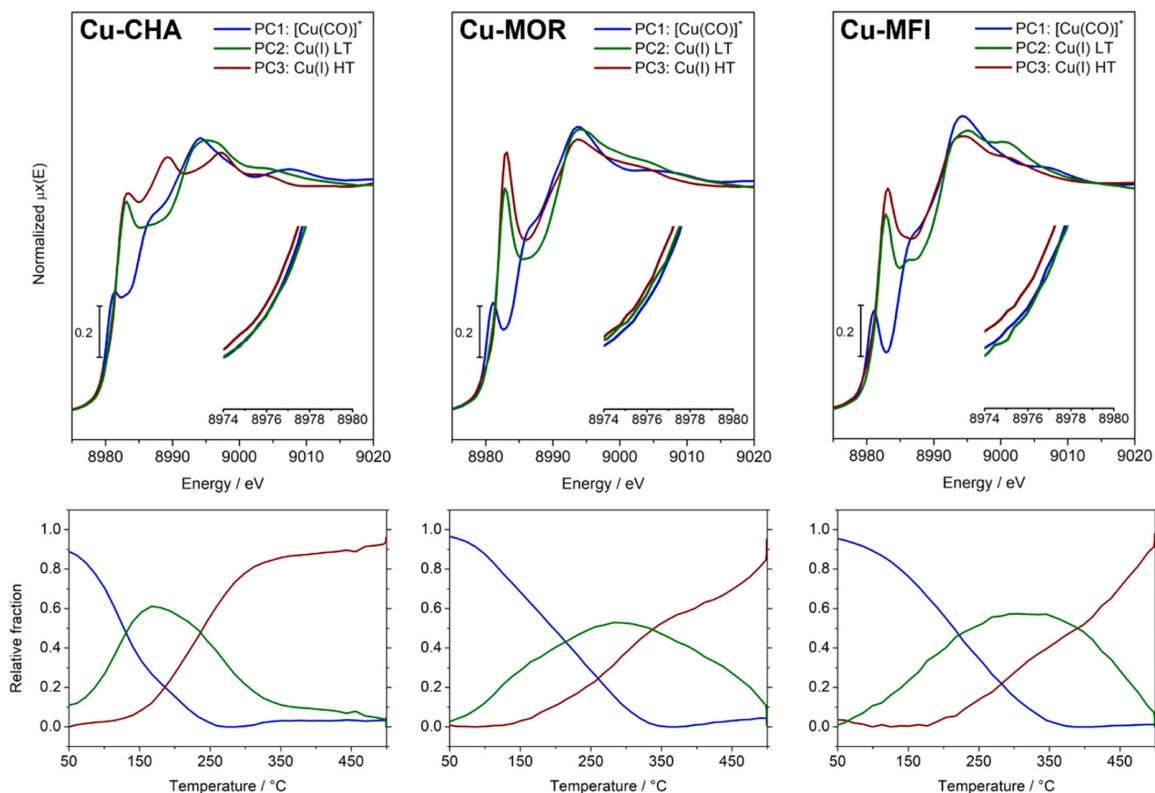


**Fig. 6.** Pure spectral (top) and concentration (bottom) profiles extracted by MCR-ALS on a sample of each framework type during the TPD procedure (vide supra). Insets: zoom on the 1 s-3d transition zone of the edge. Colour code: blue,  $[\text{Cu}(\text{CO})]^+$  complex coordinated to the framework; olive,  $\text{Cu}^+$  species at lower temperatures (LT); wine,  $\text{Cu}^+$  species at higher temperatures (HT).

**Table 3**

Electronic energies ( $\Delta E$ ), enthalpies ( $\Delta H$ ) and Gibbs free energies ( $\Delta G$ ) variations associated to the formation of mono- and di-carbonyl molecular adducts on  $\text{Cu}^+$ , located at different positions within the CHA, MFI and MOR frameworks. All values are reported in kJ/mol.  $\Delta H$  and  $\Delta G$  computed at 25 °C and 1013 mbar.

		$\Delta E$			$\Delta H$			$\Delta G$		
		6-MR	8-MR	10-MR	6-MR	8-MR	10-MR	6-MR	8-MR	10-MR
CHA	$[\text{Cu}(\text{CO})]^+$	-83.8	-78.2	-38.6	-143.0	-121.8	-76.6	-143.0	-121.8	-76.6
	$[\text{Cu}(\text{CO})_2]^+$	-56.7	-51.6	-10.4	-75.2	-81.2	-40.3	-75.2	-81.2	-40.3
MFI	$[\text{Cu}(\text{CO})]^+$	-125.7	-119.2	-78.7	-169.3	-163.3	-121.0	-169.3	-163.3	-121.0
	$[\text{Cu}(\text{CO})_2]^+$	-51.0	-46.0	-8.9	-65.8	-63.7	-19.7	-65.8	-63.7	-19.7
MOR	$[\text{Cu}(\text{CO})]^+$	-121.4	-118.8	-72.3	-112.1	-111.3	-75.9	-112.1	-111.3	-75.9
	$[\text{Cu}(\text{CO})]^+ + \text{CO}$	-29.3	-22.5	7.6	-68.1	-62.9	-20.4	-68.1	-62.9	-20.4

#### 4. Conclusions

A pool of Cu-exchanged zeolites, bearing different topology and composition, has been systematically investigated after a high temperature reduction protocol in  $\text{NH}_3$  to quantify the amount of Cu involved in the reduction to  $\text{Cu}^+$ . Subsequently, interaction with CO at 50 °C and its desorption upon heating was investigated. MCR-assisted time-resolved XAS spectroscopy is consistent with a quantitative reduction for all studied materials, with a different spectral behaviour in the specific case of CHA. Interaction with CO at lower temperature promotes the formation of  $[\text{Cu}(\text{CO})_2]^+$  complexes, that easily decompose to  $[\text{Cu}(\text{CO})]^+$  upon flushing with inert. Once formed, the latter adducts are stable with

the exception of CHA, which shows a very slow but measurable decomposition to  $\text{Cu}^+$  and CO. In all cases, thermal treatment up to 500 °C in inert promotes the desorption of CO to form two different bare  $\text{Cu}^+$  species depending on the temperature. For CHA, the low temperature species is different compared to the one obtained by reducing the sample and cooling it down; this new species is more similar to the ones obtained for the other samples, and it is likely related to a different geometric arrangement inside the CHA pores. Isothermal volumetric CO adsorption measurements at 50 °C were in agreement with the results found by XAS: although it is more affected by the CO desorption kinetics, this indirect methodology allows  $\text{Cu}^+$  quantitative assessment without the necessity for large scale facility applications. The particular

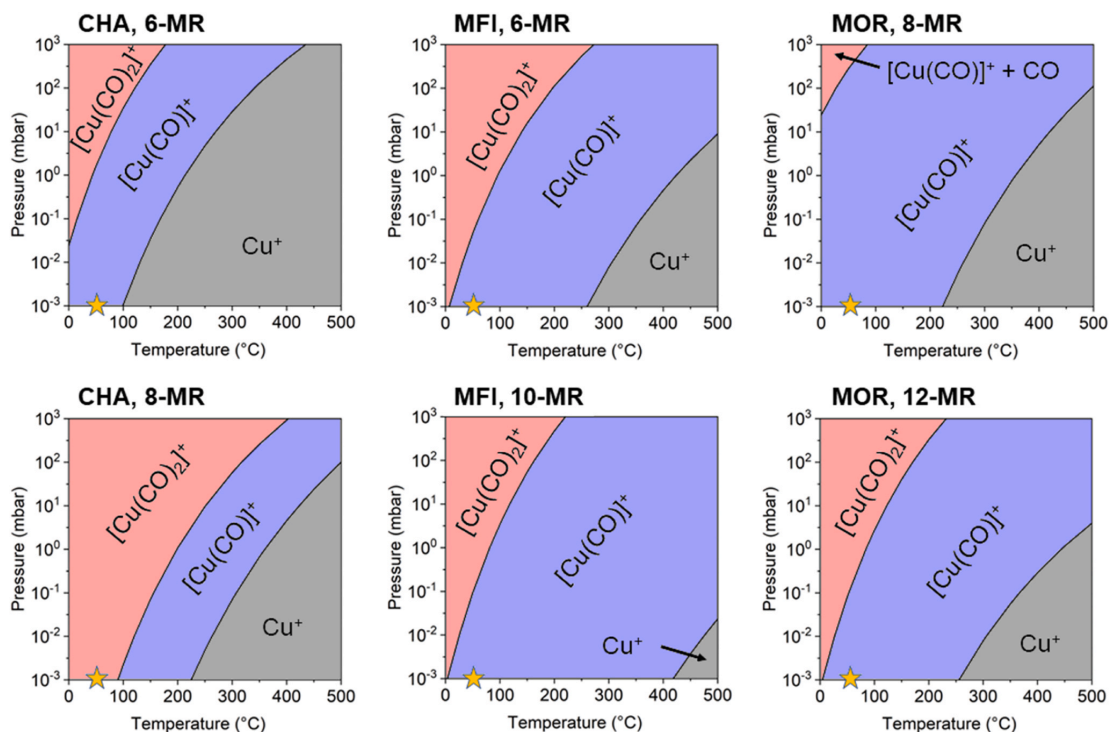


**Fig. 7.** Phase diagrams depicting the relative stabilities of isolated  $\text{Cu}^+$ ,  $[\text{Cu}(\text{CO})]^+$  and  $[\text{Cu}(\text{CO})_2]^+$  as a function of temperature and pressure, for each structural model considered in this work. Yellow stars label the condition at which  $\text{Cu}^+$  content is evaluated via monocarbonyls titration in the volumetric measurement. As can be seen in the top-right panel, no stable dicarbonyl adducts are found in the case of the 8-MR in MOR (labelled as  $[\text{Cu}(\text{CO})]^+ + \text{CO}$ ).

behaviour of CHA was studied by periodic DFT calculations and compared to properties of the other frameworks, confirming the lower stability of the carbonyl adducts for this framework; calculation of state diagrams highlighted as the dependence on the temperature and CO partial pressure were in agreement with the trends retrieved during temperature-dependent desorption analysed by MCR, with specific differences depending on the Cu siting within the different frameworks.

#### CRedit authorship contribution statement

**Gabriele Deplano:** Conceptualization; Methodology; Formal analysis; Writing – original draft; Writing – review & editing; Visualization; Investigation. **Matteo Signorile:** Conceptualization; Methodology; Data curation; Writing – original draft; Writing – review & editing; Visualization; Investigation; Supervision. **Cesare Atzori:** Methodology; Investigation. **Davide Salusso:** Investigation. **Elisa Borfecchia:** Conceptualization; Supervision. **Valentina Crocella:** Methodology; Investigation; Supervision. **Silvia Bordiga:** Conceptualization; Supervision; Project administration Funding acquisition.

#### Declaration of Competing Interest

The authors declare that they have no known competing financial interests or personal relationships that could have appeared to influence the work reported in this paper.

#### Data availability

Data will be made available on request.

#### Acknowledgements

The work is financially supported by the European Research Council (ERC), under the Horizon 2020 research and innovation program: CuBE ERC-Synergy project (Grant agreement n°856446). The authors acknowledge the European Synchrotron Radiation Facility (ESRF) for the provision of beamtime at the X-ray Absorption Spectroscopy beamline BM23. GD, MS, EB, VC and SB acknowledges support from the Project CH4.0 under the MUR program "Dipartimenti di Eccellenza 2023–2027" (CUP: D13C22003520001). This work has been partially supported by the Spoke 7 "Materials and Molecular Sciences" of ICSC – Centro Nazionale di Ricerca in High-Performance Computing, Big Data and Quantum Computing, funded by European Union – NextGenerationEU.

#### Appendix A. Supporting information

Supplementary data associated with this article can be found in the online version at [doi:10.1016/j.cattod.2023.114403](https://doi.org/10.1016/j.cattod.2023.114403).

#### References

- [1] M.A. Newton, A.J. Knorrp, V.L. Sushkevich, D. Palagin, J.A. van Bokhoven, Active sites and mechanisms in the direct conversion of methane to methanol using Cu in zeolitic hosts: a critical examination, *Chem. Soc. Rev.* (2020), <https://doi.org/10.1039/c7cs00709d>.
- [2] S. Mohan, P. Dinesha, S. Kumar, NOx reduction behaviour in copper zeolite catalysts for ammonia SCR systems: a review, *Chem. Eng. J.* (2020) 384, <https://doi.org/10.1016/j.cej.2019.123253>.
- [3] E. Borfecchia, P. Beato, S. Svelle, U. Olsbye, C. Lamberti, S. Bordiga, Cu-CHA-a model system for applied selective redox catalysis, *Chem. Soc. Rev.* 47 (22) (2018) 8097–8133, <https://doi.org/10.1039/c8cs00373d>.



- [4] V.F. Kispersky, A.J. Kropf, F.H. Ribeiro, J.T. Miller, Low absorption vitreous carbon reactors for operando XAS: a case study on Cu/zeolites for selective catalytic reduction of NOx by NH<sub>3</sub>, *Phys. Chem. Chem. Phys.* 14 (7) (2012) 2229–2238, <https://doi.org/10.1039/c1cp22992c>.
- [5] S.H. Krishna, C.B. Jones, J.T. Miller, F.H. Ribeiro, R. Gounder, Combining kinetics and operando spectroscopy to investigate the mechanism and active site requirements of NOx selective catalytic reduction with NH<sub>3</sub> on Cu-zeolites, *J. Phys. Chem. Lett.* 11 (13) (2020) 5029–5036, <https://doi.org/10.1021/acs.jpcclett.0c09093>.
- [6] L. Negahdar, N.E. Omori, M.G. Quesne, M.D. Frogley, F. Cacho-Nerin, W. Jones, S. W.T. Price, C.R.A. Catlow, A.M. Beale, Elucidating the significance of copper and nitrate speciation in Cu-SSZ-13 for N<sub>2</sub>O formation during NH<sub>3</sub>-SCR, *ACS Catal.* 11 (21) (2021) 13091–13101, <https://doi.org/10.1021/acscatal.1c03174>.
- [7] S.H. Krishna, A. Goswami, Y.J. Wang, C.B. Jones, D.P. Dean, J.T. Miller, W. F. Schneider, R. Gounder, Influence of framework Al density in chabazite zeolites on copper ion mobility and reactivity during NOx selective catalytic reduction with NH<sub>3</sub>, *Nat. Catal.* 6 (3) (2023) 276–285, <https://doi.org/10.1038/s41929-023-00932-5>.
- [8] K. Kvande, D.K. Pappas, E. Borfecchia, K.A. Lomachenko, Advanced X-ray absorption spectroscopy analysis to determine structure-activity relationships for Cu-zeolites in the direct conversion of methane to methanol, *ChemCatChem* 12 (9) (2020) 2385–2405, <https://doi.org/10.1002/cctc.201902371>.
- [9] G. Berlier, V. Crocella, M. Signorile, E. Borfecchia, F. Bonino, S. Bordiga, Characterization of Metal Centers in Zeolites for Partial Oxidation Reactions. In *STRUCTURE AND REACTIVITY OF METALS IN ZEOLITE*, in: J.P. Pariente, M. Sanchez-Sanchez (Eds.), Materials, Vol. 178, 2018, pp. 91–154, [https://doi.org/10.1007/430\\_2018\\_24](https://doi.org/10.1007/430_2018_24).
- [10] M. Mao, L.M. Liu, Z.H. Liu, Recent insights into Cu-based catalytic sites for the direct conversion of methane to methanol, *Molecules* 27 (21) (2022), <https://doi.org/10.3390/molecules27217146>.
- [11] J.L. Chen, W. Huang, S.Z. Bao, W.B. Zhang, T.Y. Liang, S.K. Zheng, L. Yi, L. Guo, X. Q. Wu, A review on the characterization of metal active sites over Cu-based and Fe-based zeolites for NH<sub>3</sub>-SCR, *RSC Adv.* 12 (43) (2022) 27746–27765, <https://doi.org/10.1039/d2ra05107a>.
- [12] B. Guan, H. Jiang, Y. Wei, Z. Liu, X. Wu, H. Lin, Z. Huang, Density functional theory researches for atomic structure, properties prediction, and rational design of selective catalytic reduction catalysts: current progresses and future perspectives, *Mol. Catal.* 510 (2021), 111704, <https://doi.org/10.1016/j.mcat.2021.111704>.
- [13] E. Broclawik, P. Kozyra, M. Mitoraj, M. Radoń, P. Rejmak, Zeolites at the molecular level: what can be learned from molecular modeling, *Molecules* (2021), <https://doi.org/10.3390/molecules26061511>.
- [14] M.H. Mahyuddin, Y. Shioita, A. Staykov, K. Yoshizawa, Theoretical overview of methane hydroxylation by copper–oxygen species in enzymatic and zeolitic catalysts, *Acc. Chem. Res.* 51 (10) (2018) 2382–2390, <https://doi.org/10.1021/acs.accounts.8b00236>.
- [15] R. Millan, P. Cnudde, V. van Speybroeck, M. Boronat, Mobility and reactivity of Cu + species in Cu-CHA catalysts under NH<sub>3</sub>-SCR-NOx reaction conditions: insights from AIMD simulations, *JACS Au* 1 (10) (2021) 1778–1787, <https://doi.org/10.1021/jacsau.1c00337>.
- [16] D.W. Fickel, R.F. Lobo, Copper coordination in Cu-SSZ-13 and Cu-SSZ-16 investigated by variable-temperature XRD, *J. Phys. Chem. C* 114 (3) (2010) 1633–1640, <https://doi.org/10.1021/jp9105025>.
- [17] U. Deka, A. Juhin, E.A. Eilertsen, H. Emerich, M.A. Green, S.T. Korhonen, B. M. Weckhues, A.M. Beale, Confirmation of isolated Cu<sup>2+</sup> ions in SSZ-13 zeolite as active sites in NH<sub>3</sub>-selective catalytic reduction, *J. Phys. Chem. C* 116 (7) (2012) 4809–4818, <https://doi.org/10.1021/jp1212450d>.
- [18] X. Tang, J. Ye, L. Guo, T. Pu, L. Cheng, X.-M. Cao, Y. Guo, L. Wang, Y. Guo, W. Zhan, S. Dai, Atomic insights into the Cu species supported on zeolite for direct oxidation of methane to methanol via low-damage HAADF-STEM, *Adv. Mater.* 35 (25) (2023) 2208504, <https://doi.org/10.1002/adma.202208504>.
- [19] J. Song, Y. Wang, E.D. Walter, N.M. Wash-ton, D. Mei, L. Kovarik, M.H. Engelhard, S. Proding, Y. Wang, C.H.F. Peden, F. Gao, Toward rational design of Cu/SSZ-13 selective catalytic reduction catalysts: implications from atomic-level understanding of hydrothermal stability, *ACS Catal.* 7 (12) (2017) 8214–8227, <https://doi.org/10.1021/acscatal.7b03020>.
- [20] A.G. Greenaway, A. Marberger, A. Thetford, I. Lezcano-González, M. Agote-Arán, M. Nachttegaal, D. Ferri, O. Kröcher, C.R.A. Catlow, A.M. Beale, Detection of key transient Cu intermediates in SSZ-13 during NH<sub>3</sub>-SCR DeNOx by modulation excitation IR spectroscopy, *Chem. Sci.* 11 (2) (2020) 447–455, <https://doi.org/10.1039/C9SC04905C>.
- [21] D.K. Pappas, E. Borfecchia, M. Dyballa, I.A. Pankin, K.A. Lomachenko, A. Martini, M. Signorile, S. Teketel, B. Arstad, G. Berlier, C. Lamberti, S. Bordiga, U. Olsbye, K. P. Lillerud, S. Svella, P. Beato, Methane to methanol: structure-activity relationships for Cu-CHA, *J. Am. Chem. Soc.* 139 (42) (2017) 14961–14975, <https://doi.org/10.1021/jacs.7b06472>.
- [22] A. Martini, E. Borfecchia, Spectral decomposition of X-ray absorption spectroscopy datasets: methods and applications, *Crystals* (2020), <https://doi.org/10.3390/cryst10080664>.
- [23] A.A. Guda, S.A. Guda, A. Martini, A.N. Kravtsova, A. Algasov, A. Bugaev, S. P. Kubrin, L.V. Guda, P. Sot, J.A. van Bokhoven, C. Copéret, A.V. Soldatov, Understanding X-ray absorption spectra by means of descriptors and machine learning algorithms, *npj Comput. Mater.* 7 (1) (2021) 203, <https://doi.org/10.1038/s41524-021-00664-9>.
- [24] C. Negri, E. Borfecchia, A. Martini, G. Deplano, K.A. Lomachenko, T.V.W. Janssens, G. Berlier, S. Bordiga, In situ X-ray absorption study of Cu species in Cu-CHA catalysts for NH<sub>3</sub>-SCR during temperature-programmed reduction in NO/NH<sub>3</sub>, *Res. Chem. Intermed.* 47 (1) (2021) 357–375, <https://doi.org/10.1007/s11164-020-04350-1>.
- [25] G. Deplano, M. Signorile, V. Crocella, N.G. Porcario, C. Atzori, B.G. Solemsli, S. Svella, S. Bordiga, Titration of Cu(I) sites in Cu-ZSM-5 by volumetric CO adsorption, *ACS Appl. Mater. Interfaces* 14 (18) (2022) 21059–21068, <https://doi.org/10.1021/acsaami.2c03370>.
- [26] C. Lamberti, S. Bordiga, M. Salvalaggio, G. Spoto, A. Zecchina, F. Geobaldo, G. Vlaic, M. Bellatreccia, I.R. XAFS, and UV–Vis study of the cui environment in Cu-ZSM-5, *J. Phys. Chem. B* 101 (3) (1997) 344–360, <https://doi.org/10.1021/jp9601577>.
- [27] H. Yamashita, M. Matsuoka, K. Tsuji, Y. Shioya, M. Anpo, M. Che, In-situ XAFS, photoluminescence, and IR investigations of copper ions included within various kinds of zeolites. Structure of Cu(I) ions and their interaction with CO molecules, *J. Phys. Chem.* 100 (1) (1996) 397–402, <https://doi.org/10.1021/jp952666g>.
- [28] A. Zecchina, S. Bordiga, G.T. Palomino, D. Scarano, C. Lamberti, M. Salvalaggio, Mono-, Di-, and tricarboxylic species in copper(D)-exchanged zeolite ZSM-5: comparison with homogeneous copper(I) carboxylic structures, *J. Phys. Chem. B* 103 (19) (1999) 3833–3844, <https://doi.org/10.1021/jp9842289>.
- [29] S. Bordiga, G. Turnes Palomino, D. Arduino, C. Lamberti, A. Zecchina, C. Otero Areán, Well defined carbonyl complexes in Ag<sup>+</sup>- and Cu<sup>+</sup>-exchanged ZSM-5 zeolite: a comparison with homogeneous counterparts, *J. Mol. Catal. A Chem.* 146 (1–2) (1999) 97–106, [https://doi.org/10.1016/S1381-1169\(99\)00082-5](https://doi.org/10.1016/S1381-1169(99)00082-5).
- [30] T.V.W. Janssens, H. Falsig, L.F. Lundegaard, P.N.R. Venneström, S.B. Rasmussen, P. G. Moses, F. Giordanino, E. Borfecchia, K.A. Lomachenko, C. Lamberti, S. Bordiga, A. Godiksen, S. Mossin, P. Beato, A consistent reaction scheme for the selective catalytic reduction of nitrogen oxides with ammonia, *ACS Catal.* 5 (5) (2015) 2832–2845, <https://doi.org/10.1021/cs501673g>.
- [31] D.K. Pappas, A. Martini, M. Dyballa, K. Kvande, S. Teketel, K.A. Lomachenko, R. Baran, P. Glatzel, B. Arstad, G. Berlier, C. Lamberti, S. Bordiga, U. Olsbye, S. Svella, P. Beato, E. Borfecchia, The nuclearity of the active site for methane to methanol conversion in Cu-mordenite: a quantitative assessment, *J. Am. Chem. Soc.* 140 (45) (2018) 15270–15278, <https://doi.org/10.1021/jacs.8b08071>.
- [32] G. Deplano, A. Martini, M. Signorile, E. Borfecchia, V. Crocella, S. Svella, S. Bordiga, Copper pairing in the mordenite framework as a function of the Cu/I cation speciation, *Angew. Chem. - Int. Ed.* 60 (49) (2021) 25891–25896, <https://doi.org/10.1002/anie.202109705>.
- [33] O. Mathon, A. Beteva, J. Borrel, D. Bugnazet, S. Gatla, R. Hino, I. Kantor, T. Mairs, M. Munoz, S. Pasternak, F. Perrin, S. Pascarelli, The time-resolved and extreme conditions XAS (TEXAS) facility at the european synchrotron radiation facility: the general-purpose EXAFS bending-magnet beamline BM23, *J. Synchrotron Radiat.* 22 (6) (2015) 1548–1554, <https://doi.org/10.1107/S1600577515017786>.
- [34] <https://doi.esrf.fr/10.1515/ESRF-ES-780223803>.
- [35] D. Bellet, B. Gorges, A. Dallery, P. Bernard, E. Pereira, J. Baruchel, A 1300K furnace for (in situ) X-ray microtomography, *J. Appl. Crystallogr.* 36 (2) (2003) 366–367, <https://doi.org/10.1107/S0021889803001158>.
- [36] C. Lamberti, S. Bordiga, F. Bonino, C. Prestipino, G. Berlier, L. Capello, F. D'Acapito, F.X. i Xamena, A. Zecchina, Determination of the oxidation and coordination state of copper on different Cu-based catalysts by XANES spectroscopy in situ or in operando conditions, *Phys. Chem. Chem. Phys.* 5 (20) (2003) 4502–4509, <https://doi.org/10.1039/B305810G>.
- [37] S. Bordiga, E. Groppo, G. Agostini, J.A. van Bokhoven, C. Lamberti, Reactivity of surface species in heterogeneous catalysts probed by in situ X-ray absorption techniques, *Chem. Rev.* 113 (3) (2013) 1736–1850, <https://doi.org/10.1021/cr2000898>.
- [38] M. Newville, Larch: an analysis package for XAFS and related spectroscopies, *J. Phys. Conf. Ser.* 430 (1) (2013) 12007, <https://doi.org/10.1088/1742-6596/430/1/012007>.
- [39] J. Jaumot, R. Gargallo, A. de Juan, R. Tauler, A graphical user-friendly interface for MCR-ALS: a new tool for multivariate curve resolution in MATLAB, *Chemom. Intell. Lab. Syst. J.* 76 (1) (2005) 101–110, <https://doi.org/10.1016/j.chemolab.2004.12.007>.
- [40] C. Ruckebusch, Resolving Spectral Mixtures: With Applications from Ultrafast Time-Resolved Spectroscopy to Super-Resolution Imaging, Elsevier, Amsterdam, 2016.
- [41] P. Conti, S. Zamponi, M. Giorgetti, M. Berrettoni, W.H. Smyrl, Multivariate curve resolution analysis for interpretation of dynamic Cu K-edge X-ray absorption spectroscopy spectra for a Cu doped V2O5 lithium battery, *Anal. Chem.* 82 (9) (2010) 3629–3635, <https://doi.org/10.1021/ac902865h>.
- [42] Crocella, V.; Atzori, C.; Latini, G.; Signorile, M. A Kit for Volumetric Measurements of Gas Adsorption. PCT/IB2021/051769, 2021.
- [43] A. Erba, J. Baima, I. Bush, R. Orlando, R. Dovesi, Large-scale condensed matter DFT simulations: performance and capabilities of the crystal code, *J. Chem. Theory Comput.* 13 (10) (2017) 5019–5027, <https://doi.org/10.1021/acs.jctc.7b00687>.
- [44] [https://europe.iza-structure.org/IZA-SC/ftc\\_table.php](https://europe.iza-structure.org/IZA-SC/ftc_table.php).
- [45] A.D. Becke, A new mixing of hartree-fock and local density-functional theories, *J. Chem. Phys.* 98 (2) (1993) 1372–1377, <https://doi.org/10.1063/1.464304>.
- [46] C. Lee, W. Yang, R.G. Parr, Development of the colle-salvetti correlation-energy formula into a functional of the electron density, *Phys. Rev. B* 37 (2) (1988) 785–789, <https://doi.org/10.1103/PhysRevB.37.785>.
- [47] S. Grimme, J. Antony, S. Ehrlich, H. Krieg, A consistent and accurate ab initio parametrization of density functional dispersion correction (DFT-D) for the 94 elements H-Pu, *J. Chem. Phys.* 132 (15) (2010), 154104, <https://doi.org/10.1063/1.3382344>.
- [48] R. Nada, J.B. Nicholas, M.I. McCarthy, A.C. Hess, Basis sets for Ab initio periodic hartree-fock studies of zeolite/adsorbate interactions: He, Ne, and Ar in silica sodalite, *Int. J. Quantum Chem.* 60 (1996) 809–820.

- [49] M. Catti, G. Valerio, R. D. and M. C. Quantum-mechanical calculations of the solid-state equilibrium  $\text{MgO} + \text{Alpha-Al}_2\text{O}_3 \text{ MgAl}_2\text{O}_4$  (Spinel) versus pressure, *Phys. Rev. B* 49 (1994) 14179–14187.
- [50] A. Schäfer, C. Huber, R. Ahlrichs, Fully optimized contracted gaussian basis sets of triple zeta valence quality for atoms Li to Kr, *J. Chem. Phys.* 100 (8) (1994) 5829–5835, <https://doi.org/10.1063/1.467146>.
- [51] Dovesi, R.; Saunders, V.R.; Roetti, C.; Orlando, R. et al. CRYSTAL17 User's Manual. 2017.
- [52] D.W. Breck, *Zeolite Molecular Sieves: Structure, Chemistry, and Use*, Wiley, New York, 1974.
- [53] C. Paolucci, I. Khurana, A.A. Parekh, S. Li, A.J. Shih, H. Li, J.R. Di Iorio, J. D. Albarracin-Caballero, A. Yezerets, J.T. Miller, W.N. Delgass, F.H. Ribeiro, W. F. Schneider, R. Gounder, Dynamic multinuclear sites formed by mobilized copper ions in NOx selective catalytic reduction, 898 LP – 903, *Sci. (80-. )* 357 (6354) (2017), <https://doi.org/10.1126/science.aan5630>.
- [54] M. Signorile, E. Borfecchia, S. Bordiga, G. Berlier, Influence of ion mobility on the redox and catalytic properties of Cu ions in zeolites, *Chem. Sci.* 13 (35) (2022) 10238–10250, <https://doi.org/10.1039/D2SC03565K>.
- [55] G. Turnes Palomino, A. Zecchina, E. Giamello, P. Fiscaro, G. Berlier, C. Lamberti, S. Bordiga, Polycarboxylic and Polynitrosylic Species in CuI-Exchanged ZSM-5,  $\beta$ , Mordenite and Y Zeolites: Comparison with Homogeneous Complexes. In *12th International Congress on Catalysis*, in: A. Corma, F.V. Melo, S. Mendioroz, J.L. G. Fierro (Eds.), *Studies in Surface Science and Catalysis*, Vol. 130, Elsevier, 2000, pp. 2915–2920, [https://doi.org/10.1016/S0167-2991\(00\)80914-3](https://doi.org/10.1016/S0167-2991(00)80914-3).
- [56] K. Góra-Marek, A.E. Palomares, A. Glanowska, K. Sadowska, J. Datka, Copper sites in zeolites - quantitative IR studies, *Microporous Mesoporous Mater.* 162 (2012) 175–180, <https://doi.org/10.1016/j.micromeso.2012.06.029>.
- [57] K.A. Tarach, M. Jablonska, K. Pyra, M. Liebau, B. Reiprich, R. Glaser, K. Góra-Marek, Effect of zeolite topology on NH3-SCR activity and stability of Cu-exchanged zeolites, *Appl. Catal. B-Environ.* (2021) 284, <https://doi.org/10.1016/j.apcatb.2020.119752>.